Deformation of Tibet: InSAR analysis and viscous flow models

Matthew Campbell Garthwaite

Submitted in accordance with the requirements for the degree of
Doctor of Philosophy

The University of Leeds
School of Earth and Environment
November 2011

Declaration

The candidate confirms that the work submitted is his own, except where work which has formed part of jointly-authored publications has been included. The contribution of the candidate and the other authors to this work has been explicitly indicated below. The candidate confirms that appropriate credit has been given within the thesis where reference has been made to the work of others.

Chapter 5 contains material from the publication:

Garthwaite, M. C. and G. A. Houseman (2011), Validity of the thin viscous sheet approximation in models of continental collision, *J. Geophys. Res.*, *116*(B02404), doi:10.1029/2010JB007770.

In this paper, Matthew Garthwaite carried out the numerical modelling and wrote the paper, whilst Gregory Houseman provided the codes and contributed to the writing.

Acknowledgements

Completing this PhD would not have been possible without the help and encouragement of the following people.

Firstly, I thank my supervisors Greg Houseman and Tim Wright. They have taught me a lot about how to conduct scientific research and their support, patience and advice has been excellent. Many thanks also to Philip England and Andy Shepherd for taking the time out from busy schedules to examine this thesis.

I am indebted to Hua Wang for his extensive assistance and ideas with the InSAR work and for developing the *π-rate* software. His contribution was like that of a third supervisor. Thanks to Piroska Lorinczi and Lynn Evans for assistance with the *Oregano* and *Basil* programs respectively. Richard Rigby deserves a special mention for providing excellent IT support throughout my PhD. Numerous ideas were borne out of stimulating discussions with members of the COMET+ group and the Institute of Geophysics and Tectonics at Leeds.

This research was made possible with funding from a NERC quota studentship (NE/F008325/1). I am also grateful for the travel grants awarded by the Royal Astronomical Society and the Geological Remote Sensing Group. ESA and the Dragon initiative are acknowledged for providing the SAR data used in this thesis. Most figures in this thesis have been produced using the excellent open-source Generic Mapping Tools (GMT) software.

Many thanks to the following people for providing materials from their own work, sometimes in advance of publication: John Elliott provided his coseismic model files for the Damxung earthquake; Isabelle Ryder provided her viscoelastic model input files for the Kokoxili postseismic signal and gave assistance with the use of the VISCO1D software; Brendan Meade provided his block model profile data plotted in Figure 7.2.

Thanks to all those I have shared an office with during my time at Leeds, and those who have shared numerous cups of tea or pints of beer. A particular shout out goes to members of the 'Unit' (Carl, Ian, Paddy, Ben and Tom), Hannah, Haggis, Julia, Babs and Sheona. My time in Leeds has been all the better for times shared with these guys. A special thank you to Julia and Steven for graciously giving me a place to stay during the final weeks of my write up.

Finally, thanks to my family for their unwavering love and support over the years, my good friends Ian and Sam for providing an 'electronic' ear for my problems, and to Kat for being there for me and sharing the highs and lows of the PhD process.

Abstract

The Tibetan plateau in central Asia is a prime example of the distributed deformation that occurs in the lithosphere as a result of continental collision. Large scale lithospheric deformation can be estimated using viscous continuum models that balance the vertical stress induced by lateral variations of potential energy, and horizontal stress induced by tectonic boundary forces. I find that the 2-dimensional Thin Viscous Sheet (TVS) model gives a good approximation to deformation during continental collision, providing that the indenter half-width is greater than the lithospheric thickness. However even when this ratio approaches one, reasonable correspondence exists when the strain-rate exponent (n) of the rheological constitutive law is ≤ 3.

By applying the TVS to model the contemporary deformation of Asia, I find that the first order features of the geodetically-determined velocity field can be explained. Models which can best predict the observed velocity field have n between 2 and 5, Argand numbers of between 1 and 4, and the strength of the Tibetan plateau and Tien Shan is between 3 and 8 times weaker than the foreland regions. Models with these parameters give a value of F_L = 7-15x10^{12} N m^{-1} for the vertically integrated horizontal driving force on the Himalayan arc.

I describe the *π-rate* method for determining slow linear deformation rates from Interferometric Synthetic Aperture Radar (InSAR) observations and validate it using synthetic data. When using real data, the *π-rate* method out-performs the conventional stacking method. The RMS difference between the two methods and observed GPS measurements are 3.7 and 7.1 mm/yr for *π-rate* and stacking respectively.

I used the *π-rate* method to determine the interseismic velocity field across the Tibetan plateau in an approximately north-south orientated, $\sim$1000 km-long swath using ESA Envisat data spanning a period of 6.23 years. The resulting InSAR rate map indicates a factor of 2 variation in the magnitude of line-of-sight (LOS) velocity between the latitudes of 29-40^{o}N. Significant localisation of deformation around mapped fault zones is not observed. A deviation of up to 8 mm/yr in LOS between the InSAR rate map and GPS-derived horizontal velocity field suggests either $\sim$8 mm/yr of vertical uplift, an additional $\sim$20 mm/yr of eastward motion, or a combination of horizontal and vertical motion that has not been measured using horizontal-component campaign GPS data. Comparison of InSAR and GPS observations with predictions of kinematic block and viscous continuum models suggests that the latter provides a more useful description for large-scale continental deformation.

Contents

List of Figures

List of Tables

Conventions

Symbols

	InSAR	**Modelling**
α	Noise decay length scale	
$\mathbf{A}$	Design matrix for inversion	
Ar		Argand number
B		Viscosity coefficient
$\mathbf{B}$	Interferometric baseline	
$B_{\parallel}$	Parallel baseline	
$B_{\perp}$	Perpendicular baseline	
Γ		Dimensionless boundary-normal traction
γ	Interferometric coherence	Mean difference measure
Δ	Difference	Difference
$\mathbf{d}$	Data observations for inversion	
D		Horizontal model length scale
$\dot{\varepsilon}$		Strain rate
$\dot{E}$		Second invariant of the strain--rate tensor
e		Surface elevation
F_L		Vertically integrated strength
g		Gravitational acceleration
η		Viscosity
θ	Incidence angle	
κ	Finite difference smoothing--parameter	Standard deviation difference--measure
λ	Radar wavelength	Maximum difference measure
L		Lithospheric thickness
μ	Shear modulus	Shear modulus
$\mathbf{m}$	Model parameters for inversion	

	InSAR	**Modelling**
n		Power-law exponent, or strain--rate exponent
Ξ	Rate map residual--ratio threshold	
ξ		3D Argand number equivalent
p		Pressure
ρ		Density
r	Path length	
R		Earth radius
Σ_Φ	Variance-covariance matrix	
Σ_v	Errors on the rate	
σ	Covariance	Stress
S		Crustal thickness
τ		Deviatoric stress
$\mathbf{T}$	Interferometric time-spans	
t	Time	Time
Υ	Rate map maximum standard--deviation threshold	
u, U		Velocity
v, V	Velocity or rate	
Φ	Interferometric displacement	
ϕ	Interferometric phase	
Ψ	Rate map coherent observations--threshold	
Ω		Vorticity
ω		Angular velocity

Abbreviations

2D	2-dimensional
3D	3-dimensional
APS	Atmospheric Phase Screen
ASI	Italian Space Agency
ATF	Altyn Tagh Fault
BNS	Bangong-Nujiang Suture
CONAE	Argentinian space agency
CSA	Canadian Space Agency
CTCFZ	Central Tibet Conjugate Fault Zone
DEM	Digital Elevation Model
DLR	German Aerospace Center
DORIS	Doppler Orbitography and Radio-positioning Integrated by Satellite
EHS	Eastern Himalayan Syntaxis
ESA	European Space Agency
FDS	Finite Difference Smoothing
FEM	Finite Element Method
FFT	Fast Fourier Transform
GPE	Gravitational Potential Energy
GPS	Global Positioning System
GSRM	Global Strain Rate Map
IZS	Indus-Zangbo Suture
IDM	Initial Deformation Model
InSAR	Interferometric SAR
JAXA	Japan Aerospace eXploration Agency
LAB	Lithosphere-Asthenosphere Boundary
LOS	Line-Of-Sight
MCF	Minimum Cost Flow
MFT	Main Frontal Thrust
MST	Minimum Spanning Tree
NASA	National Aeronautics and Space Administration (USA)
PS	Persistent Scatterer method
RDC	Range-Doppler Coordinates
RMS	Root Mean Square
SAR	Synthetic Aperture Radar
SBAS	Small BAseline Subset method
SLC	Single Look Complex
SNR	Signal to Noise Ratio
SRTM	Shuttle Radar Topography Mission
SVD	Singular Value Decomposition
TVS	Thin Viscous Sheet
VCM	Variance-Covariance Matrix

Chapter 1

Introduction

Tectonic forces are responsible for the deformation occurring in the continents we live on. These forces cause large earthquakes that can devastate populations situated close to the epicentre. During the course of my PhD research, 5 particularly damaging earthquakes have occurred within continental settings: Sichuan, China (12/05/2008), L'Aquila, Italy (6/4/2009), Port-au-Prince, Haiti (12/01/2010), Christchurch, New Zealand (22/02/2011) and Van, Turkey (23/10/2011). These earthquakes all caused devastating loss of life and destruction, yet little was known beforehand about the seismic hazard of the faults that ruptured. This again reminds us that as a society, we are still a long way off being able to forecast when and where earthquakes might occur. In order that we might move toward this goal, it is of great importance that we study the tectonic deformation in continents so that global seismic hazard assessment can be improved. Even if predictions are impossible in the short time periods leading up to an earthquake (as some researchers believe, e.g. Geller et al., 1997), identification of the locations that are most at risk can help mitigate the human effects of earthquakes.

In this thesis, I measure the present day velocity field in Tibet using satellite based geodetic observations. I also use continent-scale models to interpret the broader scale velocity field of Asia and quantify the forces that are driving continental collision in this region. Models of this type can be used to identify those regions where seismic hazard is elevated.

1.1 Plate tectonic theory

The theory of plate tectonics was formalised in the late 1960s and brought the separate ideas of continental drift and sea-floor spreading together into a widely accepted

framework for describing the kinematic behaviour of the Earth's uppermost layer. The following important concepts form the basis of the theory (Le Pichon et al., 1973):

1 The mechanical behaviour of the crust and mantle layers depends on a rheological stratification involving a strong 'lithosphere' overlying a weaker 'asthenosphere' (e.g. McKenzie, 1967, Oliver and Isacks, 1967).

2 The lithosphere can be split into a small number of rigid 'plates', whose relative motions on a spherical Earth can be described as a rotation around an Euler pole (e.g. Morgan, 1968, McKenzie and Parker, 1967, Le Pichon, 1968).

3 The vast majority of strain at the Earth's surface is along narrow zones which coincide with plate boundaries (e.g. Isacks et al., 1968).

The theory successfully explains the motion of plate interiors and their interaction at oceanic plate boundaries, but it has long been recognised that some aspects of the theory inadequately describe the situation at continental plate boundary zones (e.g. McKenzie, 1972, Molnar and Tapponnier, 1975). In particular, concepts 2 and 3 come into question since global seismicity (Figure 1.1) shows distributed deformation across continental regions. Therefore the global definition of a relatively small number of tectonic plates is inadequate to describe the observations in the continents.

In general, earthquakes at oceanic plate boundaries are tightly clustered in a narrow zone no more than 100 km wide. Relatively few occur in oceanic plate interiors, except where there is a hot-spot (e.g. Hawaii in the Pacific ocean). Perhaps the biggest exception to this rule is a diffuse zone of deformation around the Indo-Australian plate boundary in the Indian Ocean (e.g. Molnar et al., 1993, Royer and Gordon, 1997). Although it is not realistic to assume that oceanic tectonic plates are rigid throughout their interiors, the amount of internal deformation is insignificant in most places compared with the net motion observed (e.g. Kreemer et al., 2003, Kreemer, 2009)). Earthquakes at continental plate boundaries are often distributed across a much wider zone which can extend for thousands of kilometres into the plate interior (Figure 1.1).

The number of individual plates in global plate models has increased through time, from 20 at the advent of plate tectonics (Morgan, 1968) to 52 in a recent compilation (Bird, 2003; plotted in Figure 1.1). Part of the reason for this is the increase in the quality and quantity of plate motion observations, which prove to be more difficult

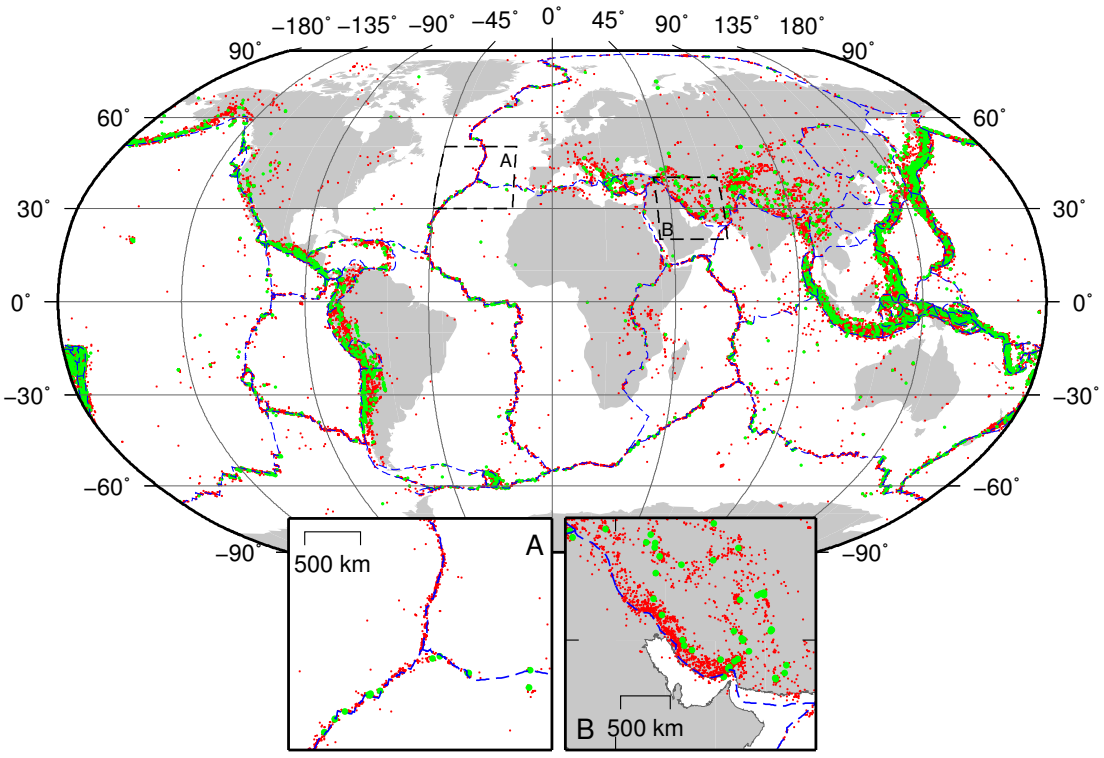

Figure 1.1: Main map: global distribution of seismicity with M≥5.0 since 1973 (data from USGS catalogue at http://earthquake.usgs.gov/earthquakes/eqarchives/epic/). Inset A: close up view of the oceanic plate boundary zone in the Mid-Atlantic Ocean. Inset B: close up view of the continental plate boundary zone in Iran. Red dots are 5.0≤M<6.0 earthquakes and green dots are M≥6.0 earthquakes. Dashed blue lines are the boundaries of 52 plates as defined by Bird (2003).

to fit with simple models. As a result, global models have become more complex with the addition of smaller 'micro'-plates in order to improve the overall fit to the data. MORVEL (DeMets et al., 2010) is the most recent global model that quantifies geologically-recent plate motions for the 25 largest tectonic plates in Bird's model. This is a significant improvement on the 12 plates modelled in the earlier NUVEL-1 and NUVEL-1A models (DeMets et al., 1990, 1994). Summed least-squares differences between GPS observations and model estimates are 50% larger for NUVEL-1A than MORVEL (DeMets et al., 2010).

Plate-like models constrained by increasingly large geodetic data-sets have been used to study the distributed deformation in individual continental plate boundary zones. These 'micro-plate' or 'block' models differ from global plate models in that the length scale of the blocks is much smaller (10^0-10^2 km) and departures from block rigidity can often be measured (Thatcher, 2009). As the block length scale becomes smaller, the re-

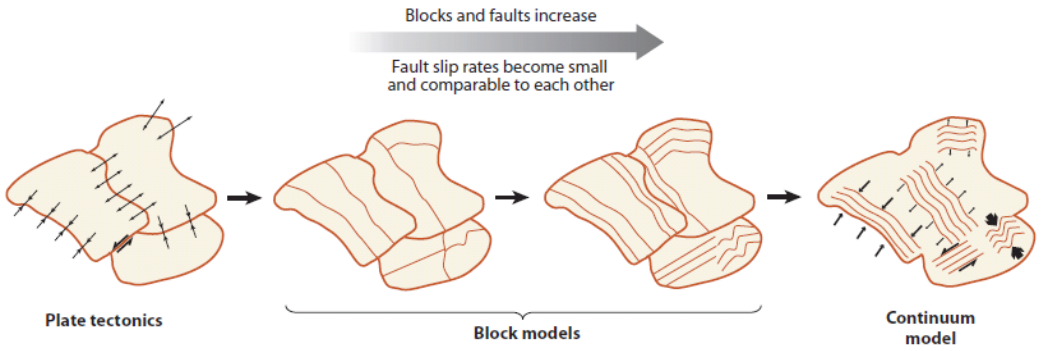

Figure 1.2: Cartoon of the transition from global plate models, through continental-scale block models to continuum models. After Thatcher (2009).

sulting kinematic deformation becomes indistinguishable from a continuum description in which spatial deformation gradients are low and vary smoothly (Figure 1.2). The length scale of blocks is often required to be only a few tens of kilometres when the geodetic observation density is very dense, for example in south California (Meade and Hager, 2005) and Nevada (Hammond et al., 2011). However, larger blocks can often be used to model deformation adequately where geodetic observations are sparser, for example in Tibet (Thatcher, 2007, Meade, 2007). Floyd et al. (2010) find that multiple block configurations can explain the observed GPS velocity field in Greece and the Aegean equally well, providing the block length scale is in the 100-200 km range. However, they find that a continuum description gives a better fit than the best block models. Further description of block and continuum models with application to the Tibetan plateau is given in §2.6.

1.2 Lithospheric rheology

The relative success of plate tectonics in describing deformation in oceanic and continental regions can be attributed to the differing rheologies of oceanic and continental lithosphere (Chen and Molnar, 1983). The increase of temperature and pressure with depth within the Earth results in distinctive variations in rheological strength within the oceanic and continental lithosphere, which are dependent on composition (Figure 1.3; Jackson, 2002, Bürgmann and Dresen, 2008).

The strength of the upper crust is limited by faults on which slip occurs, often in the form of earthquakes. This behaviour follows a linear friction law known as Byerlee's law,

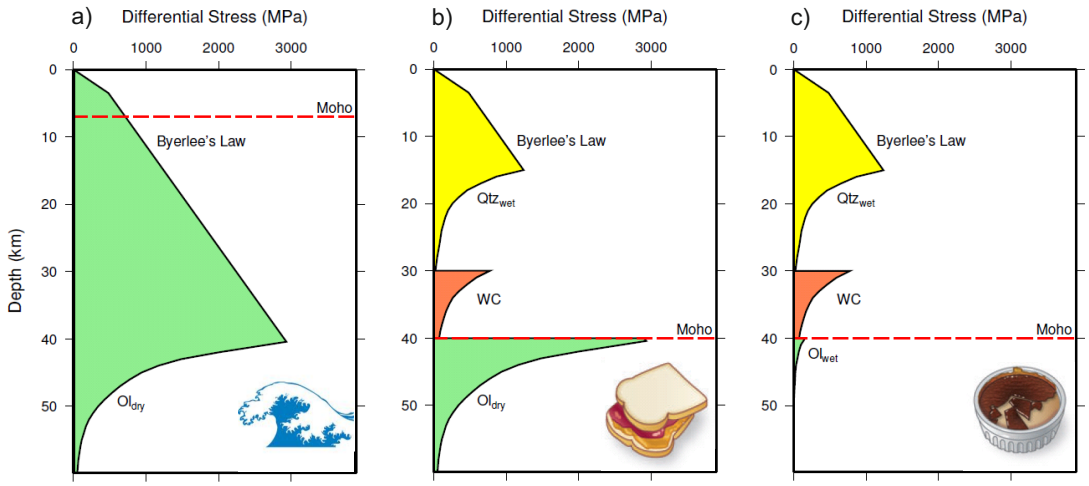

Figure 1.3: Comparison of indicative Brace-Goetze type strength envelopes for a) oceanic, b) jelly sandwich and c) crème brûlée rheologies reproduced from Elliott (2009) after Jackson (2002). Byerlee's law describes the frictional failure controlling brittle deformation (straight line). Viscous deformation occurs in either wet or dry quartz (Qtz), olivine (Ol), or undried granulite (WC). Differential stresses are calculated at a strain-rate of 10^{-15} s^{-1}.

with friction coefficients in the range of 0.6-1.0 from laboratory testing (Byerlee, 1978). The pressure dependence of the friction law ensures that the strength of rock increases with depth. However, this strength increase is tempered by ductile creep processes that are activated by the increase in temperature with depth. These creep processes act to reduce the viscous strength and give rise to a brittle-ductile transition zone at depth. At low stress levels the dominant creep mechanism is diffusion, in which atoms migrate through vacancies in the crystalline lattice. Deformation is Newtonian since the relationship between stress and strain rate is linear. As the stress level increases, diffusion gives way to dislocation creep where imperfections in the crystal lattice migrate through the material. Deformation is non-Newtonian, with a power-law relationship between stress and strain rate.

Oceanic crust and mantle are both composed predominantly of olivine with an empirically-derived flow law that applies when the differential stress ($(\sigma_1 - \sigma_3)$, where σ_1 and σ_3 are the maximum and minimum principal stresses respectively) is greater than 200 MPa (Goetze, 1978):

$$(\sigma_1 - \sigma_3) = \sigma_o \left(1 - \sqrt{\frac{RT}{Q_o} \ln\left(\frac{\dot{\varepsilon}_o}{\dot{\varepsilon}}\right)}\right) \tag{1.1}$$

where σ_o is the critical stress which must be exceeded, $\dot{\varepsilon}_o$ is the critical strain rate,

Q_o is the activation energy for olivine creep, R is the universal gas constant and T is temperature. On the other hand, the continental crust is composed predominantly of weaker quartz with an empirically derived flow law of the form (Brace and Kohlstedt, 1980):

$$(\sigma_1 - \sigma_3) = \left(\frac{\dot{\varepsilon}}{A_q}\right)^{\frac{1}{n}} \exp\left(\frac{Q_q}{nRT}\right) \tag{1.2}$$

where A_q is a material constant for quartz, Q_q is the activation energy for quartz, R is the universal gas constant, T is temperature and n is the power-law exponent for quartz (Brace and Kohlstedt (1980) find that $n \approx 3$).

These flow laws, plotted in Figure 1.3, show that olivine is stronger than quartz at the same temperature. Therefore the upper region of strength penetrates deeper in oceanic lithosphere (~50 km) than in the continents (~25 km) (Brace and Kohlstedt, 1980). Large uncertainties in the applicability of these flow laws exist due to the extrapolation of laboratory results to the low ambient strain rates occurring geologically. Additionally, the presence of water can significantly reduce the viscous strength of olivine, quartz and other rock constituents (Bürgmann and Dresen, 2008). As a result, debate continues on the distribution of strength in the continental lithosphere (e.g. Jackson, 2002, Burov and Watts, 2006). Two possible models have been termed the 'jelly sandwich' and 'crème brûlée' models.

1.2.1 Jelly sandwich

The 'jelly sandwich' model (Figure 1.3b) arose from the laboratory experiments of Brace and Kohlstedt (1980) and the focal depth observations of Chen and Molnar (1983). This rheology contains two zones of strength in the upper crust and upper mantle, separated by a weaker zone in the lower crust. The implication of this rheological structure is that the upper mantle is the strongest part and controls overall lithospheric deformation.

Based on this assumption, Sonder and England (1986) showed that the vertical average of the continental rheological profile can be well approximated by a single power-law relationship over a range of tectonic conditions and for strain rates in the range 10^{-13}-10^{-17} s^{-1}. They calculate the vertically integrated strength of the lithosphere as:

$$F_L = \int_0^L (\sigma_1 - \sigma_3)\, dz \tag{1.3}$$

where L is the lithospheric thickness. For values of F_L corresponding with the magnitudes of tectonic driving forces (see §1.3.3), Sonder and England (1986) estimate a power law exponent n of between 5 and 10 for describing deformation of the whole lithosphere. Molnar and Lyon-Caen (1988) find that the value of F_L required to support the elevated Tibetan plateau is on the order of ~7 x 10^{12} N m^{-1}, whereas Copley et al. (2010) estimate a value of 5-6 x 10^{12} N m^{-1}. The simplified rheology of Sonder and England (1986) has been used in 2-dimensional numerical models which explain continental deformation as a viscous continuum (see §2.6.3 and Chapter 5).

1.2.2 Crème Brûlée

Jackson (2002) contested the applicability of the jelly sandwich model based on reassessed earthquake depths and gravity anomalies. He instead proposes the crème brûlée model (later named by Burov and Watts (2006)) in which the lower crust is stronger than the lithospheric mantle beneath (Figure 1.3c). Improved data quality allowed Maggi et al. (2000a,b) to find that earthquakes previously thought to be in the mantle might actually have occurred in the lower crust. This observation suggests the existence of a single layer of strength in the lithosphere concentrated in the upper crust, but extending over the whole crust in Precambrian shield areas. A full review of the arguments for a crème brûlée rheology is given by Jackson et al. (2008).

Burov and Watts (2006) argue that the crème brûlée model is only appropriate for certain tectonic settings and the jelly sandwich is more widely applicable. Using numerical models, they demonstrate that a lithosphere with jelly sandwich rheology can promote the long term stability of high topography whereas a lithosphere with crème brûlée rheology cannot. However, Jackson et al. (2008) point out that in the case of the Himalayan orogen, support is provided by under-thrust rigid Indian crust rather than a strong lithospheric mantle.

Burov and Watts (2006) also show that the process of lithospheric subduction requires a strong mantle in order to maintain the integrity of the down-going slab. With a weak mantle rheology, instabilities tend to develop at the base of the lithosphere resulting in convective removal of the mantle lithosphere and the collapse of surface topography. A similar dynamic situation has been proposed to explain deformation in the Carpathian-Pannonian orogeny (Houseman and Gemmer, 2007).

Although advances have been made in recent years, the rheology of the continents remains a great unknown. Knowledge of the strength of the lithosphere is critical for understanding the elastic stress cycle in the brittle upper crust, and thereby quantifying earthquake hazard. It is still a matter of debate whether the distributed style of continental deformation is controlled by viscous flow in a mantle stronger than the crust, or by weakened shear zones penetrating throughout the lithosphere where the crust represents the strongest layer (Bürgmann and Dresen, 2008).

1.3 Dynamic analysis of continental collision

Plate tectonic models are concerned only with the kinematic description of plate motion; that is the horizontal motion of the plates on a spherical surface. Although this is adequate for undeforming plate interiors, it breaks down at collisional plate boundary zones where vertical motions associated with mountain building are produced.

The collision of two continental plates often results in mountain building over a very broad area. This is in contrast to collision between oceanic plates which generally results in subduction of one relatively undeformed plate beneath the other. The reasons for this difference are the contrast in strength, density and thickness between oceanic and continental lithosphere (Stüwe, 2002). The larger thickness and lower density of continental lithosphere makes it difficult to subduct, whilst the lower strength means that internal deformation processes can occur that accommodate the convergent strain. The process of deformation in such tectonic regimes can be described by analysing the forces acting on the lithosphere and the response to these forces.

1.3.1 State of stress

The state of stress in the lithosphere can be described using a 9 component tensor:

$$\sigma_{ij} = \begin{bmatrix} \sigma_{xx} & \sigma_{xy} & \sigma_{xz} \\ \sigma_{yx} & \sigma_{yy} & \sigma_{yz} \\ \sigma_{zx} & \sigma_{zy} & \sigma_{zz} \end{bmatrix} \tag{1.4}$$

wherein the diagonal elements with repeated indices are the 'normal' stress components, the remaining 6 components are 'shear' stresses and x, y and z are the three Cartesian coordinate directions. Normal stresses are directed perpendicular to the plane upon which they act, whereas shear stresses act parallel to the plane. By rotating the co-

ordinate system so that the shear stress components equal zero, the normal stresses become the 'principal' stresses σ_1, σ_2 and σ_3 from most to least compressive. If the state of stress in the lithosphere is isotropic all principal stress components are equal, and are equivalent to the pressure:

$$p = \sigma_1 = \sigma_2 = \sigma_3. \tag{1.5}$$

When the principal stresses are not equal, the pressure is equal to their average.

1.3.2 Isostasy

The continental crust tends to be more buoyant than the underlying mantle because the density of the main constituent of crustal rocks (quartz) is less dense than that of the mantle (olivine; $\rho_{\text{quartz}} = 2.65$ g cm^{-2} and $\rho_{\text{olivine}} = 3.27$ g cm^{-2}). A form of hydrostatic equilibrium exists between the crust and the mantle, known as isostatic equilibrium. Isostatic equilibrium is an idealised state in which vertical columns of material above some 'compensation' depth have equal mass. If the force per unit area acting on a material column is increased (for instance, by crustal thickening during orogenesis, or by the onset of glaciation) then the surface elevation will adjust to accommodate this. Increasing the surface elevation requires the development of a low density root at depth in order to maintain isostatic equilibrium (Turcotte and Schubert, 1982). Assuming Airy-type isostatic compensation in which the crust and mantle layers have constant density ρ_c and ρ_m respectively, the crustal thickness S can be estimated from surface topography e (Turcotte and Schubert, 1982, Stüwe, 2002):

$$S = S_0 + \frac{\rho_m(e - e_0)}{\rho_m - \rho_c} \tag{1.6}$$

where S_0 is the crustal thickness of a reference column with a surface elevation of e_0.

1.3.3 Driving forces

It is generally thought that the 'ridge push' and 'slab pull' forces in oceanic lithosphere are primarily responsible for driving plate tectonics (Stüwe, 2002; and references therein). Ridge push acts on young oceanic lithosphere whose topography gives increased gravitational potential energy (GPE) that results in a horizontal force directed away from the ridge. Slab pull occurs at subduction zones where subducted oceanic

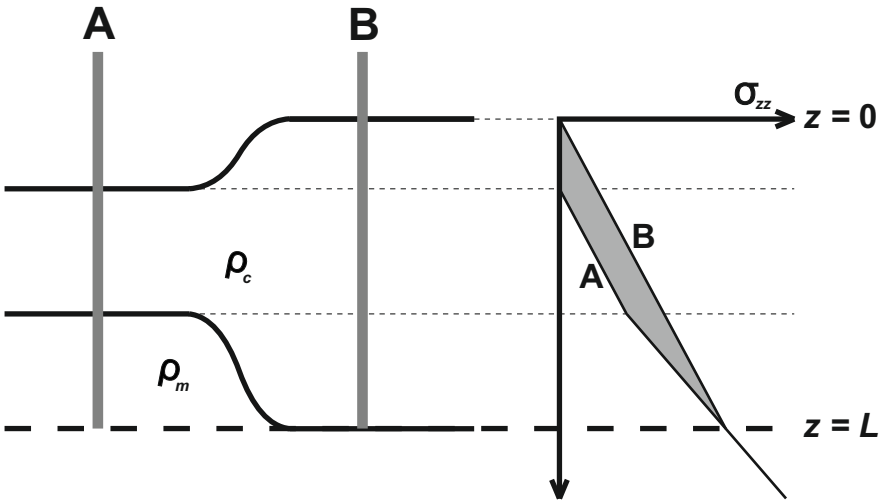

Figure 1.4: Schematic drawing showing the distribution of vertical stress ($\sigma_{zz} = \rho g z$) within the lithosphere. Column B represents a mountain range with thickened crust and elevated topography relative to an undeformed foreland region (Column A) with normal crustal thickness and topography. $z = 0$ is a level below which no lateral density variations exist and ρ_c and ρ_m are the uniform densities of the crust and mantle layers. The shaded region of the graph shows the difference in vertical stress between mountain and foreland which results in a horizontal force being applied to the foreland by the mountain. Integrating the shaded area with respect to depth gives the gravitational potential energy difference between mountain and foreland. Redrawn from Molnar and Lyon-Caen (1988).

lithosphere has negative buoyancy which tends to pull the plate vertically downward. Turcotte and Schubert (1982) show that the slab pull force ($\sim$5x10^{13} N m^{-1}) is an order of magnitude greater than the ridge push force ($\sim$4x10^{12} N m^{-1}). However, the two may be comparable in magnitude once resistive forces acting on the subducted slab are accounted for.

Vertical forces originating from lateral differences in GPE are important in continental tectonics. These vertical forces resist the horizontal driving forces imparted upon them and prevent mountain ranges growing indefinitely. Consider the simple situation in Figure 1.4, where a thickened orogen borders an unthickened foreland region in continental lithosphere. Plotted in the adjacent graph is the variation of vertical stress with depth for a column through each. The vertical stress is the force acting due to the weight of overlying lithosphere:

$$\sigma_{zz} = \int_0^L \rho g dz. \tag{1.7}$$

If density is constant, as in column B, vertical stress is a linear function of depth

z with a slope proportional to ρg. Below the level of isostatic compensation at depth $z = L$, it is assumed that there are no lateral variations in density and therefore the vertical stress is equal for columns A and B. By integrating the vertical stress from the surface $z = 0$ to $z = L$, the GPE of the lithospheric column is obtained in units of force per unit area:

$$\text{GPE} = \int_0^L \sigma_{zz} dz = \int_0^L \int_0^L \rho g dz dz. \tag{1.8}$$

The graph in Figure 1.4 shows that there is a difference in GPE between columns A and B, equal to the shaded area between the two curves:

$$\Delta\text{GPE} = \text{GPE}_B - \text{GPE}_A = L\left(\sigma_{zz}^B - \sigma_{zz}^A\right). \tag{1.9}$$

Since the vertical stress is always greater in column B than column A, there is a difference in the relative stress state between the foreland and the orogen. Dalmayrac and Molnar (1981) show that the horizontal stress σ_{xx} in the lithosphere does not vary laterally as the vertical stress does. Therefore if the situation exists where $\sigma_{zz}^A < \sigma_{xx} < \sigma_{zz}^B$ the foreland will deform by convergence whilst the orogen deforms by extension.

1.3.4 Change of deformation regime

In a collision zone, convergence in one direction can be accommodated by thickening in the vertical dimension, extension in the second horizontal dimension, or a combination of these two mechanisms. When thickening and topographic uplift occurs, the GPE of the lithosphere increases. Therefore, over time the force exerted by the orogen on its surroundings increases in magnitude. It is thought that the rate of India-Asia convergence has been reduced due to the increased GPE of the Tibetan plateau during collision (see §2.1.2). At some point, the increased GPE becomes large enough to alter the balance of vertical and horizontal stress and consequently change the mode of deformation (Figure 1.5).

At the onset of collision the elevations of India and Eurasia may have been comparable. In that case no appreciable GPE variation would exist and horizontal forces would have dominated (Figure 1.5a). However, after a sustained period of mountain building the GPE difference between Eurasia and India gets larger and the magnitude of the vertical stress becomes comparable to the horizontal stress. Following from Eq.

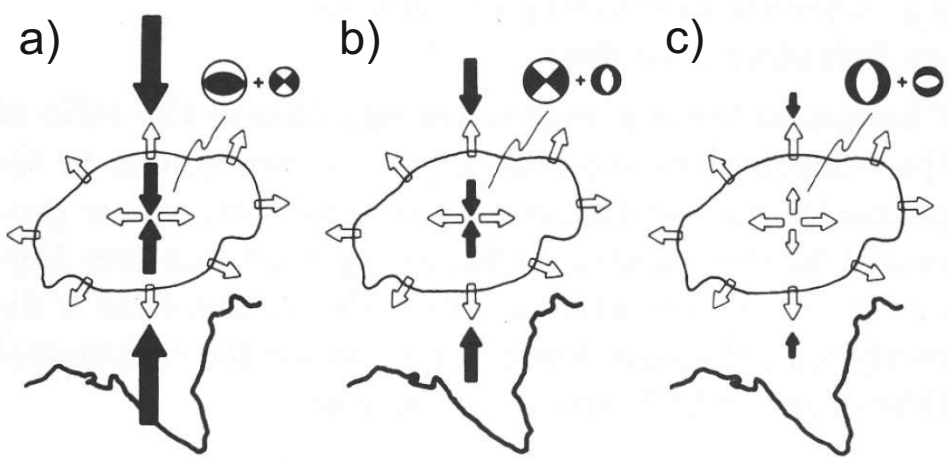

Figure 1.5: Cartoon of the horizontal stress regime at various stages during the evolution of the Tibetan plateau. a) Situation shortly after India-Asia collision. The horizontal tectonic force dominates and deformation occurs mainly as thickening but with some shear. b) Situation at present time. After gradual thickening of the lithosphere the vertical stress increases in magnitude but the horizontal force still dominates. Further thickening is resisted by the increase in GPE and deformation is mainly by lateral shearing with some extension in the high topography regions. c) Possible future situation when India-Asia collision ceases. Vertical forces now dominate and act to reduce the high elevations by extension. Beach-balls indicate expected seismic focal mechanisms for each deformation regime within the plateau. In all cases a force perpendicular to contours of topography exists due to the horizontal force created by the variations in GPE between plateau and foreland. This results in thrust faulting at the edge of the plateau. After England and Houseman (1989).

1.9 and the principle of isostasy, England and Houseman (1989) show that GPE increases approximately as the square of surface elevation. Therefore more work must be done to raise a high mountain range by one metre than a low one. As a result, for any particular driving force there is a limit to the elevation that can be attained. Once this limit has been reached, the horizontal and vertical stresses will be equal and the orogen will resist further convergence, unless it can spread horizontally in the third direction or the horizontal stress increases (Figure 1.5b). Should the tectonic driving force cease altogether, the consequent reduction in horizontal stress would allow the mountain range to collapse under the influence of gravity (Figure 1.5c).

1.3.5 Force balance

A system of differential equations, derived from the Navier-Stokes equations for fluid flow, can be used to describe the dynamic force balance in the lithosphere:

$$\begin{aligned} \frac{\partial \sigma_{xx}}{\partial x} + \frac{\partial \sigma_{xy}}{\partial y} + \frac{\partial \sigma_{xz}}{\partial z} &= 0 \\ \frac{\partial \sigma_{yx}}{\partial x} + \frac{\partial \sigma_{yy}}{\partial y} + \frac{\partial \sigma_{yz}}{\partial z} &= 0 \\ \frac{\partial \sigma_{zx}}{\partial x} + \frac{\partial \sigma_{zy}}{\partial y} + \frac{\partial \sigma_{zz}}{\partial z} &= \rho g \end{aligned} \tag{1.10}$$

where each term on the left describes the stress gradients in 3 directions acting on one of 3 faces of a cubic element and the vertical stress gradients are balanced against buoyancy. By using a set of boundary conditions these equations can be integrated analytically or numerically to obtain the state of stress throughout a deforming region. Furthermore, finite deformation can be calculated by relating stress to strain-rate using a constitutive relationship and integrating forward in time (see Chapters 5 and 6).

1.4 Earthquake cycle

Earthquakes occur because the friction which prevents movement on a fault plane is overcome by the gradual build up of stress in the crust. The earthquake cycle refers to the ongoing periodic process whereby elastic strain is accumulated on a fault (known as the 'interseismic' period) only for it to be released abruptly during an earthquake (known as the 'coseismic' period). Long before plate tectonics was formalised, the deformation occurring during the earthquake cycle had been studied and incorporated into a conceptual model known as the elastic rebound theory (usually credited to Reid, 1910). Using geodetic measurements from a triangulation network spanning the San Andreas fault before and after the 1906 San Francisco earthquake, Reid observed that the strain released during the earthquake was concentrated at the fault and was opposite to the slow build up of strain occurring at times between earthquakes. Furthermore, the summation of the coseismic and interseismic deformation signals yields a step function of displacement across the fault, so that all the strain is concentrated at the fault and none in the far field (Figure 1.6).

Assuming that interseismic strain accumulation is a linear process, the periodicity

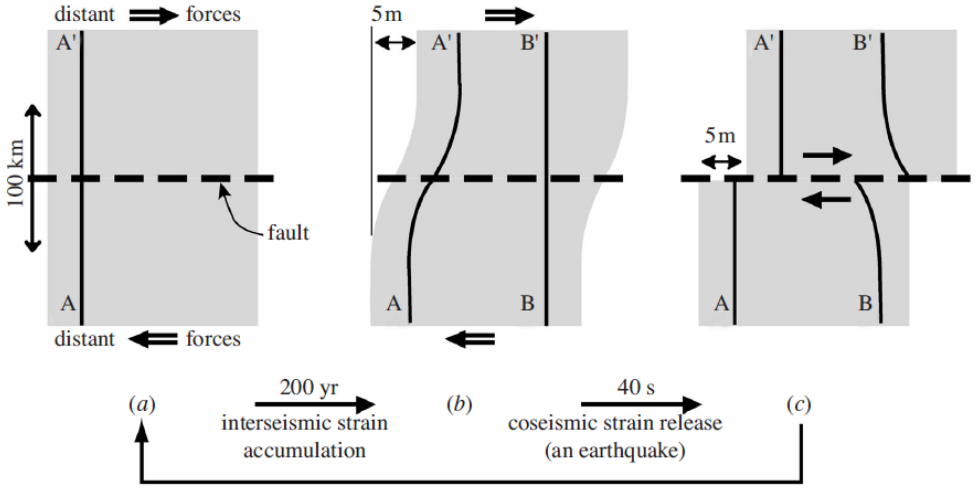

Figure 1.6: The elastic rebound model of the earthquake cycle. a) Schematic map view of a right lateral strike-slip fault cutting an elastic lithosphere which is driven at its edges by distant boundary forces. b) The same area after 200 years of interseismic strain accumulation on the fault. The originally straight profile A-A' has become a curved line with strain concentrated around the fault. c) The same area after an earthquake. Profile A-A' has recovered its previous straight form, but with an offset at the fault. Profile B-B', straight before the earthquake, has become curved with the same fault offset as profile A-A'. Diagram reproduced from Wright (2002).

of the earthquake cycle implies that the timing of coseismic strain release can be predicted. Unfortunately to date there are few places where measurements cover the entire earthquake cycle, and therefore the rupture process remains poorly understood. Nevertheless, the elastic rebound theory provides a reasonable approximation for studying coseismic and interseismic deformation.

More recent geodetic observations have shown evidence for transient viscoelastic deformation signals originating after an earthquake (Bürgmann and Dresen, 2008). These signals can persist for tens of years following the coseismic strain release (e.g. Gourmelen and Amelung, 2005). This discovery has led to the definition of a 'postseismic' period, which is distinctly different from the interseismic period.

1.4.1 Coseismic deformation

Traditionally, earthquakes have been studied and classified based on seismic methods. The 1992 Landers earthquake in California was the first to be observed using remote sensing when Massonnet et al. (1993) used Interferometric Synthetic Aperture Radar (InSAR) to map the ground displacement pattern. Since then, most large continental earthquakes have been studied in this way (e.g. Elliott, 2009, Weston et al., 2011).

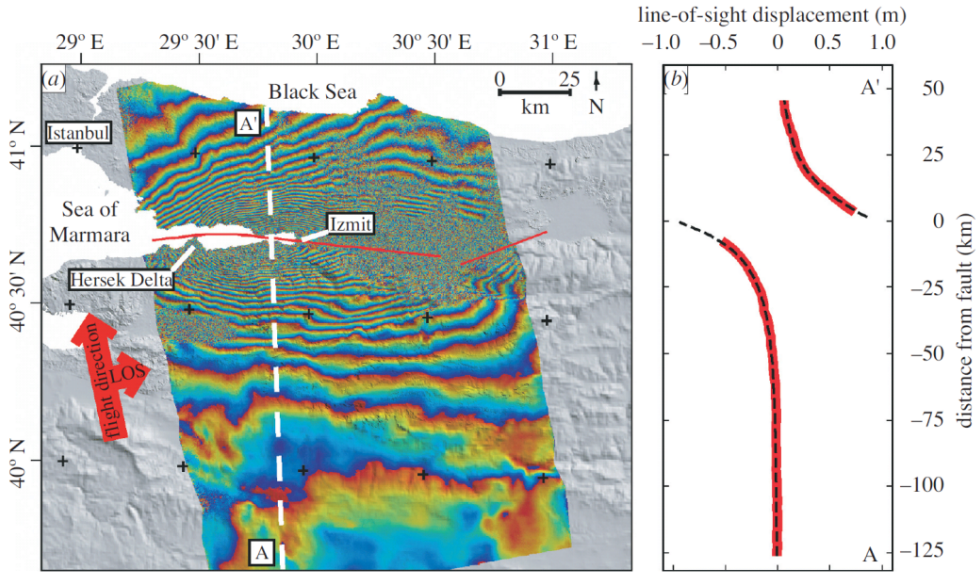

Figure 1.7: a) Coseismic interferogram showing the ground displacement pattern due to the 1999 Izmit earthquake. Each coloured fringe corresponds to a range change of 28 mm in the satellites line of sight (LOS), which is in the direction of the labelled arrow and on average 23^o from vertical. See Figure 3.2 for the viewing geometry. b) Profile A-A' through the interferogram after summing the number of fringes (unwrapping). Red line is the LOS displacements and black dashed line is the prediction of the best fitting elastic dislocation model. Figure reproduced from Wright (2002), who used results of Wright et al. (2001a).

For example, Wright et al. (2001a) used InSAR to quantify the ground displacements and map the surface rupture of the 1999 Izmit earthquake (Figure 1.7). They then inverted the data to obtain earthquake source parameters using the Monte Carlo method and a simple elastic dislocation model (Okada, 1985). The results showed that the surface rupture extended into the Gulf of Izmit, which could not be mapped by field geologists. This discovery has serious implications for the determination of future seismic hazard in the region (Wright, 2002). InSAR was also crucial in determining the fault responsible for the 2003 Bam earthquake, which had previously been unmapped (Talebian et al., 2004).

Obtaining earthquake source parameters from InSAR is now a routine method and results are usually available for an earthquake shortly after the first post-earthquake SAR acquisition has been made (e.g. see COMET+ working group website). Presently, the usefulness of this method as a tool for aiding early ground response is limited by the acquisition of data, which is bound to the repeat time of the satellite's low polar orbit. The minimum repeat time of presently operating satellites is 11 days (see Table

3.1). By 2015, the European Space Agency (ESA) plans to have Sentinel-1, a twin SAR satellite mission in operation that should cut the revisit time for all points on Earth to 6 days (see §7.5). A future SAR satellite with a geosynchronous orbit and positioned above a seismically active region would be able to provide even more prompt measurements following an earthquake (e.g. Guarnieri et al., 2011).

The Global Positioning System (GPS) is an alternative geodetic method that is used for rapid determination of the spatial variation of displacements occurring in earthquakes. If an extensive continuous GPS network is operational in a seismically active region, such as currently in Japan or California, it can be used to measure the coseismic ground deformation in real time (e.g. Wright et al., 2011). In the not-too-distant future this information will be used in tandem with seismic signals in early warning systems that can shut down infrastructure before the arrival of the most damaging seismic waves.

1.4.2 Interseismic deformation

The simple earthquake cycle model describes the slow build up of strain which is eventually released coseismically. This slow build up of strain is known as the interseismic period of the earthquake cycle, and usually invokes the idea of steady-state (constant with time) deformation associated with the background (or secular) motion of the tectonic plates.

When measured geodetically, the expected interseismic deformation signal has a magnitude of up to tens of mm/yr spread over a lateral zone generally observed to be on the order of 100 km for a single fault, giving a strain-rate on the order of $1\text{x}10^{-9}$ to $1\text{x}10^{-7}$ yr^{-1}. Interseismic velocities measured at the surface have two components. The first is the background (or secular) velocity imparted by plate tectonic motions. The second is a localised deviation from this motion due to the build-up of elastic strain around locked faults. Depending on the location of measurement, the observation may be biased towards one or the other of these two components.

Although GPS has been used for some time to create models of the secular motion of tectonic plates (the most recent being Argus et al., 2010), the first InSAR studies did not occur until nearly 10 years after the first coseismic study (e.g. Wright et al., 2001b, Peltzer et al., 2001). Measuring the interseismic signal with InSAR has proved difficult due to its low magnitude and the relatively high magnitude of noise in the data (see

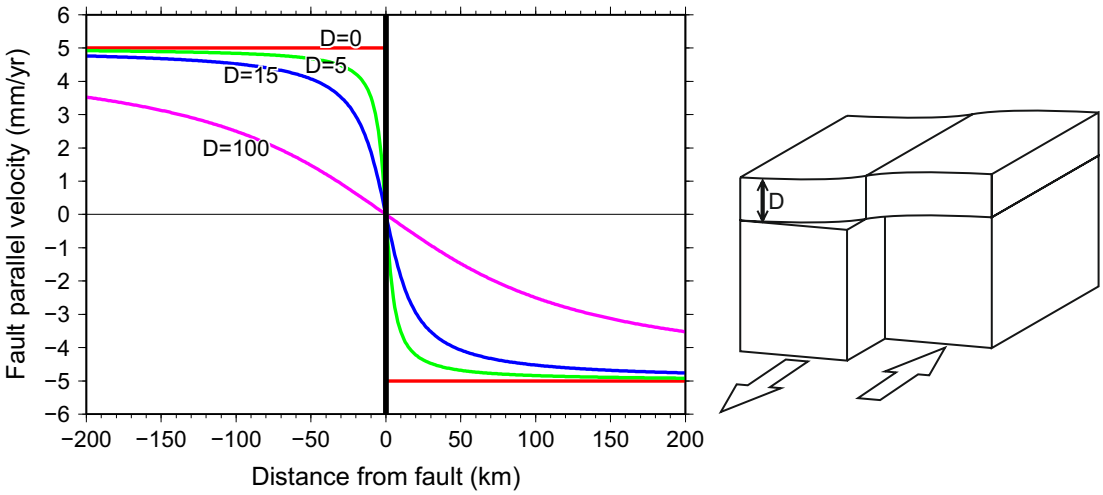

Figure 1.8: Fault-parallel interseismic velocity predictions from an elastic screw dislocation model for a range of locking depths and an across-fault relative velocity of 10 mm/yr. The depth to which the fault is locked is D in km. Below this depth the fault slides freely. Smaller values of D tend to concentrate elastic strain closer to the fault.

§3.1 for further discussion). Wright et al. (2001b) and Peltzer et al. (2001) interpreted their InSAR results using an elastic screw dislocation model to obtain an estimate of the slip rate and locking depth.

Savage and Burford (1973) were the first to apply an elastic screw dislocation model to geodetic data to explain interseismic deformation on the San Andreas fault, California. The analytical model relates fault-parallel velocity u to the depth of a locked elastic layer D and the slip velocity b of the freely sliding fault beneath:

$$u = \left(\frac{b}{\pi}\right) \tan^{-1}\left(\frac{x}{D}\right). \tag{1.11}$$

In this model, the locking depth defines the length scale over which deformation associated with the fault is spread (Figure 1.8). As a general rule of thumb, 50% of displacement strain occurs within a distance of $1D$ of the fault, and 90% occurs within $\sim 6.3D$ (Savage and Burford, 1973). The model implies that 10% of deformation occurs at distances far from the fault. Therefore when using this model, observations sufficiently far from the fault should be included if possible in order to constrain the parameters.

An alternative model recognises that the elastic part of the lithosphere is limited to the upper-most layer and that deformation beneath this layer is broadly distributed. Prescott and Nur (1981) showed that surface velocities for such a 'shear zone' model

can be obtained by the summation of numerous dislocations within a defined width (equal to the shear zone width) if the interseismic velocity varies linearly across this zone.

Many more complicated earthquake cycle models have been devised that calculate the evolution of displacement on a strike-slip fault through time (e.g. Savage and Prescott, 1978, Pollitz, 2003a, Hetland and Hager, 2006, Johnson et al., 2007). In general, these time dependent models must mature by being 'spun up' over several earthquake cycles until a steady-state process of interseismic strain accumulation, coseismic release and postseismic rebound is established on a fault. Savage and Prescott (1978) adapted the viscoelastic model of Nur and Mavko (1974) (devised to explain postseismic deformation) but included interseismic loading in the far field. However, they found that the predicted surface velocities from the viscoelastic model were very similar to those of an elastic dislocation model. Consequently, the simplicity of the two-parameter elastic dislocation model has meant it remains a popular choice for inverting geodetically determined interseismic velocities in order to find the relative interseismic displacement rate across a fault, despite the probable inaccuracy of the physical model for the continental lithosphere.

Use of the elastic dislocation model to constrain geodetic observations has sometimes led to very low relative displacement rates across locked faults. Particularly in the Tibetan plateau, these geodetic slip rates are significantly lower than 'long-term' slip rates calculated using geological techniques (see §2.3 for more discussion). As a result of this discrepancy, He and Chery (2008) question the suitability of the screw dislocation for modelling interseismic velocities. They propose that a more appropriate model might be a thin elasto-plastic plate overlying a ductile lower crust and mantle. Instead of an arctangent-shaped function for velocity across a fault, such a model gives a linear trend during the interseismic period (assuming postseismic transients have decayed away) and a step-like velocity profile in the long term.

The simple Savage and Burford interseismic model for a single strike-slip fault is not accurate for many plate boundary zones in which relative plate motion can be accommodated on multiple faults in a wide transitional shear zone. For such plate boundary zones in New Zealand and California, averaged geodetic observations show a smooth velocity profile with no localisation at known fault zones (Figure 1.9). To explain this, Bourne et al. (1998) adopt a model in which motion of elastic crustal blocks

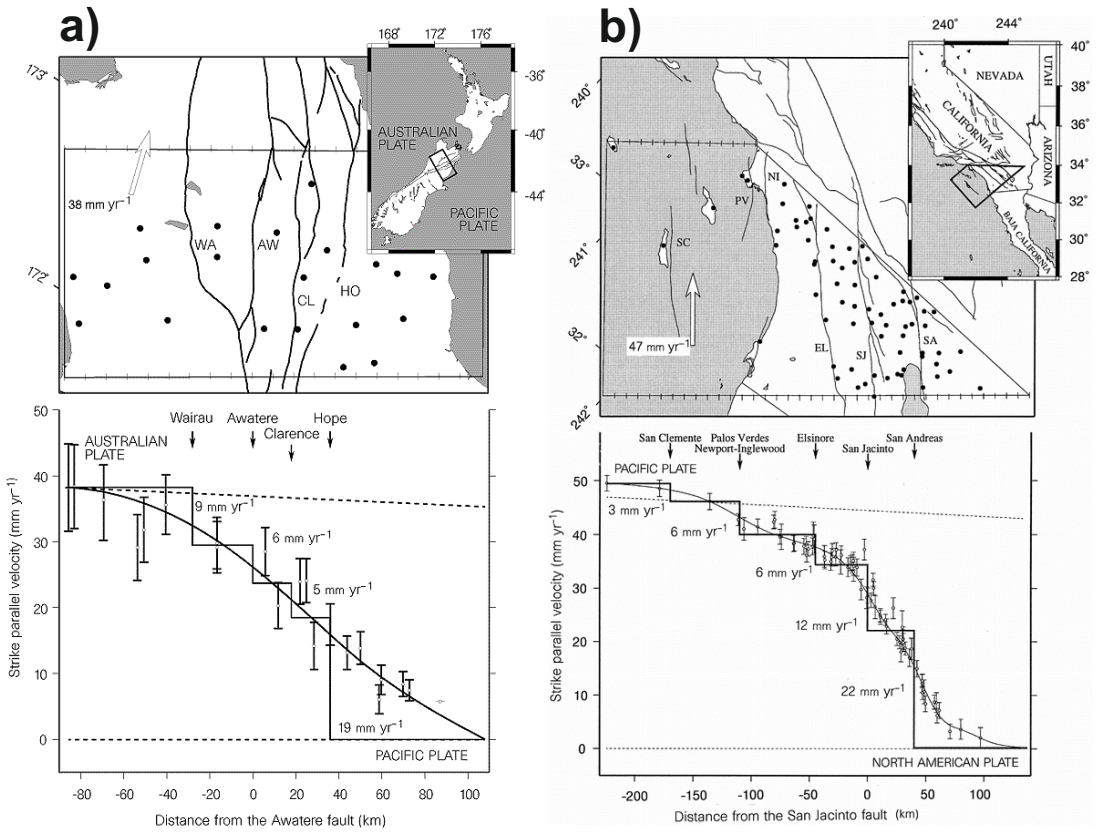

Figure 1.9: Profiles of strike-parallel interseismic velocity across the a) South Island, New Zealand and b) southern California strike-slip plate boundary zones. Geodetic observations are from GPS measurements between a) 1982-1994 and b) 1970-1995 and are used to constrain the smooth interseismic profile across the region, which is interpreted to be determined by the upper mantle velocity field. Step-like profiles show the displacement rates predicted on major faults bounding elastic blocks. After Bourne et al. (1998).

is driven by tractions on their bases imparted by a Newtonian viscous layer beneath whose deformation is laterally distributed. The 'interseismic' or short term motion of the elastic and ductile layers is therefore averaged across the width of the zone, but the long term motion of the brittle layer is block-like over many earthquake cycles. The important implication of this model is that geodetically determined interseismic velocities represent the motion of the deep lithosphere and can therefore be used to directly constrain dynamic models of lithospheric deformation based on viscous constitutive laws (see Chapter 6). However, using models that assume an elastic upper crust overlying Newtonian viscoelastic lower crust and upper mantle layers, Zatman (2000), Savage (2000) and Hetland and Hager (2004) find that surface velocities are distinctly different from secular velocities in the mantle, but are sensitive to transient velocities

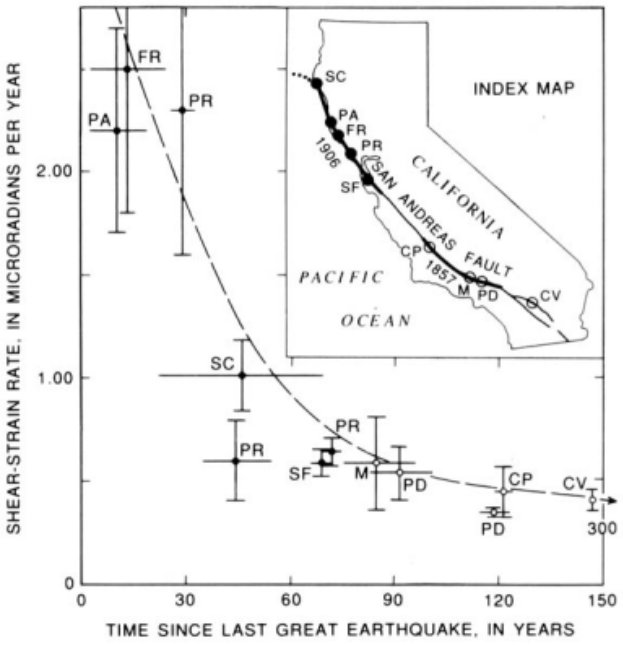

Figure 1.10: Shear-strain rates evaluated from triangulation data plotted against time since the last earthquake on the San Andreas fault after Thatcher (1983). Dots refer to data from the 1906 San Francisco earthquake rupture in North California and circles refer to data from the 1857 Fort Tejon earthquake rupture in South California. Vertical error bars are 1-sigma and horizontal error bars give time interval between triangulation surveys. Dashed line represents the prediction of an elastic half space model, although Thatcher finds many models and parameter combinations that satisfactorily fit the data. Locations of data points are shown in the inset map of California.

in these layers related to postseismic relaxation.

1.4.3 Postseismic deformation

Large earthquakes can cause significant changes to the ambient stress field around a fault. This change results in transient postseismic deformation that may persist for decades following the earthquake. Thatcher (1983) compiled post-earthquake shear-strain rate data for the San Andreas fault and found a temporal decrease persisting for ~ 30 years and perhaps for over 100 years after the most recent large earthquake in that area (Figure 1.10). The data plotted are derived from triangulation data (Thatcher, 1975) which are much less precise than modern geodetic techniques. In recent years, InSAR and GPS have enabled increased spatial and temporal sampling of these signals.

Three mechanisms of postseismic deformation have been identified: viscoelastic relaxation (e.g. Nur and Mavko, 1974, Pollitz, 1997), poro-elastic effects (e.g. Peltzer

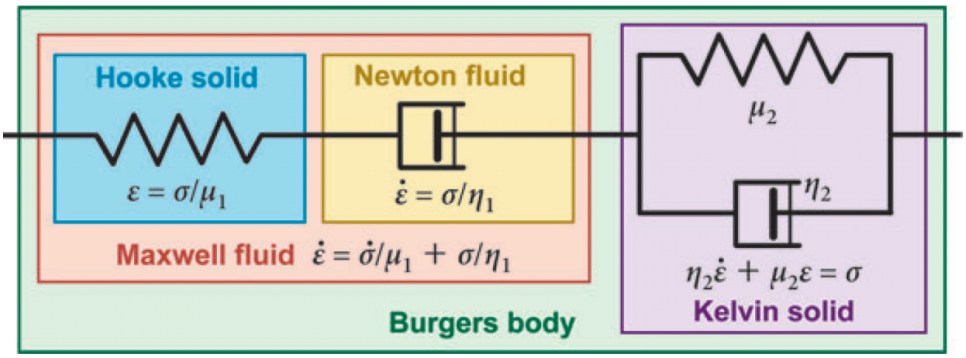

Figure 1.11: Representation of viscoelastic rheologies with combinations of dash-pot and spring elements as described in the text. Each coloured box encloses the components of a particular rheology. The equations give the appropriate constitutive relationship for each assemblage. After Bürgmann and Dresen (2008).

et al., 1998, Jónsson et al., 2003) and after-slip (e.g. Smith and Wyss, 1968, Bürgmann et al., 2002). The time-scale of these processes may vary from hours to years. The observed postseismic signal may contain components from each of these mechanisms, but distinguishing between them is difficult (Segall, 2010). For instance, models based on all three mechanisms, or combinations thereof, can be used to explain geodetically observed deformation following the 1992 Landers and 1999 Hector Mine earthquakes in California (see references in Bürgmann and Dresen, 2008). This non-uniqueness makes it challenging to characterise postseismic deformation.

Viscoelastic relaxation

As discussed in §1.2, the elastic upper crust gives way to ductile lower crust and mantle as the temperature increases with depth. Although the ductile layer deforms viscously over long time periods, its response to instantaneous coseismic stress changes will be elastic. Observed deformation of this 'viscoelastic' body is usually interpreted in terms of a linear rheology involving combinations of Newtonian fluid (i.e. dash-pot) and Hooke solid (i.e. spring) elements (Figure 1.11). The simplest rheology is a Maxwell fluid, which involves elastic and viscous elements connected in series. This gives an immediate elastic response followed by a sustained viscous response as long as the stress persists. On the other hand, a Kelvin solid contains elastic and viscous elements in parallel, which gives a viscously-damped elastic response. Both rheologies have a relaxation function with an exponential form and a characteristic relaxation time equal

to the viscosity divided by the shear modulus. The more complicated Burgers rheology uses Maxwell and Kelvin elements in series (Pollitz, 2003b). This is a bi-viscous rheology that has two characteristic relaxation times associated with the separate Kelvin and Maxwell elements. Such a rheology can be used to fit postseismic signals that exhibit rapidly decaying early transients (Kelvin element) followed by a more gradually decaying relaxation (Maxwell element; e.g. Ryder et al., 2011). However these signals could be equally well explained using alternative mechanisms, such as a power-law rheology or a combination of poroelastic or after-slip effects.

Complication of the earthquake cycle

Since postseismic deformation signals can be long-lived, they can easily be assumed to be coseismic or interseismic deformation when measured geodetically. Due to the decaying nature of the signal, the largest strain rates occur directly following an earthquake. When studying coseismic displacements with InSAR it can be many days before an image is acquired following the earthquake. As a result a coseismic interferogram will potentially contain a large contribution from the postseismic response. Background interseismic deformation is typically much smaller in magnitude than postseismic signals. For instance, Thatcher (1975) first observed postseismic deformation from the 1906 San Francisco earthquake that was 4 times the magnitude of interseismic strain rates. Ideally, postseismic signals would be modelled out of geodetic data in order to leave the background interseismic signal. But in reality this is not realistic for postseismic signals originating from earthquakes that occurred prior to the recent era of dense geodetic monitoring. Therefore we must assume that any measured signal is a combination of steady-state interseismic deformation and any number of postseismic transients whose spatial distribution is unknown. A better understanding of the interseismic and postseismic contributions to observed geodetic signals will follow when we have a comprehensive data archive spanning an entire earthquake cycle.

1.5 Thesis overview

The motivation for the research documented in this thesis has been the question of 'how does Tibet deform?' and therefore the focus is on the Tibetan plateau and immediate surrounds. However, in more general terms the interest is in the mode of deformation occurring in all continental plate boundary zones. In particular, I aim to contribute to

answering the following questions:

- Does the observed interseismic velocity across an entire deforming zone indicate focussed strain on individual faults or a smoothly varying deformation field? (see Chapter 4)
- Are postseismic transients distinguishable from interseismic deformation in geodetic data? (see Chapter 4)
- Do simplified 2-dimensional dynamic models provide a useful approximation to fully 3-dimensional viscous deformation of the lithosphere? (see Chapter 5)
- Can these 2-dimensional viscous models explain the present-day velocity field in Asia measured geodetically during the last decade? (see Chapter 6)

The thesis is organised as follows:

In Chapter 2 I review the current understanding of the deformation occurring in the Tibetan plateau.

In Chapter 3 I describe the InSAR method and its use in measuring slow interseismic deformation.

In Chapter 4 I measure the interseismic deformation occurring across the central Tibetan plateau with a long swath of InSAR data.

In Chapter 5 I describe the 2-dimensional 'thin viscous sheet' model of continental deformation and compare it to analogous 3-dimensional models.

In Chapter 6 I use the thin viscous sheet to model present day deformation occurring across the Tibetan plateau and surrounding regions.

Finally, in Chapter 7 I discuss the implications of my results and possibilities for future work.

Chapter 2

Tectonics of Tibet

The India-Asia collision is the archetype of intra-continental deformation and has therefore been a major focus for work on continental tectonics. This collision has formed the largest present day topographic features on the Earth: the Himalayan mountain range and the Tibetan plateau. Due to its immense size, it is thought that the Tibetan plateau has a controlling influence on the global climate (Molnar et al., 1993). As a result, geological and geophysical studies aimed at understanding the complex evolution and deformation of the plateau are of great importance to society. In this chapter, I review the current understanding of the formation and present day deformation in the Tibetan plateau.

2.1 India-Asia collision

The main continental landmass in Asia sits on the Eurasian plate (Figure 2.1). In the MORVEL model (DeMets et al., 2010), the tectonically complex eastern margin of the Eurasian plate in south-east Asia has been formally divided into three smaller plates: the Amur, Yangtze and Sundaland plates. In a fixed Eurasia reference frame, these plates are moving roughly eastward toward the subduction interface with the Philippine Sea plate in the east with an absolute velocity of ∼10 mm/yr or less. The oceanic Philippine Sea plate moves roughly westward at 70-80 mm/yr, and is subducted beneath the continental plates on the Asian eastern margin. At the southern margin of the Eurasian plate, the Indian and Eurasian plates are converging. The northward velocity of India varies between ∼40 and ∼53 mm/yr between the western and eastern syntaxes of the Himalayan arc. It is this convergence between India and Eurasia which is responsible for the widespread tectonic deformation seen in Asia.

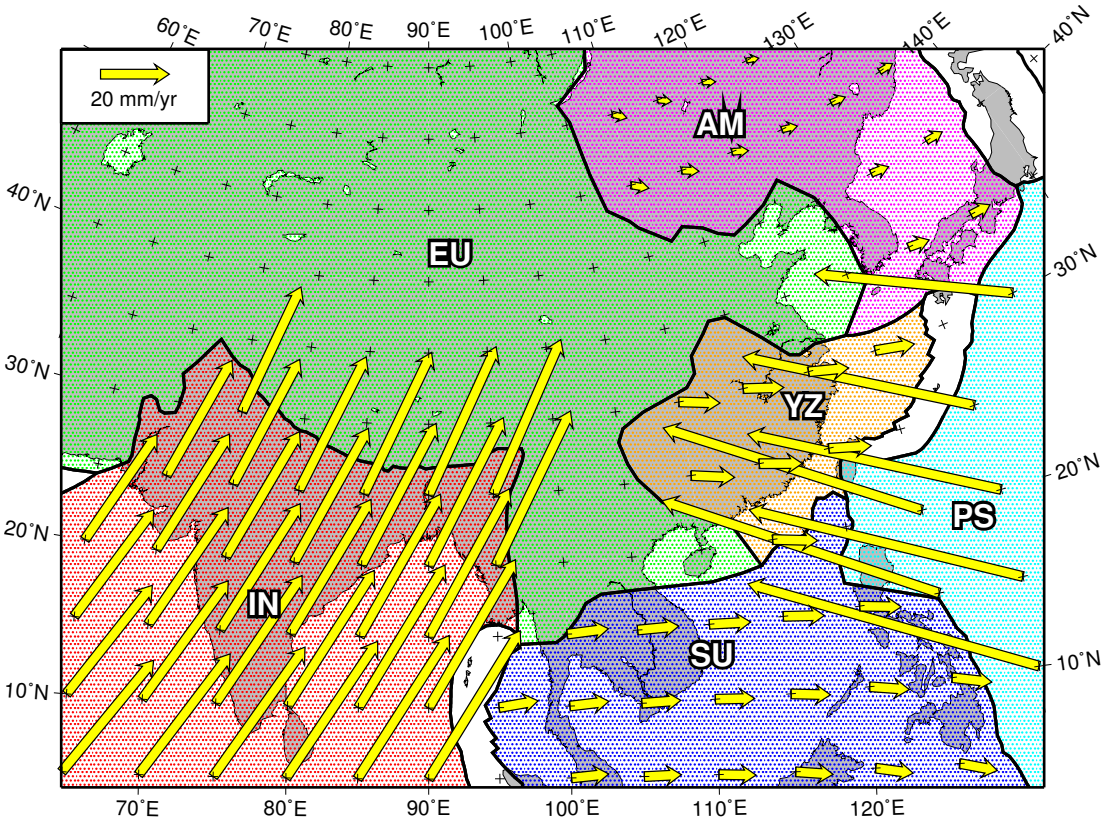

Figure 2.1: Tectonic plates and geologically current plate motions in Asia. Plate boundaries are from the compilation of Bird (2003) and velocities relative to fixed Eurasia are calculated from the Euler poles given in the MORVEL global plate motion model (DeMets et al., 2010). Name acronyms for the coloured plates as follows: EU - Eurasia, IN - India, SU - Sundaland, YZ - Yangtze, AM - Amur, PS - Philippine Sea. Transverse Mercator projection.

Argand (1924) was the first to realise that the recent tectonics of Asia could be explained by convergence between the paleo-continents of Gondwana and Laurasia. Convergence has resulted in widespread shortening and a doubling of crustal thickness over a region up to 2000 km north of the India-Eurasia suture (Dewey et al., 1988). Prior to India's collision with Eurasia, a sequence of subductions in the Tethys Ocean (since the Permian) led to the accretion of island arcs and continental terranes to the Eurasian plate (Dewey et al., 1988, Yin and Harrison, 2000). As a result, the Tibetan-Himalayan orogen is composed of a complex melange of crustal rocks welded together along numerous east-west trending suture zones within the continent, including the Bangong-Nujiang Suture (BNS) and the Indus-Zangbo/Tsangpo Suture (IZS) in central Tibet (Figure 2.2). For a comprehensive review of the pre-collisional tectonics in Asia the reader is referred to Yin and Harrison (2000), whereas Royden et al. (2008)

give a concise review of the geological evolution of the orogen.

2.1.1 Timing of collision

The timing of India-Asia collision is not well constrained (Rowley, 1996, 1998), and remains a subject of active research. The commonly cited onset time of collision is at ∼50 Ma during the early Eocene epoch. From biostratigraphic analysis and radiometric dating, Guillot et al. (2003) give the onset of India-Asia contact as slightly earlier, between 53-57 Ma. Broadly consistent with this age, the final shallow marine sediments were deposited at 50.5 Ma (Green et al., 2008). A recent paleomagnetic study by Chen et al. (2010) constrains the onset to within 55-60 Ma. Rowley (1996, 1998) gives evidence from stratigraphic data and subsidence history for a progressive collision starting in the west in the late Ypresian (∼<52 Ma) and migrating to the east by the end of the Lutetian (∼40 Ma).

2.1.2 Post-collisional slow-down

Using an updated plate reconstruction and force balance calculations, Copley et al. (2010) give evidence of a slow-down in the convergence rate following the onset of collision. The slow-down was a direct consequence of continued crustal thickening in Tibet, which eventually created a horizontal resistive force directed outward from the plateau (see §1.3.4). At the time of collision (∼50 Ma) the convergence rate was around 150 mm/yr but this quickly reduced to 50 mm/yr by around 35 Ma (Copley et al., 2010). Molnar and Stock (2009) obtain a similar convergence time series in an independent plate reconstruction. They argue for an additional period of slow-down beginning at 20 Ma, coincident with rapid surface uplift of around 1-2 km in Tibet. The proposed mechanism involves convective removal of mantle lithosphere (or mantle delamination), which results in buoyant uplift of the crust over a short time-scale. The increase in height significantly changes the force balance. Following removal of the mantle lithosphere, the plateau would exert an outward force on its surroundings which could cause the observed slow down of the Indian plate (England and Houseman, 1989, Molnar et al., 1993, Molnar and Stock, 2009).

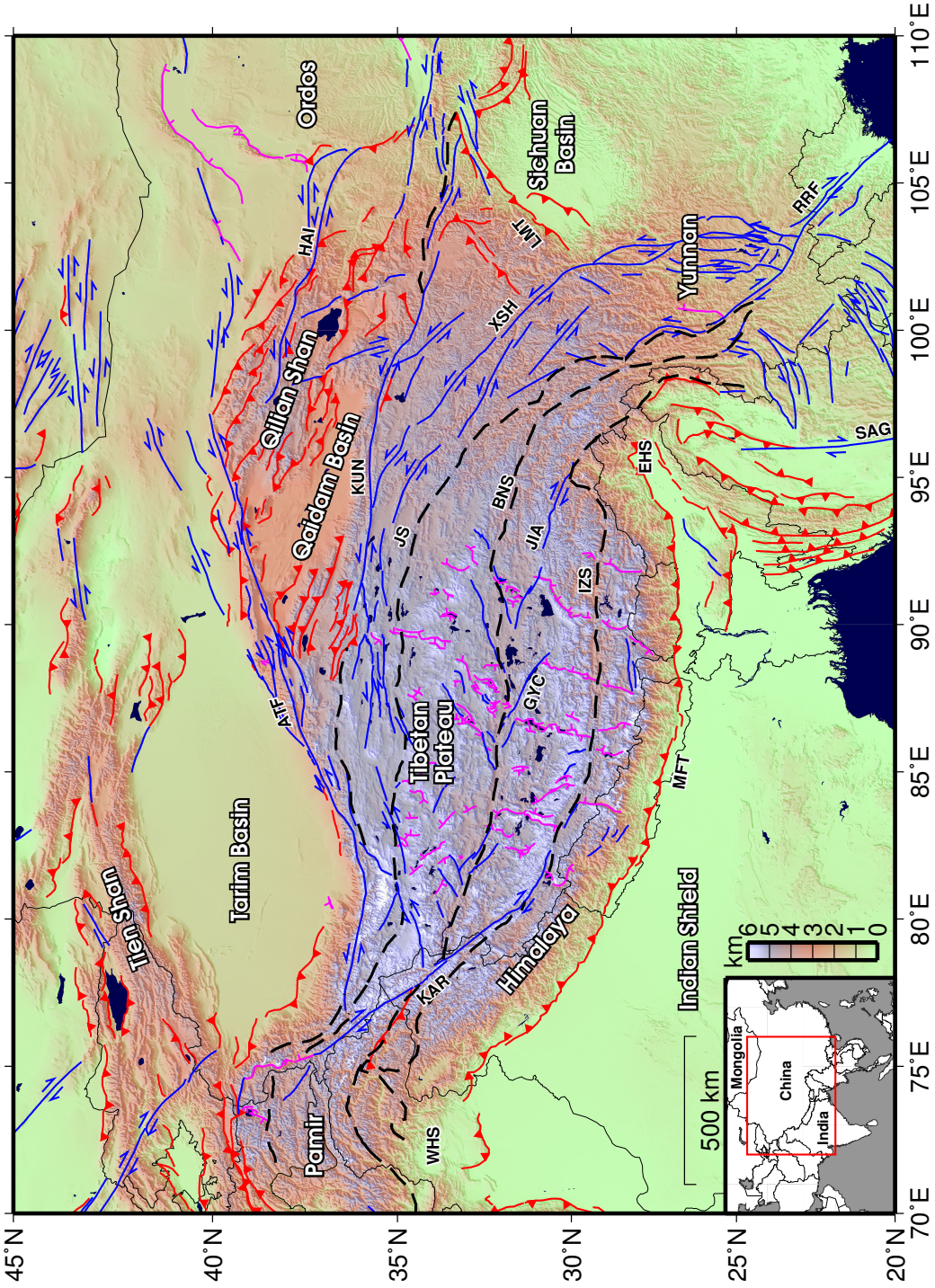

Figure 2.2: Topographic map of Tibet and surrounding area with Quaternary active faults and geological sutures from the compilation of Taylor and Yin (2009). Black dashed lines are sutures, red lines are thrust faults, blue lines are strike-slip faults and magenta lines are normal faults. Symbols on faults indicate sense of movement with ticks on the hanging wall for normal faults and barbs on the upper plate for thrust faults. Name abbreviations for major features as follows: ATF - Altyn Tagh fault, BNS - Bangong-Nujiang Suture, EHS - Eastern Himalayan Syntaxis, GYC - Gyaring Co fault, HAI - Haiyuan fault, IZS - Indus-Zangbo Suture, JIA - Jiali fault, JS - Jinsha Suture, KAR - Karakoram fault, KUN - Kunlun fault, LMT - Longmen Shan Thrust, MFT - Main Frontal Thrust, RRF - Red River fault, SAG - Sagaing fault, WHS - Western Himalayan Syntaxis, XSH - Xianshuihe fault. Mercator projection.

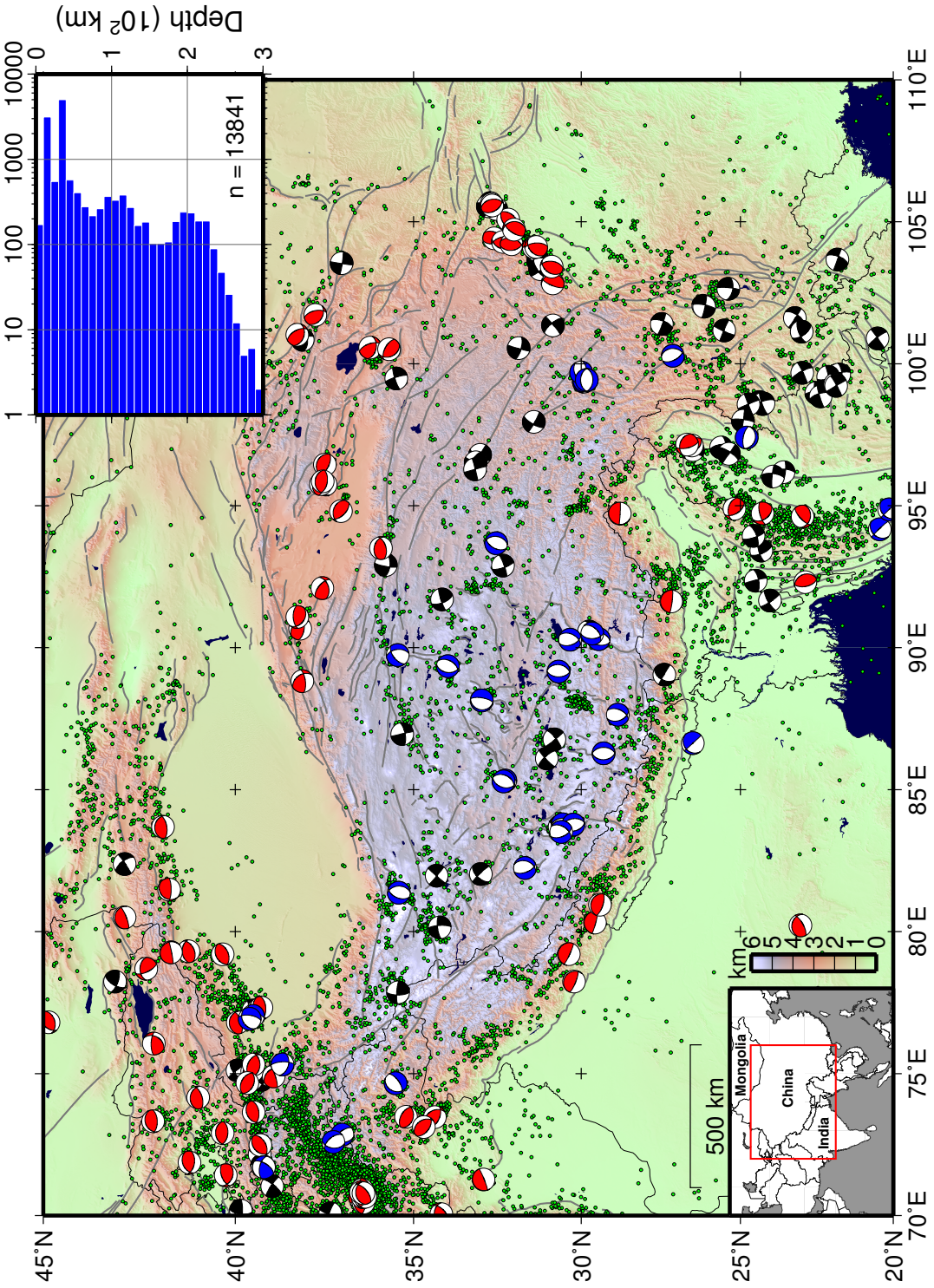

Figure 2.3: Seismicity of Tibet and surrounding region. Green dots are earthquakes from the USGS catalogue between 1976-2010 with M>4.0. Seismic moment tensors are from the Harvard CMT catalogue also between 1976-2010 and plotted as best fitting double couples. Red mechanisms are predominantly thrust earthquakes, blue predominantly normal earthquakes and black predominantly strike-slip earthquakes. Symbols have no magnitude scaling. Grey lines are faults as in Figure 2.2. Mercator projection. The histogram in the upper right shows the depth distribution of the plotted USGS seismicity. Note the logarithmic frequency scale.

2.1.3 Plateau uplift

Uplift of the Tibetan plateau followed the closure and subduction of the Tethys ocean and the subsequent continental collision. Estimates of the amount of crustal shortening that has occurred since the onset of collision range between 1400 km and 3500 km (Dewey et al., 1988, Molnar et al., 1993, Yin and Harrison, 2000; and references therein). Rowley and Currie (2006) used a paleoaltimetry method based on oxygen isotope ratios to conclude that the south plateau had attained its current elevation by 39 Ma. By combining these observations with the thermo-mechanical channel flow model of Beaumont et al. (2004), they estimate the time it took for the plateau to expand northward. The Qaidam basin (toward the north-eastern margin of the plateau; Figure 2.2) is estimated to have reached 4 km elevation by 13 Ma. Rowley and Currie (2006) argue that removal of the mantle lithosphere could not have occurred since 39 Ma because the determined paleo-elevations are similar in magnitude to current elevations. However, the paleoaltimetry method is relatively coarse and 95% confidence limits on the data encompass errors of ±1 km. Furthermore, Molnar et al. (2006) argue that uplift following mantle removal was followed by crustal thinning associated with the onset of normal faulting in the high plateau at ∼8 Ma (Armijo et al., 1986, Molnar et al., 1993) that would return the plateau to its current elevation, consistent with the paleo-elevation estimates.

2.2 Topography of the plateau

2.2.1 Topographic features

The present day topography of Asia reveals many features of the deformation caused by the India-Asia collision (Figure 2.2). The ∼2500 km-long arcuate Himalayan range marks the onset of high topography and contains eight of Earth's ten highest peaks (Hodges, 2000). The Himalayan orogen is defined to be the ∼250 km-wide belt between the Main Frontal Thrust in the south and the IZS in the north (Yin, 2006), with the IZS marking the tectonic suture between the Indian and Eurasian plates. The combination of high peaks and deep valleys gives the Himalaya an average elevation no higher than the low relief Tibetan plateau directly to the north. Fielding et al. (1994) reports a mean elevation of 5023 m for the interior of the Tibetan plateau, with average slope angles of about 5°. The approximate dimensions of the region at ∼5 km elevation

is 3500 km by 1000 km, giving an area of ∼3.5 million km^2, which ensures that the plateau is easily the largest topographic feature on the Earth's surface.

Encompassing the high plateau on north and east sides is a belt of Precambrian shield (Molnar and Tapponnier, 1981). This belt includes the Tarim, Qaidam and Sichuan basins and the Ordos block in north China. Low levels of seismicity indicate that these areas are undeforming (Figure 2.3) and therefore are inherently stronger than other parts of the Eurasian lithosphere (Molnar and Tapponnier, 1981, England and Houseman, 1985). Since thermal properties can indicate the strength of the lithosphere, heat flow measurements can be used to back up this assertion: the Tarim basin (45 mW/m^2), Qaidam basin (54 mW/m^2), Sichuan basin (53 mW/m^2) and Ordos block (60 mW/m^2) all exhibit low average heat flow compared with south Tibet (82 mW/m^2) (Wang, 2001). Braitenberg et al. (2003) also infer strong lithosphere for Tarim and Qaidam from elastic thickness estimates. Outboard of the Tarim and Qaidam basins are the Tien Shan and Qilian Shan mountain ranges. Both of these are actively deforming as indicated by thrusting focal mechanisms and pronounced seismicity (Figure 2.3). The densest region of seismicity, indicating the most actively deforming part of Asia, is found in the Pamir/Hindu Kush region north-west of the western Himalayan syntaxis. Studies of this earthquake cluster have suggested that either Indian lithosphere is being subducted beneath Eurasia here with a contorted S-shaped geometry (e.g. Pegler and Das, 1998), or that northward subduction of India beneath the Hindu Kush and southward subduction of Eurasia beneath the Pamir is occurring (e.g. Fan et al., 1994).

2.2.2 Topographic profiles

Figure 2.4 shows topographic profiles across the plateau and surrounding region. These profiles confirm the ∼5 km elevation and low relief across the interior of the plateau, but also that the plateau margins can be classified by two types (Clark and Royden, 2000). The first type of margin is characterised by very steep topography. The Himalayan front marks the southern boundary of the plateau, and this exhibits an average topographic gradient of about 1:40 (profiles C-C' and D-D' at 600 km). Similarly, the northern and north-eastern margins border the Tarim and Qaidam basins where the average topographic gradient is about 1:50 (profile C-C' at 1400 km) and 1:100 (profile D-D' at 1500 km) respectively. Steeper still is the eastern margin where the plateau

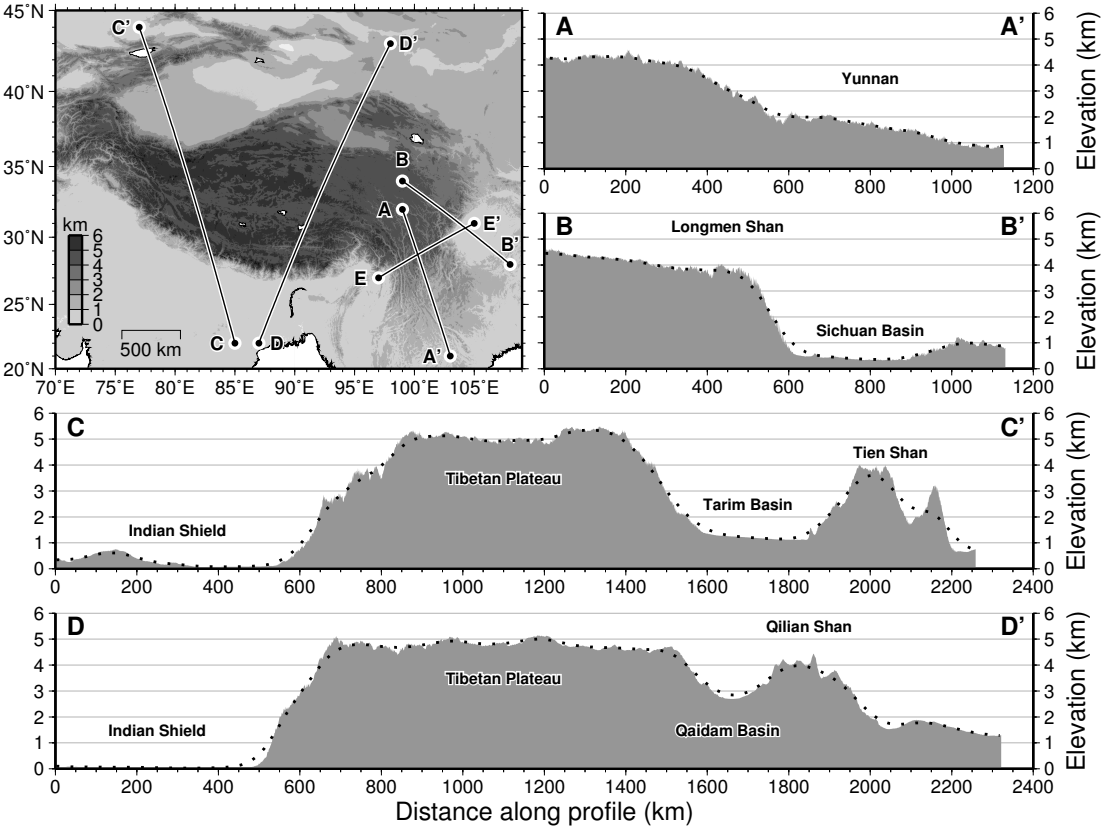

Figure 2.4: Topographic profiles for the Tibetan plateau and surrounding regions. The mean topography is calculated from SRTM data resampled to 1 arc-minute resolution and binned at 1 km intervals along profile and within a 100 km swath on either side of the profile. Black dotted line is the mean topography for the same data smoothed with a Gaussian filter of 250 km width (see Figure 2.10a) and binned in 5 km intervals. Profile E-E' is plotted in Figure 2.8b. Vertical scale of profiles is 16x exaggerated. Profile lines are not straight in the overview map due to the Mercator projection used.

borders the low-lying Sichuan basin, with a topographic gradient of just less than 1:30 (profile B-B'). It is thought these steep margins exist because the plateau abuts much stronger and undeforming Precambrian lithosphere in these locations (Molnar and Tapponnier, 1981, Clark and Royden, 2000). The second type of margin is characterised by very low gradients on the order of 1:200-1:300, which are evident on either side of the Sichuan basin in NE-SW and NW-SE (profile A-A') orientations from the plateau interior towards Ordos and Yunnan respectively. Profile E-E' (plotted in Figure 2.8b) shows a cross-section between the eastern Himalayan syntaxis and the Sichuan basin where the topography is almost symmetrical.

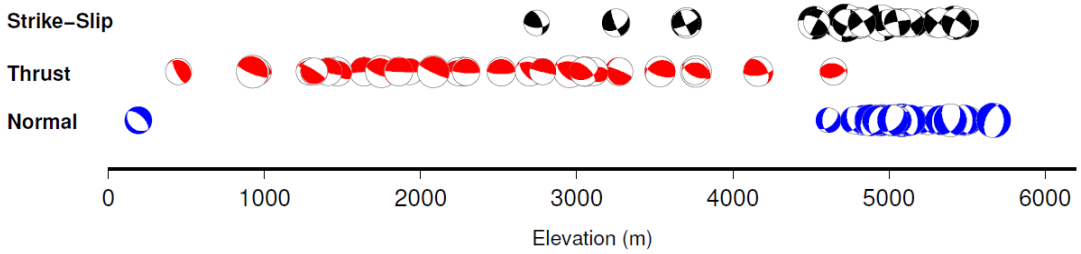

Figure 2.5: M>5.5 Earthquake mechanisms versus elevation in the Tibetan plateau region after Elliott et al. (2010). Data from Harvard CMT catalogue (1976-2008) and Molnar and Lyon-Caen (1989) (1966-1975).

2.3 Active faulting

Convergence in the collision zone is accommodated in the brittle crust by extensive faulting over a broad region extending far into the Eurasian plate (Figure 2.2). Normal, thrust and strike-slip faults have all been observed in this region (Taylor and Yin, 2009).

2.3.1 Thrust and normal faulting

The southern margin of the plateau is marked by the Main Frontal Thrust (Figure 2.2), which together with the Main Boundary Thrust, Main Central Thrust and South Tibetan Detachment accommodate the majority of shortening across the Himalayan orogen (Yin and Harrison, 2000). Present day geodetic measurements indicate around 15 mm/yr of shortening across the Himalaya (Banerjee and Bürgmann, 2002). The surface thrust faults toe in to the Main Himalayan Thrust; a major subduction shear zone that has been imaged as a strong seismic discontinuity dipping beneath the Himalaya at a shallow angle of ∼9° (Zhao et al., 1993, Nabelek et al., 2009).

In Eurasia, focal mechanisms show that thrust faulting is absent from high elevation areas above 4 km (Figure 2.5) and instead concentrate on the plateau margins and within the lower elevation Qilian Shan, Longmen Shan and Tien Shan mountain belts (Figure 2.3). Up to 20 mm/yr of convergence is currently accommodated via thrust faulting in the Tien Shan, which is about two thirds of the total India-Asia convergence (Zubovich et al., 2010). The Longmen Shan is a highly active thrust belt (Figure 2.3) that produced the devastating M7.9 Wenchuan earthquake of 12 May 2008. Thrusting here facilitates vertical uplift of Tibet as material is forced against the rigid Sichuan basin to the east (Royden et al., 2008).

Normal faulting occurs almost exclusively in the high plateau at elevations above

Table 2.1: Slip rates (mm/yr) of major strike-slip faults in Asia

Fault	Sense	Rate	Range	Reference
Altyn Tagh	sinistral	10	±2	
Gyaring Co	dextral	14	±7	Taylor and Peltzer (2006)
Haiyuan	sinistral	6	±2	
Jiali	dextral	15	±7	Armijo et al. (1989)
Karakoram	dextral	4	±2	
Kunlun	sinistral	10	±2	
Red River	dextral	2	±1	
Sagaing	dextral	18	±8	
Xianshuihe	sinistral	10	±2	

Unless stated, rates summarise the review of Molnar and Dayem (2010)

4.5 km (Figure 2.5). Elliott et al. (2010) find that 85% of the moment release from recent normal faulting earthquakes has been at 5 km elevation or higher. Molnar and Tapponnier (1978) first observed the north-south trending normal faults bounding rifts in central Tibet. These have since been found to accommodate up to 20% of the plateau's east-west extension measured geodetically (Elliott et al., 2010).

Two groups of normal faulting earthquakes occur at 100°E, 30°N (E-W striking nodal planes) and 100°E, 27°N (N-S striking nodal planes; see Figure 4.6). Copley (2008) explain these in terms of gravitational flow between the Sichuan basin and eastern syntaxis. Increased southward velocities cause N-S extension on the edge of the high plateau (first cluster) and divergence of the flow into the surrounding lowland causes E-W extension (second cluster).

Observations of thrust and normal faulting suggest that today the plateau is not increasing its elevation, but instead is collapsing aided by east-west extension (e.g. Molnar and Lyon-Caen, 1989, England and Houseman, 1989). Meanwhile, the mountain ranges on the plateau margins are in a compressive stress regime and are now absorbing much of the collisional convergence.

2.3.2 Strike-slip faulting

Strike-slip faults and earthquakes are prevalent over the deforming area (Figure 4.6) and occur at most elevations, but predominantly above 4.5 km (Figure 2.5). Large strike-slip faults within the Tibetan plateau have been identified as major structures that have controlled eastward extrusion of the plateau (e.g. Molnar and Tapponnier, 1975, Tapponnier et al., 1982). However, the high geological slip rates cited to support

this hypothesis are contested by much lower rates observed using both geological and geodetic methods. There is ongoing debate over the equivalence of slip rate estimates made using geodetic methods, that use data on a decadal time scale, and geological methods, that are applicable over periods spanning back thousands of years. Many argue that the slip rate observed today may not represent the true interseismic slip rate, but some part of the earthquake cycle where the rate is accelerated or decelerated (e.g. Hetland and Hager, 2006, Hilley et al., 2009). Others advocate a recent decrease in slip rate that can explain slip rate discrepancies (e.g. Chevalier et al., 2005). There can also be large discrepancies in geomorphologically estimated rates depending on the interpretation methods used (e.g. Houlié and Phillips, 2011).

Molnar and Dayem (2010) find that most fast ($\geq$10 mm/yr) strike-slip faults around the world are situated next to strong objects such as cratons or oceanic lithosphere. The reason for this being that strain in a viscous medium localises at lithospheric strength discontinuities (Dayem et al., 2009a). In Tibet, we see the Altyn Tagh fault adjacent to the Tarim basin, the Kunlun fault situated next to the Qaidam basin, and the most active segment of the Xianshuihe fault close to the Sichuan basin. All three basins are inferred to be stronger than Tibet (Molnar and Tapponnier, 1981, Braitenberg et al., 2003). Therefore the hypothesis of Molnar and Dayem might explain the presence of these relatively fast faults at the edges of the plateau, and the apparent lack of long, fast strike-slip faults in the central portion of the plateau.

In the following I describe these and other major strike-slip faults in Asia, all of which are plotted in Figure 2.2. Current slip-rate estimates for these faults are summarised in Table 2.1. Molnar and Dayem (2010) give an overview of slip rate estimates for the major strike-slip faults in Asia and worldwide, whilst Searle et al. (2011) give a comprehensive overview for the Altyn Tagh and Karakoram faults where a lot of research has been focussed.

Altyn Tagh fault

The Altyn Tagh fault is a major left-lateral strike-slip fault of over 2000 km length that runs along the northern edge of the Tibetan plateau with a NE-SW strike. The fault originates in the east at 77°E where it intersects the Karakoram fault and terminates at 97°E in the west where it splays into thrust faults in the Qilian Shan ranges. The fault marks the northern boundary of high topography, with the steep topographic gradient

down to the lower Tarim basin on its northern side. The slip rate of the Altyn Tagh has proved contentious, with geological, Quaternary and geodetic methods giving a wide range of estimates (Searle et al., 2011).

Evidence for a slip rate in excess of 20 mm/yr on the Altyn Tagh has been gathered from geomorphological offsets measured using satellite images (Peltzer et al., 1989), paleomagnetic rotations (Chen et al., 2002), and cosmogenic dating (Tapponnier et al., 2001a, Mériaux et al., 2004). These high slip rates have been used to support extrusion models of Tibetan deformation (Tapponnier et al., 1982, 2001b). However, not only do other studies of the Quaternary slip rate yield values less than 15 mm/yr (e.g. Zhang et al., 2007, Cowgill, 2007, Cowgill et al., 2009), but geodetic measurements from GPS and InSAR yield slip rates consistently within the range 5-15 mm/yr (e.g. Bendick et al., 2000, Wallace et al., 2004, Wright et al., 2004a, Jolivet et al., 2008, Elliott et al., 2008). Furthermore, multiple studies have found that the slip rate at the eastern end of the Altyn Tagh fault decreases to less than 5 mm/yr as slip is partitioned onto more easterly fault splays (e.g. Meyer et al., 1996, Zhang et al., 2007). A rate of 10±2 mm/yr now seems to be consistent with most data for the central segment of the Altyn Tagh fault (Molnar and Dayem, 2010).

Karakoram fault

The Karakoram fault is a right-lateral strike-slip fault of around 1000 km length on the western margin of the Tibetan plateau. The fault strikes NW-SE running from the Pamir to south-west Tibet. Similar to the Altyn Tagh fault, the slip rate of the Karakoram fault has proved controversial with a wide range of estimates (Searle et al., 2011).

Liu (1993) and Avouac and Tapponnier (1993) inferred a Quaternary rate between 24 and 40 mm/yr for the fault, which would lend support to this fault's role in major eastward extrusion of the plateau. However, most other Quaternary (e.g. Brown et al., 2002, Phillips et al., 2004) and InSAR (Wright et al., 2004a, Wang and Wright, 2011) studies give low slip rates less than 5 mm/yr. A more recent Quaternary rate of 10.7±0.7 mm/yr is also cited in favour of an extrusion model (Chevalier et al., 2005). However, Houlié and Phillips (2011) re-analyse the same data-set and get a lower estimate with higher errors (8.5±3 mm/yr) that is more in line with other estimates. At this stage more evidence is required in order for us to understand the role of the

Karakoram in overall Tibetan deformation, but episodic order of magnitude changes in slip rate and seismicity in the last 200 kyr are feasible (Houlié and Phillips, 2011).

Kunlun fault

The Kunlun fault is an east-west trending, left-lateral strike-slip fault of over 1500 km length. For the most part the fault bounds the southern margin of the Qaidam basin and therefore marks the north-eastern extent of high plateau topography. It originates in the plateau interior at around 86°E and dies out in the west near the plateau's margin but still within the high topography at around 102°E. Although its role is considered less important than the Altyn Tagh fault, it is recognised as one of three major faults along which a large amount of strain is accommodated (Molnar and Tapponnier, 1975).

Quaternary and geodetic slip rates for the central portion of the fault adjacent to the Qaidam basin tend to agree within the range of 10±2 mm/yr (e.g. Kidd and Molnar, 1988, Van der Woerd et al., 1998, Zhang et al., 2004, Hilley et al., 2005). Kirby et al. (2007) and Duvall and Clark (2010) find that the Quaternary and geodetic slip rate decreases from these values to zero over a distance of 150-200 km from the eastern fault termination. Strain is therefore distributed over a broad region around the fault tip and is transferred to the Haiyuan fault in the north-east (Duvall and Clark, 2010). The decrease of slip rate observed toward the end of the Kunlun fault is similar to the Altyn Tagh fault at 97^{o}E.

The western and central segments of the Kunlun fault are seismically active, with large strike slip earthquakes having occurred at Manyi in 1997 (M_w 7.6, Funning et al., 2007) and Kokoxili in 2001 (M_w 7.8, Lasserre et al., 2005). In contrast, Kirby et al. (2007) find that there have been no historical seismic ruptures east of 99°E. The Manyi and Kokoxili earthquakes have both generated long-lived postseismic transient signals that are measurable using geodetic techniques (Ryder et al., 2007, 2011). Hilley et al. (2009) argue that these processes bias geodetic measurements, which can then cause a discrepancy with estimated long term slip rates.

Other plateau strike-slip faults

Other than the three large faults discussed above, there are a number of less studied strike-slip faults which contribute to the present day deformation of the Tibetan plateau.

The left-lateral Xianshuihe fault is on the eastern margin of the plateau where it facilitates the movement of crustal material towards Yunnan. Although geological methods have not found a consistent slip-rate, GPS and InSAR studies give rates in the region of 10±2 mm/yr (Shen et al., 2005, Wang et al., 2009).

The Haiyuan fault is a ∼1000 km long left-lateral, nearly E-W trending fault which runs through the Qilian Shan on the north eastern margin of the Tibetan plateau and connects with the Qinling Shan at the southern edge of the Ordos block. Slip rates ranging between 4 and 19 mm/yr are obtained from geomorphological studies (Li et al., 2009a, Lasserre et al., 2002). Molnar and Dayem (2010) disagree with the upper bound of these estimates, and favour a low slip rate of 4-8 mm/yr as indicated by InSAR (Cavalié et al., 2008).

The Jiali fault is a right-lateral fault trending NW-SE which runs from the BNS into Yunnan in a position close to the eastern Himalayan syntaxis. Armijo et al. (1989) originally postulated a continuous Karakoram-Jiali system which allowed large scale eastward extrusion of the north plateau away from the collision zone. They estimated 15 mm/yr of slip at a time when there were no well defined geological markers on the fault. The slip rate of the Jiali fault remains poorly constrained.

Long strike-slip faults are absent in central Tibet. Taylor et al. (2003) studied a set of conjugate strike-slip faults in central Tibet that simultaneously accommodate both N-S shortening and E-W extension. North of the BNS, faults strike NE-SW, whereas south of the suture they trend NW-SE with sets of faults merging at the suture zone. By studying long period SAR interferograms covering three of the conjugate strike-slip faults, Taylor and Peltzer (2006) argue for concentrated strain with slip rates less than 6 mm/yr for two of the faults, suggesting a relatively young age compared with other major plateau faults. However, they estimate a slip rate between 7.5 and 20.8 mm/yr for the Gyaring Co fault and argue that this range correlates with the 15 mm/yr estimated by Armijo et al. (1989) for the Jiali fault. The inference here is that the two faults are structurally related.

Oblique subduction of India to the west of Yunnan and Sundaland is partitioned between thrusts and a single strike-slip fault. This is the 1100 km long Sagaing fault, which is right-lateral and trends N-S in the lowland region of Myanmar inboard but parallel to the India-Eurasia collision boundary. The fault has a rapid slip rate of 18 mm/yr as determined geodetically (e.g. Vigny et al., 2003, Maurin et al., 2010).

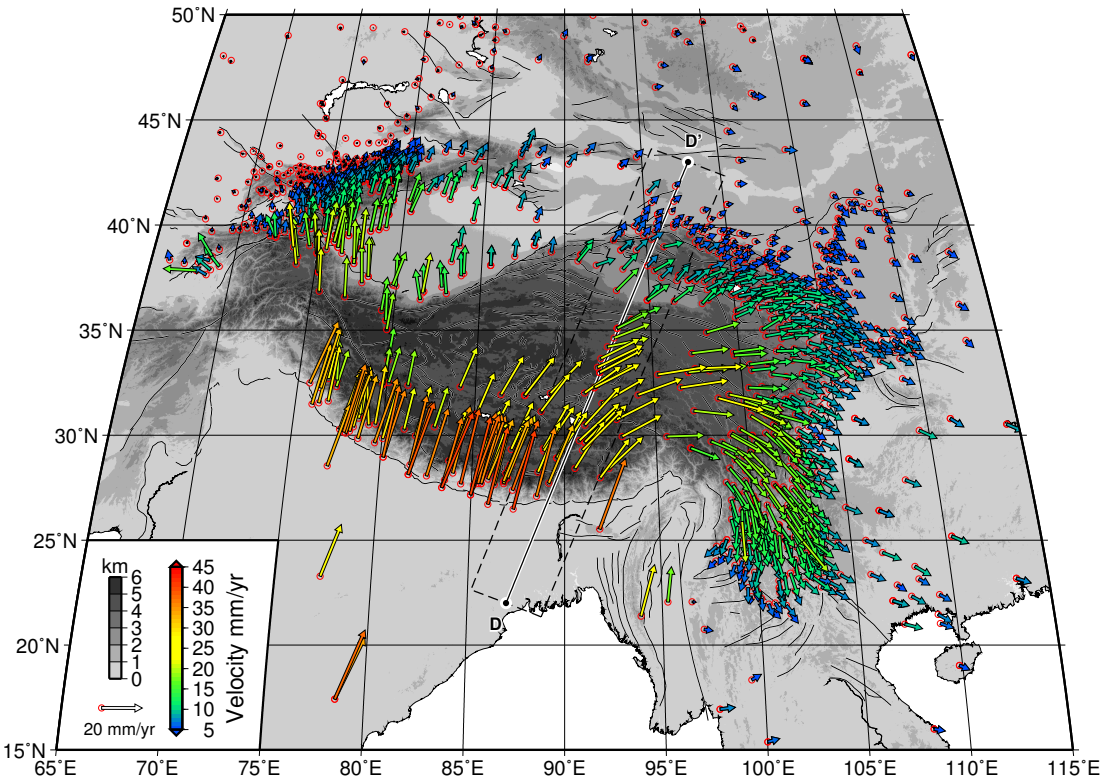

Figure 2.6: GPS velocity field for Asia relative to a stable Eurasian reference frame. The plotted arrows are a combined data-set including published data-sets from Calais et al. (2006), Gan et al. (2007) and Zubovich et al. (2010) (see §6.1.3). Arrows are coloured according to the vector magnitude. Red circles give station locations. Fault data from Taylor and Yin (2009) are plotted as black-on-white lines. Profile D-D' is plotted in Figure 2.7 with points falling in the black dashed swath 200 km from the line. Sinusoidal projection.

The Red River fault is a ∼1000 km long, right-lateral strike-slip fault trending NW-SE in the Yunnan region, to the south of the main Tibetan plateau. It is often inferred to be the boundary between separate Sundaland and Yangtze/Indo-China plates and may have accommodated left-lateral motion between these two plates in the Miocene (Tapponnier et al., 1986). However, both Quaternary and current estimates for the slip rate are low, typically around 2 mm/yr (e.g. Allen et al., 1984, Shen et al., 2005).

2.4 Surface motion

2.4.1 GPS velocities

Advances in the use of the Global Positioning System (GPS) since the 1980s have led to the routine use of this satellite constellation to detect motions with a precision on the millimetre level (e.g. Hager et al., 1991, Dixon, 1991). By applying this technique

to the study of land movements we can gain insight into the kinematics of continental deformation. The global coverage of GPS stations is increasing rapidly as deployment costs decrease. However, in some parts of central and western Tibet the coverage remains fairly sparse due to the remoteness of these parts of the plateau. Unfortunately, this is limiting the effectiveness of using GPS data to determine the mode of deformation in the plateau, with several types of model adequately fitting the sparse data.

Several compilations for Tibet have been published (e.g. Chen et al., 2000, Wang et al., 2001, Zhang et al., 2004, Shen et al., 2005, Gan et al., 2007), with generally dense coverage in the Himalaya and in the north-east and eastern margins of the plateau. The most recent compilation by Gan et al. (2007) is plotted in Figure 2.6 in a fixed Eurasian-plate reference frame with additional measurements from Calais et al. (2006) and Zubovich et al. (2010) for the surrounding regions.

DeMets et al. (2010) report that GPS data give a current linear velocity of India that is ∼7 mm/yr lower than the geological rate given by MORVEL (greater than 2 times the combined uncertainties of MORVEL), providing further evidence for a possible recent slow down of India-Asia convergence. Wang et al. (2001) find that shortening in the Tibetan plateau is greatest in the direction of India's convergence which has an average value of N21°E. The total shortening in this orientation is ∼40 mm/yr, with a generally linear gradient across Tibet and velocities reaching a background level of less than 5 mm/yr to the north-east of the Qilian Shan (Figure 2.7). This indicates that the Tibetan orogen is currently absorbing all the convergence without significant deformation of Mongolia to the north-east of the plateau.

In the western Himalaya, Banerjee and Bürgmann (2002) find that ∼15 mm/yr of the total shortening is accommodated by the Himalaya in a narrow 100 km wide zone which tracks the southern edge of the mountain range. However, a GPS profile further east (Figure 2.7) shows this degree of shortening across a ∼300 km wide zone.

Profile-perpendicular GPS velocities in Figure 2.7 show that up to 20 mm/yr of eastward motion is localised in the high Tibetan plateau. No step-like change in velocity or velocity gradient is obvious amongst data scatter at major strike-slip faults, with eastward velocity offsets certainly much less than the 10 mm/yr or higher slip rates suggested for these faults (Table 2.1). Scatter of data points is due to a combination of measurement error and the fact that measurement points are offset up to 200 km across the profile line.

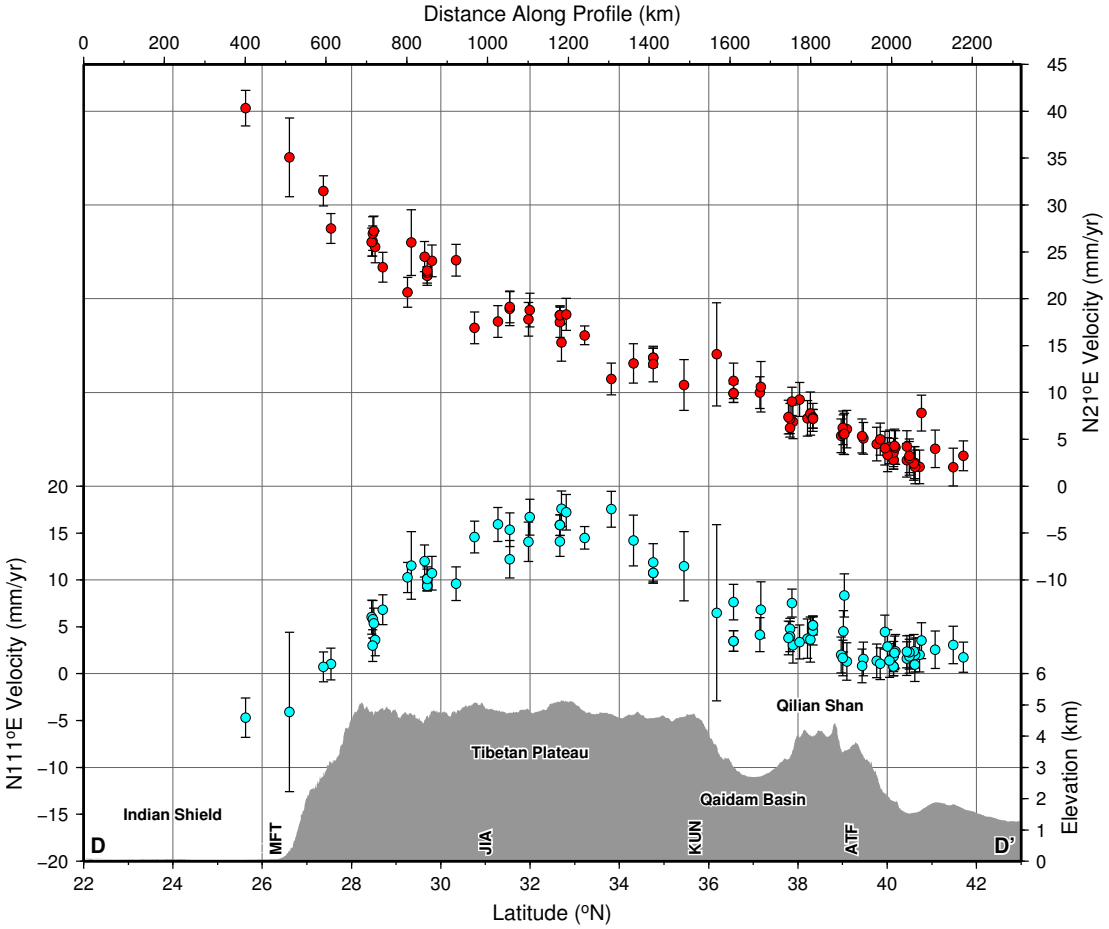

Figure 2.7: Profile through the GPS velocity field shown in Figure 2.6 in the orientation of greatest India-Asia convergence (N21°E). The profile is coincident with topographic profile D-D' shown in Figure 2.4. Velocities within a 200 km swath either side of the profile are projected onto the line. North and east velocity components are converted into profile parallel (N21°E, red points) and profile perpendicular (N111°E, cyan points) components. Error bars give the 95% confidence intervals. GPS data from Gan et al. (2007) in Eurasia-fixed reference frame. Fault name abbreviations are the same as Figure 2.2).

Zubovich et al. (2010) compiled GPS data for the Tien Shan mountains that reveals shortening of 20 mm/yr across the range. At this rate, the current mountain range would be built in 10 Ma and thus the GPS data suggests that the present Tien Shan has evolved only late in the India-Asia collision process (Zubovich et al., 2010). However, geological evidence suggests the Tien Shan were reactivated by the India-Asia collision, having been formed previously by island arc accretion since the Paleozoic (Windley et al., 1990).

Gan et al. (2007) calculate a best fitting rigid rotation for the Tibetan plateau and estimate that around 50% of the north-eastward directed motion imparted by

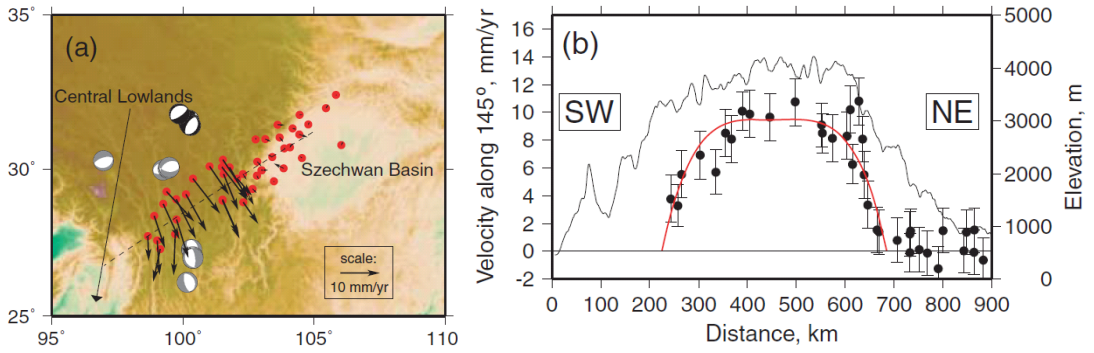

Figure 2.8: Correspondence of topography and GPS velocity magnitudes in south-east Tibet. a) Topography, and subset of GPS velocities from Shen et al. (2005) in a South China-fixed reference frame. The profile line is drawn between the eastern syntaxis and Sichuan basin, perpendicular to the down-slope direction = 145°. b) Topographic profile (black line) and profile-perpendicular component of GPS velocities plotted in a). After Copley and McKenzie (2007).

India is accommodated by this rotational component and eastward extrusion. The residual velocity field, representing a Tibet-fixed reference frame, highlights certain aspects of the internal deformation of the plateau. These include noticeable velocity discontinuities across the Haiyuan, Kunlun and Xianshuihe faults, abrupt shortening across the Himalaya, and a 'glacier-like' flow pattern between the eastern syntaxis and Sichuan basin with a 'fan-like' flow termination in Yunnan (Gan et al., 2007).

The most striking feature of the Eurasia-fixed GPS velocity field (Figure 2.6) is the smooth clockwise rotation around the eastern syntaxis, with velocity directions changing from north-east in the high plateau, through east, to a southerly direction in Yunnan. There is also a strong positive correlation between velocity magnitudes and the symmetrical topographic form between the eastern Himalayan syntaxis and Sichuan basin (Figure 2.8). These observations have led to the hypothesis that weaker Tibetan crustal material is flowing out of the plateau through this gap between the two strong regions into the surrounding low-lands under the influence of gravity (e.g. Copley and McKenzie, 2007, Copley, 2008).

Wang et al. (2001) point out the separate coherent block-like motion of the Tarim basin, north China and south China (the regions modelled as the Amur and Yangtze plates in MORVEL). The slower eastward movement of south China relative to the eastern plateau suggests that out-flow from Tibet is being constricted by this stronger lithosphere.

2.4.2 Velocity fields

GPS velocity measurements represent a discrete and (usually) uneven sampling of a deformation field. In order to gain insight into the deformation regime occurring throughout the lithosphere, the data can be inverted to obtain a smooth velocity field. Additionally, different types of surface motion data can be incorporated into the velocity field. The velocity field can then be used to calculate strain rates that directly indicate the variation of deformation throughout the region.

England and Molnar (1997a) calculated a coarse velocity field for Asia using published Quaternary fault slip rates. They find that the corresponding strain rates in Asia are consistent with continuum deformation (see §2.6.3) and not with the high slip rates measured using geological methods for the Altyn Tagh and Karakoram faults (see §2.3.2). Furthermore, the velocity field indicates that ~85% of India-Asia convergence is accommodated by thickening and that South China is not being extruded quicker than 10 mm/yr to the east. In order to try and explain the kinematic velocity field by dynamic deformation in Asia, England and Molnar (1997b) use the velocity field to infer variations of viscous stress in the continent. They find that gradients of stress point towards regions of greatest crustal thickness in the plateau centre. As a result, England and Molnar (1997b) explain deformation in terms of buoyancy-driven viscous flow with a viscosity of 10^{22} Pa·s for the Tibetan lithosphere.

Holt et al. (2000) and England and Molnar (2005) calculate self consistent velocity fields for Asia (the latter updating their previous study). Both incorporate Quaternary fault slip rate data, in addition to GPS velocity data (Holt et al., 2000) and baseline length changes between GPS sites (England and Molnar, 2005; Figure 2.9). In both studies, the authors argue for the same conclusions as England and Molnar (1997a,b). However, block-like behaviour is found to successfully describe the deformation in a few regions, namely Tarim, Amur, South China and Siberia, which exhibit internal strain of less than $5\text{x}10^{-9}$ yr^{-1} (see Figure 2.9b).

The studies of Holt et al. (2000) and England and Molnar (2005) include data covering different time scales. Quaternary slip rates are effectively averaged over a period of ~10^4 years, whereas GPS velocities are unlikely to be averaged over longer than the last 10^1 years. England and Molnar (2005) find that discrepancies between the two data-sets are within the uncertainties of the methods. Therefore the two data-sets are consistent and do not indicate a change in the velocity field during the last 10^4

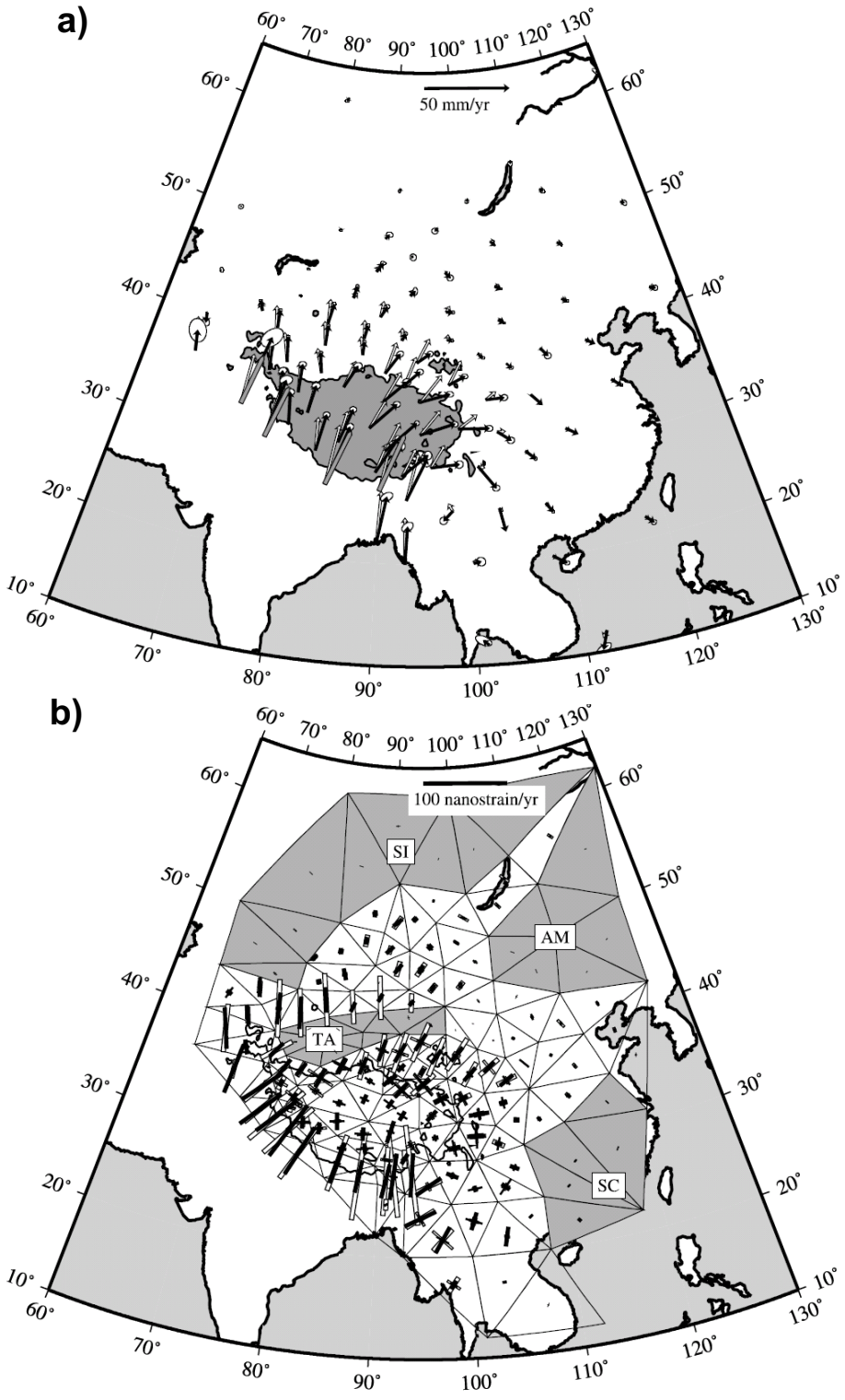

Figure 2.9: Velocity and strain rate fields of Asia determined from Quaternary fault slip rates (QFSR) and baseline length changes between GPS stations (BLC; after England and Molnar, 2005). a) Velocities at mesh nodes calculated with QFSR (white arrows) and, additionally, BLC (black arrows). Grey arrows show India's velocity relative to Eurasia from model of Sella et al. (2002). b) Principal strain rate directions for each triangle. Thicker bars are compressional whilst thinner bars are extensional. Black and white bars represent the same components as in a). Shaded mesh triangles show those found to be deforming almost rigidly due to low strain rate values ($<5\text{x}10^{-9}$ yr^{-1}). AM - Amur, SC - South China, SI - Siberia, TA - Tarim.

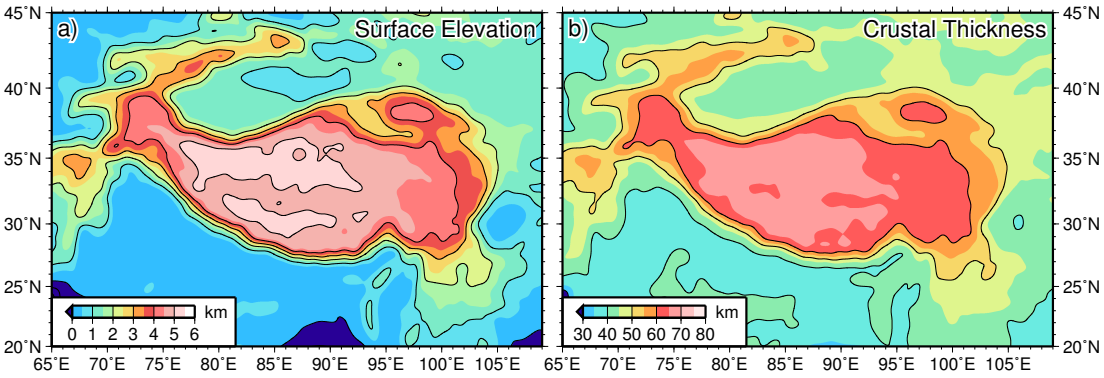

Figure 2.10: Comparison of long wavelength topography and predicted crustal thickness in Tibet and surrounding regions. a) SRTM topography resampled to 1 arc-minute and smoothed using a Gaussian filter with 250 km width. A large proportion of the plateau has an elevation of 5 ± 0.5 km. b) Crustal thickness predictions based on the assumption of Airy isostasy (Eq. 1.6). Calculated using elevations from a), densities $\rho_c = 2800$ kg m^{-3} and $\rho_m = 3300$ kg m^{-3}, an average continental crustal thickness of 38 km (Mooney et al., 1998) and an average continental elevation of zero. These predictions indicate that no significant proportion of the plateau has a thickness exceeding 70 km.

years.

2.5 Deep structure of the plateau

In addition to uplifted topography, the Eurasian crust has been significantly thickened from a global average value for continental crust of 38 km, to 70 km beneath the Tibetan plateau (Christensen and Mooney, 1995, Mooney et al., 1998), or even as much as 80-90 km locally (Priestley et al., 2008; and references therein). Through the concept of isostasy (§1.3.2), the crustal thickness can be estimated from surface elevation (Eq. 1.6). Figure 2.10 shows the crustal thicknesses predicted in this way for the region of the Tibetan plateau based on long wavelength components of the topography, $S_0 = 38$ km and $e_0 = 0$. Beneath the flat interior of the plateau, predictions suggest a crustal thickness exclusively within the range 60-70 km. Thicknesses beneath the south of the plateau are not well estimated by this method because the crust is not in isostatic equilibrium; Bouguer gravity anomalies across the Himalaya reveal that the flexure of the under-thrust Indian plate supports the load of the Himalaya and plateau above (Lyon-Caen and Molnar, 1985). Therefore, reported thicknesses as high as 90 km may be limited to parts of the plateau under-thrust by Indian crust.

Seismological techniques have become the primary tool for imaging sub-surface structures and providing evidence for models of the India-Asia collision. In the last 20 years

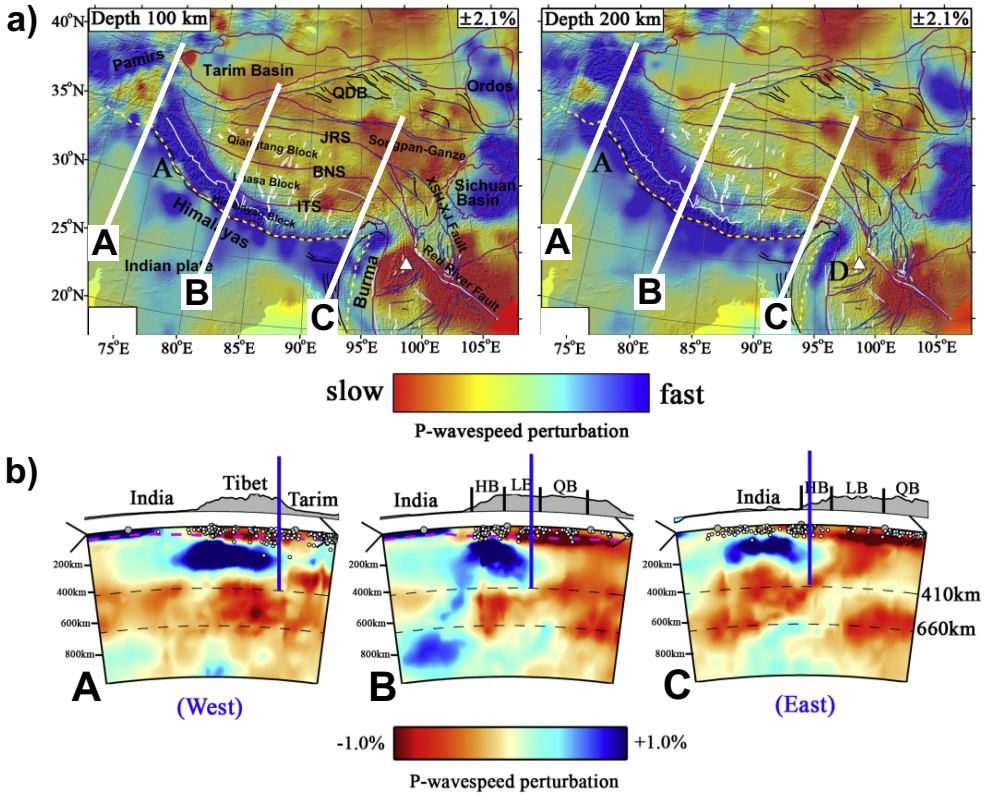

Figure 2.11: P-wave tomography model covering the Tibetan plateau from Li et al. (2008). a) Depth slices through the 3D model at 100 and 200 km showing the subducted Indian lithosphere as a fast anomaly beneath the southern plateau and the Tibetan lithosphere as a relatively slow anomaly. b) Cross sections through the 3D model at the locations marked by white lines in a). Cross sections depict the Indian lithosphere down to ∼300 km and with lateral penetration beneath the plateau decreasing from west to east. The leading edge of subducted Indian lithosphere is marked by the vertical blue line in each cross section. Modified from Figures 6 and 8 of Li et al. (2008).

the volume of collected data in Tibet has increased markedly, with ongoing international experiments such as INDEPTH (2002) and Hi-CLIMB (2005) expanding the spatial coverage of seismographs. In the following sections I briefly describe some of the results obtained using various seismological methods.

2.5.1 Seismic tomography

Seismic tomography can be used to identify variations of seismic wave speed in the lithosphere and is particularly sensitive to subtle lateral changes in the seismic properties. Tomographic images display perturbations of seismic wave speed relative to a chosen velocity model, where fast anomalies are generally interpreted as colder, denser lithosphere and slow anomalies are relatively warm and less dense. Tilmann et al. (2003)

produced a tomographic image from INDEPTH data which they say shows the Indian mantle lithosphere underlying Tibet as far north as the BNS, below which it descends sub-vertically into the asthenosphere. They argue that a counter-flow of asthenospheric material beneath the northern plateau could explain the presence of relatively warm mantle here, inferred from a localised region of poor Sn phase propagation (Barron and Priestley, 2009). Using finite-frequency tomography, Ren and Shen (2008) concentrate on the south-eastern corner of the plateau around the eastern Himalayan syntaxis. Here they interpret a localised upwelling of asthenosphere above a tabular portion of delaminated Indian mantle lithosphere.

Li et al. (2008) present a 3D P-wave tomographic model over the entire plateau (Figure 2.11). This shows the Indian lithosphere as a fast anomaly penetrating beneath the southern plateau. The distance of northward penetration decreases from west to east. In the west the fast anomaly underlies the entire Pamir, whereas in the east the fast anomaly is no further north than the IZS. At the longitude of the INDEPTH profile, the leading edge of the fast anomaly is close to the BNS and therefore agrees with Tilmann et al. (2003). An eastward dipping fast anomaly south of the eastern Himalayan syntaxis shows ongoing subduction beneath Burma. The results of Li et al. (2008) are in good agreement with those from surface wave tomography (Lebedev and van der Hilst, 2008), which reveals similar structures. The surface wave tomography of Priestley et al. (2006) shows a fast anomaly present to depths of ∼200 km beneath the entire plateau. This, they say, is indicative that the Indian mantle lithosphere is intact and has not been removed. Furthermore, results are compatible with concurrent northward under-thrusting of India and southward under-thrusting of Eurasia (e.g. Tapponnier et al., 2001b).

2.5.2 Receiver functions

Receiver functions measure conversions of P- and S-waves at seismic impedance contrasts and can be used to image sharp sub-horizontal boundaries such as the Moho, Lithosphere-Asthenosphere boundary (LAB) and the 410 and 660 km discontinuities in the asthenospheric mantle. Several studies have used this technique to image the Indian lithosphere beneath south Tibet in addition to mapping crustal and lithospheric thicknesses throughout the plateau. Kosarev et al. (1999) interpreted a northward dipping P-to-S conversion in teleseismic receiver functions as the top of delaminated

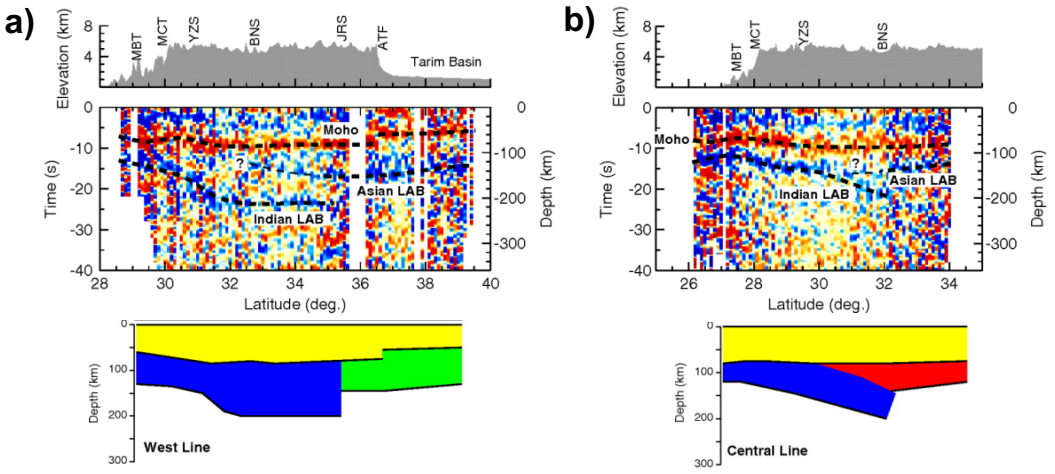

Figure 2.12: S-wave receiver function profiles across central Tibet from Zhao et al. (2010). Shown are topographic profiles (top), interpreted receiver function profiles (middle) and cartoon sketches (bottom) for two N-S orientated profile lines at a) ∼83°E and b) ∼88°E. For receiver functions, positive amplitudes are coloured red indicating downward increasing velocity and negative amplitudes are blue indicating downward decreasing velocity. The Moho appears relatively flat at ∼80 km beneath the plateau but with an abrupt jump to 60 km beneath the Tarim basin. The Indian lithosphere appears to under-thrust the plateau to a depth of ∼200 km with possible delamination in b). In cartoons, yellow represents crustal material, blue represents Indian mantle lithosphere, green represents Asian mantle lithosphere and red is interpreted by Zhao et al. as a deformable zone. Modified from Figures 2 and 4 of Zhao et al. (2010).

Indian lithospheric mantle which extends northward to the BNS at ∼32°N. Dipping southward from the northern plateau margin is a broken P-to-S conversion interpreted as a possible southward subduction of Eurasian lithosphere. Kind et al. (2002) further image this southward dipping interface using a densified receiver profile. Nabelek et al. (2009) interpret shallower receiver function images from a denser array as consistent with an underplating model. In their results, the Indian crust is inferred to be present beneath Tibet to a latitude of 31°N.

Using both P- and S-receiver functions and multiple profiles, Zhao et al. (2010) image the Moho and LAB beneath the plateau in four approximately N-S orientated profiles (The two central profiles are shown in Figure 2.12). In the central plateau, they find that shortening is accommodated by a combination of under-thrusting in the south and homogeneous thickening in the north. The northern extent of penetration of the Indian lithosphere varies along strike of the orogen in broad agreement with the tomographic result of Li et al. (2008). In the east, the mantle lithosphere is inferred to delaminate in a similar location to the findings of Ren and Shen (2008). In the far

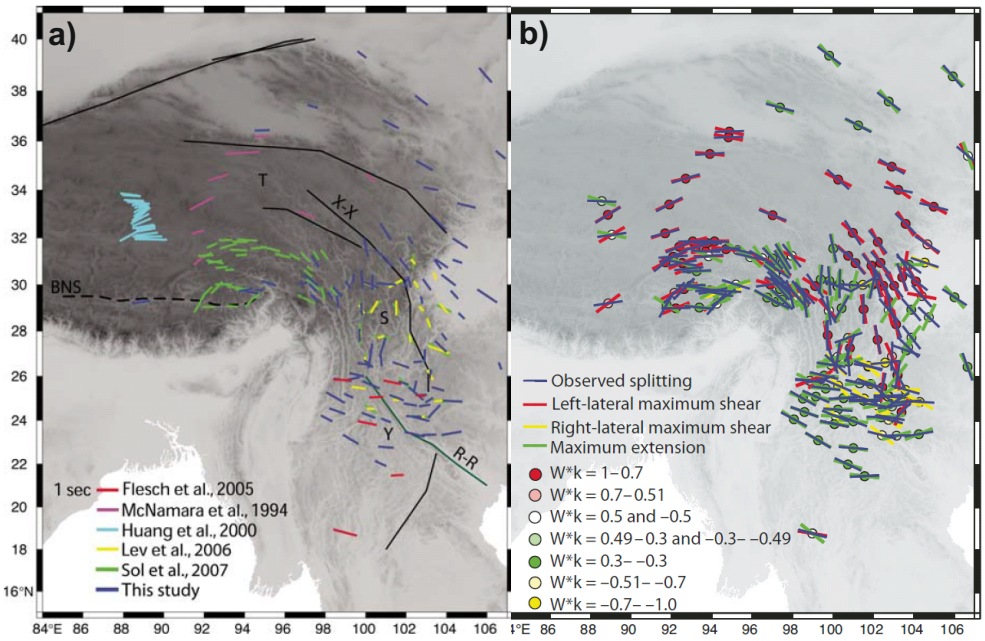

Figure 2.13: Comparison of shear wave splitting and splitting predictions derived from geodetic measurements in south-east Tibet reproduced from Wang et al. (2008). a) Shear wave splitting results from several published studies cited in the text indicating fast polarisation directions and delay times. b) Comparison of observed and predicted splitting orientations. Predicted splitting orientations are calculated from the surface strain rate field. Bars are coloured depending on the dominant deformation regime for each observation, determined using the kinematic vorticity number W^*k. This is the ratio between rotation and shear components of the strain rate tensor. $W^*k = \pm 1$ for right/left lateral simple shear and 0 for pure shear (Wang et al., 2008).

west beneath the Pamir and Tien Shan, Eurasian lithosphere is interpreted as being subducted under the intact Indian lithosphere.

Zhao et al. (2010) find that crustal thickness varies across the plateau, from 50 km in the south to a maximum of 80 km in central Tibet. They observe an abrupt offset in Moho depth from 80 to 60 km at the Tarim basin boundary, which is similar in magnitude to offsets seen at the Qaidam basin (Karplus et al., 2011; 70 to 50 km) and the Sichuan basin (Zhang et al. (2009), 60 to 35 km; Wang et al. (2010), 70 to 40 km) boundaries. Abrupt Moho offsets at strong region boundaries suggest homogeneous thickening of Tibet by pure shear in these locations without any under-thrusting.

2.5.3 Seismic anisotropy

Measuring the splitting of seismic shear waves can give an indication of the anisotropy in the mantle. The commonly held hypothesis for the production of this anisotropy is

that mantle minerals, particularly olivine, obtain a preferred orientation in their crystal lattices during tectonic deformation (Nicolas and Christensen, 1987, Silver and Chan, 1991). Results from core-refracted (SKS and SKKS) shear waves at receivers in Tibet show significant delay times and spatial heterogeneity (McNamara et al., 1994, Huang et al., 2000, Sol et al., 2007, Wang et al., 2008, Chen et al., 2010, Zhao et al., 2010). Davis et al. (1997) find that the observed splitting in Asia is explained better by internal straining of the lithospheric mantle, rather than due to motion of the lithosphere over the asthenosphere as would occur in plate-like deformation. The presence of strong splitting and high Sn attenuation in north-eastern Tibet is interpreted by Zhao et al. (2010) as being caused by the presence of a deformable zone sandwiched between the Indian and Eurasian mantle lithospheres.

Very low splitting is observed in parts of southern Tibet, which has been inferred to be due to the presence of the under-thrust Indian plate (e.g. Huang et al., 2000), although more recent studies observe moderate splitting south of 32°N (Sol et al., 2007, Wang et al., 2008; Figure 2.13a). However, high splitting is observed north of 32°N in central Tibet, and more widespread in eastern Tibet indicating that the Eurasian lithosphere has been deformed substantially where Indian lithosphere is not present. The pattern of splitting observations in east Tibet (Figure 2.13a) shows clockwise rotation of orientations around the eastern Himalayan syntaxis and exhibits a good correlation with active geological structures and GPS velocity vectors (Figure 2.6). An abrupt change in splitting orientations south of ∼26°N in Yunnan from N-S to E-W does not correlate with surface deformation, indicating a possible change of lithospheric structure (Lev et al., 2006). The precise configuration of plate boundaries in this region is not well known, and the contrast may mark the boundary of the Sundaland or Yangtze plates with greater Eurasia.

Wang et al. (2008) predict anisotropy directions from the surface strain rate field and compare these to SKS splitting measurements in east Tibet (Figure 2.13b). A good correlation is obtained over most of the region, and shows the systematic change from simple shear deformation on the plateau, to pure shear on its boundaries and borderlands. Many authors argue that this correspondence of mantle and surface splitting orientations provides strong evidence for mechanical coupling between the crust and lithospheric mantle (e.g. Holt, 2000, Flesch et al., 2005, Sol et al., 2007, Wang et al., 2008).

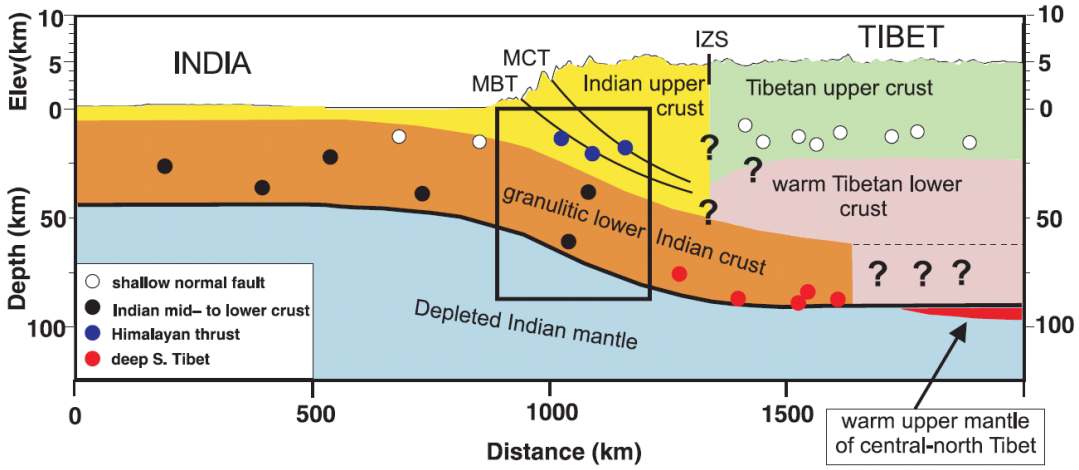

Figure 2.14: Schematic crustal cross-section of India and Tibet showing depth distribution of earthquakes (after Priestley et al., 2008). Earthquakes can be grouped into 4 categories based on their depth and spatial distribution as indicated by the different coloured dots. IZS - Indus-Zangbo Suture, MCT - Main Central Thrust, MBT - Main Boundary Thrust.

2.5.4 Earthquake depths

Molnar and Chen (1983) determined the depths of 16 strike-slip and normal earthquakes within the plateau. They found that all but two of these earthquakes occurred between 5 and 10 km depth. The other two normal earthquakes occurred beneath the south plateau at depths between 80 and 90 km, placing them in the mantle. They conclude that an aseismic lower crust exists above a brittle upper mantle. From this and other global focal depth observations, Chen and Molnar (1983) formalised what later became known as the 'jelly sandwich' rheology for continental lithosphere (§1.2). This rheology contains two strong regions in the upper crust and upper mantle, separated by a weaker zone in the lower crust (Brace and Kohlstedt, 1980). Maggi et al. (2000b) challenged the 'jelly sandwich' rheology by re-analysing earthquake depths for a number of regions. Earthquakes that were at first thought to be in the mantle were found to re-plot in the lower crust, suggesting that there is in fact no strong zone in the upper mantle and that lithospheric strength resides entirely in the crust.

Priestley et al. (2008) provide an explanation for the existence of the deep earthquakes observed by Molnar and Chen (1983). These earthquakes occur in the underthrust Indian lower crust (Figure 2.14). Due to its age, the temperature of the Indian lower crust is low and earthquakes occur until it warms above $\sim 600°C$. The northernmost extent of these deep earthquakes roughly coincides with the change in shear wave

splitting properties at ~32°N, providing strong evidence for the Indian crust being present beneath Tibet to this latitude. Beneath south Tibet, shallow earthquakes occur in the Tibetan upper crust and the Indian lower crustal layers with the Tibetan middle crust being warmer and aseismic. Although there is a bimodal distribution with depth, the complex geodynamic setting beneath the Himalaya and south Tibet means this observation should not be taken as direct evidence for a 'jelly sandwich' type rheology for continental lithosphere (Priestley et al., 2006).

2.6 Models of Tibetan deformation

Many different models have been proposed to explain the features observed in the India-Asia collision zone. As shown in Figure 1.2, two broad end-members can be defined as follows:

- Plate-like models based on the kinematic description of plate tectonics.
- Continuum models in which deformation is like that of a viscous fluid.

In plate-like models, the whole Tibetan plateau is split into a series of quasi-rigid blocks or micro-plates which sustain minimal internal deformation. Strain is concentrated instead at the block boundaries as major strike-slip faults that penetrate throughout the lithosphere. As a result of the blocks rigidity, the model requires high slip rates and large fault displacements along plateau bounding faults such as the Karakoram and Altyn Tagh faults. In general, a small number of large blocks with high boundary fault slip rates may be split into a larger number of small blocks with lower slip rates. In early models, the boundary faults were thought to control the 'extrusion' or lateral escape of blocks to the east as they were displaced by the advancing Indian plate (§2.6.1). In more recent models, geodetic velocity data is inverted to find a best-fitting configuration of kinematic plate movements (§2.6.2).

Many of the plate-like models assume plane-strain deformation in which vertical strain is negligible. Clearly, vertical deformation has been an important part of the accommodation of India-Asia convergence, and alternative models which strive to explain both vertical and horizontal deformation have been developed. The main premise of these models is that the lithosphere, or some part thereof, behaves on average as a viscous continuum. Under this assumption faults only cut the brittle upper crust, but slip rates are controlled by stresses supported in the viscous layer beneath (e.g.

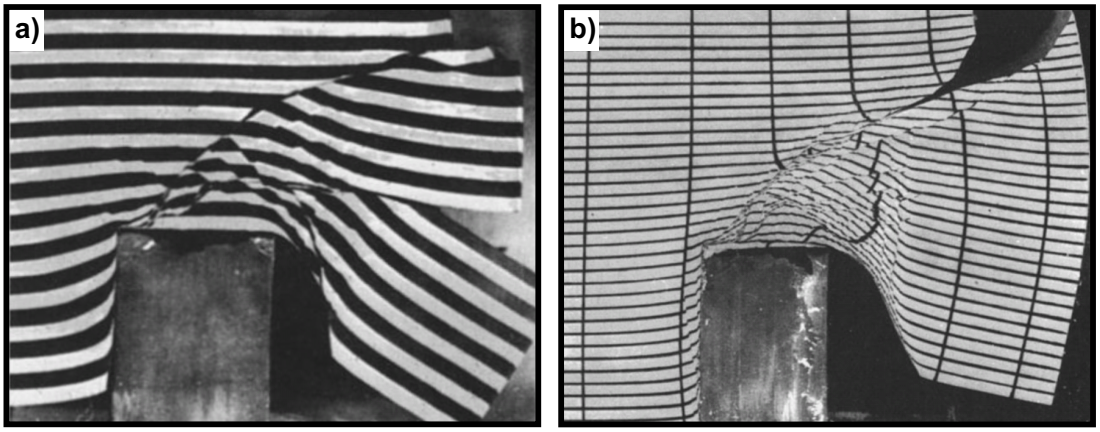

Figure 2.15: Plasticine indentation models of surface deformation resulting from the India-Asia collision after Peltzer and Tapponnier (1988). The models are confined on the left, upper, top and bottom boundaries. a) The model is constructed from vertical layers of alternating colour plasticine initially orientated perpendicular to the indentation direction. b) The model is constructed from five horizontal layers of plasticine with strain markers drawn on the surface. The differing styles of deformation show that the pre-collisional fabric of the model has an important bearing on the style of faulting.

Bourne et al., 1998). Two sub-types of continuum model have been proposed. In the first, the whole lithosphere deforms by pure shear thickening (§2.6.3). In the second, the lithosphere has a weak layer in the lower crust or upper mantle which deforms by viscous flow (§2.6.4).

2.6.1 Extrusion models

Based on the analysis of satellite imagery, Molnar and Tapponnier (1975) were the first to highlight the importance of strike-slip faulting in accommodating shortening in Asia. Using slip line theory of a plastic medium indented by a flat rigid die they noted the similarity in the sense and distribution of faulting in the Tibetan plateau. This observation led to a series of studies by Tapponnier and co-workers in which eastward extrusion was considered the dominant mechanism involved in accommodating the India-Asia collision (e.g. Tapponnier et al., 1982, Peltzer and Tapponnier, 1988, Avouac and Tapponnier, 1993, Peltzer and Saucier, 1996).

Tapponnier et al. (1982) and Peltzer and Tapponnier (1988) carried out indentation experiments using unscaled analogue models to describe the deformation pattern resulting from the India-Asia collision (Figure 2.15). In their models, the Indian plate is represented as a rigid indenter which is pushed at a constant rate into a deformable

plasticine block, representing the Eurasian lithosphere. Conditions of plane-strain were imposed using horizontal plates ensuring that the plasticine block was confined from above and below. One free lateral boundary allowed escape of material from the collision zone; a condition Tapponnier et al. (1986) justify due to the proximity of western Pacific subduction zones. Peltzer and Tapponnier (1988) find that certain models could approximate the present day strike-slip faulting pattern seen in Tibet and Asia depending on the pre-collisional structural fabric of the model (see Figure 2.15). In particular, Peltzer and Tapponnier argue that the best models involve strain softening that controls the localisation of faulting. Strain softening was introduced when rolling the plasticine into layers, which were then vertically aligned to construct the model.

England and Molnar (1990) provided an alternative explanation for the left lateral E-W trending major faults of eastern Tibet. Right-lateral north trending shear across Tibet results in clock-wise rotation of crustal blocks separated by E-W trending pre-collisional structural weaknesses. This explains the observed left-lateral strike-slip faults without the requirement of large-scale extrusion of material to the east.

Avouac and Tapponnier (1993) produced the first kinematic block model for the Tibetan region, constrained by the then-current high slip-rate estimates on the Altyn Tagh and Karakoram faults (Peltzer et al., 1989, Liu, 1993) and shortening across the Himalaya and Tien Shan. From this four block model they conclude that the mechanics of Tibetan deformation can be described by localisation of strain on the block boundaries. Peltzer and Saucier (1996) used the finite element method to invert for a kinematic velocity field in Asia constrained by far field plate motions and then-current fault slip-rate estimates on the major faults. By minimising the strain in the interior of quasi-rigid blocks they find that 80% of strain can be accounted for by localisation on large faults. By evaluating the surface area decrease across the model domain over the last 10,000 years, Peltzer and Saucier (1996) find that crustal thickening absorbs ∼73% of collisional shortening, whilst lateral extrusion absorbs the remaining ∼27%. To address the formation of thick crust and high elevations in the presence of ongoing lateral extrusion, Tapponnier et al. (2001b) describe a framework in which Asian lithospheric mantle is subducted to the south in a north-eastward migrating series that might explain the time dependent growth of the plateau. The obliquity of the subductions results in strain partitioning, enabling extrusion of blocks along strike-slip faults in the crust which toe-in to the subduction interfaces at depth.

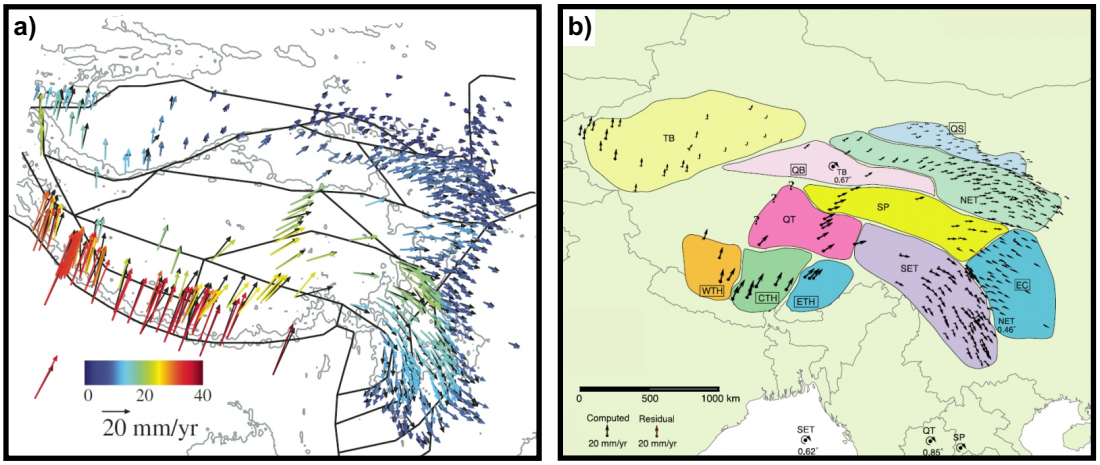

Figure 2.16: Two block models giving independent interpretations of the geodetically determined deformation field in the Tibetan plateau from a) Meade (2007) and b) Thatcher (2007). In both cases the observed velocities are from the GPS data-set of Zhang et al. (2004).

2.6.2 Geodetic block models

More recent kinematic block models have taken advantage of the ever increasing number of geodetic velocity observations for Asia (see §2.4.1). A general observation of such models is that as the number of geodetic observations increases, not only does the number of blocks needed to provide a satisfactory fit increase, but the uniqueness of any particular model decreases (Flesch and Bendick, 2007).

Based on the method of Meade and Hager (2005), Meade (2007) produced an elastic block model for Tibet which accounts for both rigid body rotations and interseismic fault locking at block boundaries (Savage and Burford, 1973). He divided the region sampled by the GPS observations of Zhang et al. (2004) into 17 blocks ranging in scale from plate size down to 10,000 km^2 (Figure 2.16a). Most block boundaries follow mapped structures, but some cut across regions devoid of mapped structures. The model predicts slip rates of between ~5-10 mm/yr on the major strike slip faults, which is consistent with those measured geodetically but significantly less than those used to support the extrusion model. However, an anomalous zone of high right-lateral slip is predicted in western Tibet where no such structure is evident. The lack of GPS observations in this region limits the accuracy of the model here. Meade (2007) finds that a constant fault locking depth of 17 km minimises the velocity misfits in the model and gives good agreement between the estimated moment accumulation rate on the block boundaries and the seismic moment release rate calculated from the historical

moment tensor catalogue.

Using a subset of the same GPS data-set, Thatcher (2007) devised an independent model with 11 blocks covering the same region (Figure 2.16b). He used a simpler approach than Meade (2007) by neglecting the effects of locking at block boundaries in order to concentrate on just fitting the angular motion of the blocks, which are assumed rigid. The model similarly predicts low slip rates for the major faults in Tibet. Thatcher (2007) concludes that large systematic misfits represent internal deformation of the blocks which could be resolved if modelled using a larger number of smaller blocks.

Wang et al. (2011) update and expand the model of Meade (2007) by modifying block boundaries in south-east Tibet, adding blocks to the whole of mainland China, and using a denser GPS data-set (Gan et al., 2007). Although the estimated slip rates in Tibet vary from those reported by Meade (2007), the conclusions remain the same. Loveless and Meade (2011) test a 24 block model for the possibility of internal deformation away from block boundaries. They find that internal block deformation is statistically distinguishable from observational noise in only 6 of the blocks, mainly in the central and western parts of the plateau. Furthermore, 85% of the surface deformation measured through GPS observations is attributable to slip at block boundaries with the rest accommodated by internal processes.

The conclusions of these more recent block modelling studies are that the geodetic surface deformation in the Tibetan plateau can be explained predominantly by the motions of a finite number of rigid blocks with strain localised at their boundaries. However, these models differ from the earlier extrusion models in that the fault slip rates are low (<15 mm/yr) and relatively uniform throughout the plateau.

2.6.3 Lithospheric thickening models

The idea of the lithosphere deforming as a viscous fluid in collision settings was first described by England and McKenzie (1982). They developed the 'thin viscous sheet' (TVS) approximation in which the lithosphere is represented as a thin sheet that flows in response to the competition between horizontal tectonic forces and vertical buoyancy forces (Figure 2.17). The TVS provides a simple way to explain the large scale features of the orogenic system without the complication of the finer details, such as individual fault structures. It uses a vertically averaged viscous rheology and a simplifying as-

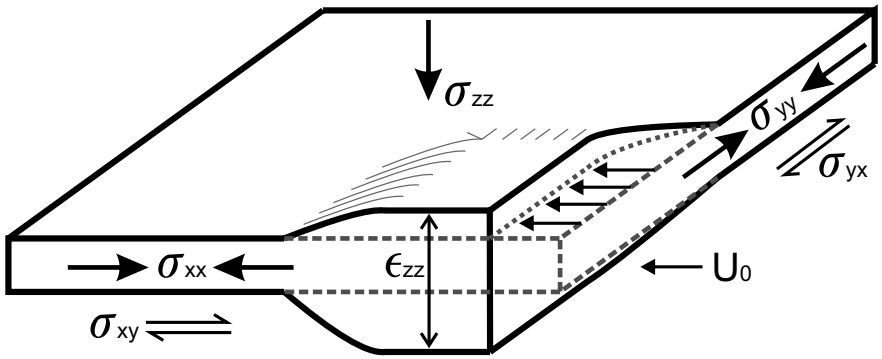

Figure 2.17: Schematic of the thin viscous sheet model of continuum deformation redrawn from Houseman and England (1996). The lithosphere is represented as a thin layer which deforms primarily by crustal thickening (ϵ_{zz}) when its boundary is indented with velocity U_0. The significant stress components (σ) for such deformation are indicated.

sumption that horizontal flow velocities are invariant with depth in order to reduce the 3-dimensional problem to 2D. With this assumption, deformation occurs by pure shear and is governed by two parameters: the power law exponent (n) of the viscous constitutive law that relates stress to strain rate, and the Argand number (Ar). Named after Emile Argand, who made the first interpretation of Asian tectonics (Argand, 1924), the Argand number is a measure of the importance of forces arising from gravitational potential energy (GPE) contrasts relative to tectonic boundary forces. When $n = 1$, deformation is said to be linear or Newtonian. A non-linear, non-Newtonian rheology is any where the power law exponent is greater than 1.

(England and McKenzie, 1982) found that as the Argand number increases, GPE variations have more effect on the subsequent deformation and the lithosphere flows more in response to thickening. Consequently, a plateau of thickened crust adjacent to the indenting boundary does not develop with high Argand numbers. In a similar study, Vilotte et al. (1982) modelled collisional deformation under conditions of both plane-strain and plane-stress. Calculations for these mechanisms confirmed the fundamental difference in deformation style for the two cases in which buoyancy forces are overwhelming, or negligible.

Since the work of England and McKenzie (1982), TVS models have been successfully used to explain a number of deformation phenomena occurring in the India-Asia collision.

Growth of a plateau

Houseman and England (1986) and England and Houseman (1986) found that a plateau of thickened crust developed in front of the indenter for calculations with $n > 3$ and Ar between 1 and 10. Furthermore, they found satisfactory agreement between models with these parameters and present day observations from Asia. Within these bounds, the lithosphere deforms initially by pure shear thickening. As buoyancy forces become increasingly large, simple shear deformation becomes dominant in order to facilitate the lateral flow of material away from the region of greatest thickness. As a general rule in TVS calculations, the horizontal length scale of deformation increases with Ar but decreases with n (Houseman and England, 1986). Schueller and Davy (2008) summarised a broad range of analogue models that are scaled for gravity and consist of a layered rheology. They find that the dominant deformation regime observed in collisional experiments is dependent on the interplay between the Argand number and a brittle-to-ductile strength ratio.

Recent extension

England and Houseman (1989) sought to explain the occurrence of E-W extension in the plateau within the TVS framework. None of the aforementioned TVS calculations could explain the recent extension occurring since ~8 Ma (Armijo et al., 1986, Molnar et al., 1993). They hypothesised that the change from thickening to extension was a consequence of disturbing the vertical force balance by convective removal of a thickened lithospheric mantle root (e.g. Houseman et al., 1981). In the TVS framework this was simulated using two values of Ar; one that applies at the beginning of shortening, and a second larger value that accounts for the expected GPE increase after convective thinning has removed the thickened mantle lithosphere (England and Houseman, 1989). Jiménez-Munt and Platt (2006) expand on this problem by adding thermal effects to the TVS approach. Their modelling shows that a single rapid removal of a thickened lithospheric root and the subsequent increase in mantle heat flow can reproduce the present day topography, thinning, E-W extension and rotation around the eastern syntaxis.

Lateral escape

Houseman and England (1993) used the TVS model to describe continental-scale defor-

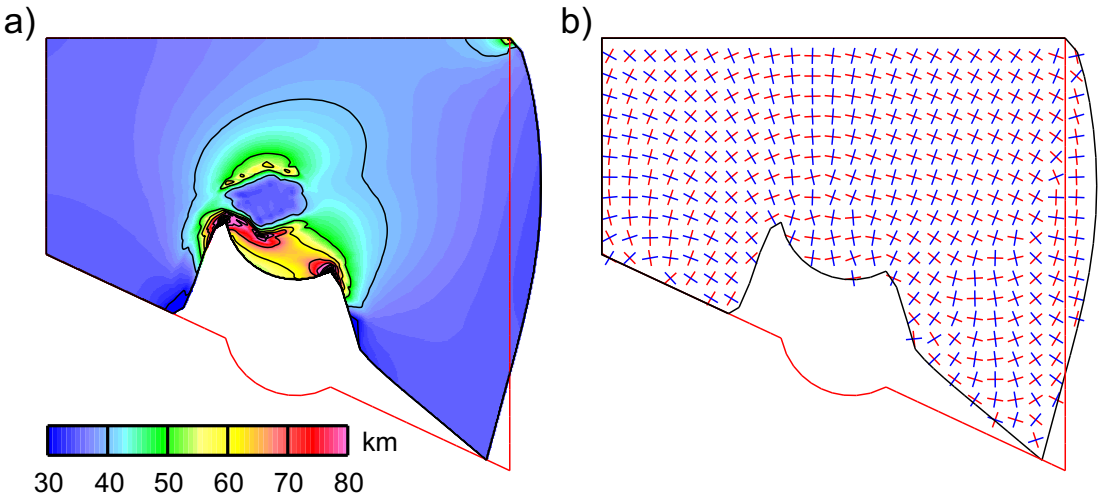

Figure 2.18: Deformation in a thin viscous sheet calculation with $n = 3$ and $Ar = 1$ after 50 Ma of indentation (after Houseman and England, 1996). The calculation has an embedded region of 10x greater strength representing the Tarim basin that resists thickening and a lithostatic eastern boundary which accommodates some lateral escape. North and west boundaries are rigid. Initial boundary configuration is shown in red. a) Predicted crustal thickness. Note the concentrations of thick crust on the southern and northern edge of the Tarim basin, which acts as a secondary indenter. b) Principal stress directions (magnitudes not plotted). Principal compressive stress directions (blue bars) show a radial pattern around the plateau, pointing towards the region of greatest thickness as observed in Asia (e.g. England and Molnar, 2005).

mation with a 'lithostatic' eastern boundary for a range of geometries. The lithostatic condition allows for boundary movement if the stress on that boundary is increased above its initial value by the evolving collision. For experiments able to produce a plateau of thickened crust comparable to present day Tibet, they found that only 10 to 30% of the shortening strain is accommodated by easterly movement of the lithostatic eastern boundary. Consequently, Houseman and England conclude that total convergent strain in Asia is probably partitioned between crustal thickening and eastward extrusion in a ratio of 4:1. This is in broad agreement with the quasi-rigid kinematic model of Peltzer and Saucier (1996), and also Davy and Cobbold (1988), who first investigated this problem using scaled analogue models. In these models, Davy and Cobbold found that thickening is equally as important as lateral escape.

Lateral strength heterogeneities

Another aspect of the India-Asia collision to be investigated using the TVS was the presence of high strength regions within the model lithosphere as a proxy for the Tarim basin (England and Houseman, 1985, Vilotte et al., 1984, 1986, Neil and Houseman,

1997, Dayem et al., 2009a,b; Figure 2.18). Calculations by England and Houseman (1985) show that such a strength heterogeneity can focus stress, giving enhanced thickening on the northern side (i.e. Tien Shan) and enhanced shear on the southern side (i.e. Altyn Tagh fault). Dayem et al. (2009a) explore this strain localisation further. With increased indentation the shear strain zone narrows, but to get a strain zone narrow enough to explain the Altyn Tagh fault additional weakening (e.g. from shear heating) is required. Neil and Houseman (1997) find that while Tarim lithosphere must be more resistant to deformation, the Tien Shan must be less resistant than the hinterland regions in order to match present day crustal thickness estimates for rheologies with n between 3 and 10. Using a similar model set-up, Dayem et al. (2009b) constrain the timing of deformation in northern Tibet to around the same time as the onset of collision, whereas previous TVS models had suggested a northward advancing deformation front (e.g. England and Houseman, 1986).

Flesch et al. (2001) solve the force balance equations in a thin sheet with stress boundary conditions and GPE differences to obtain the vertically averaged deviatoric stress field. From this they are able to infer the spatial distribution of vertically-averaged effective viscosity in the Asian lithosphere. In the Tibetan plateau, the viscosity is found to be within the range 0.5-5x10^{22} Pa·s, compared with a range of 1-2.5x10^{23} Pa·s for the more rigid regions of Asia surrounding the plateau.

England and Molnar (2005) subsequently provided a 'proof of concept' for the TVS approximation by showing the similarity between the velocity and strain-rate fields of Asia determined from GPS and Quaternary fault slip rates with those from a laterally homogeneous TVS calculation. They suggest that existing mismatches east of the Tibetan plateau would be improved by introducing lateral strength variations to the calculation.

Whitehouse (2004) investigates this assumption by inverting for strength variations using the velocity field of England and Molnar (2005) and topography as constraints to a TVS calculation. She finds that thin sheets with n in the range 3-10 can all adequately fit the observations. Estimated viscosities are 10^{21}-10^{22} Pa·s for the plateau margins, 3x10^{22}-10^{23} Pa·s for the plateau interior and 10^{23}-10^{24} Pa·s for shield regions.

Vergnolle et al. (2007) tested the balance between buoyancy forces and boundary conditions in a faulted thin sheet model covering much of Asia. They demonstrate that the best fit with observed GPS occurs with strong plate coupling at the India-Eurasia

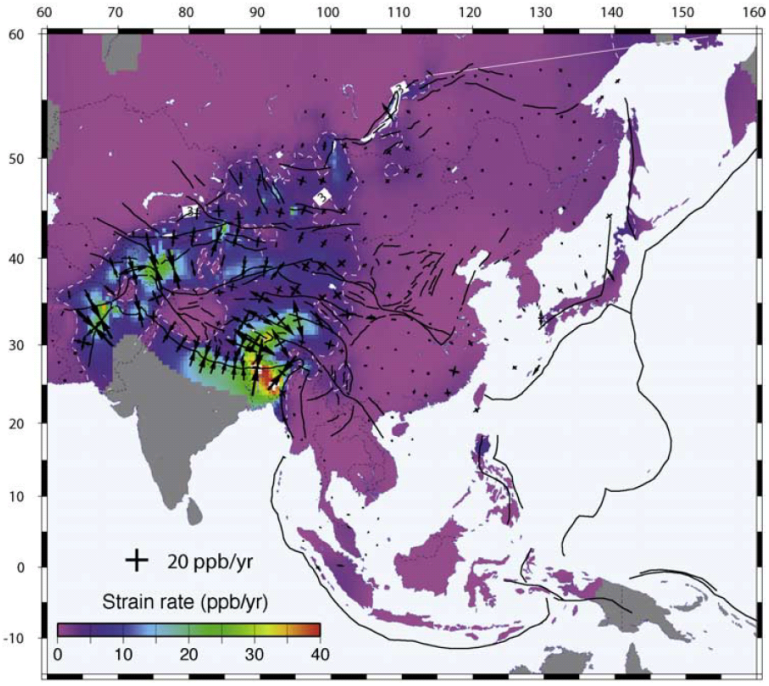

Figure 2.19: Magnitude of strain-rates (second invariant) in Asia from best fitting TVS model of Vergnolle et al. (2007). The 3 ppb/yr level is contoured white. Below this value, strain rates are not significant compared with the precision of the GPS data used. Black crosses are principal strain rate directions.

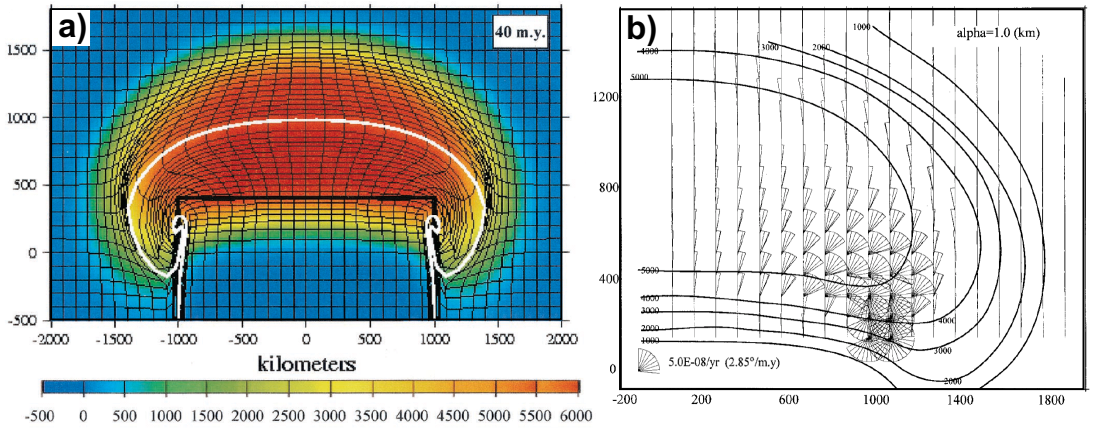

Figure 2.20: Predictions of a layered viscous model with a moderately weak lower crust after 40 m.y. of convergence (from Shen et al., 2001). a) Predicted topography in metres with mesh showing finite deformation. White and black lines show position of India-Asia surface and mantle sutures respectively. b) Instantaneous surface rotation rates for the eastern margin of the plateau.

boundary, which transmits stress northward into the continent. Also, eastern margin oceanic subductions, rather than extrusion, are responsible for pulling North China, South China and Sundaland to the east. Large parts of Asia exhibit very low strain rates and are therefore inferred to deform in a block-like fashion (Figure 2.19). High rates of deformation are limited to high elevation areas and lateral strength variations must have a major influence on the pattern of deformation observed in Asia (Vergnolle et al., 2007).

2.6.4 Crustal flow models

Zhao and Morgan (1987) first proposed a model in which part of the crust flows to explain the uplift of the Tibetan plateau and the observed surface deformation. In this model, under-thrust Indian crust is injected into the fluid-like Eurasian lower crust. In this way the lower crust acts as a hydraulic jack which maintains high and constant elevations throughout the plateau. Bird (1991) described the extrusion of lower crust from beneath high topography. In a rapid process lasting between 0.03-0.13 m.y., an initial topographic perturbation will flatten and create a plateau with steep, outward moving margins and a flat Moho, as seen beneath the Tibetan plateau. The reason for such flow is due to lateral pressure gradients induced by topographic variation acting on the warm and weak lower crust.

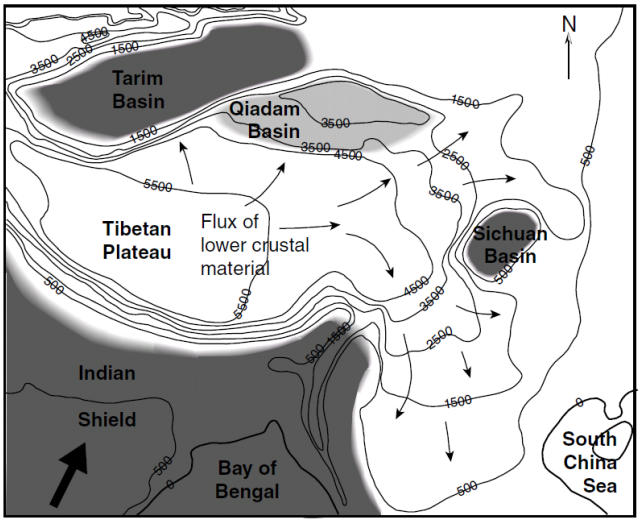

Figure 2.21: Schematic interpretation of Tibetan plateau morphology as the flow of lower crustal material between lateral strength heterogeneities (after Clark and Royden, 2000). Contours represent smoothed (filtered) elevation, which emphasise topographic gradients.

Royden (1996), Royden et al. (1997) and Shen et al. (2001) investigated laterally homogeneous viscous models with depth-dependent rheology (Figure 2.20). In these models, the deformation in the upper crust is decoupled from the mantle by a weak lower crustal layer which flows. Observed surface deformation is coupled to the mantle at the margins of the plateau but is decoupled in the plateau interior. Furthermore, shortening and extension can occur simultaneously in different parts of the orogen and without the presence of lateral strength heterogeneities or eastward movement of adjacent crust. The model also predicts the clockwise rotation of material around the eastern syntaxis, caused by dextral shear between India and Asia at depth, and gravitational spreading (Figure 2.20b).

Clark and Royden (2000) compared observed topographic profiles (Figure 2.4) with predictions from a simple 2-dimensional model of Newtonian fluid flow in a lower crustal channel of defined thickness. Their results infer that the topographic gradient depends on the viscosity of the flowing fluid. Steep margins have a viscosity of 10^{21} Pa·s and shallower margins have 10^{18} Pa·s, whereas an upper bound beneath the central plateau is 10^{16} Pa·s. They also interpret the present day morphology in terms of lower crustal material flowing out of the plateau between rigid inclusions (Figure 2.21). Clark et al. (2005) attribute the presence of the Longmen Shan to the production of dynamic topography due to the obstruction of lower crustal flow against the Sichuan basin. Cook

and Royden (2008) expand the whole plateau model of Shen et al. (2001) to include lateral strength heterogeneities in a simplified geometry. The results can reproduce the recognisable morphology of the plateau when strong regions represent the Sichuan and Tarim basins. In order to produce the low topographic gradient observed between Tibet and Yunnan, the initial model set-up requires the region covering Yunnan to have a slightly weaker lower crust than Tibet, which accelerates the development of lower crustal flow there (Cook and Royden, 2008).

Copley and McKenzie (2007) compare GPS velocities with those from a model of fluid flow driven by topographic pressure gradients. In an India-fixed reference frame, they find that Tibetan crust behaves like a gravity current spreading out over the low-lying shield, with the under-thrust Indian crust acting as a rigid base. The best fitting viscosity for Tibetan crust of such a model is 10^{20} Pa·s. They also explain the south-eastern Tibet outflow in terms of a gravity current with a viscosity 10^{22} Pa·s and a stress-free base. Copley (2008) further examines the outflow and finds that models with either significant vertical velocity gradients or deformation by pure shear can both match surface velocities in the region.

Beaumont et al. (2001, 2004) study the evolution of lower crustal channel flows using 2D plane-strain thermo-mechanical models. Radioactive heating in hot orogens reduces the viscosity of the crust and a weaker channel is formed. When coupled with focussed erosion at the orogen margin, high-grade metamorphic rocks are exhumed from this low viscosity channel as material is extruded under pressure driven by basal traction. Beaumont et al. (2001, 2004) interpret the formation of the Himalaya in this way, with climate feedback increasing the rate of exhumation. Avouac and Burov (1996) also consider the role of erosion on mountain growth although they find, in the context of the Tien Shan, that erosion results in a net influx of lower crustal material towards the orogen.

The coupling implied by the correspondence of mantle splitting measurements and predicted splitting from surface geodetic data (Figure 2.13) precludes the existence of a weak lower crust as vertical stresses would not be transmittable through this layer into the mantle. Using a 3D numerical model of continental collision with a weak lower crust, Lechmann et al. (2011) show that upper crustal and upper mantle velocity fields are near identical despite these layers being mechanically decoupled. However, this model uses an idealised indenting velocity boundary condition that is invariant with

depth. Copley et al. (2011) give evidence for a lack of a weak lower crust in south Tibet where under-thrust Indian crust is present. They observe that normal faulting earthquakes are concentrated in the southern part of the plateau whereas strike-slip earthquakes, although more evenly distributed, tend to cluster north of the inferred leading edge of the under-thrust Indian crust. By comparing the principal axes of the horizontal component of the earthquake moment tensors with modelled principal axes of the horizontal strain-rate tensor, Copley et al. (2011) find that a model with mechanical coupling between the rigid Indian crust and the Tibetan upper crust gives the best match to the observed dichotomy.

Chapter 3

Measuring interseismic deformation using InSAR

3.1 Introduction

Interferometric Synthetic Aperture Radar (InSAR) is now an established and widely used geodetic tool that is useful for quantifying ground displacements associated with a large variety of deformation phenomena. Two separately acquired Synthetic Aperture Radar (SAR) images of the same area are differenced to give a map of range change between the ground and satellite at a dense spatial resolution (∼10 pixels/km) and millimetric precision (Massonnet and Feigl, 1998).

InSAR was first used to quantify coseismic ground displacements that occurred during the 1992 Landers earthquake in California (Massonnet et al., 1993). It has since been used to measure earthquakes (Wright et al., 2001a, Talebian et al., 2004), volcanoes (Massonnet et al., 1995, Amelung et al., 2000), rifting and dyke intrusion (Wright et al., 2006, Hamling et al., 2009), landslides (Fruneau et al., 1996, Kimura and Yamaguchi, 2000), ice flow (Goldstein et al., 1993, Shepherd et al., 2001) and signals related to anthropogenic activities like CO_2 sequestration (Vasco et al., 2010, Gourmelen et al., 2011), oil extraction (Fielding et al., 1998, Li et al., 2009b) or water extraction (Amelung et al., 1999, Lopez-Quiroz et al., 2009).

Some of the phenomena mentioned above are associated with discrete or instantaneous ground displacements that occur over a short time period (i.e. an appreciable deformation occurs between two satellite passes). Additionally, some of the above phenomena can result in signals with a large magnitude; typically tens of centimetres. For example, Pritchard and Fielding (2008) use InSAR to observe up to 1.1 m of coseis-

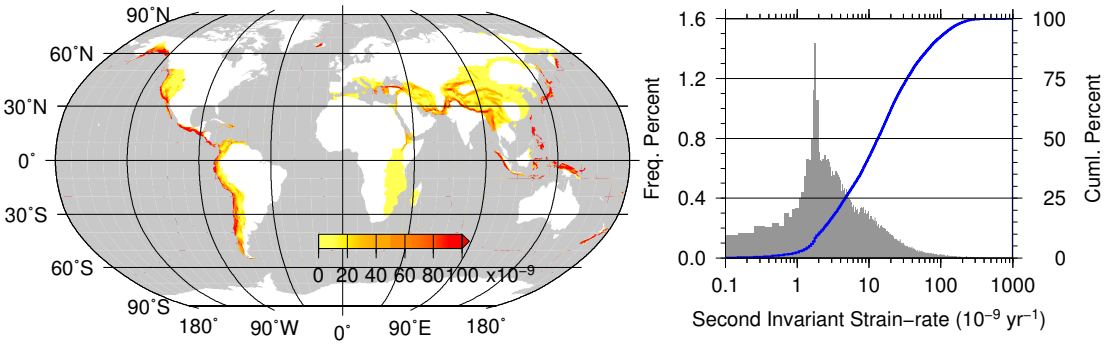

Figure 3.1: Onshore variation of strain rate magnitude from the Global Strain Rate Model (GSRM, Kreemer et al. (2003)). Plotted on the map are onshore strain rates that can potentially be measured using InSAR. The GSRM is at a resolution of 0.2 x 0.2 deg, and the magnitude is defined as the second invariant of the strain rate tensor $\dot{E} = (\dot{\varepsilon}_{xx}^2 + \dot{\varepsilon}_{yy}^2 + 2\dot{\varepsilon}_{xy}^2)^{\frac{1}{2}}$. Histogram shows the distribution of strain rate magnitudes in terms of percentage of total frequency (grey) and cumulative percentage (blue). It shows that ~90% of the deforming area is straining within the range 10^{-9} yr^{-1} and 10^{-7} yr^{-1}.

mic displacement following the 2007 Peruvian M_w 8.0 mega-thrust earthquake. Signals of this size are easily discriminated from sources of noise that are often present in interferograms, such as orbital errors or atmospheric path delays.

Crustal deformation which occurs during the interseismic portion of the earthquake cycle (§1.4.2) is more difficult to detect using InSAR. Typically, onshore deforming regions have a strain rate that falls between 10^{-9} yr^{-1} and 10^{-7} yr^{-1} (Kreemer et al., 2003; Figure 3.1). These strain rates are equivalent to a measurable displacement rate on the order of 0.1-10 mm/yr across a distance of 100 km. The measurable tectonic signal often has a smaller magnitude than the noise in an individual interferogram (§3.2.2). Additionally, in order to obtain a single interferometric fringe, an interferogram spanning a time-period of several years would be necessary. Unfortunately, it is seldom possible to maintain interferometric coherence over such long time periods. Therefore, to study interseismic deformation it is necessary to form many interferograms from numerous SAR acquisitions and combine the observations in some way.

Wright et al. (2001b) were the first to use InSAR to quantify ongoing interseismic deformation. They stacked four short-period interseismic interferograms to obtain the mean phase change over a period of 7.4 years associated with motion on the locked strike-slip North Anatolian fault in Turkey. Stacking is a simple technique that attempts to increase the signal-to-noise ratio (SNR) by averaging the observations of many short period interferograms over a much longer time period. The method works well if a large

number of coherent interferograms are available and/or the velocity gradient across the target fault is high. However, these conditions are not met in all locations and other strategies must be employed to extract interseismic deformation from the InSAR signal.

In this chapter I give an overview of the InSAR method and how it can be used to study interseismic deformation in conditions that are challenging for repeat-pass interferometry. In depth methodological reviews on InSAR are given in several articles (Bamler and Hartl, 1998, Massonnet and Feigl, 1998, Bürgmann et al., 2000, Rosen et al., 2000), books (Curlander and McDonough, 1991, Hanssen, 2001) and thesis chapters (Wright, 2000, Funning, 2005, Elliott, 2009), therefore only a brief explanation of the methods and concepts is given here.

3.2 InSAR method

3.2.1 Synthetic aperture radar

The SAR antenna on-board satellites (such as ESA's Envisat) is an active microwave instrument which usually transmits in the 1-10 GHz frequency range. Figure 3.2a shows the imaging geometry of a side-looking SAR instrument. The SAR-capable satellite flies at a nominal orbital altitude h above a reference datum and illuminates the ground with radar waves within a range of incidence angles measured from the nadir track (θ being the incidence angle). The radar waves propagate along the satellite's line of sight (LOS) and hit targets on the ground within a swath of finite width S. When operating in different swath modes, the satellite uses different ranges of incidence angles to give different swath widths. In the case of Envisat operating in image mode IS2, h = 800 km, S = 105 km and θ = 19-26°. Radar waves are reflected (back-scattered) at the ground surface and then received by the antenna and encoded as complex numbers, $Z = Ae^{i\phi}$, where A is the amplitude component and ϕ is the phase component. The amplitude component records the reflectivity properties of the ground surface. The phase component is used in interferometry to determine any changes in path length between the ground and the satellite. The raw data are processed to obtain amplitude and phase images in the 'range-Doppler' coordinate system (RDC) of the satellite viewing geometry.

The imaging geometry of the SAR system results in the lateral displacement of high relief topographic features via the phenomena of foreshortening, layover and shadowing

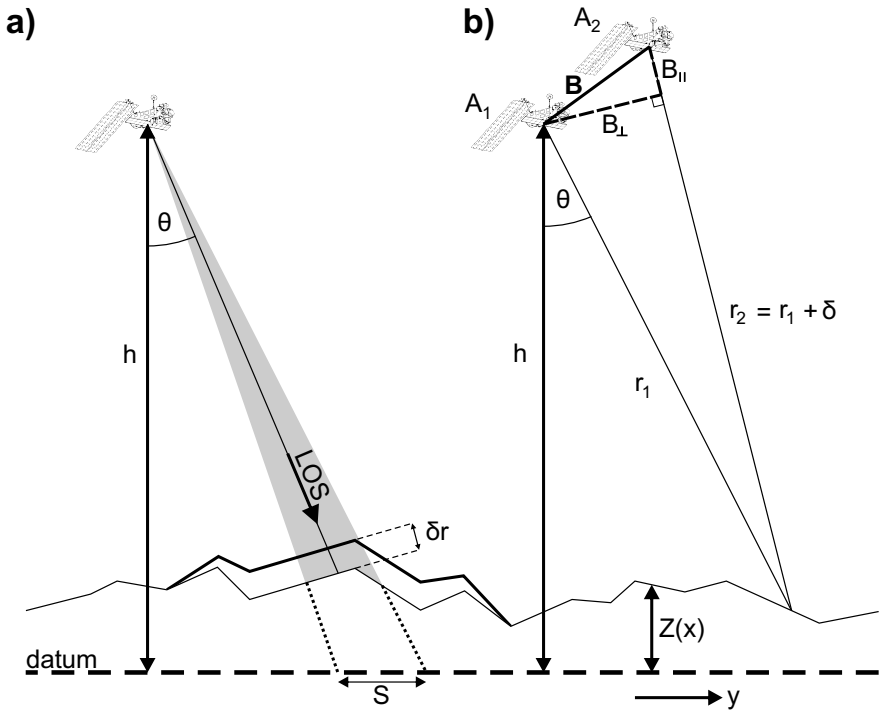

Figure 3.2: Imaging geometry for a) a conventional side-looking SAR antenna (redrawn from Peyret et al., 2011) and b) for repeat-pass interferometry (redrawn from Bürgmann et al., 2000). In both, the satellite travels on a vector perpendicular to the page. Terms are described in the text.

in SAR images (Hanssen, 2001). All relate to the slope angle of ground targets compared to the local slope of the radar wave-front. Foreshortening occurs when the ground slope is less than the wave-front slope and results in shortening of the object in the radar image. Layover occurs when the topographic slope is greater than the wave-front slope, resulting in the top of the slope being imaged before the base. Shadowing occurs behind high relief because radar energy is not returned from the features hidden behind the feature. The distortions from foreshortening can be corrected during geocoding of radar images using a Digital Elevation Model (DEM). However, layover and shadowing result in mixed phase values that can not be corrected.

3.2.2 Repeat-pass interferometry

In repeat-pass interferometry (Figure 3.2b), a ground target is imaged at different times with a different viewing geometry (Bürgmann et al., 2000). The two acquisition times are conventionally referred to as the master (A_1) and slave epochs (A_2; in this thesis the later acquisition of the pair is always defined as the slave epoch). A change in the path

length (δr) between the two acquisitions results in a difference in the measured phase of the returned radar waves. Since phase is a cyclic quantity of modulo 2π, the differential signal maps out as a pattern of fringes in what is termed the differential interferogram. Ambiguity in the absolute phase at any pixel in an interferogram means that the method only provides relative measurements between the two acquisitions. Establishment of absolute ground displacements in a frame of reference requires information from other observations, such as GPS measurements.

Signal components of the interferogram

A number of phenomena combine to give the observed fringe pattern in an interferogram $\Delta\phi_{int}$:

$$\Delta\phi_{int} = \Delta\phi_{def} + \Delta\phi_{coh} + \Delta\phi_{orb} + \Delta\phi_{topo} + \Delta\phi_{atm} + \Delta\phi_{other} \tag{3.1}$$

where ϕ_{def} is the deformation signal of interest, ϕ_{coh} represents decorrelation noise, ϕ_{orb} is a signal associated with the orbital geometry, ϕ_{topo} is due to topographic phase, ϕ_{atm} is atmospheric noise, and ϕ_{other} is any other sources of noise (e.g. unwrapping errors, instrument noise, filter noise etc). The symbol Δ refers to the differencing of each signal component at the master and slave epochs.

Phase contribution from decorrelation $\Delta\phi_{coh}$

Interferometry relies on the phase response within a pixel on the ground remaining the same between acquisitions. Temporal decorrelation occurs if the characteristics of the ground's phase response changes over time. Many point scatterers combine within the area of a single pixel to give the total phase response, so small changes to individual scatterers could combine to cause a loss of correlation. Stationary surfaces such as bare rock tend to remain coherent over a long time period, whereas dynamic surfaces such as vegetation, water or ice lose coherence rapidly. Coherence is a function of both radar wavelength and time, with better coherence generally ensuing with longer wavelengths and over shorter time periods.

A pixel can also lose coherence via geometrical decorrelation. This occurs if the path-length difference between the near and far ranges of the pixel is greater than the radar wavelength, since the phase response will sum differently.

Interferometric correlation (or coherence), γ, is a measure of the statistical similarity

of the phase response within a window between two SAR images. If the phase response is identical then $\gamma = 1$, while complete decorrelation results in $\gamma = 0$.

Phase contribution from the geometry $\Delta\phi_{orb}$

Geometrical phase contributions arise due to variation of the satellite's orbit over time. The nominal orbit is constantly perturbed by conservative forces (e.g. the gravity field and tidal effects) and non-conservative forces (e.g. atmospheric drag or solar radiation; Scharroo and Visser, 1998). However, satellites are not continuously steered to correct for these perturbations because of the finite on-board fuel supply. Excessive use of fuel would only act to reduce the useful life of the satellite. As a result, it is rare for the satellite to have an identical viewing geometry on each pass. Examining the configuration in Figure 3.2b, we see that the path length is r_1 and r_2 for acquisitions A_1 and A_2 respectively, where r_2 is greater than r_1 by some increment δ which is small in comparison to the total path length. The resulting round-trip phase shift is $\phi = \frac{4\pi\delta}{\lambda}$, where λ is the radar wavelength. The corresponding baseline separation $\mathbf{B}$ between the two acquisitions can be decomposed into the perpendicular baseline $B_\perp$ and the parallel baseline $B_\parallel$. The former has the strongest influence on InSAR and is used as a criteria to select suitable SAR images for interferometry. The change in phase across the interferogram can be approximated as (Wright, 2000):

$$\frac{\partial\phi}{\partial\theta} \approx \frac{4\pi}{\lambda} \cdot B_\perp. \tag{3.2}$$

Thus, the phase varies with incidence angle dependent purely on the perpendicular baseline. For a flat earth, this results in a phase ramp that varies in the range direction y (Wright, 2000):

$$\frac{\partial\phi}{\partial y} = \frac{4\pi}{\lambda} \cdot \frac{B_\perp cos^2\theta}{h}. \tag{3.3}$$

Any error in the perpendicular baseline will contribute a residual to this phase ramp. Quoted accuracies of the orbits for the ERS satellites are 5-7 cm radially and 10-15 cm cross-track (Scharroo and Visser, 1998). Assuming the same errors for Envisat, this gives a maximum residual phase ramp of ~0.16 mm km^{-1} in the range direction. Additionally, a smaller magnitude phase ramp in the azimuth direction is introduced by along-track deviations of the orbit.

Therefore, inaccurate orbital knowledge can mean that a long-wavelength residual signal remains within the interferogram following processing. This can be ignored if the interest is in small-scale large-magnitude signals such as coseismic deformation. However it must be estimated and removed when it can potentially mask small-magnitude long-wavelength signals such as interseismic deformation. Methods for estimating and removing the orbital error are described in §3.2.6.

Phase contribution from topography $\Delta\phi_{topo}$

Spatial variation of topography in the satellite's viewing swath will contribute towards the observed phase signal since the relative path lengths of neighbouring pixels will be different. The height of ambiguity h_a is defined as the magnitude of topography that will create a 2π fringe in the interferogram Hanssen (2001):

$$h_a = \frac{R_s \lambda \sin\theta}{2B_\perp}, \tag{3.4}$$

where R_s is the slant range of the slave epoch. Therefore any non-zero perpendicular baseline will result in topographic fringes that appear as a contour-pattern in the interferogram. Clearly, larger values of perpendicular baseline will result in more fringes for a given topographic feature. For deformation studies, the topographic phase contribution can be removed during interferometric processing using a suitable DEM, although errors in the DEM will leave residual topographic phase errors in the interferogram.

Phase contribution from the atmosphere $\Delta\phi_{atm}$

Radar waves must propagate through the Earth's atmosphere and are therefore sensitive to temporal and spatial variation of the refractivity in the tropospheric layer. Since atmospheric conditions will invariably be different over the repeat times of SAR satellites (Table 3.1), the difference at the two acquisition times will result in a phase delay signal. There are two components to the tropospheric delay signal (Hanssen, 2001): a turbulent component and a vertically stratified component. Furthermore, there are two components to the turbulent atmosphere, usually termed the 'wet' and 'dry' delays.

The dry delay is dependent on temperature and pressure variations throughout the tropospheric layer. Even though the magnitude of the dry delay can potentially be large, the expected long-wavelength spatial variation means that it is less critical to interferometry (Zebker et al., 1997). On the other hand, the wet delay is dependent on

the level of water vapour held in the lower troposphere, and depending on the structure of the ambient weather system at the time of acquisition, can introduce delays on the order of tens of centimetres over very short length scales (Zebker et al., 1997). Emardson et al. (2003) estimated from continuous GPS measurements that the magnitude of the neutral (dry+wet) phase delay varies with the length scale L as $2.5L^{0.5}$. Although the phase delay is only ∼2.5 mm for observations separated by 1 km, it increases to ∼25 mm for the 100 km length scale over which interseismic deformation is expected to vary.

Vertical stratification of the atmosphere is caused by lateral changes of the topography. The total atmospheric phase delay may contain a significant component that is correlated with the terrain. Areas of high relief are more at risk since this can generate a delay that varies significantly on the length scale of the swath width (e.g. across the steep topographic slopes surrounding the Tibetan plateau; Elliott et al., 2008).

The ionosphere can also contribute to the atmospheric phase delay due to the presence of charged particles in this layer. These particles have a dispersive effect on radar waves that has a larger effect on lower frequency (longer wavelength) radar systems, such as L-band.

Since an atmospheric delay manifests in the interferogram as a difference in path length, it can either be mistaken for, or completely mask the deformation signal of interest. Strategies for mitigating the effect of the atmosphere in interferograms are discussed in §3.2.5.

Phase contribution from deformation $\Delta\phi_{def}$

Assuming that $\Delta\phi_{orb}$, $\Delta\phi_{topo}$ and $\Delta\phi_{atm}$ have been successfully removed, the remaining signal is associated with any ground displacement that has occurred between the two acquisitions. The signal is expressed as a range change Δr in the satellite's LOS (Wright, 2000):

$$\Delta\phi_{def} = \frac{4\pi\Delta r}{\lambda} = -\left(\frac{4\pi}{\lambda}\right)\hat{\mathbf{l}}\cdot\mathbf{u} \tag{3.5}$$

where $\mathbf{u}$ is the ground displacement vector and $\hat{\mathbf{l}}$ is a unit vector pointing from the ground target to the satellite. A single interferometric fringe due to ground displacement will be generated for a range change equal to half the radar wavelength. The LOS vector for an Envisat descending pass at the Equator is $\hat{\mathbf{l}} \approx [0.38, -0.08, 0.92]$ for east,

Table 3.1: Characteristics of SAR capable satellites with public access.

	Satellite	Agency	Country	Operational	Band	Repeat (days)
Expired	ERS-1	ESA	Europe	1991-2000	C	35
	JERS	JAXA	Japan	1992-1998	L	44
	Envisat	ESA	Europe	2002-2010[1]	C	35
	ALOS	JAXA	Japan	2006-2011	L	46
	ERS-2	ESA	Europe	1995-2011	C	35
Operational	Radarsat-1	CSA	Canada	1995-	C	24
	COSMO-Skymed	ASI	Italy	2007-	X	16
	TerraSAR-X	DLR	Germany	2007-	X	11
	Radarsat-2	CSA	Canada	2007-	C	24
	TanDEM-X	DLR	Germany	2010-	X	11
Planned	ALOS-2	JAXA	Japan	2013[2]	L	14
	Sentinel-1A	ESA	Europe	May 2013[2]	C	12
	Sentinel-1B	ESA	Europe	late 2015[2]	C	12
	SAOCOM	CONAE	Argentina	early 2014[2]	L	16
	Radarsat-Constellation	CSA	Canada	2014-2015[2,3]	C	12
	TanDEM-L	DLR	Germany	-[4]	L	8
	DESDynI	NASA	USA	-[4]	L	12-16

[1] Orbital height lowered Oct. 2010.
[2] Estimate as of September 2011.
[3] Per satellite in 3 satellite constellation.
[4] Proposed missions.

north and up components respectively. From this we can see that the viewing geometry of Envisat is insensitive to range change in the north direction, which is approximately aligned with the satellite's azimuth direction.

3.2.3 SAR capable satellites

There are currently 5 SAR capable satellites in operation above the Earth, in addition to expired and planned missions (Table 3.1). These satellites employ SAR antennas which fall into 3 microwave bands. The X-, C-, and L-bands used correspond to wavelengths of ∼31 mm, ∼56 mm and ∼236 mm respectively. Early SAR capable satellites predominantly used C-band antennas and therefore the largest data archives are currently from these missions. At C-band, interferometric coherence is never achieved in the Equatorial tropical rainforests or the boreal forests of the northern hemisphere between ∼50-70°N (Figure 3.3). In addition, coherence is lost over long time periods in most of sub-Saharan Africa, India, Europe, east Asia, central South-America and central North-America, although it can be maintained in these areas over peri-

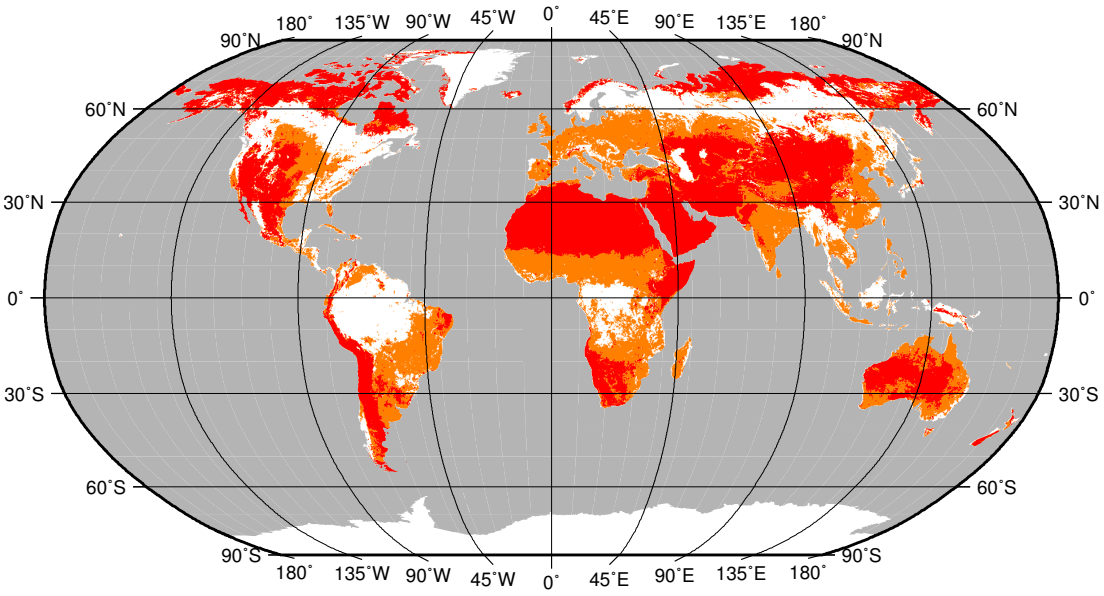

Figure 3.3: Global distribution of potential interferometric coherence from a C-band SAR satellite for interferograms with temporal baselines of ∼1-year (red area) and ∼1-month (red area + orange area) time periods. White indicates no coherence over any time period. The coverage is estimated by categorising the expected coherence for 24 land-cover classifications in a global database (Loveland et al., 2000) using interferometric examples from the literature. Robinson projection.

ods of ∼1 month. Recently launched or planned missions either stick with C-band for data continuity or employ shorter wavelength X-band with very short orbital repeat times. Although short repeat times are highly beneficial for maintaining coherence and building up a large data archive, the current X-band SAR satellites are commercially operated. This has meant that X-band acquisitions are targeted at specific small regions and a regular global archive is not being built. Therefore, current X-band satellites are less useful for studying large-scale crustal deformation where small signals are to be measured over long time periods and large areas.

The recently-failed ALOS satellite employed an L-band antenna whose longer wavelength offers greater penetration in vegetated areas, giving greater temporal and spatial coherence (Rosen et al., 1996, Sandwell et al., 2008). As a result, some future missions also propose the use of L-band, as coherence can be maintained over a much larger proportion of the global land surface. Work in this thesis uses SAR data from the Envisat satellite. Due to its high elevation, Tibet has a barren, sparsely vegetated landscape and therefore coherence is expected to be relatively good at C-band.

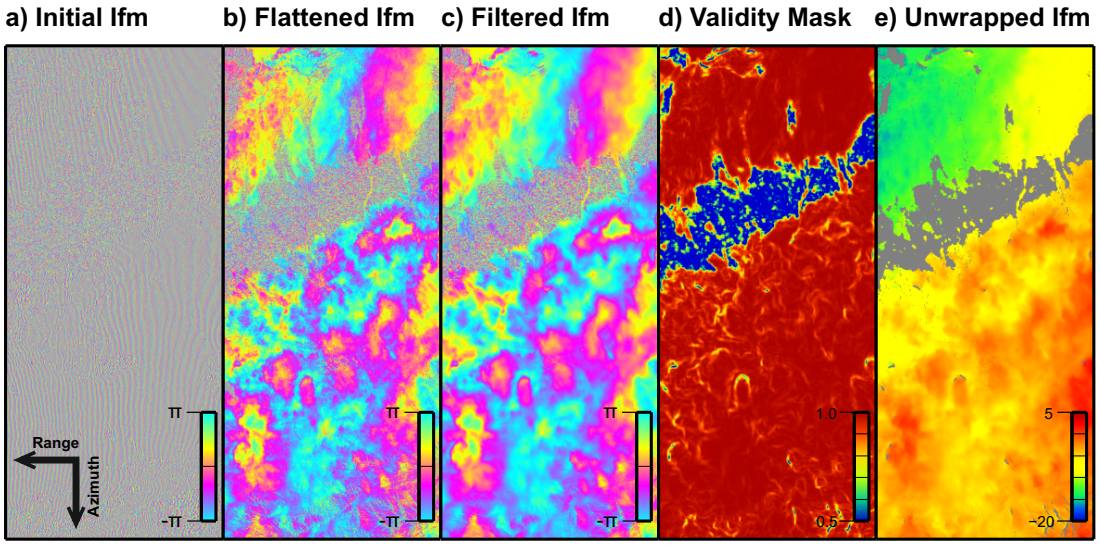

Figure 3.4: Stages of interferometric processing in *Gamma* for the example 070520-070624. A small subset of the full interferograms is plotted here. Units in a) b) c) and e) are radians, whereas d) is dimensionless. The range-Doppler coordinate system of the processing is highlighted by the arrows in a).

3.2.4 Interferometric processing procedure

In this thesis, interferometric processing is done using the *Gamma* software (Werner et al., 2000) and the procedure outlined in this section.

Single Look Complex

The raw SAR data is used to generate single look complex (SLC) images for every acquisition. The SLC image contains both amplitude and phase components encoded as complex numbers for each pixel. It is the phase component which is used in interferometry. Each SLC is then co-registered to a common master image. In this study, epoch 070520 (date format YYMMDD) is chosen. A DEM mapped into the RDC geometry of the master SLC is used to generate a look-up table for every other slave image in turn. This initial look-up table contains the range and azimuth pixel offsets needed to resample the slave SLC into the geometry of the master SLC. The offsets in the initial look-up table are then refined by cross-correlating the master and slave amplitude images. At this stage the images are down-sampled in a process known as multi-looking, which involves averaging the phase within a defined window of pixels. In the full resolution SLC, the pixel size is 4 m in azimuth (parallel to the satellite's flight direction) and 20 m in range (perpendicular to flight direction). Square pixels

approximately 80 m in size are achieved by multi-looking the phase within a window of 4 pixels in range and 20 pixels in azimuth.

Initial interferogram

The initial interferogram is then formed by differencing the phase of the master and slave SLCs at each pixel. This forms an image with fringes (Figure 3.4a) where each fringe corresponds to a phase change of 2π radians.

Flattened interferogram

The interferograms are flattened by removing the estimated phase contribution due to changes in topographic height throughout the scene and along-track changes in the geometrical baseline between passes. A 3 arc-second DEM from the SRTM (Farr et al., 2007) and DORIS precise state vectors are used to generate a simulated interferogram which is then subtracted from the initial interferogram (Figure 3.4b). For a C-band satellite, fringes in the flattened interferogram correspond to a range change of 28 mm in the LOS. This is half the C-band wavelength since a two-way signal is measured. The LOS direction of the Envisat satellite is right looking, perpendicular to the direction of travel. The pixel size of the flattened interferogram (∼80 m) is broadly similar to that of the DEM used.

Filtered interferogram

A power spectrum filter (Goldstein and Werner, 1998) is applied to reduce the phase noise in the interferograms, which aids the phase unwrapping step. Interferograms are divided into overlapping patches and the power spectrum $Z(u, v)$ of each patch is calculated by FFT. The filter adapts to the local fringe rate and the response $H(u, v)$ is then:

$$H(u, v) = |Z(u, v)|^{\alpha} \tag{3.6}$$

where α is the non-linear operator which governs the filtering strength. An α value of 0 results in no smoothing whilst 1 results in the strongest smoothing. Interferograms are filtered with $\alpha = 0.5$ to give moderate smoothing. The filtered interferogram (Figure 3.4c) is again multi-looked to 8 range and 40 azimuth looks by averaging the phase values in a 2 by 2 pixel window, giving a pixel size of approximately 160 m.

Validity mask

At this stage, a validity mask is generated for the filtered interferogram based on the coherence of each pixel (Figure 3.4d). Pixels for which the coherence is estimated to be less than 0.7 are masked from the interferogram. In high relief areas such as mountainous terrain, layover and shadowing can be a problem (see §3.2.1). Although shadowing does not add signal to the interferogram, regions of layover are typically characterised by both high phase noise and high image intensity. To remove these noisy regions from the interferogram, the co-registered amplitude image is consulted. Any pixel whose intensity is 6 times greater than the average image intensity is masked at this stage.

Unwrapped interferogram

Next the interferograms need to be unwrapped. Unwrapping is the process of converting the modulo 2π phase fringes to a continuous smooth signal (Figure 3.4e). Unwrapping is performed using a minimum cost flow (MCF) algorithm (Costantini, 1998). The advantage of this method of phase unwrapping compared to other methods (such as the traditional branch cut method; Goldstein et al., 1988) is that all regions with high enough coherence will be unwrapped, regardless of whether patches are connected or not. This is extremely advantageous for very long interferograms (as used in this thesis) and reduces the manual work needed in creating bridges to link in isolated patches of signal. However, this advantage comes at the expense of computational efficiency and possibly with additional errors if large phase gaps or large deformation signals (such as coseismic signals) are present in the data. Using the MCF algorithm, Biggs (2007) demonstrated an improvement in the unwrapped area by a factor of 2.6 over the branch cut method in the interferometrically challenging region of Alaska.

Unfortunately, phase unwrapping algorithms are prone to errors that introduce 2π jumps in phase along image discontinuities. The next step of processing is to manually correct these errors using the principle of phase closure (Biggs, 2007). Phase signals associated with orbital errors or deformation behave in a predictable way. That is, if we perform the operation $\phi_{lm} + \phi_{mn} - \phi_{ln}$, where ϕ_{lm} is the interferogram constructed from the acquisitions l and m, the expected residual phase is zero. Unwrapping errors do not behave in this way, and will have a residual of some multiple of 2π, which can be spotted when plotted spatially.

Geocoding

The final stage of processing, known as geocoding, is to convert the satellite based coordinate system based on range and azimuth coordinates to a geographical coordinate system based on latitude and longitude relative to the WGS-84 reference ellipsoid. The look-up table used to map the DEM into range-Doppler coordinates during SLC co-registration is used to project the fixed unwrapped interferograms into latitude and longitude coordinates. As a result, pixels in the geocoded interferogram have the same size as the DEM; in this case 3 arc-seconds or approximately ∼90 m. If the resolution of the interferogram in RDC geometry is poorer than this, interpolation is used to achieve the denser sampling.

3.2.5 Mitigating atmospheric errors in interferograms

Since we are only interested in the tectonic deformation signal, other signal components that are not routinely removed during processing, such as atmospheric delays signals, represent sources of noise. Much research has concentrated on how to estimate and remove atmospheric delays from interferograms. I summarise some of the advances in this section.

Stacking is a simple way of reducing the impact of atmospheric noise by averaging a large number of interferograms. Using GPS measured atmospheric delay functions, Emardson et al. (2003) showed that the delays are uncorrelated over periods longer than a day. Therefore by stacking N independent interferograms the noise is reduced by a factor of $N^{-0.5}$. However, the method is only useful for determining linear deformation and requires pixels to remain coherent throughout the interferogram network. Furthermore, when stacking a small number of interferograms, any SAR acquisition perceived to contain excessively large atmospheric or orbital errors can dominate the signal. More complicated methods have been developed to characterise the orbital and atmospheric errors and then remove them from the data, in theory leaving only the tectonic deformation.

The Persistent Scatterer (PS) methodology developed by Ferretti et al. (2001) avoids the problem of temporal and spatial decorrelation (explained in §3.2.1) by only exploiting those pixels that have consistent scattering properties through time. However, these scatterers tend to be man-made objects and therefore the technique is best suited to studying urban areas. In the Small Baseline Subset (SBAS) method (Berardino et al.,

2002), only interferograms separated by small spatial baselines are used to form a network for time series inversion. Implemented in both the PS and SBAS algorithms is a procedure for determining the 'Atmospheric Phase Screen' (APS). By assuming that deformation varies smoothly through time and residuals are attributable to atmospheric artefacts, the noise can be removed by filtering. The method relies on the high spatial correlation but low temporal correlation of atmospheric phase and uses a cascade of low and high pass filter operations to estimate and remove the noise. However, deformation signals at the same temporal scale as the noise would be smoothed out by this method and therefore it is perhaps best suited to linear or slowly varying deformation processes.

The PS and SBAS methods rely on pixels being coherent throughout the data archive, but not all regions exhibit such favourable conditions. Alaska is a particularly challenging environment for interseismic analysis using InSAR because the coherence is highly variable between SAR acquisitions. Biggs et al. (2007) developed a network-based algorithm that exploits phase measurements that are coherent in some but not all of the interferograms. In this multi-interferogram method, atmospheric noise is characterised by isotropic covariance functions estimated directly from the interferograms. The data covariance is used to weight the observations in the inversion for interseismic velocities.

Several studies have noted a strong correlation between interferometric phase and topography (e.g. Taylor and Peltzer, 2006, Cavalié et al., 2007, 2008, Elliott et al., 2008). This signal is attributed to the varying thickness of the tropospheric layer due to spatial variations of topography (Hanssen, 2001). At lower elevations, the increased path length from ground to satellite means that radar waves must travel further through the tropospheric layer. Therefore, phase returns from lower elevations are more susceptible to changes in the precipitable water vapour content between acquisitions.

Cavalié et al. (2007, 2008), Elliott et al. (2008) and Doin et al. (2009a) estimate the correlation between interferometric phase and elevation, finding that although the correlation scales exponentially with height, a linear relationship provides an acceptable fit after validation with global weather models. The study of Elliott et al. (2008) focusses on the Altyn Tagh fault, across which exists a dramatic elevation change of $\sim$4 km over a horizontal distance of $\sim$150 km. The descending geometry of the SAR data and the left-lateral strike-slip fault motion results in a tectonic signal with

similar magnitude and polarity to the atmospheric delays on the north side of the fault. Particularly in this case, it is important to try and remove the atmospheric component of signal in order to provide an accurate estimate of the slip rate.

Doin et al. (2009a) present validations for examples from three test sites in Nevada, Afar and Tibet. Although they find that most interferograms can be reasonably fit with a linear approximation, examples from all sites exhibit non-linear relationships. Currently, the coarse spatial resolution of global atmospheric models limits the routine use of this technique in InSAR analysis. Lin et al. (2010) estimate the linear correlation function between topography and observed phase by decomposing the two fields using Gaussian filters with various spatial band passes. Their algorithm works on a network of redundant interferograms in order to determine the linear function at each acquisition date.

Other studies (Li et al., 2009c,d, Elliott, 2009) have tried to directly remove atmospheric signals using data collected from remote sensing instruments such as the Medium Resolution Imaging Spectrometer (MERIS; on-board Envisat) and Moderate-resolution Imaging Spectroradiometer (MODIS). These instruments measure reflected solar radiation in several bands within the infra-red and visible parts of the spectrum. By making use of the difference in absorption between two of the bands, the vertically-integrated water vapour field can be retrieved (Elliott, 2009). In an InSAR time-series analysis of postseismic motion after the 2006 Bam earthquake, Li et al. (2009c) find that the magnitude of atmospheric noise is reduced from ∼10 mm to ∼5 mm after correction in this way. Because these instruments rely on reflected solar radiation they can only be used for descending SAR data, which is collected during daylight hours. They are also limited by the presence of clouds, which absorb the infra-red radiation and mask the water vapour signal from beneath the cloud column.

Jolivet et al. (2011) calculate spatially variable corrections for InSAR data by vertically integrating the estimation of weather models and interpolating between grid nodes to give spatially variable atmospheric corrections at interferogram resolution. In the near future, online tools are planned that will synthesise atmospheric data from weather models and remote sensing instruments and provide similar maps of phase delay that can be integrated into the InSAR processing procedure (e.g. von Allmen et al., 2010). Jolivet et al. (2011) find that correcting interferograms in this way before unwrapping can help reduce the number of unwrapping errors in areas of rough topography.

3.2.6 Mitigating orbital errors in interferograms

Orbital errors arise because the precise location of the satellite on each pass is not known. Although the differential effect of the satellite baseline is removed during interferometric processing (§3.2.4), the method assumes that the Earth's surface is a smooth ellipsoid and that the orbital state vectors are accurate. However, since the precise orbit state vectors are based on models of the satellite orbits (e.g. Scharroo and Visser, 1998), residual orbital phase ramps can remain in the interferograms. If this signal is not accounted for, it can mask the long wavelength signal we expect from interseismic deformation.

A common approach is to estimate the best fitting planar ramp or quadratic surface to each interferogram and remove this (referred to from here on as the independent-interferogram method). Biggs et al. (2007) recognised that a set of interferometric observations are inherently linked because they share a finite number of SAR acquisitions. In a typical network, each acquisition may be used to construct more than one interferogram. They describe a network method that uses the entire network of interferograms to deduce the best fitting orbital residual at each acquisition. The orbital correction for each interferogram is then obtained simply by subtracting the slave acquisition from the master acquisition. Using the network method, Biggs (2007) found an improvement over the independent-interferogram method of ~9% to the estimated orbital parameters when testing a set of synthetic interferograms.

A problem with estimating orbital errors is that long-wavelength deformation signals can become aliased and removed erroneously. To avoid this an *a-priori* model, often constrained by independent geodetic data, can be used. Gourmelen et al. (2010) use continuous GPS data to estimate the coefficients of quadratic orbital phase errors from a large swath of InSAR data in Nevada. Using a similar approach, Wei et al. (2010) combine GPS and InSAR measurements to study interseismic deformation in California. A dense GPS network is used to constrain long wavelength deformation and a fault dislocation model. This model is then removed from the InSAR data before estimating planar orbital errors and high-pass Gaussian filtering to reduce atmospheric noise. Wei et al. (2010) find that this method improves the SNR by 20%. Although GPS data is useful for removing complex orbital errors from large swaths of data, at present this technique is limited to a few regions, such as the western USA or Japan, where there is dense continuous GPS coverage.

3.3 Description of π-*rate* software

The π-*rate* (Poly-interferogram rate and time-series estimator) software (Wang and Wright, 2010) is a collection of Matlab codes developed at the University of Leeds by Hua Wang, with significant contributions from Juliet Biggs (University of Bristol), John Elliott (University of Oxford) and Tim Wright (see Biggs et al., 2007, Elliott et al., 2008, Wang et al., 2009). By inputting a set of geocoded, unwrapped interferograms, the algorithm can produce a velocity map of steady-state deformation (otherwise referred to as a linear rate map), produce a deformation time series and estimate the uncertainties on these estimates. Additionally, orbital errors and atmospheric delays can be estimated and removed from the interferograms. Input data is expected in the format of *ROI_PAC* (Rosen et al., 2004), a popular open source interferometry package. Output from the *Gamma* software was therefore converted to *ROI_PAC* format before analysis. In this section I will describe the major processing steps and algorithms used in π-*rate* following the procedure shown in Figure 3.5.

After reading in the interferograms they are resampled to a common-sized grid and the unwrapped phase values are converted from radians to millimetres using a conversion factor of $\frac{\lambda}{4\pi}$ (where λ is the radar wavelength). At this stage the interferograms can also be down-sampled (multi-looked) and a spatial subset can be selected. If the target signal is from interseismic strain accumulation around locked faults, the expected signal is long wavelength. Therefore further multi-looking only acts to reduce the high frequency residual phase noise in the interferograms and should enhance the sought deformation signal.

3.3.1 Minimum spanning tree

To connect all of the epochs (M) in a network you need $N = M - 1$ interferograms to produce an independent network. However, for a typical network there are more interferograms than there are epochs, i.e. $N > M$. π-*rate* only uses the independent (non-redundant) observations at each pixel to produce the rate map and therefore a process is needed to determine the most reliable observations to use to create the independent network for each pixel. For this purpose, a Minimum Spanning Tree (MST) algorithm is used to determine the independent interferograms (Kruskal, 1956). The network is composed of a number of trees, where in this case a tree is an individual

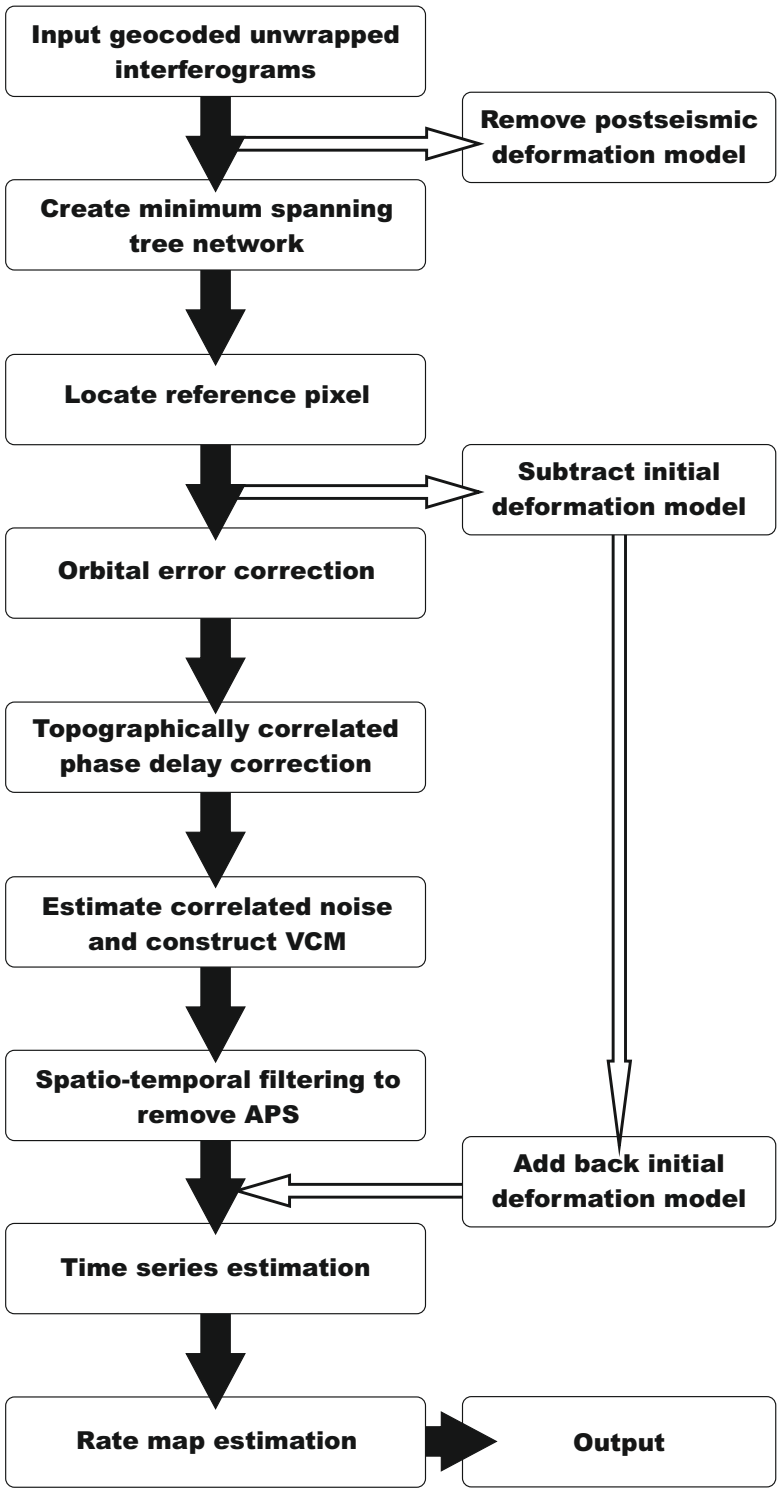

Figure 3.5: Flowchart showing the processing flow of the π-*rate* software.

Figure 3.6: Example of the entries in the MST matrix for three interferograms that share three epochs. The grey area shows the extent of each unwrapped interferogram. The red area shows the pixels that have been selected by the MST algorithm for use in the stacking. Epochs used are 26, 29 and 30 as shown in Figure 3.16.

epoch. The interferograms are branches connecting these trees and have a weight defined as the fraction of non-zero pixels. The goal is to combine the trees with the minimum number of branches ($M-1$). The algorithm begins by selecting the branch with the highest weight (i.e. the interferogram that contains the most coherent pixels). This branch is added to the MST and combines two trees into a single tree. The branch with the next highest weight is then selected. If this branch combines two separate trees it too is added to the MST, otherwise it is discarded and the branch with the next highest weight is considered. This process continues until only a single tree remains and all the observations are connected. Recall from the process of phase unwrapping (§3.2.4) that $\phi_{lm}+\phi_{mn}-\phi_{ln}=0$. Therefore the third interferogram in this simple network provides no extra information and the associated MST would contain only the two interferograms with the highest number of coherent pixels.

This process is carried out on each pixel independently and an MST matrix is created for each interferogram, which defines the pixels that will be used in the rate map

determination (pixels are either 1 if they are to be used or 0 if not; Figure 3.6). A user-defined threshold, Ψ, is used to discard pixels which have too few observations from these matrices. In this thesis, $\Psi = 15$; approximately half of the 31 independent observations. Note that if the number of input interferograms represents an independent network with $N = M - 1$, the MST matrix for each interferogram would simply represent its coherence mask.

3.3.2 Reference point

A reference point is needed to account for the differing seed locations used in unwrapping the interferograms. The reference point provides a location where the deformation is assumed to be zero. The program searches for a reference point which is common to all interferograms. A set of tie points are defined at regular intervals throughout the interferogram. At each of these locations the fraction of coherent pixels and the standard deviation is calculated within a search window around the tie point. For those locations where the coherence is above a threshold, the one with the minimum standard deviation is chosen as the reference point. The observed phase at the reference pixel is subtracted from each interferogram.

3.3.3 Orbital error correction

As discussed in §3.2.6, orbital errors (ϕ_{orb}) arise in the interferograms because the precise location of the satellite at each pass is not known. The π-*rate* software has the capability of estimating residual orbital errors using either the independent-interferogram method, or the network method as first described by Biggs et al. (2007).

Independent method

The algorithm proceeds by assuming that the interferograms are dominated by orbital error and that other signal components are sources of noise. The orbital error is approximated as a five parameter quadratic function:

$$\phi^{orb}_{ij,k} = ax_k^2 + by_k^2 + cx_k y_k + dx_k + ey_k + f \tag{3.7}$$

where x and y are the easting and northing coordinates of pixel k respectively, $a - e$ are the five quadratic orbital parameters, f is an offset for each interferogram and i and j are the master and slave epochs. Traditionally, InSAR studies have concentrated

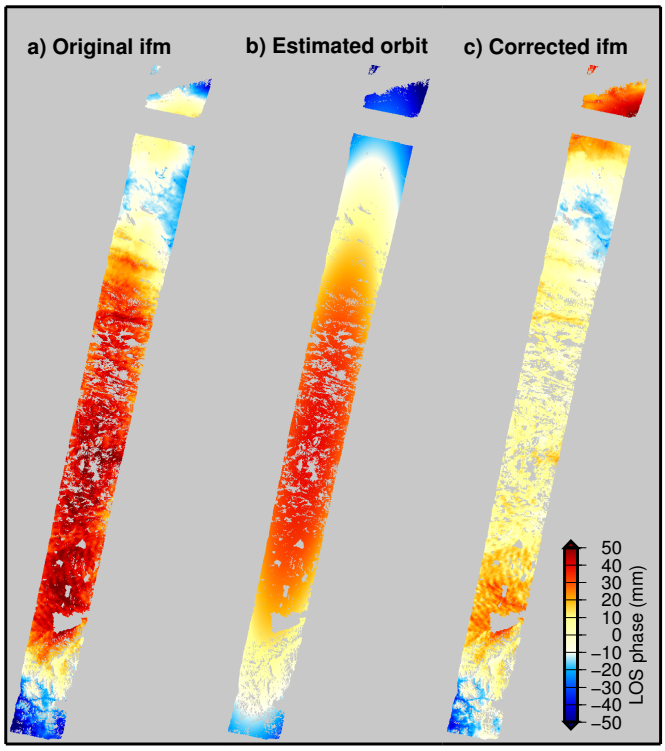

Figure 3.7: Example of an interferogram before and after orbital error correction. a) Observed interferogram 030928-031207. b) Estimated quadratic orbital error. c) Corrected interferogram after subtracting the orbital error. Note that the corrected interferogram exhibits large magnitude atmospheric signals in the north and south of the scene.

on small areas and a two parameter planar function has been considered adequate to remove the orbital signal. However, for a long swath of data such as used here, it is more appropriate to use the more complex quadratic approximation. A linear inverse problem (Menke, 1984) can be set up:

$$\mathbf{d} = \mathbf{A}\mathbf{m} \tag{3.8}$$

where $\mathbf{d}$ is the vector of interferometric phase observations at each pixel, $\mathbf{m}$ is a vector containing the five orbital parameters $a - e$ and an offset f for each interferogram, and $\mathbf{A}$ is the design matrix that has one row for each pixel in every interferogram and one column for each of the unknowns. The problem is over-determined since there are more observations than unknowns in the system and can be solved by the least squares method (Menke, 1984):

$$\mathbf{m} = [\mathbf{A}^T\mathbf{A}]^{-1}\mathbf{A}^T\mathbf{d}. \tag{3.9}$$

Network method

In contrast to the independent-interferogram method, which estimates the orbital parameters for each interferogram separately, the network method estimates the orbital error at each epoch. To do this the independent network of interferograms with the best coherence are selected using the MST algorithm (§3.3.1). For the network method Eq. 3.7 becomes:

$$\phi^{orb}_{ij,k} = (a_i - a_j)x_k^2 + (b_i - b_j)y_k^2 + (c_i - c_j)x_k y_k + (d_i - d_j)x_k + (e_i - e_j)y_k + f \quad (3.10)$$

where x and y are the easting and northing coordinates of pixel k respectively, $a - e$ are the 5 orbital parameters at epochs i and j, and f is an offset for each interferogram. Again, the design matrix has one row for each pixel in every interferogram and one column for each of the unknown orbital coefficients at each epoch. However, the problem is rank deficient because the number of interferograms is one less than the number of epochs in the MST network used. Therefore the design matrix cannot be inverted directly using the least squares solution of Eq. 3.9. Instead, Singular Value Decomposition (SVD) is used to find the minimum norm solution (see §3.3.9 for further description of the SVD method).

Because a network of interferograms contains many millions of phase observations and orbital errors are expected to exhibit only long wavelength variations, the size of the inversion is reduced by multi-looking the interferograms. Once the orbital parameters $a - e$ are determined a forward calculation determines the full resolution correction for each interferogram. Figure 3.7 shows an example of an interferogram before and after orbital correction using the network method.

3.3.4 Initial deformation model

The orbital correction seeks to identify and remove any long wavelength signals in the data. Since our expected deformation signal is of low amplitude and varies smoothly across the region, long wavelength components will be aliased and erroneously removed from the data at this stage. In order to preserve the long wavelength components of the deformation signal, an Initial Deformation Model (IDM) is used. The IDM contains a co-registered *a-priori* velocity for each pixel that is multiplied by the interferometric time spans and subtracted from each interferogram before the orbital correction is

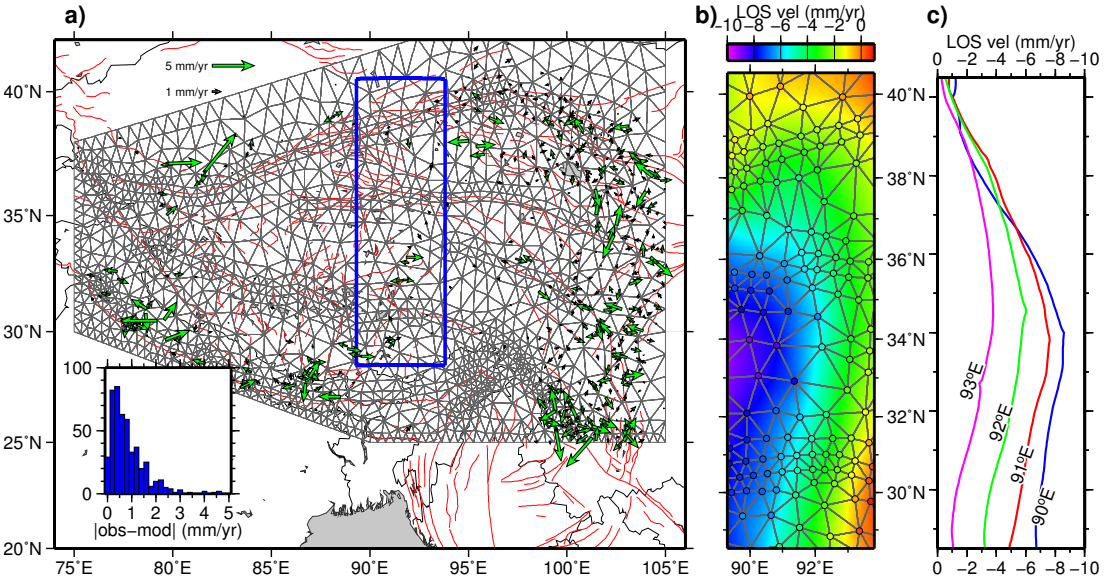

Figure 3.8: Initial deformation model (IDM) used to retain long wavelength deformation during orbital error estimation. a) Black lines depict the triangular mesh used in the velocity field inversion. Green arrows show the residuals between GPS observations and smoothed velocities, also summarised in the histogram. Blue rectangle is the region covered by the interferograms. b) Detail of the IDM at full interferogram resolution and converted to LOS for the blue rectangular region in a). Coloured circles show the triangles nodal velocities from the velocity field inversion. Background colouring is the minimum curvature surface fitted to the nodal velocities. c) Profiles through the IDM at 90°E, 91°E, 92°E and 93°E highlighting the two dimensional variation of the IDM.

evaluated. The subtracted signals are added back to the interferograms prior to rate map and time series estimation.

To construct the IDM, the velocity field method of Wang and Wright (2011) was used, which builds on the methods used by England and Molnar (2005). A triangular mesh is constructed over the plateau (Figure 3.8a) and assuming velocity varies linearly with latitude and longitude, a linear inversion is used to find the velocities at the triangular nodes from the unevenly distributed GPS observations of Gan et al. (2007):

$$\begin{bmatrix} \mathbf{d}_{GPS} \\ 0 \end{bmatrix} = \begin{bmatrix} \mathbf{A}_{GPS} \\ \kappa\nabla^2 \end{bmatrix} \mathbf{m} \tag{3.11}$$

where $\mathbf{d}_{GPS}$ is a set of GPS observations lying within the region of the triangular mesh, $\mathbf{m}$ is the matrix of nodal velocities, $\mathbf{A}_{GPS}$ is the design matrix containing interpolation shape functions for the GPS data and ∇^2 is the Laplacian smoothing operator, scaled by the smoothing parameter κ. The smoothing parameter is chosen by considering the trade-off between solution roughness and weighted residual misfit (see an example in

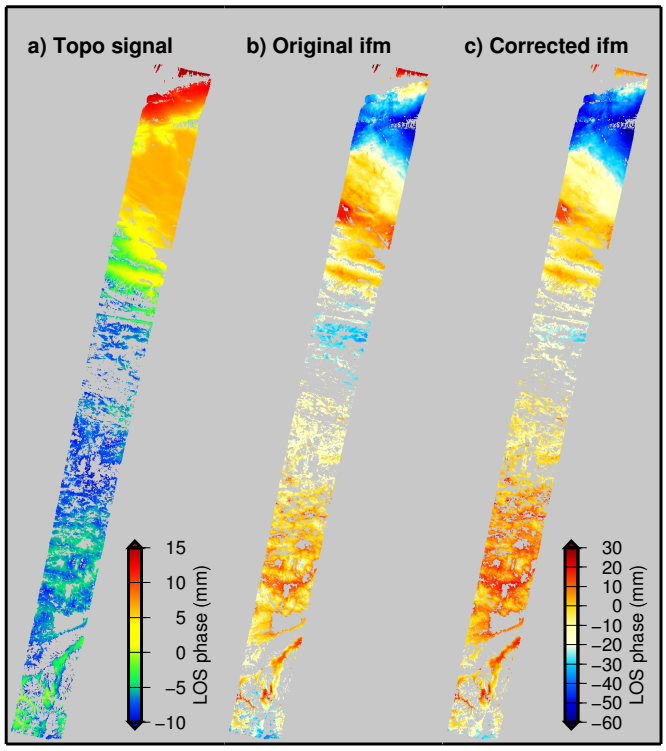

Figure 3.9: Example of an interferogram before and after topographically correlated phase delay removal. a) Estimated phase delay, where each pixel value is linearly proportional to topographic height at that pixel. b) Observed interferogram 070415-070729. c) Corrected interferogram after subtracting the estimated phase delay. This example is among the largest magnitude of phase delays. The range of estimated phase delay is around one quarter the interferogram phase range.

Figure 3.13a). The smoothing parameter used here ($\kappa = 0.06$) is chosen to minimise the velocity residuals within the interferogram region (Figure 3.8a). A smoothing parameter of zero ($\kappa = 0$) would give the best fit but would give a very rough solution. East and north components of the nodal velocities are then converted to the satellite's LOS. A velocity field with full interferogram resolution is obtained by fitting a minimum curvature surface (Figure 3.8b). The resulting IDM is a non-linear 2-dimensional velocity field with considerable variation in both east-west and north-south directions (Figure 3.8c). The use of an IDM enables the final InSAR rate map to be tied to an external reference frame. In this case, the reference frame is the fixed Eurasia frame of the Gan et al. (2007) GPS data.

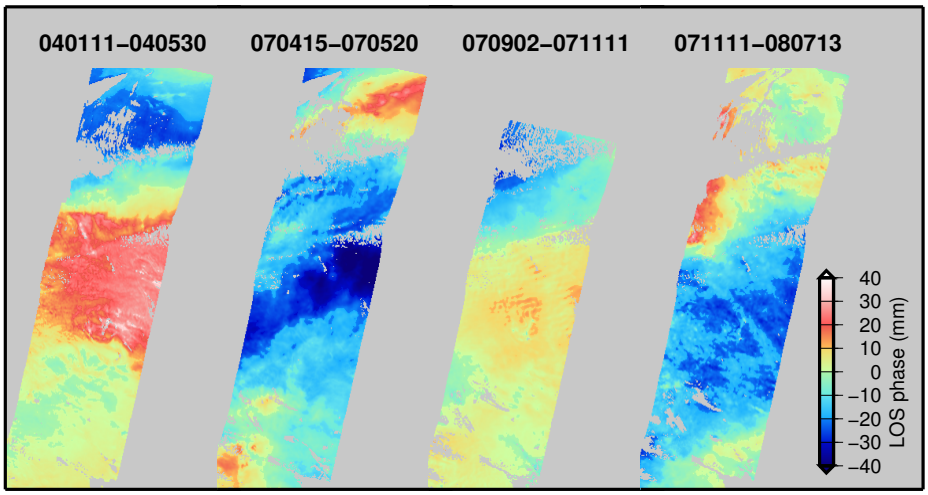

Figure 3.10: Examples of atmospheric perturbations in interferograms corrected for orbital errors. The subset of the scene shown covers the latitude range 37-40.5°N, including the Qaidam basin and steep topographic slope north of the Altyn Tagh fault. A change in atmospheric conditions often occurs in the vicinity of the Altyn Tagh fault.

3.3.5 Topographically-correlated phase delay correction

Following the work of Elliott et al. (2008) and Elliott (2009), *π-rate* can estimate and remove the signal component associated with topographically correlated atmospheric phase delays (ϕ_{atm}; as discussed in §3.2.5). The algorithm follows the same approach as the orbital correction using either the independent-interferogram or network methods (§3.3.3). In the case of the network method, the observed phase is inverted to find the difference in phase-elevation gradient between the two epochs:

$$\Delta\phi_{ij,k}^{atm} = (w_i - w_j)h_k + f \tag{3.12}$$

where w are the gradients of phase at the epochs i and j, h is the topographic height at pixel k determined from a co-registered DEM and f is an offset for each interferogram.

Again, the interferograms can be down-sampled to reduce the size of the design matrix. However it is preferable to use full resolution data wherever short-scale changes in topography are present. Figure 3.9 shows an example of an interferogram before and after correcting for topographically correlated delays.

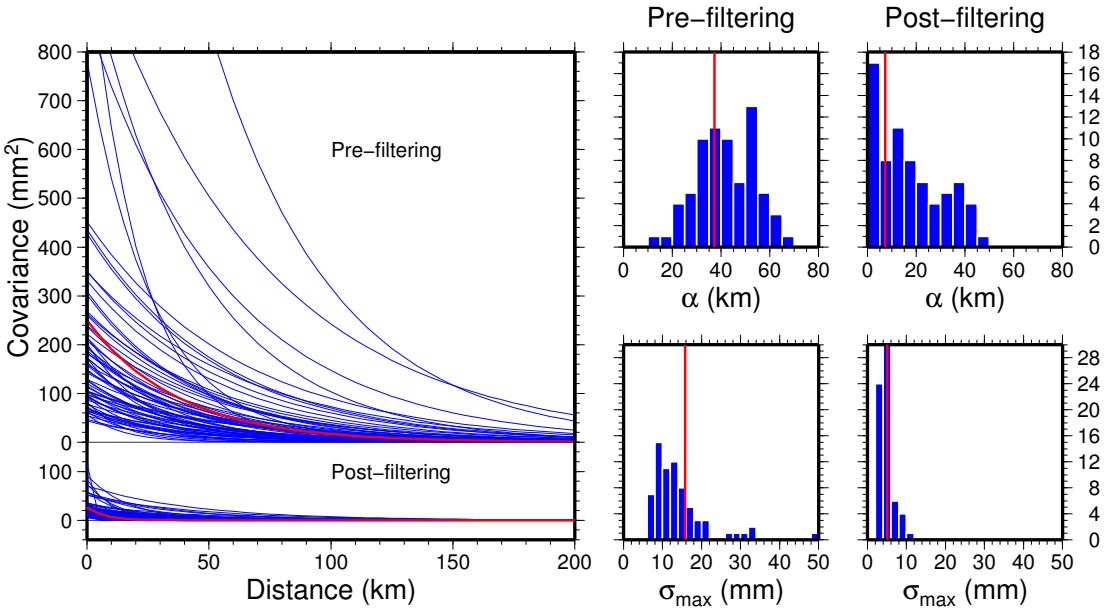

Figure 3.11: Main graph: 1D covariance functions for the original 70 interferograms in the full network (top) and the same interferograms after spatio-temporal filtering to remove the APS (bottom; see §3.3.8). Each curve has the exponential form of Eq. 3.13. The red curve is the mean covariance function in each case. Histograms show the distribution of the parameters σ_{max} (bottom) and α (top) for the pre- (left column) and post- (right column) filtered interferograms. Red lines show the mean values.

3.3.6 Spatially correlated atmospheric noise

The magnitude and length scale of atmospheric noise (ϕ_{noise}) in the interferograms can be investigated by calculating the 1D covariance function for each interferogram (Hanssen, 2001). This assumes that the noise structure is radially symmetrical and homogeneous throughout the scene, which may not be the case in the conditions of a frontal weather system. Figure 3.10 shows some examples of atmospheric perturbations in northern Tibet. The algorithm computes the 2-dimensional auto-covariance of each interferogram by Fourier transformation. The 1D covariance ($C(r)$) is then the radial average of this auto covariance and is fit with an exponential function (Hanssen, 2001, Parsons et al., 2006):

$$C(r) = \sigma^2_{max} e^{(-r/\alpha)} \tag{3.13}$$

where σ^2_{max} is the maximum covariance, α is the 'e-folding' wavelength (or length-scale of decay), and r is the pixel separation. More complicated functional forms can be used, such as Bessel functions, which allow negative covariance (e.g. Wright et al.,

2005) but I chose to use the exponential form on account of its simplicity. The set of 70 interferograms have mean values $\sigma_{max} = 15.8$ mm and $\alpha = 37.2$ km (Fig. 3.11). These values are greater than the median values estimated by Biggs et al. (2007) in Alaska ($\sigma_{max} = 7.5$ mm and $\alpha = 12.3$ km). Hanssen (2001) investigated the atmospheric errors in single frame ERS tandem interferograms (24 hour temporal baseline) over the Netherlands and found variation of the RMS values in the range ~2.2-15.6 mm over the course of a year. Emardson et al. (2003) find a strong positive correspondence between spatially-correlated atmospheric noise and length-scale of the form $\sigma = 2.5\sqrt{L}$ for long time period interferograms. Therefore it is not unreasonable that the multi-frame interferograms from Tibet exhibit a larger magnitude of noise than the single-frame interferograms from the Netherlands.

3.3.7 Variance-covariance matrix

A Variance-Covariance Matrix (VCM), Σ_Φ, is used during rate map and time series estimation to account for the temporal correlation between individual interferograms and the effect of orbital and atmospheric noise. Values in the VCM are used to weight the observations appropriately in the least-squares inversions used by these algorithms. The VCM is a symmetrical matrix containing NxN elements that each describe the correlation between two interferograms. The value of each element of Σ_Φ is estimated from the maximum variance σ^2_{max} for each interferogram deduced in §3.3.6:

$$\Sigma_{\Phi,ij} = \sigma_i \sigma_j C_{ij} \tag{3.14}$$

where i and j are the interferogram numbers and σ_i is the standard deviation of noise in interferogram i. C_{ij} is a matrix of coefficients that accounts for the correlation between master and slave epochs used in the interferograms. If l and n are the master epochs and m and q are the slave epochs of the two interferograms, the coefficients take values as follows:

$$\begin{array}{ll} C_{ij} = 1 & \text{if } l = n \text{ and } m = q \\ C_{ij} = 0.5 & \text{if } l = n \text{ or } m = q \\ C_{ij} = -0.5 & \text{if } l = q \text{ or } m = n \\ C_{ij} = 0 & \text{otherwise.} \end{array} \tag{3.15}$$

This covariance function is based on the assumption that the variance for individual

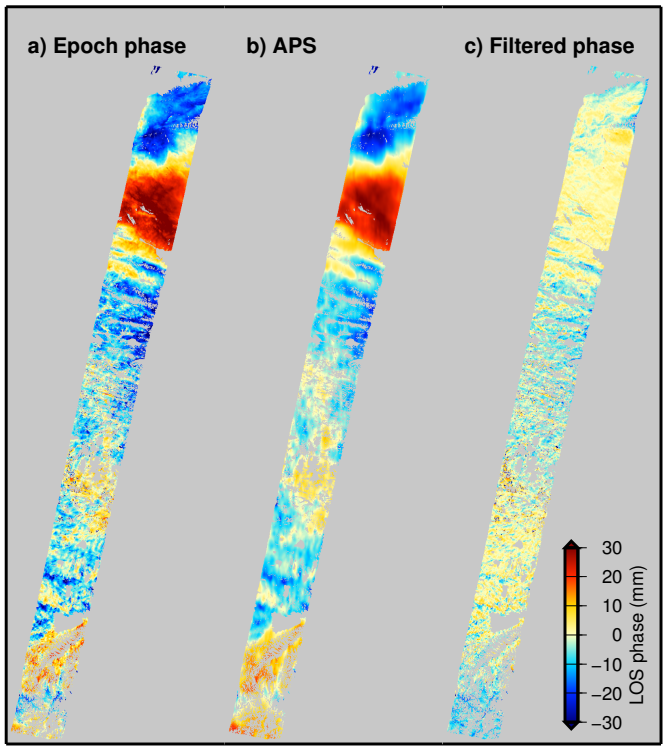

Figure 3.12: Example of the phase at an epoch before and after spatio-temporal filtering. a) Observed incremental phase at epoch 030928 calculated by rough time series analysis of the 70 interferogram network. b) Detected atmospheric phase screen. c) Filtered phase after subtracting the APS (b) from the observed phase (a).

interferograms is equal and is used here for simplicity. The spatial covariance of the data is not explicitly considered since the rate map and time series inversions operate on a pixel-by-pixel basis.

3.3.8 Spatio-temporal filtering

Since the signal component associated with atmospheric phase (ϕ_{atm}) in each interferogram exhibits high spatial correlation (Fig. 3.11) but low temporal correlation, it can be separated from the tectonic signal which has both high spatial and temporal correlation. π-*rate* uses the method originally outlined by Ferretti et al. (2001) in their PS methodology and later applied by Berardino et al. (2002) in their SBAS method. The algorithm proceeds in three steps.

Firstly, time series analysis is used to extract the signal at each epoch from the network of interferograms. The method is slightly different to that described in §3.3.9 in that no smoothing is carried out and observations are not weighted with the VCM.

Instead the raw (non-smooth) time series at each pixel is obtained via least squares.

Secondly, a Gaussian high-pass filter is used to isolate the signals which are highly correlated in time (i.e. the deformation). This is removed from each epoch to leave only those signals with low temporal correlation. Results in this thesis use a filter cut off of 0.5 years. Since the filter is double-ended, signals correlated over a period less than 1 year remain after this step.

Thirdly, each resulting epoch is spatially filtered with a low-pass first order Butterworth filter to isolate the APS. A filter cut off is determined for each epoch by calculating the e-folding wavelength α (Eq. 3.13). This accounts for the temporal variability of the atmospheric phase. The detected APS for each epoch is then subtracted from the rough time series and the interferograms are re-computed from the corresponding master and slave epochs. Figure 3.12 shows an example of the phase at an epoch before and after spatio-temporal filtering.

The lower panel in Figure 3.11 shows the results of spatio-temporal filtering the 70 interferograms of the full network. The filtering reduces the noise magnitude by ∼90% and the length-scale by ∼80%.

3.3.9 Time series analysis

In *π-rate*, time series analysis of the interferogram network can be applied in addition to the final linear rate map determination at the user's discretion. It is also applied as part of the spatio-temporal filtering step (§3.3.8) in order to isolate the temporally persistent deformation component of the interferograms. *π-rate* supports two methods for time series determination: finite difference smoothing (FDS; Schmidt and Bürgmann, 2003) and singular value decomposition (SVD; Berardino et al., 2002).

Finite difference smoothing

Signals associated with tectonic deformation are expected to form a smooth time series. Residual atmospheric and orbital errors, which are not correlated in time, therefore increase the roughness of the output time series. To minimise the impact of these residual signals, a smoothing constraint can be added to the least-squares inversion based on a finite difference approximation of the second order differential of the time

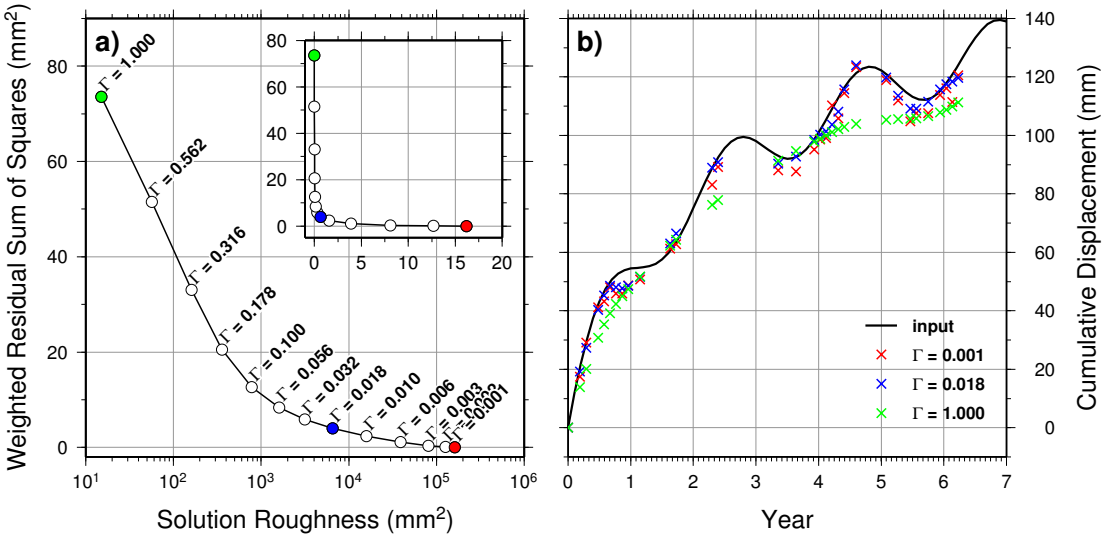

Figure 3.13: Effect of different smoothing parameters on a synthetic time series with added spatially correlated noise. a) Inset shows the L-curve that characterises the trade-off between solution roughness (units of 10^4 mm^2) and weighted residual sum of squares. Main graph shows a log-linear plot of the same data points labelled with the respective smoothing parameter κ. b) Estimated time series for an individual pixel. Input deformation is the black line and crosses give the estimated cumulative displacement at each epoch. Symbols are colour coded with those in the L-curve plot.

series:

$$\begin{bmatrix} \mathbf{\Phi} \\ 0 \end{bmatrix} = \begin{bmatrix} \mathbf{A} \\ \kappa \frac{d^2}{dt^2} \end{bmatrix} \mathbf{d} \tag{3.16}$$

where $\mathbf{\Phi} = [\phi_{12}, \phi_{23}, \phi_{34} \ldots \phi_{lm}]^T$ is a vector containing the displacement observations, $\mathbf{d} = [d_1, d_2, d_3 \ldots d_n]^T$ is a vector of the unknown incremental range change between epochs, $\mathbf{A}$ is the MxN design matrix that relates each observation to the appropriate two unknowns and κ is the parameter which governs the amount of smoothing. If $\kappa = 0$, no smoothing is applied and the resulting time series will fluctuate depending on the level of errors in individual interferograms. However, choosing a high κ value results in an overly smooth solution. Choosing the level of smoothing is largely an arbitrary process and is governed by a trade-off between solution roughness and residual misfit (Figure 3.13). The usual procedure involves assigning a range of values for the smoothing parameter, calculating the time series for each, and picking the value which appears in the corner of the resulting L-curve plotted between the weighted residual sum of squares and the solution roughness.

Once a suitable smoothing parameter is chosen, the time series can be inverted.

Schmidt and Bürgmann (2003) invert for the incremental displacement time series as shown in Eq. 3.16. Often, the interval between epochs is irregular so the displacement can vary considerably between epochs. Instead, *π-rate* inverts for the velocity at each epoch in a similar formulation to Berardino et al. (2002). For large scale tectonic deformation the velocity should vary smoothly between epochs, but this assumption breaks down for other phenomena (e.g. coseismic or volcanic deformation). For this reason it is beneficial to have regularly spaced image acquisitions for these applications. Each unknown incremental range change in $\mathbf{d}$ now becomes $v = (\phi_s - \phi_m)/(t_s - t_m)$. Following from Eq. 3.16, a five epoch example with four connecting interferograms may be:

$$\begin{bmatrix} \phi_{AB} \\ \phi_{BC} \\ \phi_{CD} \\ \phi_{CE} \\ 0 \\ 0 \end{bmatrix} = \begin{bmatrix} t_B - t_A & 0 & 0 & 0 \\ 0 & t_C - t_B & 0 & 0 \\ 0 & 0 & t_D - t_C & 0 \\ 0 & 0 & t_D - t_C & t_E - t_C \\ \kappa & -2\kappa & \kappa & 0 \\ 0 & \kappa & -2\kappa & \kappa \end{bmatrix} \begin{bmatrix} v_B \\ v_C \\ v_D \\ v_E \end{bmatrix} \tag{3.17}$$

This system of linear equations is solved using a weighted least-squares inversion (Menke, 1984):

$$\mathbf{d} = [\mathbf{A}^T \Sigma_\Phi^{-1} \mathbf{A}]^{-1} \mathbf{A}^T \Sigma_\Phi^{-1} \mathbf{\Phi} \tag{3.18}$$

where Σ_Φ is the VCM containing the weights (described in §3.3.7). The algorithm performs this inversion for each pixel unless the number of observations is less than the threshold Ψ (defined in §3.3.1). The velocity is then integrated to give the displacement between each epoch and a cumulative time series is generated.

Singular value decomposition

The FDS method works for a connected network. However, if the network is composed of two or more unconnected subsets, the number of linearly independent rows of the design matrix $\mathbf{A}$ will be less than the number of unknowns $\mathbf{m}$ and $\mathbf{A}$ will be rank deficient without the additional smoothing constraint. As a result, the quantity $\mathbf{A}^T\mathbf{A}$ will be singular and a direct inverse is unobtainable. Berardino et al. (2002) describe an alternative method for inverting such a rank deficient system using the SVD method. The pseudo-inverse of the design matrix $\mathbf{A}$ is estimated via SVD to give the minimum

norm least-squares solution:

$$\mathbf{A} = \mathbf{USV}^T \tag{3.19}$$

where **U** and **V** are unitary matrices and **S** is a diagonal matrix of the non-negative singular values of **A**. The singular values are listed in descending order, with the largest values representing the most important part of the signal. The number of singular values is equal to the rank of **A**. A rank deficiency in **A** will introduce some very small singular values. Those values that are smaller than a defined tolerance are set to zero before the pseudo-inverse is calculated. By varying the tolerance, the smoothness of the resulting time series can be varied, though I have not experimented with the tolerance here.

3.3.10 Linear rate map estimation

The final part of the π-*rate* algorithm involves forming the linear rate map (or steady-state velocity map). Even if a pixel is not coherent in all interferograms, it is important to include it in the analysis in order to provide as much constraint on the rate as possible. To manage this requirement, the algorithm operates on a pixel-by-pixel basis and uses the MST matrix (described in §3.3.1) to select the appropriate observations for each pixel. Again, the threshold Ψ is used to exclude those pixels which do not have enough coherent observations. At each pixel, k, the problem can be described by the set of linear equations:

$$\mathbf{\Phi} = \mathbf{T} \cdot v_k \tag{3.20}$$

where $\mathbf{\Phi} = [\phi_{12}, \phi_{23}, \phi_{34} \dots \phi_{lm}]^T$ are the interferometric displacement observations, $\mathbf{T} = [t_{12}, t_{23}, t_{34} \dots t_{lm}]^T$ are the interferogram time spans and v_k is the LOS velocity or rate. A weighted least-squares inversion (Menke, 1984) is used to determine the best-fitting rate v_k and associated errors Σ_k at each pixel:

$$\begin{aligned} v_k &= \Sigma_k \mathbf{T}^T \Sigma_\Phi^{-1} \mathbf{\Phi} \\ \Sigma_k &= [\mathbf{T}^T \Sigma_\Phi^{-1} \mathbf{T}]^{-1}. \end{aligned} \tag{3.21}$$

The inversion is weighted with the VCM, Σ_Φ (described in §3.3.7), which takes into

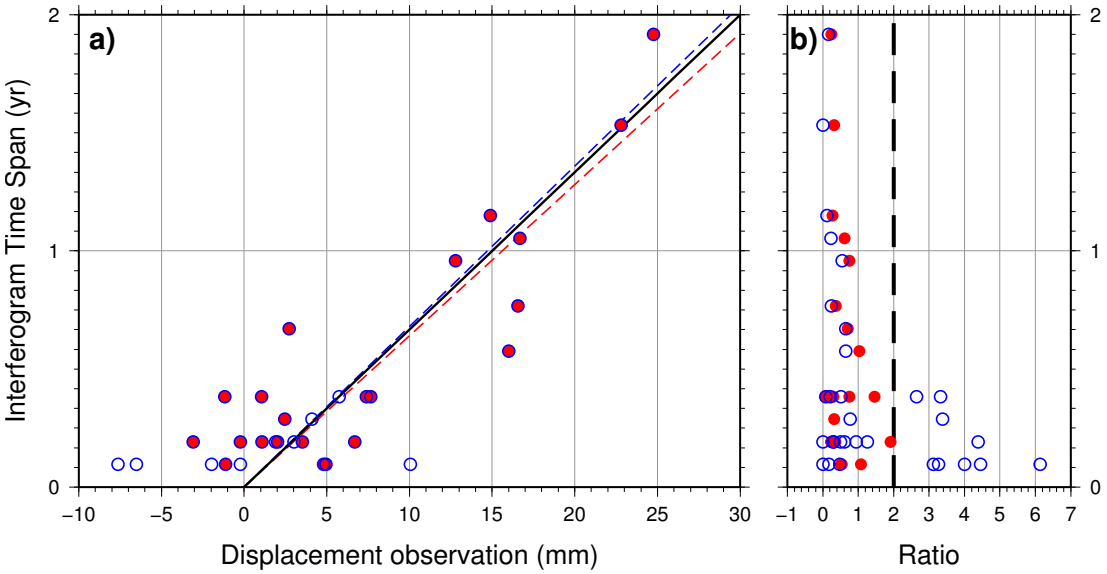

Figure 3.14: Synthetic example of linear rate determination for an individual pixel. 31 synthetic interferograms are constructed with deformation and spatially correlated noise components. The chosen pixel has a designed linear rate of 15 mm/yr (black solid line). a) Interferometric observations $\mathbf{\Phi}$ plotted against time span $\mathbf{T}$ for the network of 31 interferograms (blue open circles) and the 22 interferograms (red filled circles) for which the ratio of residual to *a-priori* standard deviation is less than Ξ (here $\Xi = 2$). Dashed blue and red lines are the corresponding estimate of the linear rate. b) Plot of the ratios of residual and *a-priori* standard deviation for the two sets of interferometric observations shown in a). Black dashed line shows the threshold Ξ. Note that the ratio for a pixel varies each iteration since the estimated rate changes.

account the temporal correlation between interferograms since epochs are present in multiple interferograms. Two user-defined parameters are used to exclude unreliable pixels from the rate map:

1. If any ratio of a residual and its associated *a-priori* standard deviation from the VCM is greater than a threshold value Ξ (typically 3), the observation with the maximum ratio is removed from the analysis. The rate is then re-evaluated with one less observation, providing that the number of coherent observations for that pixel is still greater than the threshold Ψ.

2. If the standard deviation of a pixel's estimated rate is greater than a threshold Υ (typically 2 mm), the pixel is removed from the final rate map.

Figure 3.14 shows a synthetic example of the linear rate determination for an individual pixel. The algorithm iteratively removes observations and re-inverts for the rate until all residual ratios are less than Ξ. In this example, 22 of the 31 initial observations

remain following this process. Greatest scatter in the observations occurs for interferograms with short time spans since the magnitude of deformation is typically much less than the noise. We expect the magnitude of deformation in an interferogram to increase linearly with time span. Therefore this shows that if coherence allows, it is preferential to use a network containing long period interferograms since the SNR in these is higher. Notice that in the analysis of Figure 3.14, π-*rate* has removed observations with shorter time spans.

3.4 Synthetic tests of π-*rate*

To test the validity of π-*rate* algorithms, sets of synthetic interferograms were generated following a similar approach to Biggs (2007). Each of the signal components discussed in §3.2.2 is simulated and then summed to produce a set of interferograms with the same temporal and spatial sampling as the two networks of real data used in this thesis (described in §3.4.1). Since all components are designed separately, the ability of π-*rate* to retrieve each component can be tested. Synthetic interferograms take the form:

$$\Delta\phi_{ij}^{synt} = (t_j - t_i)\, d + \left(\phi_j^{orb} - \phi_i^{orb}\right) + \left(\phi_j^{topo} - \phi_i^{topo}\right) + \left(\phi_j^{atm} - \phi_i^{atm}\right) \tag{3.22}$$

where i and j are the master and slave epochs, d is a linear deformation function (proportional to the time span) and other symbols are as in Eq. 3.1. Synthetic interferograms are constructed by first adding the individual components at each epoch, and then differencing the appropriate master and slave epochs for each interferogram (Figure 3.15). The synthetic interferograms are masked using the coherence masks of the real interferograms (used in Chapter 4) in order to realistically represent the temporal and spatial coherency properties of individual pixels.

3.4.1 Interferogram networks

Figure 3.16 shows two networks of interferograms used in this thesis to connect 32 acquired SAR epochs from Envisat descending track 176. Synthetic data is constructed using the same temporal and coherence properties as these two networks. The first network (Figure 3.16a) is an independent network containing 31 interferograms. The connections for this network are chosen using the MST algorithm (see §3.3.1) based on the number of coherent pixels in each interferogram. Most epochs have between 1

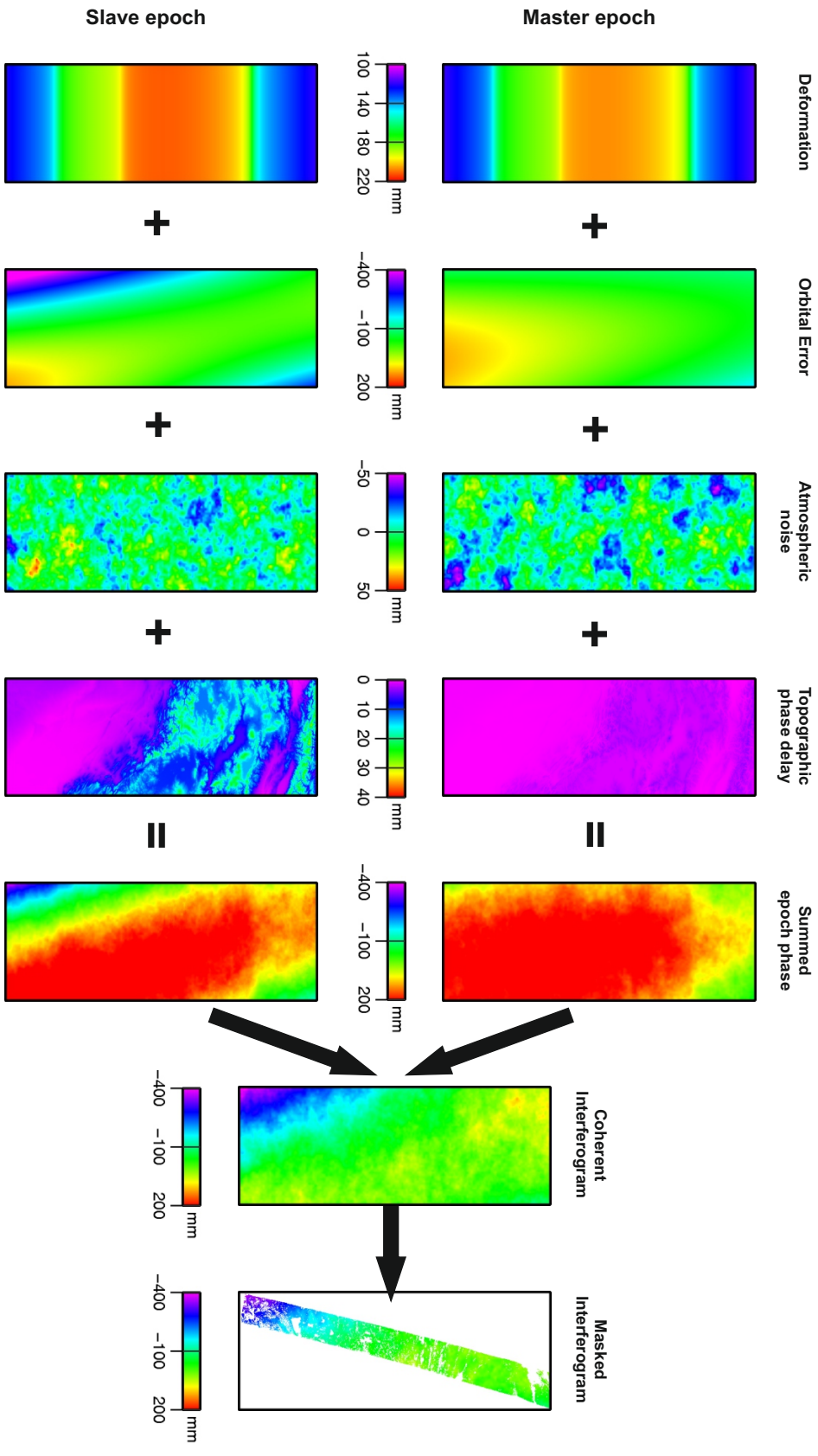

Figure 3.15: Construction of synthetic interferograms from separate signal components. Each component is produced using synthetic parameters generated from the real data parameters as detailed in the text. Components are summed for each epoch, and the interferogram is produced by subtracting the appropriate master phase from the slave phase. The synthetic interferograms are then masked using coherence masks from the real interferograms to simulate realistic temporal and spatial decorrelation patterns. This example is for the epochs 070520 (master) and 070624 (slave).

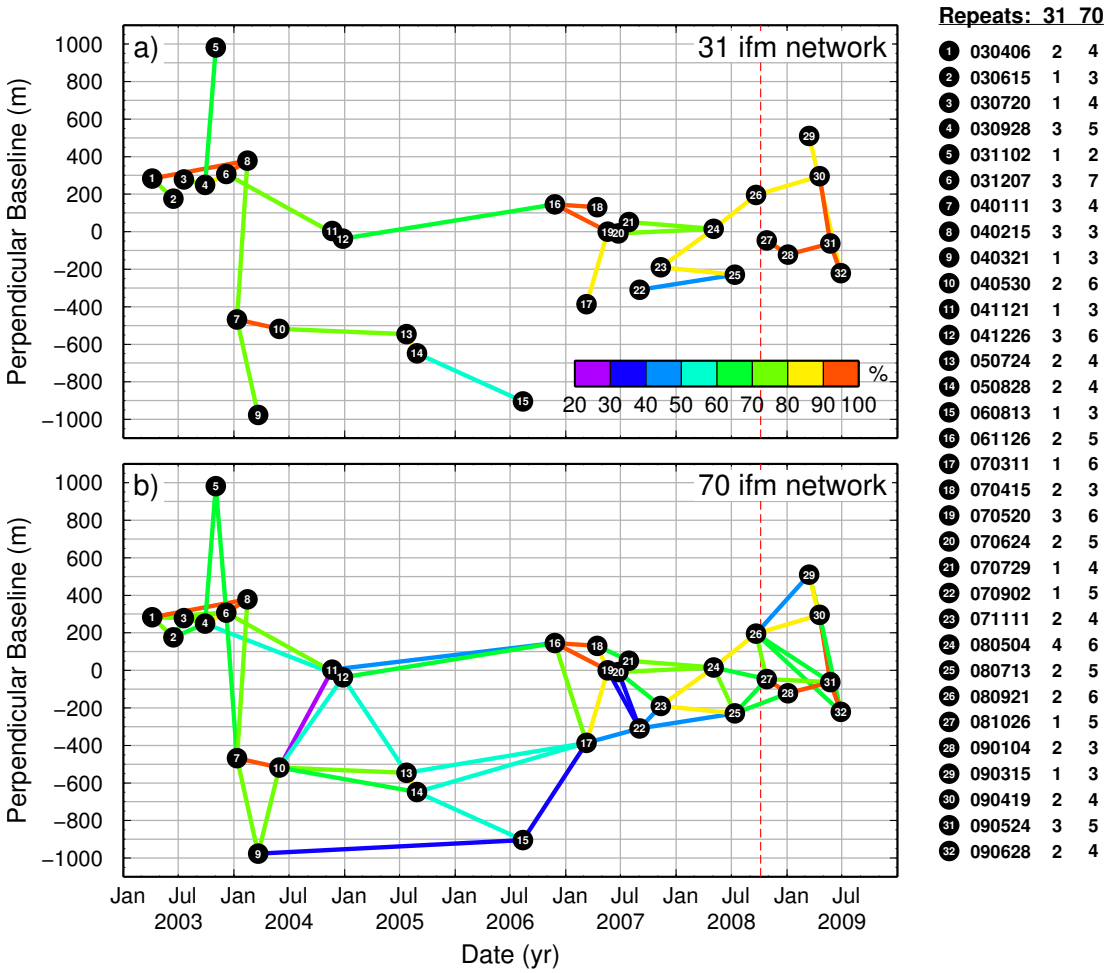

Figure 3.16: Baseline-time plots showing the two interferogram networks used for real and synthetic data. a) 31 interferogram network. b) 70 interferogram network. Lines represent interferograms and are coloured by the number of coherent ∼900 m pixels relative to the interferogram with maximum coherence (070520-070624). The dashed red line shows the occurrence of the Damxung earthquake in south Tibet (§4.3). On the right are epoch acquisition dates in the format YYMMDD followed by the number of times the epoch is used in each of the 31 and 70 interferogram networks.

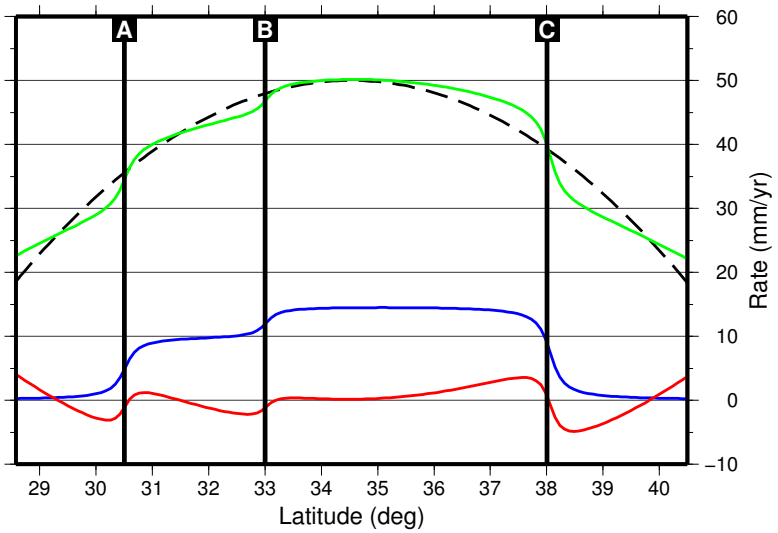

Figure 3.17: Profile of steady-state deformation signal used in the synthetic tests. Blue line: fault signals generated from summing three screw dislocation models. Red line: Modified fault signal with best fit quadratic removed. Black dashed line: Long wavelength quadratic signal. Green line: Deformation signal produced by adding modified fault signal and long wavelength signal. See text for more details.

and 3 connections to the network, with one epoch having 4 connections. The second network (Figure 3.16b) contains 70 interferograms. Most epochs have between 3 and 6 connections to the network, with the exception of one epoch that has 2 and another that has 7 connections. When using this network, the algorithm selects the best connections to use when creating an independent network for each pixel. The real data is discussed in more detail in §4.2.

3.4.2 Synthetic signal components

Deformation signal ϕ_{def} and initial deformation model

A simple model with three east-west trending strike-slip faults is generated using the screw dislocation model of Savage and Burford (1973; Fig. 3.17). The three faults have a modelled locking depth of 20 km and different slip rates of 10, 5 and -15 mm/yr (faults A, B and C respectively in Fig. 3.17). The interseismic velocity profiles for the 3 faults are calculated and summed (blue line in Fig. 3.17). A best fitting quadratic is then calculated and removed from the fault signal (red line). This modified fault signal is then added to a second long wavelength quadratic signal (black-dashed line) to give the total deformation signal (green line). The long wavelength signal is also used as the IDM in some synthetic tests.

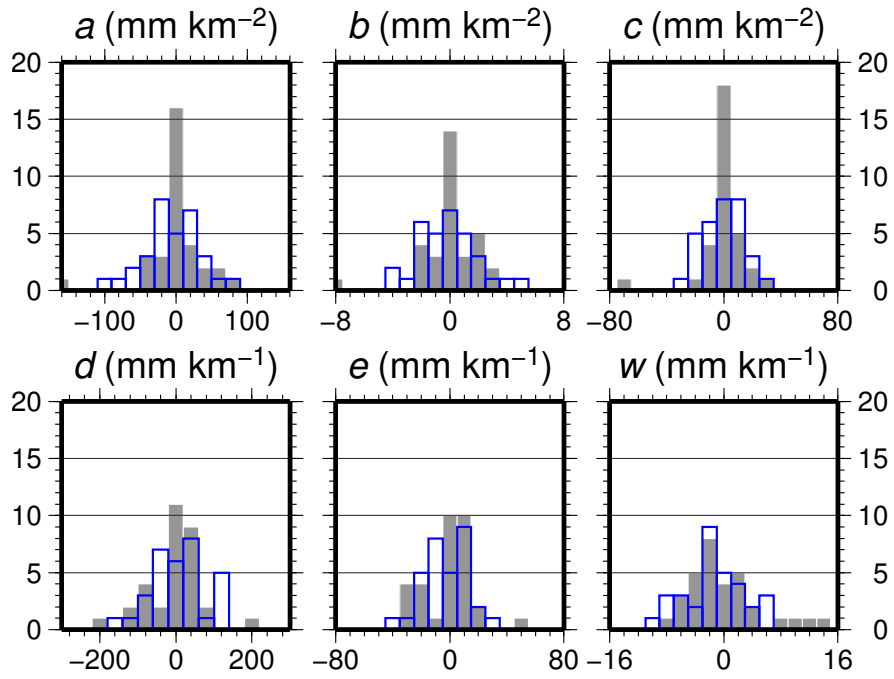

Figure 3.18: Histograms showing the distribution of the five coefficients of the orbital errors $a - e$ (Eq. 3.10) and the phase gradients of the topographically correlated phase delays w (Eq. 3.12) for the 32 epochs of the real network (filled grey bars) and synthetic data set (blue outlined bars).

The deformation profile is duplicated along strike to create the rate map, in which interseismic velocity varies only in the y-direction. The cumulative deformation at each epoch is calculated by multiplying the rate map by the time interval between the current epoch and the first epoch. When producing the synthetic interferograms, the cumulative deformation of the master is subtracted from the cumulative deformation of the slave to give the deformation signal during the interferogram time period.

Orbital errors ϕ_{orb} and topographic phase delays ϕ_{topo}

Orbital errors do not correlate through time, and atmospheric phase delays are only correlated for periods up to a day in length (Emardson et al., 2003). Therefore to create synthetic data with a realistic signal magnitude the mean and standard deviation of the evaluated coefficients $a - e$ (Eq. 3.7) and w (Eq. 3.12) from the real data are used to create a set of random parameters for each epoch with the same statistical properties (Fig. 3.18). The synthetic orbital parameters are used to calculate a full resolution quadratic surface for each epoch. Synthetic topographic phase delays are simply the product of a topographic height for each pixel and the phase gradient for each epoch.

A modified section of SRTM DEM at 30 arc-second (∼900 m) resolution was used to extract the topographic heights with a range of ∼3.5 km, similar to the range of the real co-registered DEM for track 176.

Spatially correlated atmospheric noise ϕ_{atm}

To create a set of simulated atmospheric components, the method described in Parsons et al. (2006) is followed. Using Eq. 3.13, the mean values of σ_{max} and α estimated from the real data are used to generate a spatial VCM (Σ), whose values vary based on the distance between points. A vector of correlated noise is generated from the product of the upper triangle of the VCM (L; obtained via a Cholesky decomposition, where $\Sigma = LL^T$) and multiplying this by a matrix of random noise whose dimensions are equal to the number of data points and the number of epochs. The correlated noise is then reshaped to give a full resolution noise field for each epoch.

3.4.3 Testing the orbital error and topographic phase delay algorithms

The performance of the network method in recovering the synthetic orbital and topographic phase parameters is compared with the independent-interferogram method in both orbital and topographic phase delay correction algorithms. The 70 interferogram network is used since using more interferograms should add further constraint to the inversion for orbital error at each epoch. Biggs (2007) reported an improvement of ∼9% in RMS misfit for both planar orbital parameters when the network method was used.

The algorithms are subjected to four tests in which the input interferograms contain a combination of synthetic signal components as follows:

1. $\Delta\phi_{synt} = \Delta\phi_{?}$ (IDM used)
2. $\Delta\phi_{synt} = \Delta\phi_{?} + \Delta\phi_{atm}$
3. $\Delta\phi_{synt} = \Delta\phi_{?} + \Delta\phi_{atm} + \Delta\phi_{def}$
4. $\Delta\phi_{synt} = \Delta\phi_{?} + \Delta\phi_{atm} + \Delta\phi_{def}$ (IDM used)

where $\phi_{?}$ is either ϕ_{orb} or ϕ_{topo} depending on the algorithm being tested. When spatially correlated noise is included in the synthetic signal, 100 realisations of the noise are

Table 3.2: Mean and standard deviations of synthetic and estimated orbital parameters $a - e$ (Eq. 3.7) and topographic phase gradient w (Eq. 3.12) for the network (E) and independent-interferogram (I) methods. Mean and standard deviation is calculated from the parameters for the network of 70 interferograms. Rows numbered 1-4 are for synthetics constructed from signal components as outlined in the text. Green cells indicate the network method gives a closer match to the input, whereas red cells indicate the independent method is closer to the input.

		a (mm km^{-2})		b (mm km^{-2})		c (mm km^{-2})		d (mm km^{-1})		e (mm km^{-1})		w (mm km^{-1})	
		mean	std dev	mean	std dev	mean	std dev	mean	std dev	mean	std dev	mean	std dev
input		0.306	64.485	-0.153	2.519	2.604	18.340	8.978	95.674	-0.287	22.374	-0.279	6.204
1	I	0.306	64.485	-0.153	2.519	2.604	18.340	8.978	95.674	-0.287	22.374	0.117	3.579
	E	0.306	64.485	-0.153	2.519	2.604	18.340	8.978	95.674	-0.287	22.374	0.038	3.466
2	I	0.163	64.311	-0.175	2.503	2.520	18.358	9.033	95.837	-0.284	22.317	-0.128	3.997
	E	0.245	64.133	-0.160	2.507	2.594	18.382	8.834	95.870	-0.309	22.303	-0.287	4.044
3	I	97.222	117.924	4.208	5.076	42.912	43.770	2.989	96.018	-0.389	23.639	-5.480	10.577
	E	103.930	128.689	3.962	5.088	43.735	45.279	0.553	96.455	-0.731	22.614	-8.244	12.848
4	I	1.139	64.771	-0.169	2.493	2.829	18.509	9.169	95.851	-0.092	22.266	0.397	4.259
	E	0.170	64.166	-0.189	2.503	2.531	18.329	9.002	95.909	-0.148	22.241	0.140	4.258

created and the the test is run 100 times. The mean value for each parameter in each interferogram is then calculated from the 100 estimated parameters. The mean and standard deviation of each parameter is then calculated from the 70 sets of parameters from each interferogram (Table 3.2). The parameters at each epoch from the network method are converted to interferogram parameters by subtracting the master epoch value from the slave value for comparison with the independent method.

In test 1, both methods can fully recover the input orbital parameters. However, the topographic phase gradient is not matched with either method. After adding atmospheric noise (test 2) the algorithms still do a reasonable job of recovering the parameters. The large discrepancies between input and estimated for test 3 highlight the problem of aliasing deformation into both the orbital and topographic signals. When using the IDM to address this issue (test 4) the estimated parameters are much closer for both.

Although the network method does a better job for most parameters, it is not universally better than the independent method in recovering the input parameters. This suggests there is only a minor advantage in using the network method over the independent method. In addition, the magnitude of improvement is only small compared with the total discrepancy. The SVD method used for the inversion in the network method can be unstable and therefore could generate inaccurate model estimates in some situations (e.g. when the orbital errors are not normally distributed; Hua Wang, *pers. comm.*). To avoid this possibility it may be best to rely on the direct least squares inversion used in the independent method at the cost of the perceived marginal improvement in accuracy.

3.4.4 Testing the linear rate map algorithm

The greatest motivation for these synthetic tests is to determine the reliability of evaluated linear rates from the π-*rate* software. To establish this a Monte-Carlo procedure is used in which 100 sets of interferograms are generated, each with a different realisation of spatially-correlated random noise (see §3.4.2). The mean and standard deviation of the 100 resulting rate maps is then calculated at each pixel to give the 'mean rate map'. Additionally, the RMS misfit between the full 'mean rate map' and the full input deformation signal is calculated.

Five synthetic tests were conducted, each containing combinations of signal compo-

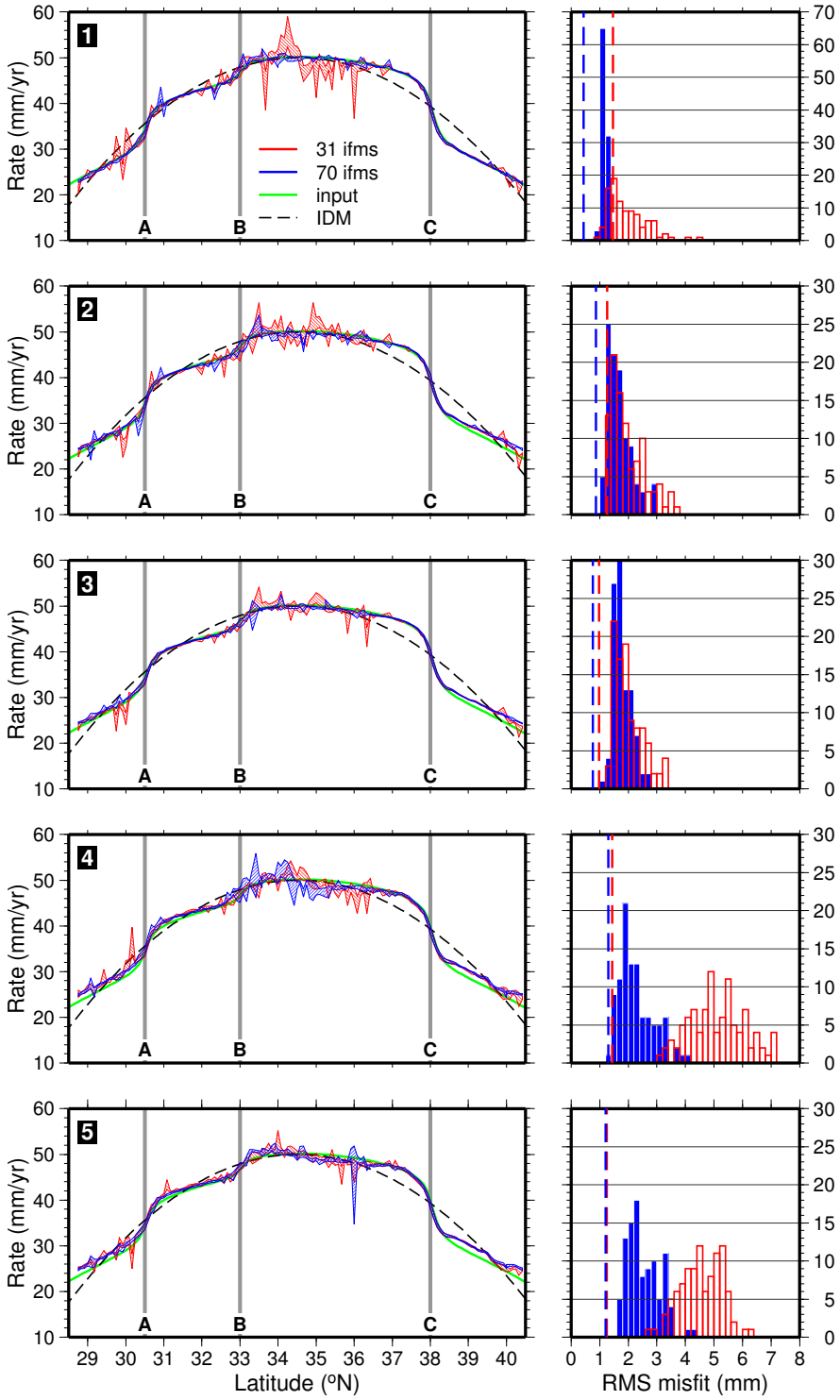

Figure 3.19: Profiles through the 'mean rate map' of the 100 estimated rate maps determined through Monte-Carlo analysis. Rows are numbered as described in the text for each synthetic test. Green line is the input deformation profile and black dashed line is the IDM profile. Red and blue polygons show the 2-sigma distribution of the 100 rate map profiles for the 31 and 70 interferogram networks respectively calculated at 10 km bin intervals. Vertical grey lines mark the location of faults A, B and C. Histograms show the associated RMS misfits between 100 π-*rate* determined linear-rate maps and the input deformation signal for the 31 (red-outlined bars) and 70 (blue-filled bars) interferogram networks. Red and blue dashed lines show the RMS misfit between the 'mean rate map' and the input deformation signal for the 31 and 70 interferogram networks respectively.

nents as follows:

1. $\Delta\phi_{synt} = \Delta\phi_{def} + \Delta\phi_{atm}$.
2. $\Delta\phi_{synt} = \Delta\phi_{def} + \Delta\phi_{orb} + \Delta\phi_{atm}$.
3. $\Delta\phi_{synt} = \Delta\phi_{def} + \Delta\phi_{orb} + \Delta\phi_{atm}$ and spatio-temporal filtering applied.
4. $\Delta\phi_{synt} = \Delta\phi_{def} + \Delta\phi_{orb} + \Delta\phi_{topo} + \Delta\phi_{atm}$.
5. $\Delta\phi_{synt} = \Delta\phi_{def} + \Delta\phi_{orb} + \Delta\phi_{topo} + \Delta\phi_{atm}$ and spatio-temporal filtering applied.

In each case the *a-priori* IDM is used to ensure the long wavelength signal components are retained and the same 100 realisations of noise are used to generate the input interferograms.

Figure 3.19 shows profiles through the resulting 'mean rate maps' and histograms of the RMS misfits between the input rate map and the 100 individually estimated rate maps. Detail of the velocity gradients across the 3 faults is well reproduced in most cases, with some scatter around fault B, with the slowest synthetic slip rate. For all five tests the RMS values show that using the full 70 interferogram network gives a better fit to the input signal than the minimum-spanning 31 interferogram network. By comparing test 2 with 3 and test 4 with 5, improvements in the fit can be seen when spatio-temporal filtering is applied before rate map evaluation. When orbital errors are included in the synthetic interferograms, offsets between input and mean rate maps can be seen toward the ends of the profile. This implies that although the quadratic model was used to generate input orbital errors, the algorithm would perhaps benefit from higher order polynomial estimation of the orbital errors for such long rate maps. Tests 4 and 5, which include topographically correlated noise, exhibit a complicated misfit in the centre of the profile. The origin of this is not precisely known, but may be related to variation in the DEM at this latitude. Coupled with the results from testing the topographic phase correction algorithm directly (§3.4.3), it appears that this method is not effective for the large extent of data used here. The simple assumption that a single linear gradient can describe the elevation-phase relationship seems to be invalidated for long scenes. This is not unexpected given the length scales of atmospheric correlation. Accordingly, the algorithm will not be used during analysis of the real data in Chapter 4.

In general, the results of synthetic testing suggest that the π-*rate* algorithms are reliable and output rate maps can be interpreted at face value. In particular, using a network with many more interferograms than epochs gives a clear advantage when evaluating the rate on a pixel-by-pixel basis. Although a network method performs better than an independent-interferogram method for determining orbital errors and topographically correlated phase delays, the advantage is marginal.

In Chapter 4, I will apply the methods discussed here to analyse interseismic deformation from a long scene of SAR data in the central Tibetan plateau.

Chapter 4

Interseismic deformation of Tibet from InSAR

In this chapter I analyse SAR data from the Envisat satellite for a very long track spanning the central Tibetan plateau, measured over a period of ∼6.25 years. The aim is to determine the extent of strain localisation at mapped fault zones, which would manifest in the data as steep velocity gradients, and the long wavelength variation of deformation across the plateau.

4.1 Previous studies

A number of published studies have used InSAR to measure interseismic deformation in Tibet (Figure 4.1). However, most of these studies concentrate on only a few frames of data surrounding individual major faults. The data is typically modelled using the locked-fault model of Savage and Burford (1973) to obtain the interseismic fault slip rate (Table 4.1). These studies are useful to gain understanding of the nature of faulting and for assessing seismic hazard in these locations. But they do not help us answer the very broad questions concerning continental deformation as outlined in §1.5.

The Altyn Tagh fault (ATF) has received the most attention. The western end of the fault is found to slip at less than 5 mm/yr. The central and eastern sections generally have a slip rate of 10 mm/yr within error bounds. A recent study at the eastern end of the ATF using Envisat data has found a slip rate of ∼5 mm/yr (Hamlyn, 2011), which is low compared with the findings of the co-located but independent studies of Lasserre et al. (2007) and Jolivet et al. (2008).

InSAR was applied to several of the faults in the Central Tibet Conjugate Fault

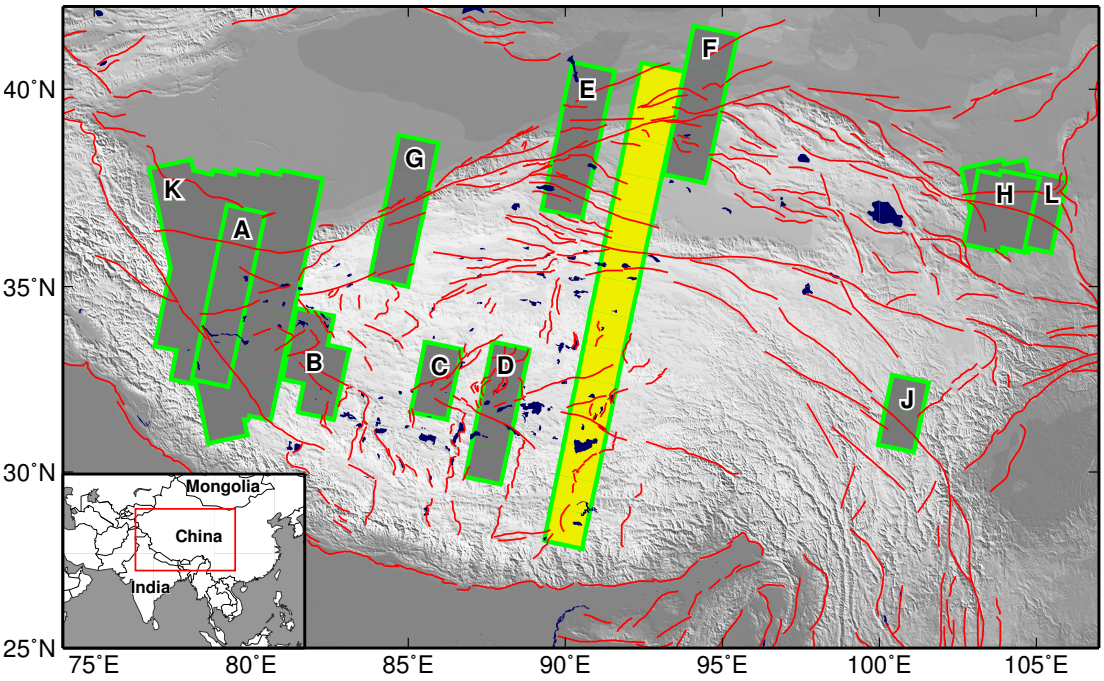

Figure 4.1: Distribution of published InSAR studies of interseismic deformation in Tibet. Grey rectangles with green outlines show the spatial extent of SAR data used in each study. See Table 4.1 for the references relating to each lettered rectangle. Extent of data used in this thesis is highlighted in the yellow rectangle with green outline. Red lines are active faults compiled by Taylor and Yin (2009). Mercator projection. Inset map: red box shows the extent of central Asia plotted.

Table 4.1: Summary of interseismic strike-slip rates in Tibet from InSAR studies.

Fault	Longitude	Slip rate (mm/yr)	Location (Fig. 4.1)	Reference
Altyn Tagh	78°E	1±2	K	Wang and Wright (2011)
	80°E	5±5	A	Wright et al. (2004a)
	80°E	2±2	K	Wang and Wright (2011)
	85°E	11±5	G	Elliott et al. (2008)
	90°E	16±5	E	Lasserre et al. (2007)
	94°E	11±2	F	Lasserre et al. (2007)
	–//–	7-9	F	Jolivet et al. (2008)
	–//–	4.7±0.5	F	Hamlyn (2011)
Gyaring Co	88°E	7.8-20.8	D	Taylor and Peltzer (2006)
Haiyuan	104°E	∼6	H	Cavalié et al. (2008)
	104°E	∼6	L	Jolivet et al. (2010)
Karakoram	77°E	1±2	K	Wang and Wright (2011)
	78°E	3±2	K	Wang and Wright (2011)
	79°E	1±3	A	Wright et al. (2004a)
	79°E	6±1	K	Wang and Wright (2011)
	80°E	1±1	K	Wang and Wright (2011)
Lamu Co	82°E	1.0-3.3	B	Taylor and Peltzer (2006)
Riganpei Co	86°E	3.4-11	C	Taylor and Peltzer (2006)
Xianshuihe	105.5°E	9-12	J	Wang et al. (2009)

Zone (CTCFZ) by Taylor and Peltzer (2006). Although the Lamu Co and Riganpei Co faults are found to have low slip rates <5 mm/yr, the Gyaring Co fault has a much higher slip rate estimate. Taylor and Peltzer (2006) make their slip rate estimates using individual interferograms and do not try to remove the orbital or atmospheric signal components they contain.

Although no InSAR studies of interseismic deformation have been published for the Kunlun fault, Ryder et al. (2011) and Wen et al. (2011) study postseismic motion following the large Kokoxili earthquake. More detail is given in §4.4.

With increasingly large SAR data archives, it is becoming possible to determine interseismic deformation over large areas. Wang and Wright (2011) combine multiple tracks of SAR data and sparse GPS velocities to solve for a high-resolution velocity field in western Tibet. The method interpolates velocity observations over a triangular mesh, assuming linear variation between mesh nodes. The relative weighting of GPS and InSAR is controlled by inclusion of the full data covariance in the inversion scheme. The resulting velocity field reveals low slip rates on the Karakoram fault and ATF, and significant velocity gradients away from the faults (Wang and Wright, 2011).

4.2 Data

4.2.1 Envisat archive for Tibet

The Envisat satellite has a number of different onboard instruments, yet only a limited power budget and down-link bandwidth to operate them with. Because of these competing interests, it is not possible to operate the SAR instrument at all times in order to collect global coverage with each complete orbital cycle. Envisat flies a sun-synchronous polar orbit, meaning it revisits the same location at approximately the same time of day on each pass. Descending passes are from north to south on the sun-lit side of the planet. Ascending passes are from south to north on the shadowed side of the planet. Since the SAR instrument requires a relatively high power load it is most frequently used on descending orbits when power can be generated from solar radiation.

Figure 4.2 shows the archive of Envisat SAR images over the Tibetan plateau between 2003 and 2010. It is immediately obvious that there is not uniform coverage across the plateau. The coverage on ascending passes is generally low, between 0 and 15 acquisitions in most frames. The exception to this is across the Altyn Tagh, Kunlun, Haiyuan and Karakoram faults on several tracks where there are up to 30 acquisitions. The coverage on descending tracks is much better, with most frames within the plateau having upwards of 20 acquisitions.

4.2.2 Descending track 176

Descending track 176 was chosen since a reasonable data archive covering the full north-south extent of the plateau was available. Figure 4.3 shows the along-track coverage of archived SAR data for this track, and indicates significant along-track variability. Not until recently have images covering the full area of interest been acquired on a regular basis. Coverage has been concentrated around the seismically active Kunlun fault and Lake Nam Co, with 50 acquisitions or more at the latitudes of these features. All SAR acquisitions are vertically polarised and collected in swath mode IS2, corresponding to a mean incidence angle (θ) of $\sim$23°. Details of the available SAR acquisitions for track 176 are given in Appendix A.

The 32 SAR acquisitions that have been used in this study (plotted as doughnuts in Figure 4.3) were used to create two interferogram networks as plotted in Figure 3.16 and

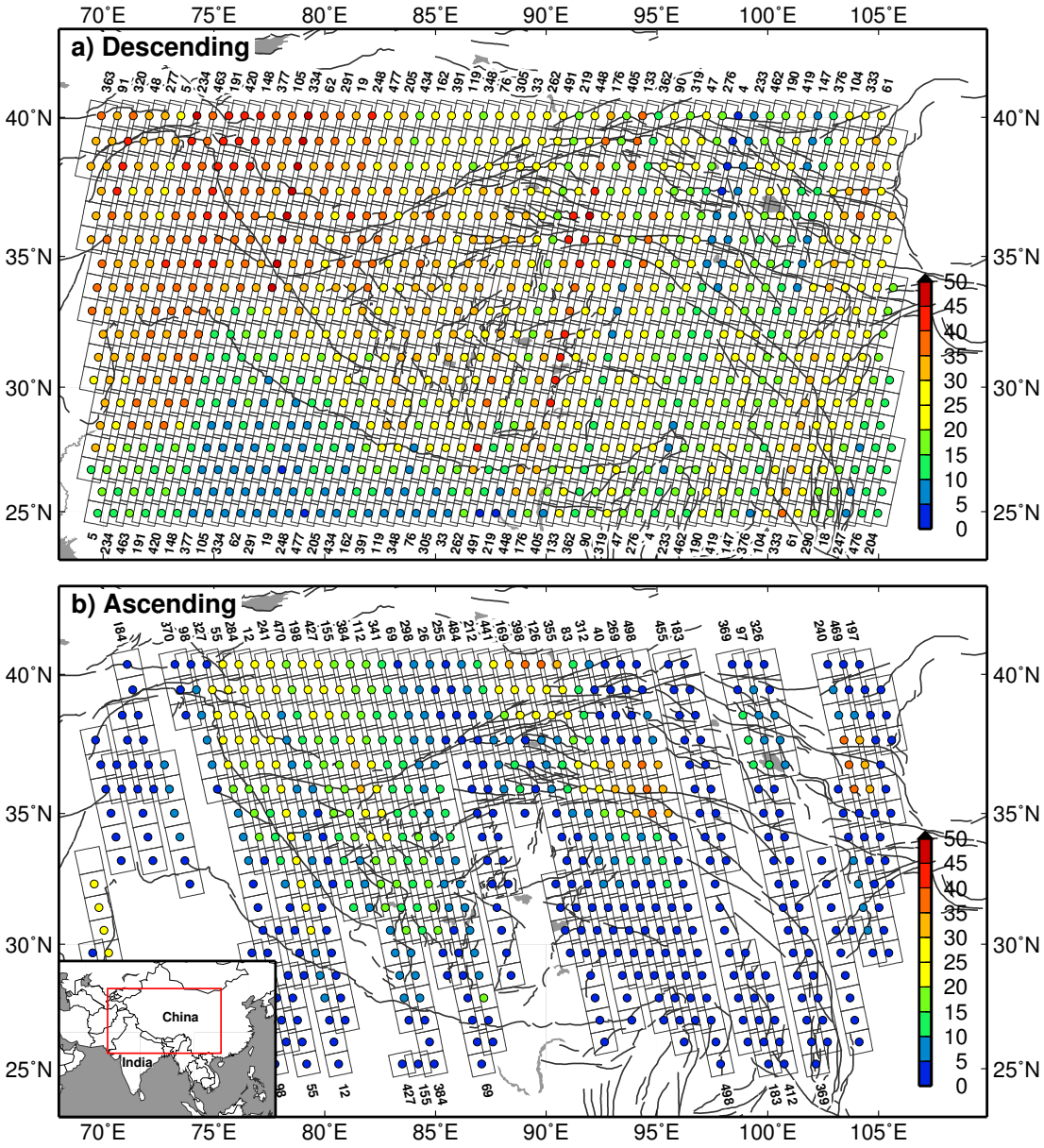

Figure 4.2: Envisat SAR data archive in Tibet for a) descending and b) ascending passes in swath mode IS2 up to 1st October 2010. Each coloured dot plotted at the centre of a frame (fine grey squares) indicates the number of images in the archive. Slanted numbers are the track reference numbers. Thicker grey lines are active faults compiled by Taylor and Yin (2009) and plotted here for spatial reference. Inset map: red box shows the extent of central Asia plotted. Mercator projection.

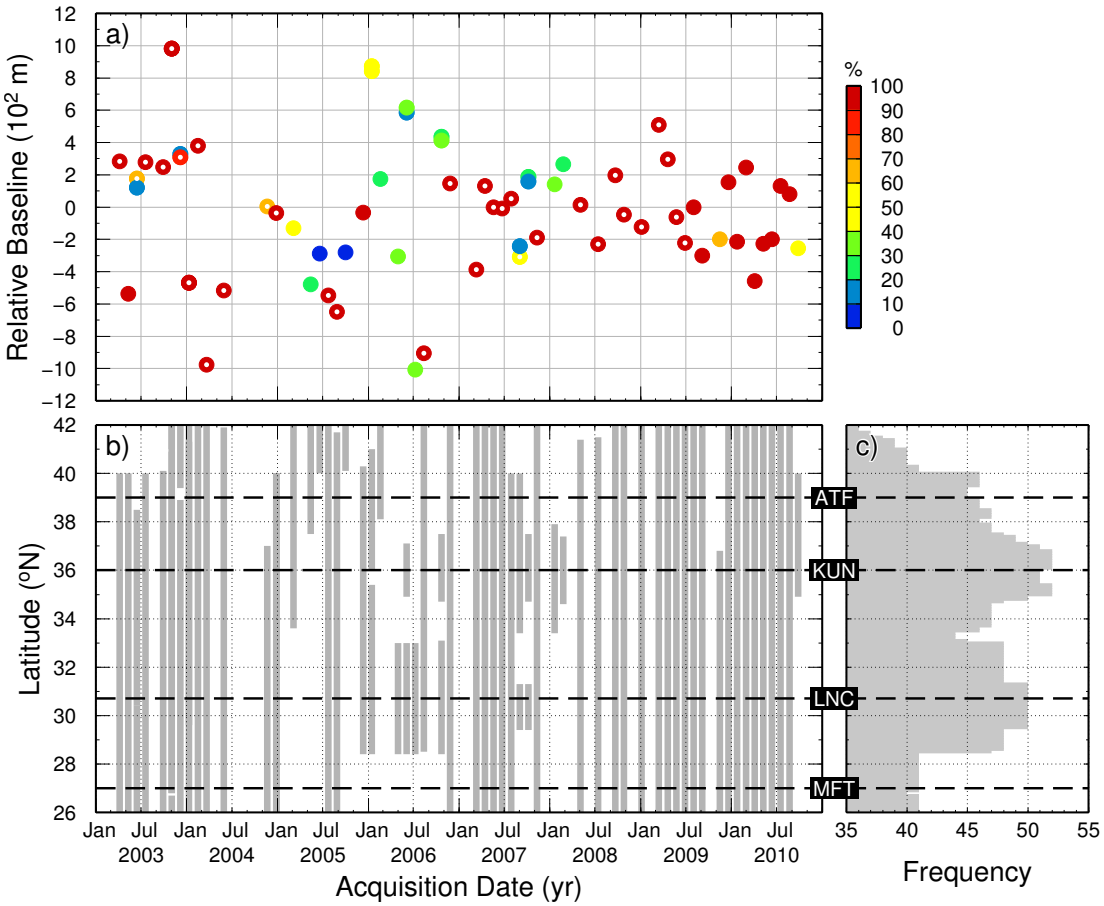

Figure 4.3: SAR data archive for Envisat descending track 176 in the region of the Tibetan plateau. a) Baseline-time plot showing the available acquisitions coloured by the percentage along-track coverage between 28.5-40.5 ^{o}N. The 32 acquisitions used in this study are represented as doughnut symbols and plotted in Figure 3.16. b) Along-track coverage of the available acquisitions. c) Histogram showing the number of archived acquisitions summed in bins of 0.1 degrees latitude. Horizontal dashed black lines indicate the approximate crossing points of the Altyn Tagh fault (ATF), Kunlun fault (KUN), Lake Nam Co (LNC) and Main Frontal thrust (MFT).

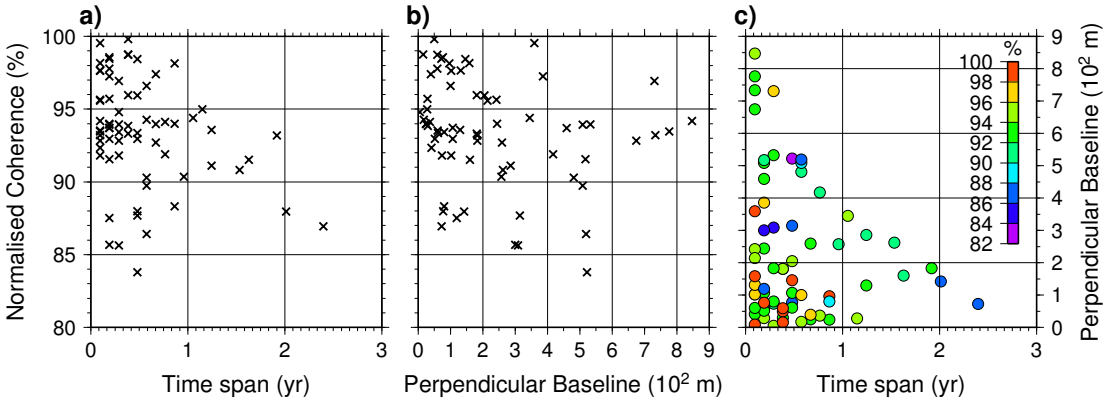

Figure 4.4: Dependence of interferogram coherence on the temporal and perpendicular baselines. a) Coherence as a function of interferogram time span. b) Coherence as a function of perpendicular baseline $B_\perp$. c) Dependence of coherence on both spatial and temporal baselines. In each, coherence is normalised to the interferogram with greatest coherence and expressed as a percentage. Differing along track coverages of individual interferograms as shown in Figure 4.3 are not accounted for in these plots.

described in §3.4.1. These networks are the 'full' network containing 70 interferograms (Figure 3.16b) and the 'independent' network containing 31 interferograms chosen by the π-*rate* MST algorithm (Figure 3.16a; §3.3.1)

A general observation with InSAR is that coherence is inversely related to the length of the temporal and spatial baselines of the interferograms. In this situation, 'coherence' is defined as the number of unwrapped pixels in an interferogram and is not to be confused with the interferometric correlation discussed in §3.2.2. Figure 4.4 shows the coherence properties of the 70 interferograms used in this study, and the general trend confirms the inverse relationship between baselines and coherence. However, the baselines appear to have only a minor impact on the coherence for this data set. When the interferograms are very long, the relationship is complicated by the variable along-track collection of data as seen in Figure 4.3. None of the interferograms used here have coherence less than ∼80% of the most coherent interferogram.

The along-track variability of coherence is shown in Figure 4.5 expressed as a percentage of the total possible number of observations for both networks. Only a small band at ∼37°N is coherent in all of the interferograms. The best coherence occurs in the Qaidam basin between 37-40°N and around the CTCFZ and lake Nam Co between 30.5-32.5°N. Nam Co is a large endorheic lake, situated entirely within track 176 at a latitude of ∼31°N (Figure 4.6). Coherence is reduced south of Nam Co by the rise of the Himalayan foothills with its associated steeper slopes and increased snow cover.

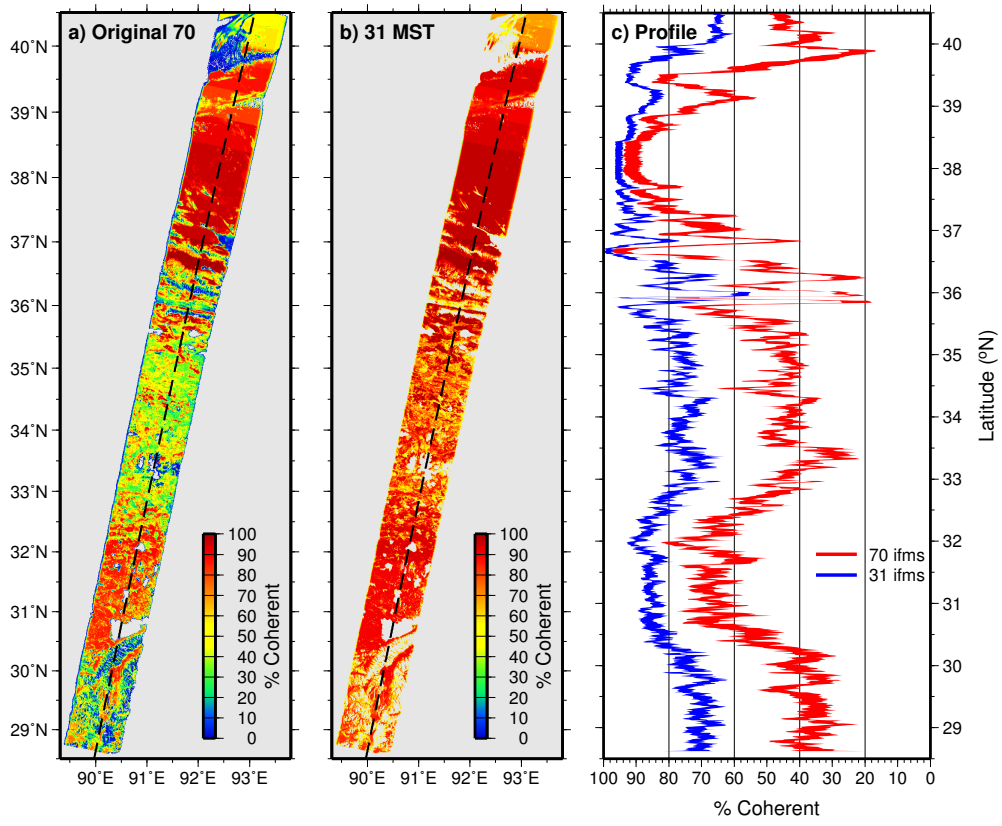

Figure 4.5: Spatial variability of coherence in the full interferogram network and MST selected independent network. Sum of coherence masks for each interferogram in a) the full interferogram network (maximum 70 observations) and b) the MST selected independent network (maximum 31 observations), expressed as percentage of maximum. c) Profiles located along the black dashed line in a) and b). The 2-sigma error envelope of the mean value calculated in 1 km bins along profile is plotted for the full (red) and independent (blue) networks. In the case of the independent network, if a pixel has less than 15 coherent observations out of 31 (i.e. ∼48%) it is excluded.

Much of the Tibetan plateau is covered with pervasive high-altitude permafrost (Cheng and Wu, 2007). This has a considerable effect on interferograms, particularly in the middle of the track between ∼32.5-36°N. Freeze-thaw cycles in the permafrost in this region cause decorrelation of pixels which can adversely affect interferograms with long spatial or temporal baselines.

4.3 Recent deformation in central Tibet

The occurrence of recent earthquakes gives a direct indication of active deformation. Since the main aim of this study is to quantify interseismic deformation, coseismic or postseismic signals resulting from earthquakes represent an additional source of noise. In some cases this signal can be modelled and removed from interferograms. Often the earthquakes are so small that the resulting deformation will not significantly affect the determination of interseismic velocities over large areas. Lohman and Simons (2005) find that earthquakes as small as M_w 4 can be detected using InSAR, providing that the depth is shallow (<5 km). Thus, coseismic deformation from any earthquake of this size or greater may appear in interferograms spanning the earthquake date.

Plotted in Figure 4.6 is the recent seismicity of Tibet with M > 4 in the immediate region of descending track 176. Swarms of earthquakes clustered in time can be observed throughout the region. Several swarms have occurred on the north-south trending rift systems, including the Yadong-Gulu rift south of Lake Nam Co and in the central region between the CTCFZ at ∼32°N and the Kunlun fault.

An M_w 6.3 earthquake occurred on the Yadong-Gulu rift in Damxung county in south Tibet on 6th October 2008 (Elliott et al., 2010) and directly within track 176. The magnitude of coseismic deformation from the earthquake is large enough that surface deformation is observable in interferograms spanning the earthquake. Elliott et al. (2010) inverted a coseismic interferogram to obtain the fault slip parameters for the earthquake (Figure 4.7). This model (shown in Figure 3.16) is subtracted from the 8 interferograms which span the date of the earthquake.

The ATF, which is thought to have a fast slip rate in the region of 11-16 mm/yr in the vicinity of track 176 (Table 4.1), has been relatively inactive during the last decade between 89°E - 96°E. A couple of isolated events occur on the CTCFZ directly north of Lake Nam Co, including the right-lateral Beng Co fault (Taylor and Peltzer, 2006). It is assumed that the M 6.3 Qinghai and M 6.6 Delingha thrust earthquakes

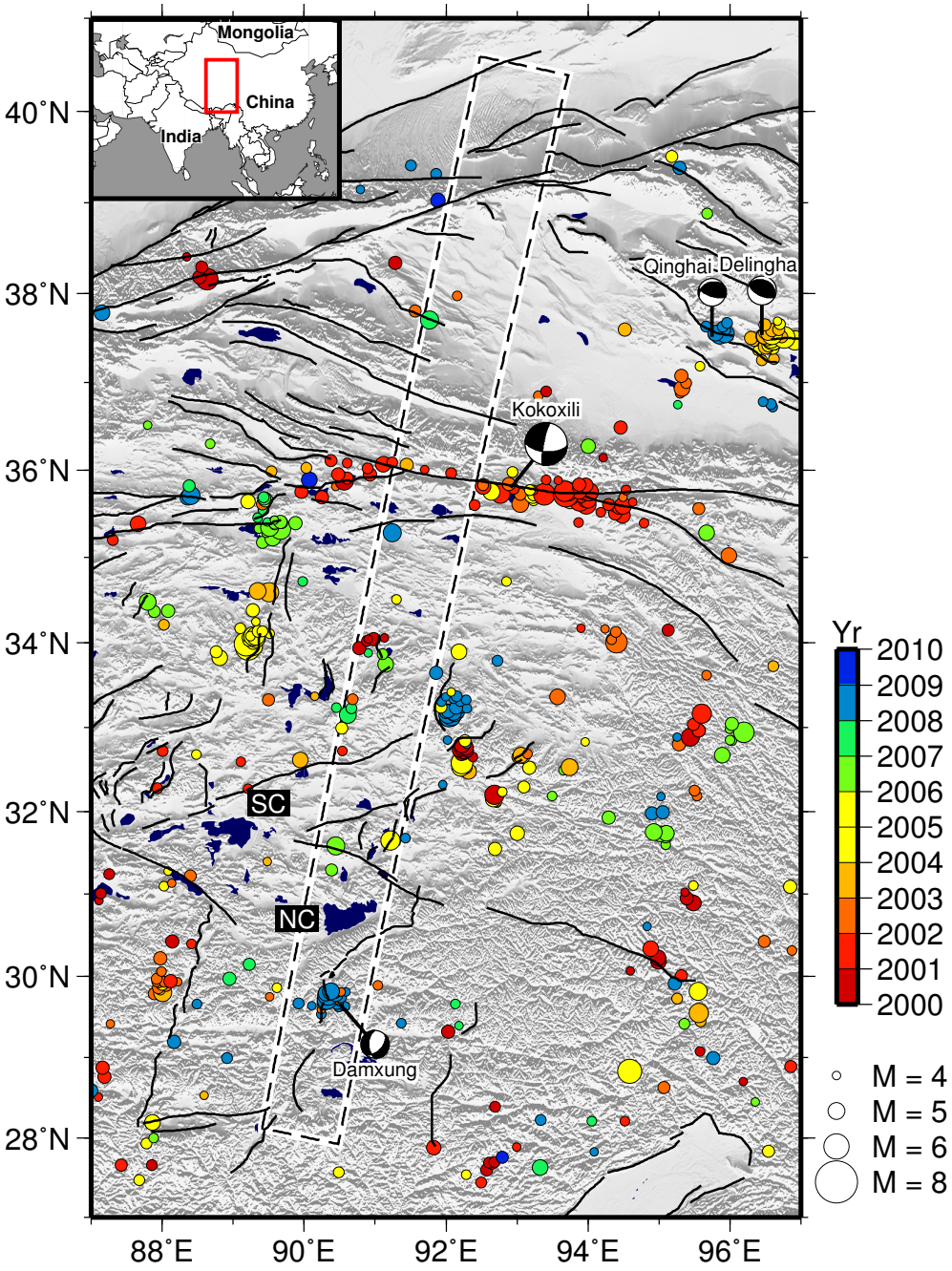

Figure 4.6: Seismicity in the region of track 176 during the period 01/01/2000 - 29/06/2009. Earthquakes between $4 \leq M < 6$ are plotted as circles and coloured according to year of occurrence. Earthquakes with $M \geq 6$ are named and plotted as double couple moment tensors. Plotted events are shallower than 70 km depth and symbol diameter scales with earthquake magnitude. White box with dashed black line delineates the location of descending track 176 SAR data used here. Black lines are faults from Taylor and Yin (2009). NC - Lake Nam Co. SC - Lake Siling Co. Earthquake locations from IRIS database and moment tensors from the Global CMT project.

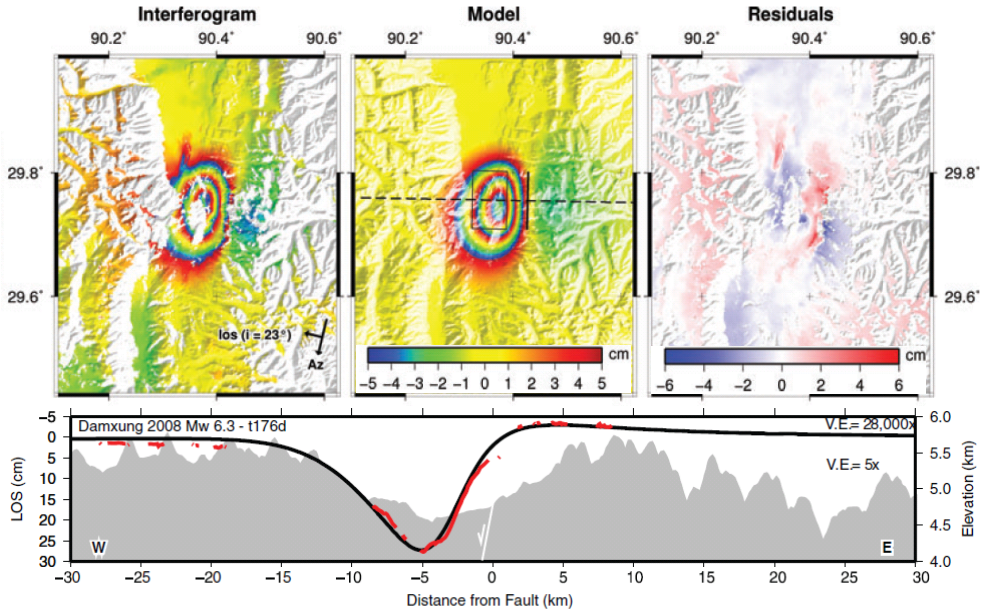

Figure 4.7: Coseismic fault model for the Damxung earthquake after Elliott et al. (2010). Shown on the top row from left to right are the wrapped track 176 descending interferogram (080921-081026), best fitting model, and residuals. The lower panel shows a profile through the interferogram (black line) and model (red line) with vertically exaggerated topography and fault location. Profile location is shown as the dashed line in the model plot.

(of 10/11/2008 and 17/04/2003 respectively) are distant enough from track 176 that coseismic or postseismic deformation from these earthquakes will not contaminate the interferograms.

The M_w 7.8 Kokoxili earthquake occurred on the Kunlun fault on 14th November 2001, to the east of data coverage used in this study (Lasserre et al., 2005). In addition, a large number of $M < 6$ aftershocks have occurred on the Kunlun fault following the main earthquake. However, only a few earthquakes actually fall within the footprint of track 176.

Doin et al. (2009b) observed a large subsidence signal associated with rapid water level rise in Siling Co (Figure 4.6). This is a similarly sized lake to Nam Co, situated ∼130 km to the north-west. I did not observe a similar signal in the interferograms around Nam Co.

4.4 Kunlun fault postseismic deformation

Ryder et al. (2011) modelled geodetically measured transient postseismic velocities resulting from the Kokoxili earthquake in terms of viscoelastic relaxation of the lower

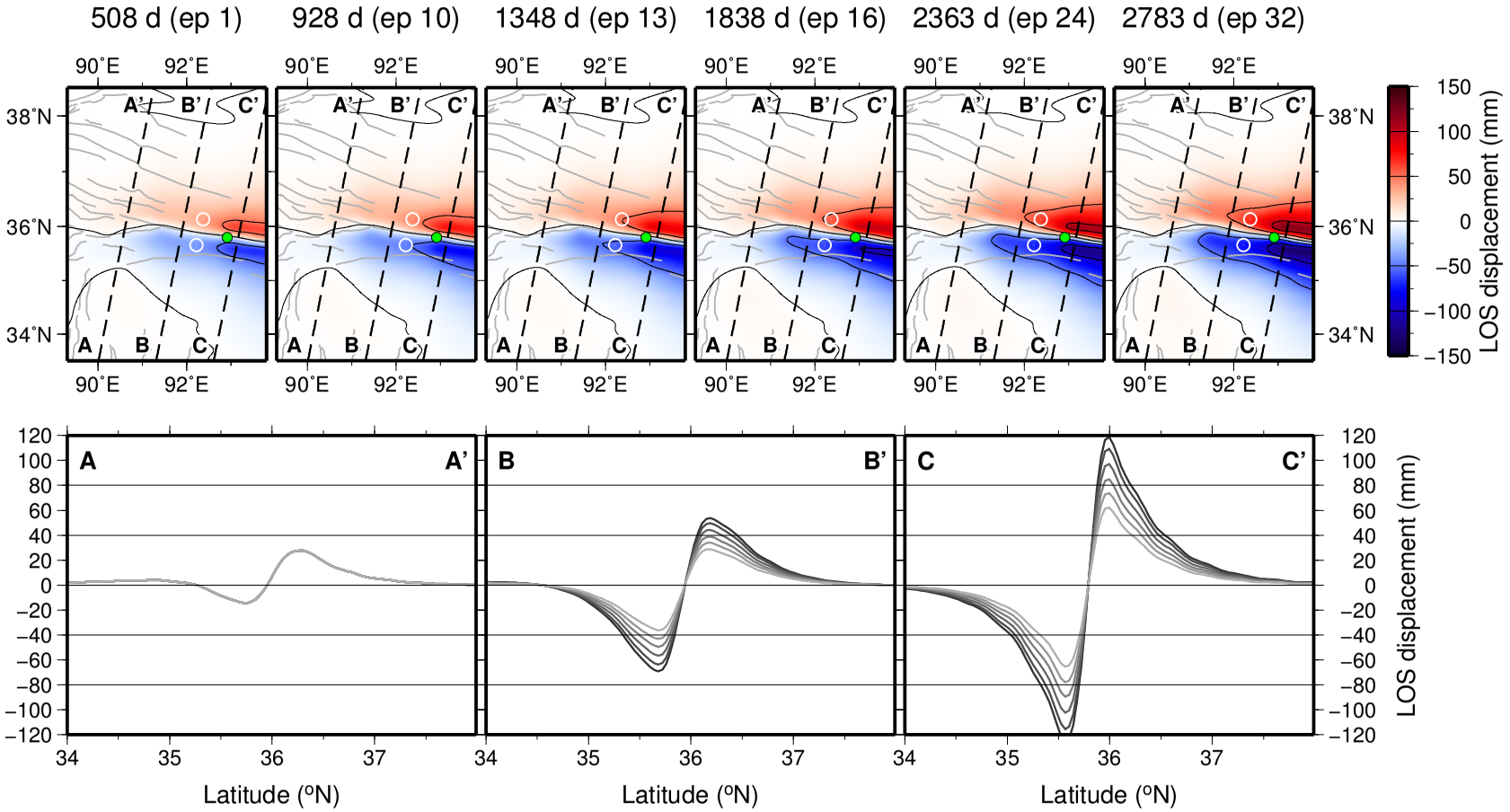

Figure 4.8: LOS postseismic deformation following the Kokoxili earthquake predicted by the 1D viscoelastic relaxation model of Ryder et al. (2011). Top row: Cumulative LOS displacements at six SAR epochs also labelled in terms of days following the earthquake. Green circle marks the earthquake epicentre. White circles show the pixels whose time series are plotted in Figure 4.9. Bottom row: Profiles A-A', B-B' and C-C' as marked in figures above. Each time step from the above figures is plotted in a different shade of grey. Note that in A-A' there is no time dependence to the signal as observed further east along the Kunlun fault.

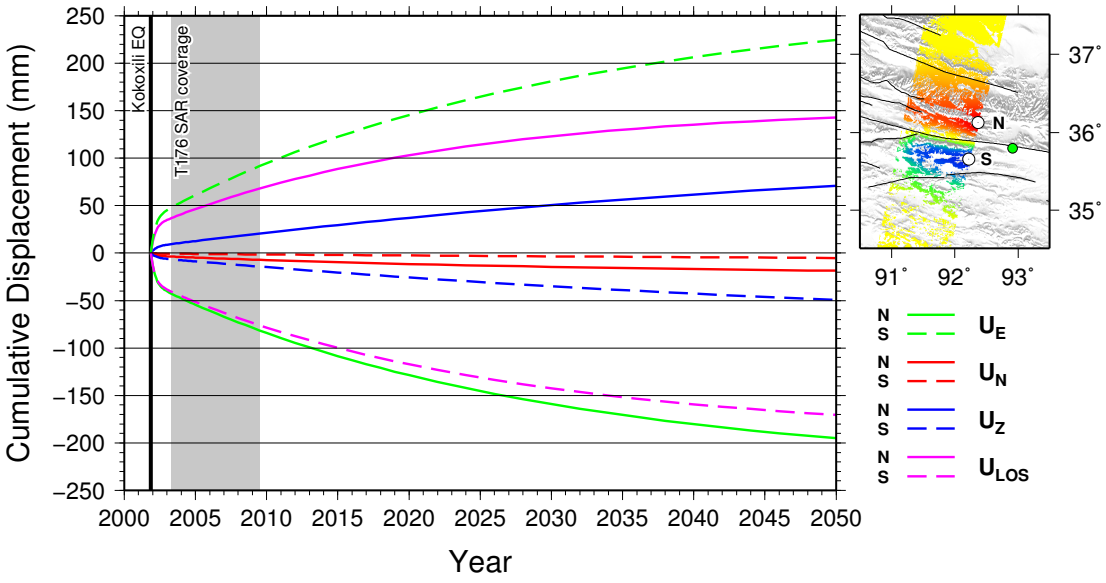

Figure 4.9: Time series of Kokoxili postseismic deformation from the 1D viscoelastic relaxation model of Ryder et al. (2011) as described in the text. East (U_E), north (U_N), up (U_Z) and LOS (U_{LOS}) components are displayed for two points within track 176 on the north (N) and south (S) sides of the Kunlun fault as shown by the location map on the right. The Kokoxili earthquake is marked as a black vertical line and the extent of track 176 SAR data used in this study is shown by the grey polygon. Significant viscoelastic relaxation is predicted to occur even 50 years following the earthquake.

crust and upper mantle (Figure 4.8). GPS data from the first year post-earthquake show a very rapid deformation rate which then gives way to a more gradual transient. Models with a Maxwell rheology under-predict the early rapid deformation but over-predict the later deformation, therefore Ryder et al. (2011) chose a bi-viscous Burgers rheology (see §1.4.3) and conducted a coarse search of the parameter space using GPS data covering the first year and 6 tracks of InSAR data covering the period between 2 and 5 years post-earthquake. A further fine grid search was performed only on the GPS data, which is located to the east of both track 176 and the earthquake epicentre. The best fitting model has a 16.5 km thick elastic layer, a 63.5 km thick viscoelastic layer, a transient (Kelvin) viscosity of $\eta_1 = 9\text{x}10^{17}$ Pa·s, a steady-state (Maxwell) viscosity of $\eta_2 = 1\text{x}10^{19}$ Pa·s and a ratio of long term to Maxwell shear moduli of 2:3.

Predictions of this model for the expected time series of surface movement for two pixels within track 176 are plotted in Figure 4.9. Following the first year of rapid transient deformation, the postseismic motion is relatively long wavelength and could be approximated as linear over the time period covered by SAR data in this study. The model predicts significant ongoing postseismic deformation rates as much as 50 years

after the earthquake occurrence, indicating the longevity of postseismic transients from large earthquakes.

4.4.1 Time series from π-*rate*

Time series analysis was applied to a spatial subset of the full interferograms surrounding the Kunlun fault in order to test the time series algorithms of π-*rate*. The results are compared to the 1D viscoelastic relaxation model of Ryder et al. (2011). Analysis was conducted on the full 70 interferogram network with quadratic orbital corrections and without the IDM. Figure 4.10 shows the time series results for 4 π-*rate* runs in which the time series method is either FDS or SVD, and spatio-temporal filtering to isolate the APS is either used or not.

The smoothing parameter of $\kappa = 0.04$ used in the FDS method gives a highly smoothed estimation of the time series. Smaller values of κ result in a time series with many high-amplitude fluctuations. Smoothing is not used in the SVD method and the resulting time series therefore exhibits fluctuations depending on the level of noise at each epoch. After first estimating and removing the APS, the time series is much smoother with both methods (i.e. less fluctuations; Figure 4.10a and b).

The time series from both methods with APS removed is broadly consistent (Figure 4.10c). Individual noisy epochs in the SVD time series cause divergence in the cumulative displacements from the two methods that can never be recovered throughout the remainder of the time series. By instead comparing the velocity at each epoch (Figures 4.10d and e), the noisy epochs can be easily determined and the consistency between the two methods can be appreciated.

In most cases shown in Figure 4.10, the time series on the southern side of the Kunlun fault gives a reasonable match to the 1D viscoelastic model. However, the time series for the northern side of the Kunlun fault consistently estimates much higher displacements than the viscoelastic model. This implies that there is a heterogeneity in properties between the north and south side of the Kunlun fault, which the 1D model cannot reproduce. Ryder et al. (2011) also notice an asymmetry in across fault geodetic data and surmise that viscosity variations between the lower crust of the Tibet and Qaidam basin must exist.

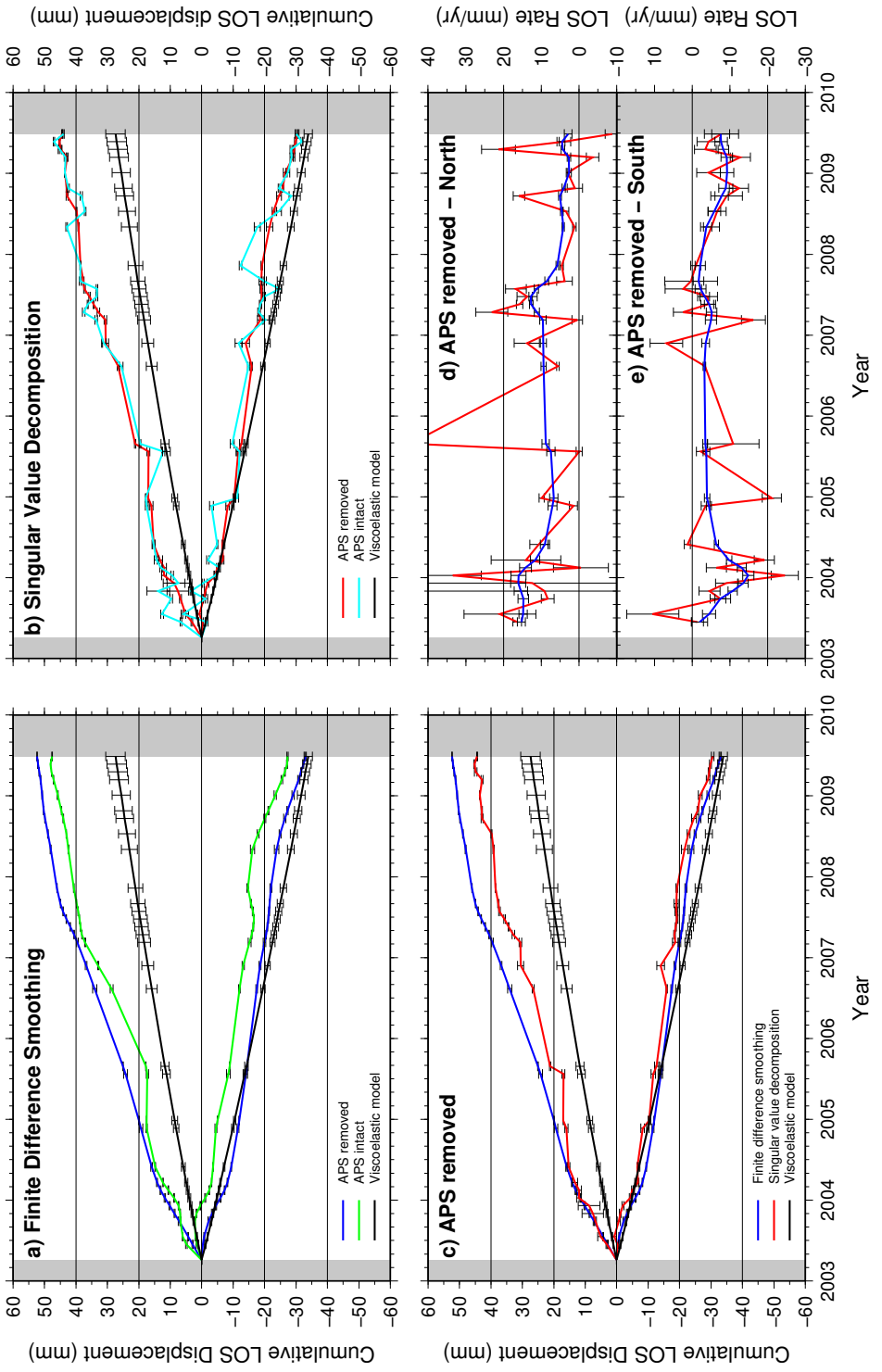

Figure 4.10: Results of time series analysis for two pixel windows north (positive displacements) and south (negative displacements) of the Kunlun fault. a), b) and c) show cumulative LOS displacements and d) and e) show LOS velocities. a) and b) compare the results before and after spatio-temporal smoothing for the FDS and SVD methods respectively. c), d) and e) compare the results of FDS and SVD methods after spatio-temporal smoothing. In a), b) and c) the black line is the prediction of the 1D viscoelastic model of Ryder et al. (2011). At each epoch the mean displacement/velocity is estimated within a 21x21 pixel window. 2-sigma error bars are plotted on this mean for each epoch.

4.5 Rate map across Tibet

Full scene rate maps were calculated after making quadratic orbital corrections using the network method, spatio-temporal filtering and using the IDM. The region north of the ATF was masked in order to avoid bias in the orbital correction. Many interferograms have poor coherence north of the fault, whilst others contain isolated patches of coherent phase (see Figure 4.5). Although the phase closure of these patches is zero it is possible that two interferograms in a loop contain erroneous jumps across this coherence discontinuity as a result of unwrapping errors. I chose to mask this region to avoid possible unwrapping errors adversely altering the orbital error corrections. Pixel size in the full rate maps is 1/120 degrees, which is approximately equal to 900-1000 m.

4.5.1 Rate map from stacking

As discussed in §3.1, many previous studies have looked at single faults and used a simple stacking procedure to determine the deformation rate on that fault. This method relies on the fact that deformation scales proportionally with time, whereas noise components do not and are essentially random. By adding together multiple interferograms to create an interferogram with a much longer time span the SNR is increased. Interferograms with a long temporal baseline, a short geometric baseline and perceived low atmospheric noise are best suited to the method, which relies on pixels remaining coherent in all interferograms. However, as the interferometric time span increases we expect an increasing number of pixels to become decorrelated (e.g. see Figure 4.4). To help maximise the number of pixels available for stacking, consistent spatial acquisition is required on each satellite pass. This has not been the situation with Envisat data coverage on Track 176 (see Figure 4.5), but the situation should improve with dedicated SAR missions planned for the future (§3.2.3).

Interferograms in the network of this study were constructed to maximise coherence, and consequently there are relatively few long time period interferograms, especially from 2007 onwards. Nevertheless, 9 interferograms with a cumulative time span of 9.49 years and good along track coherence were chosen from the full network for stacking

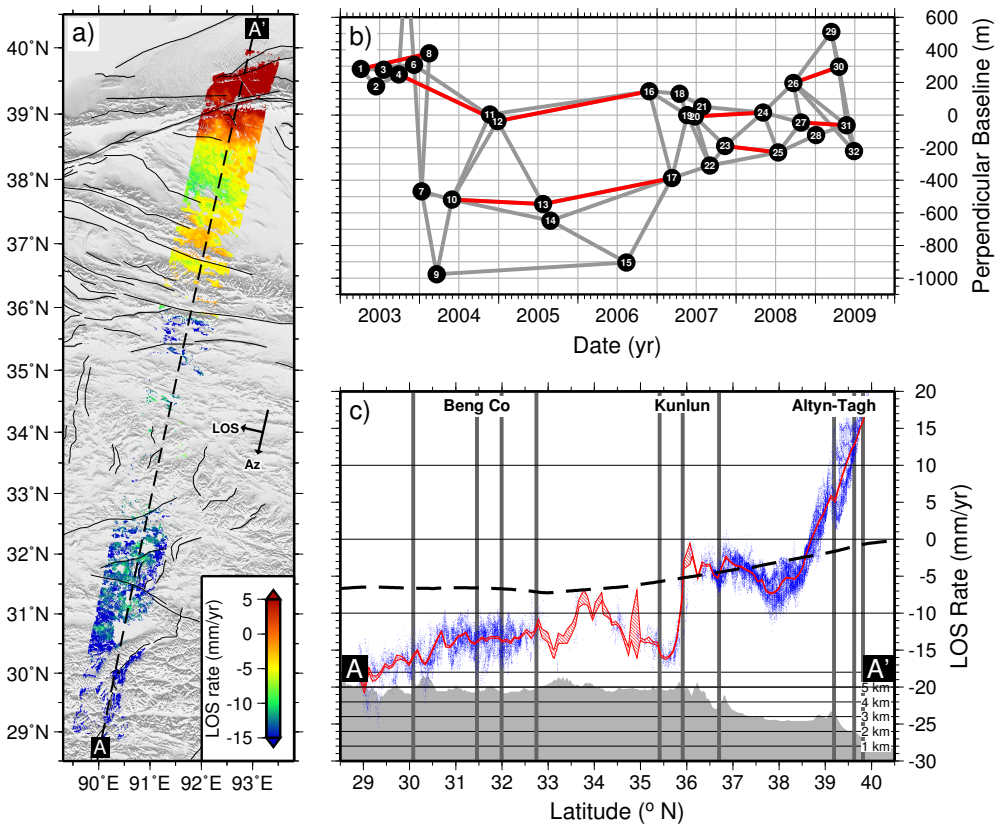

Figure 4.11: Results of simple stacking of 9 interferograms with a total duration of 9.49 years. a) LOS rate map. Dashed black line is the profile A-A' drawn in c). Solid black lines are active faults mapped by Taylor and Yin (2009). b) Baseline-time plot showing the interferograms used in the stack (red) from the 70 interferogram network (grey). c) Along-track profile (A-A') through the LOS rate map. All coherent pixels in the rate map are projected onto the profile and plotted as blue dots. Red polygon shows the 2-sigma error envelope on the mean LOS rate calculated within bins at 10 km intervals along the profile. Black dashed line is a profile through the IDM. Grey polygon shows the topography along the profile line. Locations of fault intersections with the profile line are marked by vertical grey lines.

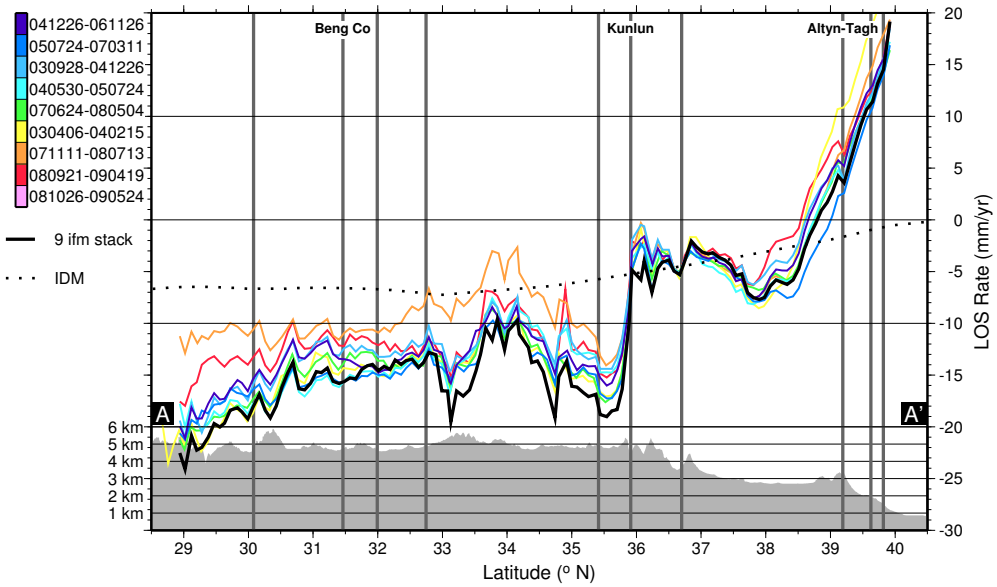

Figure 4.12: Variation of rate map profile when interferograms are excluded from the simple stack. Each coloured line is the mean LOS rate calculated at 10 km intervals along profile for stacks calculated from 8 of the 9 interferograms. The interferogram excluded in each case is indicated in the key to the upper left. The thicker black line is the 9-interferogram stacked profile from Figure 4.11c. Black dotted line is a profile through the IDM. Lower grey polygon shows the topography along the profile line. Locations of major faults or shear zones are marked by vertical grey lines.

(Fig. 4.11b). The LOS rate at each pixel k for a set of N interferograms is then:

$$v_k = \frac{\sum_{n=1}^{N} \phi_n}{\sum_{n=1}^{N} t_n} \tag{4.1}$$

If any of the phase observations are incoherent, that pixel is not included in the rate map. Figure 4.11 shows the results of stacking the 9 chosen interferograms. In this case, the full network was used, quadratic orbital corrections were made and the IDM was used to preserve long wavelength deformation.

One problem with the simple stacking technique is that any one interferogram may adversely bias the rate map as the spatially correlated atmospheric errors in the interferograms are not explicitly considered. To test the robustness of the stacked rate map, I calculate a series of rate maps and compare them in profile form (Figure 4.12). A jack-knifing technique is used, in which one interferogram is excluded from the stack in each profile. This way it can be seen if any individual interferogram biases the re-

sult. Figure 4.12 shows that most of the stacks give a consistent result in this case, but the inclusion of the interferogram 071111-080713 in the stack appears to cause the deviation away from the IDM in the southern part of the rate map.

4.5.2 Rate map from *π-rate*

As discussed in §3.3.10, the method of rate map construction in *π-rate* attempts to provide robust estimates of the rate by including pixels that are not coherent in all interferograms and weighting the inversion using the data covariance. Pixels with high uncertainty are not included in the final rate map.

Figure 4.13 shows *π-rate* rate maps for the 31 and 70 interferogram networks with their associated error map and an along-track profile. In the profiles, all pixels in the rate map are projected onto the profile running through the centre of the scene. Large across-track variation results in a reasonable scatter within the point cloud. The rate maps and profiles show a consistent result over most of the scene. The advantage of using a larger network is proved by the reduced uncertainties shown in some regions of the error map of the 70 compared to the 31 interferogram network. Furthermore, although not immediately obvious in the plotted maps, the number of pixels in the 70 interferogram rate map is greater than in the 31 interferogram rate map.

Compared with the rate map from simple stacking, the rate maps contain many more pixels in the centre of the scene between 32°N and 36°N. However, south of lake Nam Co the number of pixels is less. This demonstrates the advantage of bringing in information from additional interferograms to constrain the rate in the centre of the scene, but also removing pixels in the south where the uncertainty is too high. Despite this the three rate-maps show consistent long-wavelength variation over the central part of the scene (Figure 4.14). However, significant deviations occur at the northern end of the scene across the ATF, and south of $\sim$ 34°N.

The most prominent feature in all of the rate maps is the steep velocity gradient across the Kunlun fault of 10-12 mm/yr magnitude in LOS. Since we are aware of the postseismic deformation ongoing around this fault, we know this velocity gradient represents the average deformation of the postseismic transient over the 6.25 year observation period. This signal can be removed using the model of Ryder et al. (2011) described in §4.4.

To do this I obtained the cumulative postseismic displacement for each SAR epoch

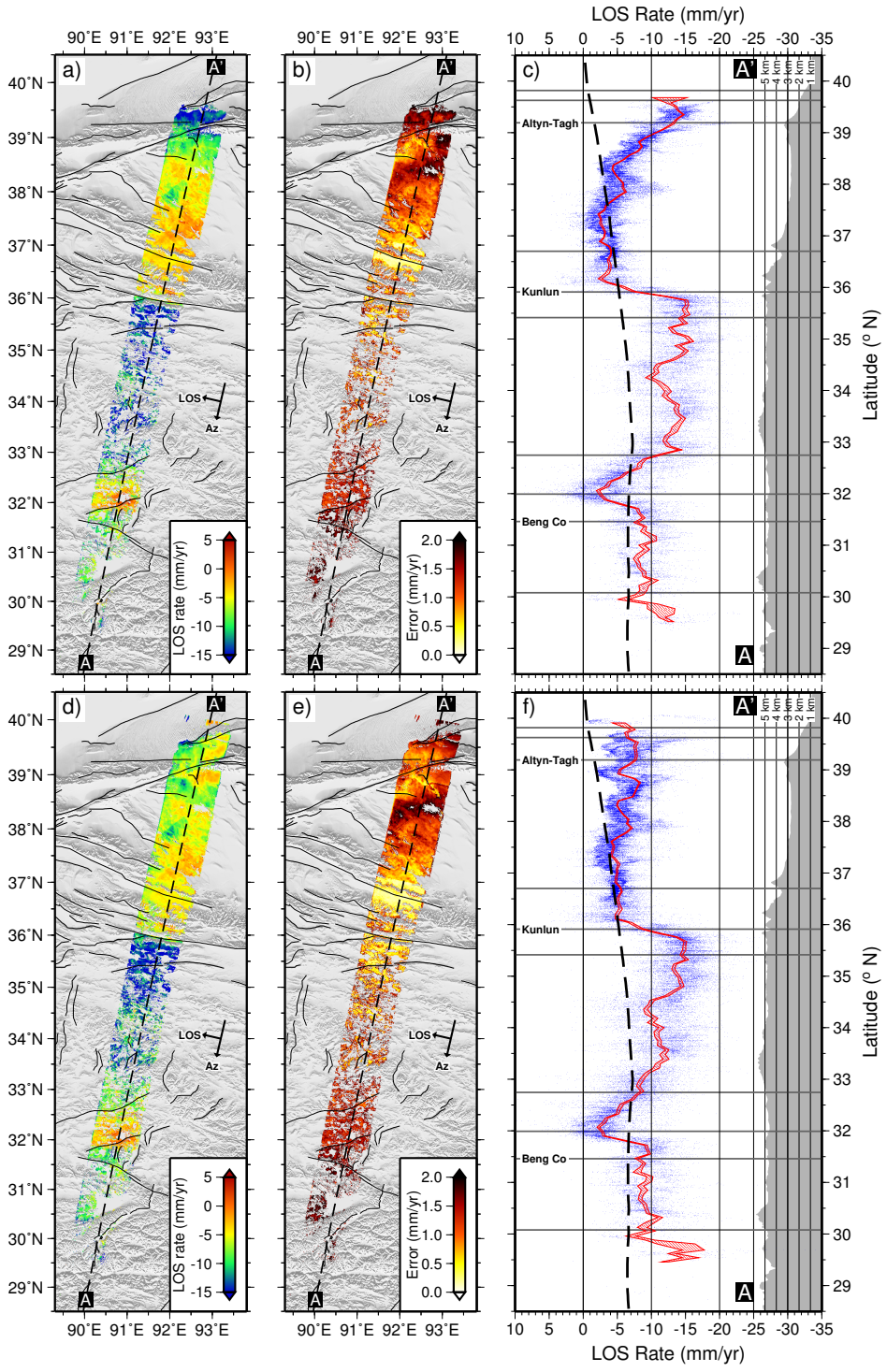

Figure 4.13: *π-rate* derived linear rate maps for 31 interferogram network (a, b, c) and 70 interferogram network (d, e, f). a,d) LOS rate maps in millimetres per year. Dashed black line is the profile A-A' drawn in c,f). Solid black lines are active faults mapped by Taylor and Yin (2009). b,e) Associated error maps with same comments as the LOS rate maps. c,f) Along-track profile (A-A') through the LOS rate map. Coherent pixels are projected onto the profile line and plotted as blue points. Red polygon shows the 2-sigma error envelope on the mean LOS rate calculated within 10 km bins along the profile. Black dashed line is a profile through the IDM. Grey polygon shows the topography along the profile line. Locations of major faults or shear zones are marked by vertical grey lines.

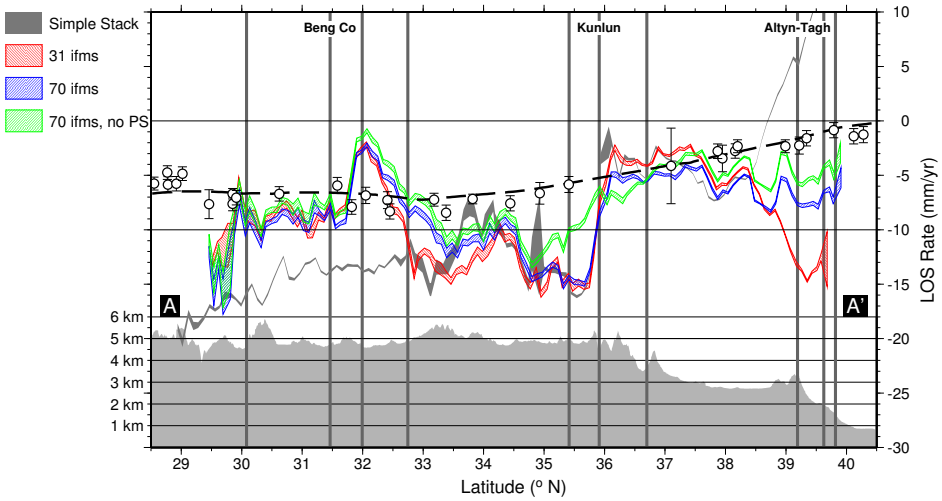

Figure 4.14: Comparison of rate map profiles. Grey polygon shows the 2-sigma error envelope on the mean LOS rate for the 9 interferogram stack (plotted in Figure 4.11). Red and blue polygons show the 2-sigma error envelope on the mean LOS rate for the 31 and 70 interferogram networks respectively (plotted in Figures 4.13c and f). Green polygon is the 2-sigma error envelope on the mean LOS rate for the 70 interferogram network following removal of the postseismic model (Figure 4.15c). White circles are GPS velocities converted into LOS and projected on to the profile. Black dashed line is a profile through the IDM. Topographic profile at the base of the plot. Locations of major faults or shear zones are marked by vertical grey lines.

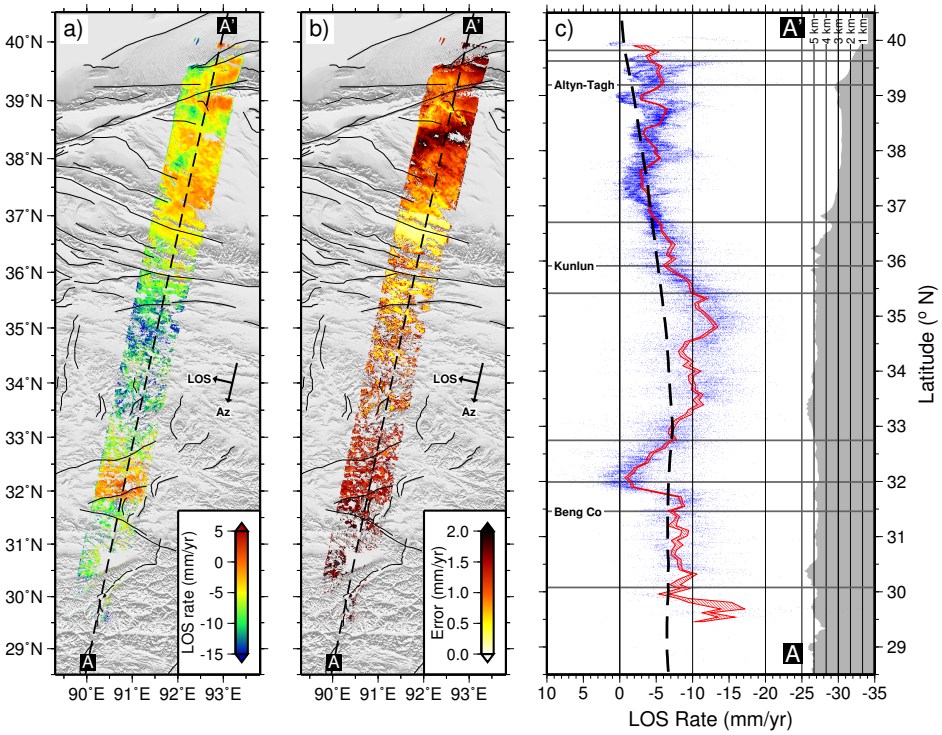

Figure 4.15: *π-rate* derived linear rate map for the 70 interferogram network following postseismic correction. Other details are the same as in Figure 4.13.

of data used at the full resolution of the interferograms using the VISCO1D code (Pollitz, 1992, 1997) and the model input of Ryder et al. (2011). I then used these displacement time-steps to construct postseismic corrections for each interferogram, which were subtracted prior to the IDM in the π-*rate* work-flow (see Figure 3.5).

The resulting rate map for the 70 interferogram network after this postseismic correction is shown in Figure 4.15. The effect of removing the postseismic signal is not only to remove the steep velocity gradient on the Kunlun fault, but to increase the rate across the entire scene by ∼1-2 mm/yr. This is due to a change in the value of phase at the reference pixel in each interferogram that is then subtracted during the orbital correction.

The rate map (Figure 4.15) shows a smoothly varying long wavelength velocity field across the Tibetan plateau with a LOS variation of between 20-25 mm/yr along the length of the scene. The negative polarity of LOS rate for the majority of pixels indicates motion towards the satellite, which could be interpreted using a combination of horizontal and vertical movements. The rate maps are referenced to the IDM, but show deviation from the IDM in the central portion of the track between the CTCFZ and the Kunlun fault. Either the central section of the plateau moves faster towards the satellite than the regions immediately to the north and south, or the deviation is a result of the fact that the LOS IDM does not contain the vertical component of motion.

The LOS signal V_{LOS} can be transformed into horizontal V_{Horz} and vertical V_{Vert} components using the following relations:

$$V_{\mathrm{Horz}} = V_{\mathrm{LOS}}/sin\theta \tag{4.2a}$$

$$V_{\mathrm{Vert}} = V_{\mathrm{LOS}}/cos\theta \tag{4.2b}$$

where θ is the LOS incidence angle; ∼19-27° for Envisat in swath mode IS2. For the middle in the incidence angle range ($\theta = 23°$), $V_{\mathrm{Horz}} = 2.6$ and $V_{\mathrm{Vert}} = 1.1$ when $V_{\mathrm{LOS}} = 1.0$. Therefore the contribution of horizontal motion to the overall LOS signal is over a factor of 2 less than for vertical motion. For example, the maximum difference between the IDM and InSAR profiles (∼8 mm/yr at 35°N) corresponds to a horizontal motion of ∼20.5 mm/yr or a vertical motion of ∼8.7 mm/yr. In the context of present day Tibetan deformation, large scale eastern movement is perhaps more realistic than

large-scale uplift. Through summation of seismic moments for earthquakes occurring in the Tibetan plateau, Elliott et al. (2010) find that normal faulting accommodates ∼20% of the total extensional strain with strike-slip faulting accounting for the rest. However, localised uplift may occur in the foot-walls of the abundant normal faults in the central plateau. The observed 8 mm/yr maximum deviation of InSAR and IDM is therefore most likely to result from a combination of faster (than the IDM) eastward motion and a smaller component of uplift, which is not measured using GPS.

Two steep velocity gradients can be seen in the profile of the corrected rate map. The first of these at ∼34.5°N does not occur on a mapped structure. In fact, this region is devoid of any mapped strike-slip faults. The rate map profile shows a change of ∼5 mm/yr in LOS with a right-lateral sense of horizontal movement. The second steep velocity gradient is at 32°N within the CTCFZ, across the southernmost of two north-east trending strike-slip faults. The rate map profile shows a change of 5-7 mm/yr in LOS with a left-lateral sense of horizontal movement.

4.5.3 Performance of *π-rate*

Table 4.2 summarises the mean deformation rate at eleven locations along-profile for the 70-interferogram *π-rate* profiles (with and without postseismic correction) and the 9-interferogram stacked profile. Furthermore, these rates are each differenced from the rate of the IDM at each location and the overall RMS difference for the three profiles is calculated. It shows that the *π-rate* method performs significantly better than the simple stacking method by nearly halving the RMS difference. Additionally, removing the postseismic signal from the data further improves the overall RMS when using *π-rate*.

4.5.4 Individual fault profiles

Other than the long wavelength deformation, also of interest is the signal around individual faults. As noted in §4.1 and Table 4.1, many studies have found velocity gradients surrounding mapped strike-slip faults in Tibet. Plotted in Figure 4.16 are profiles perpendicular to mapped strike-slip faults from the corrected rate map of Figure 4.15. Observed LOS velocities are converted to fault parallel velocities assuming

Table 4.2: Comparison of measured deformation rates along the InSAR profile in mm/yr. The IDM profile is used for comparison since it is calculated by interpolating over the unevenly distributed GPS points across the plateau. Figure 4.14 shows the good correspondence between the interpolated IDM and GPS points along the profile. Regular typed values are the observed rate at each location along profile, spaced one latitude degree apart. The bold values give the difference after subtracting the IDM rate in each case. The right-hand column gives the single RMS value for the differences from all eleven locations.

Latitude (°N)	29	30	31	32	33	34	35	36	37	38	39	RMS (mm/yr)
IDM (GPS profile)	-6.48	-6.66	-6.57	-6.7	-7.24	-6.73	-6.11	-5.14	-4.15	-3.07	-1.91	
π-*rate* 70 ifms	-4.17	-7.8	-9.34	-2.7	-8.64	-11.45	-13.97	-7.4	-4.99	-6.58	-5.32	
	2.31	**-1.14**	**-2.77**	**4.01**	**-1.4**	**-4.72**	**-7.86**	**-2.25**	**-0.84**	**-3.51**	**-3.42**	**3.65**
π-*rate* 70 ifms	-3.15	-6.97	-8.56	-1.42	-7.29	-10.71	-12	-7.11	-4.11	-4.98	-2.92	
no postseismic	**3.34**	**-0.3**	**-1.99**	**5.29**	**-0.05**	**-3.98**	**-5.89**	**-1.96**	**0.04**	**-1.91**	**-1.02**	**3.05**
Simple stack	-20.1	-16.89	-13.59	-13.81	-13.39	-9.78	-13.53	-2.28	-3.34	-6.58	4.07	
(9 ifms)	**-13.61**	**-10.23**	**-7.02**	**-7.1**	**-6.15**	**-3.04**	**-7.42**	**2.87**	**0.81**	**-3.51**	**5.98**	**7.06**

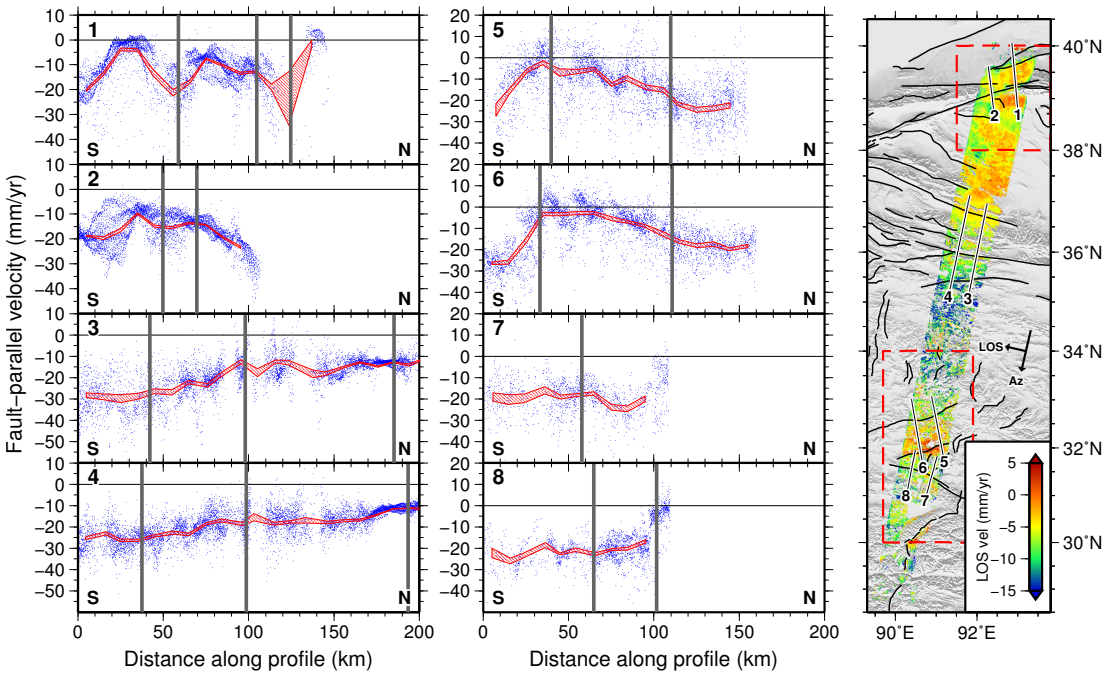

Figure 4.16: Profiles of fault parallel velocity for strike-slip faults in track 176 converted from LOS velocities using the relationship defined in Eq. 4.3. Profile locations are shown on the plotted LOS rate map. Blue pixels are those within 20 km either side of the profile line. Red envelope is the 2-sigma error on the average rate calculated in 10 km bins along profile. Negative deviations indicate presumed easterly movement. Grey vertical lines show the locations of mapped faults from Taylor and Yin (2009). Red dashed boxes show the locations of subset analyses in Figures 4.17 and 4.18.

purely horizontal motion via the following relationship:

$$V_{\text{fault}} = V_{\text{LOS}}/(sin\theta \cdot cos(\phi - f_{\text{az}})) \tag{4.3}$$

where ϕ is the horizontal azimuth of the looking vector and f_{az} is the azimuth of the fault.

Profiles 1 and 2 cross the ATF between 92 and 93°E. Profile 1 shows a symmetrical signal across the ATF, with large magnitude, which must be an atmospheric artefact. Profile 2 shows virtually no variation across the fault. From the results of previous studies (§4.1), a steep velocity gradient is expected across the ATF. However the full rate map does not show this.

Profiles 3 and 4 cross the Kunlun fault and 2 parallel faults to the north and south. Both profiles show a smoothly varying gradient across the fault system. The velocity does not vary north of the fault and decreases linearly immediately south of the fault with a gradient of 0.1-0.15 mm/yr/km. By correcting for postseismic deformation the arc-tangent velocity function has been wholly removed yet a linear trend remains.

Profiles 5 and 6 cross two of the north-east trending left-lateral strike-slip faults of the CTCFZ, inferred by Taylor and Yin (2009). The profiles indicate a significant velocity gradient near the southern of these two faults, with a left-lateral sense of motion. The change in fault-parallel velocity across the fault is in the region of 20 mm/yr. The northern fault does not exhibit any change in velocity gradient. North of the southern fault, velocities decrease with a gradient in the region of 0.1-0.2 mm/yr/km. The location of steepest velocity gradient does not entirely coincide with the surface trace of the fault as might be expected for active strike-slip faults. Furthermore, no earthquakes have occurred recently in the location of the steep velocity gradient (Figure 4.6) therefore it seems unlikely that this signal is tectonic in origin.

Since the fault in question is part of a conjugate system, we might expect a similar magnitude but opposite polarity signal on the paired fault structure. In this case, that structure is the south-east trending right-lateral Beng Co fault to the south. Profiles 7 and 8 cross this fault and show no such signal, with velocity remaining constant across the fault.

A profile through the sum of the coherence masks (Figure 4.5) indicates coverage discontinuities at the location of the steep gradients at 32°N and 34.5°N. It could be that the variation in along-track coverage adversely affects the rate inversion, resulting

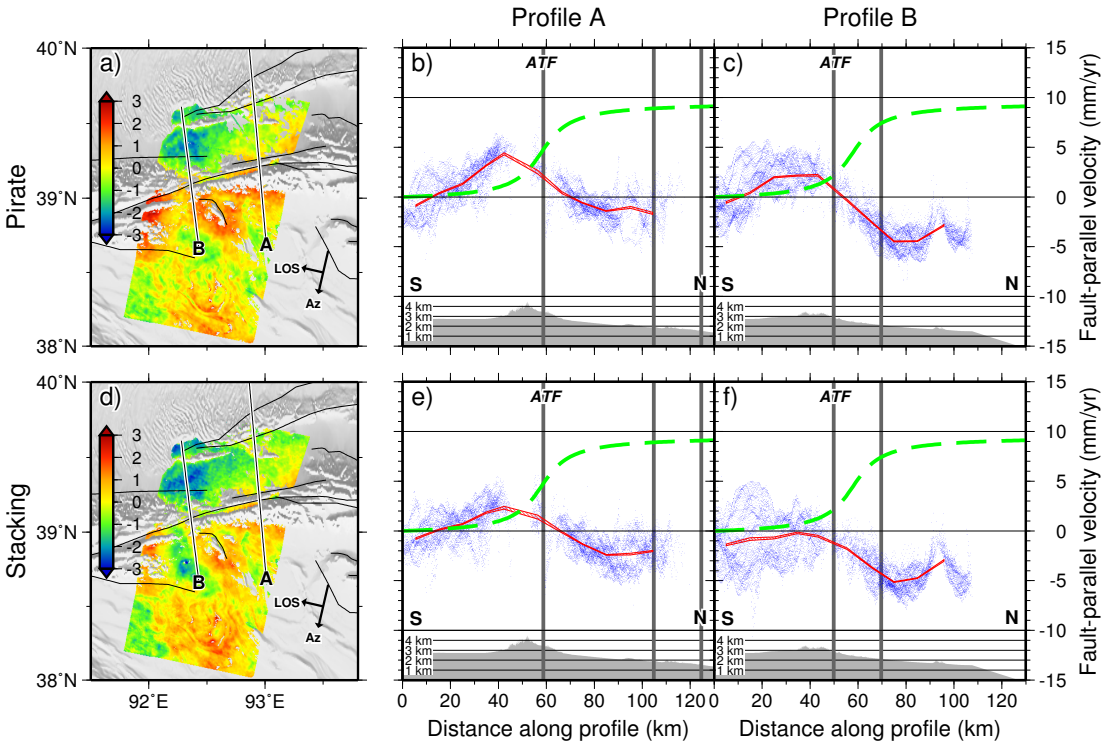

Figure 4.17: LOS rate maps across the Altyn Tagh fault from a) π-*rate* and d) stacking from a subset of the full interferograms. Details of analysis is given in the text. Fault-parallel velocity profiles A and B converted from LOS using Eq. 4.3 for the π-*rate* (b, c) and stacked e, f) rate maps. Blue pixels are those within 20 km either side of the profile line. Red envelope is the 2-sigma error on the average of these pixels calculated in 10 km bins along profile. The main strand of the Altyn Tagh fault is labelled 'ATF' in each profile. Green dashed lines show an indicative interseismic velocity profile calculated using the screw dislocation model with a locking depth of 9 km and slip rate of 10 km.

in very different estimates for adjacent pixels across the discontinuity. In order to confirm the origin of the steep velocity gradient in the CTCFZ and the lack of gradient at the ATF, a smaller area was extracted from the full scene and re-analysed using a network of interferograms that cover the entire sub-scene. The results are described in §4.6 for the ATF and §4.7 for the CTCFZ.

4.6 Altyn Tagh fault rate map

Approximately two frames of data were extracted from the full interferograms around the ATF between 38-40°N. 58 interferograms from the full 70 had good coherence across the scene. These interferograms span 30 individual epochs. Quadratic orbital errors were estimated using the network method with no masking or IDM and spatio-temporal filtering was used with the default parameters. Pixel size is 1/240 degrees, which is

approximately equal to 450-500 m. Rate maps were evaluated using both the *π-rate* algorithm and simple stacking. Due to the good coherence of the interferograms, the *π-rate* parameter Ψ was set at a relatively high value of 29. All 58 interferograms were used in the simple stacking, giving a total stack length of ∼30.5 years.

The two resulting LOS rate maps are remarkably consistent (Figures 4.17a and d). The good coherence throughout the interferograms means that most pixels are present in both rate maps. In profiles A and B (Figures 4.17b, e and c, f respectively), the LOS velocity has been converted to fault-parallel velocity using the relationship in Eq. 4.3. The calculated values of RMS difference between the stacked and *π-rate* mean profiles are 1.1 mm/yr for A and 1.7 mm/yr for B. These relatively low RMS values indicate the close similarity between the methods when temporal and spatial SAR data coverage is good. The profiles indicate a change in velocity of 4-7 mm/yr with a negative gradient across the ATF from south to north. Since easterly movement is still negative in polarity, this implies a right-lateral sense of strike-slip motion, which is at odds with the tectonic expectation of left-lateral slip.

Using SAR data from the ERS satellite two tracks to the east (T133), Jolivet et al. (2008) constrain a fault model with a locking depth of 7-9 km and a left-lateral slip rate of 8-10 mm/yr. An interseismic velocity profile from a screw dislocation model (Savage and Burford, 1973) with these parameters is plotted in Figure 4.17 for comparison, and is not remotely fitted by the data.

Although the shape of the profiles could be consistent with a typical interseismic arc-tangent function, it can also be seen to follow the trend of profile-coincident topography. In particular, positive deflections occur around localised topographic ranges. The topographic phase correction algorithm of *π-rate* (§3.3.5) was run on the data but did not significantly change the results shown in Figure 4.17.

If the data presented here is to be believed, then the ATF is found to slip at around 4-6 mm/yr with a right-lateral sense of motion. More likely is that this signal is an uncorrected topographically correlated atmospheric artefact that has not been removed by the spatio-temporal filter. Use of *a-priori* atmospheric data to correct interferograms may help to improve the estimates of tectonic deformation across the ATF with this data (e.g. by using the methods of Li et al., 2009d, von Allmen et al., 2010, Jolivet et al., 2011).

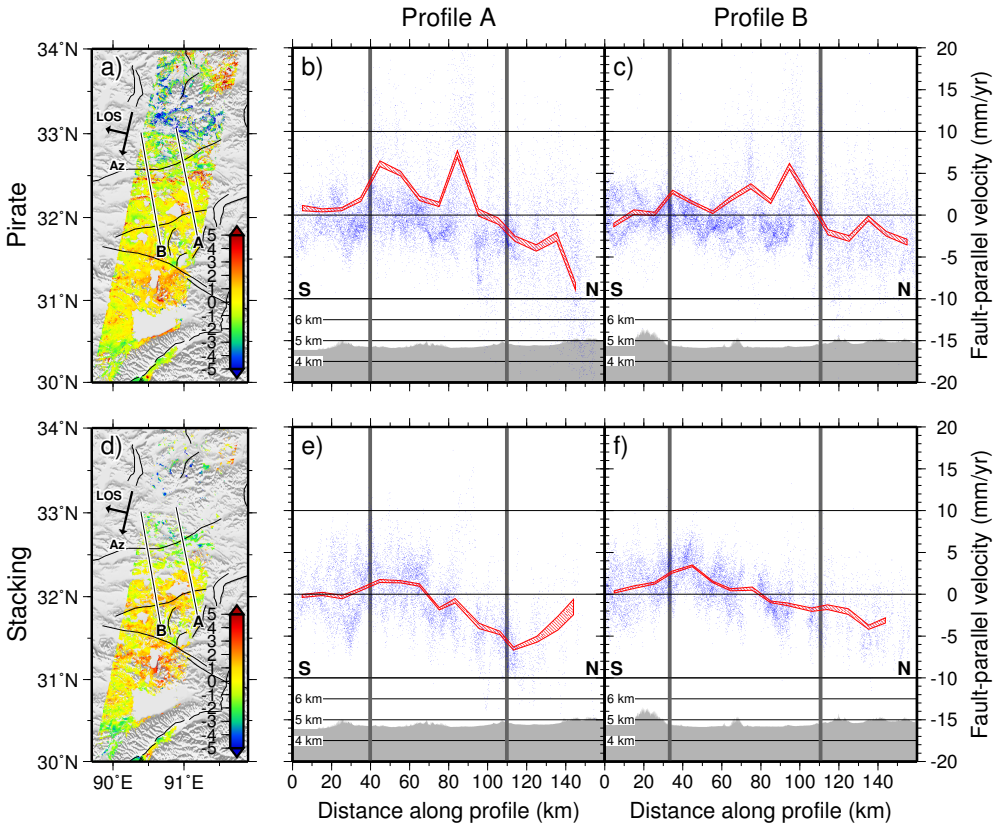

Figure 4.18: LOS rate maps across the CTCFZ from a) *π-rate* and d) stacking from a subset of the full interferograms. Details of analysis is given in the text. Fault-parallel velocity profiles A and B converted from LOS using Eq. 4.3 for the *π-rate* (b, c) and stacked e, f) rate maps. Blue pixels are those within 20 km either side of the profile line. Red envelope is the 2-sigma error on the average rate calculated in 10 km bins along profile. Easterly movement is negative in polarity.

4.7 Central Tibet conjugate fault zone rate map

A region of approximately 4 SAR frames in length (∼400 km) was extracted from the full interferograms around the CTCFZ between 30-34°N. 60 interferograms from the full 70 have full coverage of the scene, but with variable coherence. The interferograms span 30 individual epochs. Quadratic orbital errors were estimated using the network method with no masking or IDM and spatio-temporal filtering was used with the default parameters. Pixel size in the full rate maps is 1/240 degrees, which is approximately equal to 450-500 m. Due to variable coherence of the interferograms, the *π-rate* parameter Ψ was set at a value of 20, whilst all 58 interferograms were used in the simple stacking.

The two resulting LOS rate maps are broadly similar (Figures 4.17a and d). The

northern quarter of the region has particularly poor coherence, and as a result the rate map from stacking contains very few pixels. The π-*rate* rate map has many more pixels in this region, but the scatter is high. Crucially, neither rate map reveals a large gradient across the southern of the two north-easterly trending strike-slip faults as seen in the full rate map (Figure 4.15). Although the phase is patchy, the signal magnitude varies only about 2 mm/yr LOS across the rate map.

Profiles A and B (Figures 4.18b, e and c, f respectively) show the trend of fault-parallel velocity across the two north-easterly trending faults of the CTCFZ. The calculated values of RMS difference between the stacked and π-*rate* mean profiles are 3.3 mm/yr for A and 2.7 mm/yr for B. The results from the two methods are less similar than for the ATF subset, presumably because there are comparably less coherent pixels in this region. Despite the scatter in the point cloud, a low negative gradient can be seen, with a magnitude variation of 5-7 mm/yr. A positive gradient of 2-3 mm/yr can be seen in the two stacked profiles across the southern of the two faults. However, this is not evident on the π-*rate* determined profiles.

The results of Figure 4.18 suggest that faults of the CTCFZ have slip rates that are too low to be detectable by InSAR with the currently available data. The data do not agree with the relatively high slip rate estimates for similar faults in the CTCFZ system to the west by Taylor and Peltzer (2006).

4.8 Summary

This study has shown that investigating interseismic deformation over large areas with InSAR is a challenging endeavour at present, given the current archive of SAR data over inhospitable environments such as the Tibetan plateau. I have produced a ~1000 km-long InSAR rate map which reveals smooth variability of deformation across the Tibetan plateau. A significant long wavelength deviation from the IDM occurs in the centre of the scene between 32-36°N, approximately bounded by the CTCFZ and Kunlun fault. This deviation could be interpreted as up to ~20 mm/yr of increased eastward motion (relative to stable Eurasia) or ~8 mm/yr of vertical uplift, although an unknown combination of vertical and horizontal motion is most likely. Interpreting the deviation as predominantly east-west motion is compatible with the mapped motion on the Kunlun and Jiali fault systems and with the overall sense of displacement in the more complex CTCFZ.

Mapped fault zones do not tend to show the steep velocity gradients characteristic of some locked faults with high slip-rates (e.g. the San Andreas fault or the North Anatolian Fault). Velocity gradients with a magnitude of even 10 mm/yr would be obvious above the levels of noise in the data. One exception is the Kunlun fault upon which occurred a large strike-slip earthquake in 2001, prior to the SAR data used here. The resulting postseismic signal manifests in the rate map as an abrupt velocity discontinuity, which could be mistaken for a steady-state interseismic signal. Time series analysis of this signal suggests that the postseismic model of Ryder et al. (2011) underestimates the transient deformation following the earthquake on the north side of the Kunlun fault. Nevertheless, this model is used to correct interferograms and presumably leave behind interseismic deformation signals. Following postseismic correction, the rate map shows a very smooth velocity gradient across the Kunlun fault as seen across the rest of the rate map.

Using a spatial subset of the data, a right-lateral slip rate of ∼5 mm/yr is found for the ATF. This unrealistic slip rate is most likely due to uncorrected topographically correlated atmospheric phase delay signals that the current π-*rate* algorithms can not correct. However, relatively high left-lateral slip rates found by other studies are not supported by the data. Another spatial subset or data shows no significant changes in velocity gradient across strike-slip faults in the CTCFZ.

Large velocity gradients seen at 32°N and 34.5°N in the full π-*rate* rate maps seem to be related to the variable along-track coverage of the interferograms used in the network. When the interferograms that contain this discontinuity are excluded from the analysis (e.g. in the subset over the CTCFZ, and in the stacked full rate map) the observed steep velocity gradients disappear. Using data with full coverage over the region of interest is therefore essential for studies over large areas in order to avoid potentially misleading results.

The power of the π-*rate* method lies in incorporating interferometric observations from a larger data network in order to increase the number of pixels in the rate map, whilst also screening for noisy observations that can degenerate the rate estimates. The number of pixels in the full rate map is significantly improved when using π-*rate* compared with the simple stacking approach. When comparing the full rate maps produced using π-*rate* and the simple stacking methods with the smoothed GPS horizontal deformation field (IDM) in the Tibetan plateau, I find RMS differences of 3.65 mm/yr

and 7.06 mm/yr for π-*rate* and stacking respectively. Therefore, π-*rate* offers a considerable advantage over stacking when conditions are challenging for measuring slow deformation signals with InSAR.

Chapter 5

The Thin Viscous Sheet approximation for continental collision

As discussed in §2.6.3, one description of continental deformation involves representing the lithosphere as a viscous fluid which deforms continuously in response to the balance between lateral and gravitational forces over geological time. A commonly used approximation to full 3-dimensional (3D) continuum deformation is known as the 'Thin Viscous Sheet' (TVS). In this Chapter, I first outline the TVS concept and its development (§5.1). Then I describe the governing equations (§5.2) and the finite element method used in their solution (§5.3). Finally I present a comparison between results of the 2-dimensional (2D) TVS model and a fully 3D model (§5.4). The work in §5.4 has been published (Garthwaite and Houseman, 2011).

5.1 Development of the thin viscous sheet concept

Bird and Piper (1980) were the first to use a TVS to study geodynamic problems. Using a 2D formulation, they applied the finite element method to model the crust of the southern Californian transform boundary as a thin layer within which horizontal flow velocities are invariant with depth and upon which the mantle imparts no shear tractions. England and McKenzie (1982, 1983) applied this concept directly to the continental collision problem and incorporated the major gravitational buoyancy forces arising from crustal thickness variations. Indentation of the TVS was represented by a velocity boundary condition on the periphery of the sheet and the system of equations

solved using a finite-difference method. They used a depth-averaged rheological model for the layer to describe the deformation of broad regions whose horizontal dimension D is much greater than the layer thickness L (i.e. $D >> L$).

Sonder and England (1986) demonstrate that the vertically averaged rheology of the lithosphere can be well approximated by a single power law relationship under conditions of vertically coherent deformation and strain rates between 10^{-13} and 10^{-17} s^{-1}. Thus, the average mechanical behaviour of the lithosphere can be described by only two parameters: the power-law exponent n of the viscous constitutive law, and the Argand number Ar. The Argand number describes the impact of buoyancy forces on deformation relative to the viscous stresses imparted by the horizontal boundary conditions. For greater Argand numbers, crustal thickness variations produce greater internal stresses, and consequently the formation of a topographic plateau and thickened crust adjacent to the indenter is resisted. However, if the Argand number is sufficiently small and erosion is negligible, very large crustal thicknesses can be attained (England and McKenzie, 1982).

England and McKenzie (1982) found that the horizontal length scale of deformation decays with increasing n. England et al. (1985) examined this dependence using analytical and approximate solutions to the TVS equations for a range of n. They quantified the decay length-scale as approximately $\frac{1}{\sqrt{n}}$ times the boundary condition wavelength for convergent regimes and $\frac{1}{4\sqrt{n}}$ for strike-slip regimes.

Houseman and England (1986) refined the method for solving the TVS governing equations using the finite element method and the addition of deforming model boundaries. Further studies applied this method to describe aspects of the observed deformation in the India-Asia collision zone (see §2.6.3).

One shortcoming of the TVS approximation is that strain rates are assumed constant with depth. As a result, shortening processes such as folding or thrusting are not explicitly represented. However, this approximation is valid for very broad-scale deformation providing that gradients of crustal thickness are small. Other models, as discussed in §2.6, have been proposed to address the different styles of localised deformation phenomena expected within the collision problem.

Medvedev and Podladchikov (1999) define the England and McKenzie (1982) TVS formulation as a 'pure shear' approach, and go on to summarise other TVS formulations that may be applied to geodynamic problems. In the 'simple shear' approach,

deformation is driven solely by shear tractions which act on the base of the layer. With this condition, buoyancy forces are balanced against basal shear stress and velocity can vary with depth in the model. Ellis et al. (1995) compared pure and simple shear TVS models for oblique convergence. They found that for pure shear models the deformation length scale depends on the length scale of the applied velocity boundary condition, whereas in basally driven models it depends on the degree of crust-mantle coupling. However, Ellis et al. (1995) conclude that both models are capable of reproducing the deformation observed in the India-Asia collision. On a global-scale, Ghosh et al. (2008) find that shear tractions imparted on the base of a thin sheet by density-driven mantle circulation are required to reproduce the present day deviatoric stress field in the presence of known topography. Therefore at very large length scales, basal shear is likely to be an important component of the force balance. Medvedev and Podladchikov (1999) added sub-horizontal rheological layering to the TVS approximation whilst also allowing simultaneous application of velocity or traction conditions to all external model boundaries. This extended TVS formulation allows for more accurate description of 3D deformation (such as folding) whilst maintaining the efficient computation of the 2D formulation.

Despite recent developments, the classic pure shear 2D TVS formulation continues to be widely used for modelling tectonic deformation (e.g. Robl and Stüwe, 2005a,b, Wang et al., 2005, Whitehouse et al., 2005, Jiménez-Munt et al., 2005a,b, Robl et al., 2008, Stüwe et al., 2008, Lorinczi and Houseman, 2010; in addition to those discussed in §2.6.3 that focus on Tibet). The validity of the TVS approximation for a range of problems is therefore of continuing interest to the geodynamic community. In this Chapter I address this question for a collisional-type indentation model.

5.2 Governing equations

5.2.1 Viscous flow

The continental lithosphere is assumed to deform over geological time by creeping viscous flow. Although in reality different deformation mechanisms may apply at different levels or lateral localities within the lithosphere, here it is assumed that the overall effect of these different mechanisms (elastic and viscous) is represented over long time periods and large areas by continuum deformation. For deformation occurring at geological

strain rates the change of momentum is negligible due to the relatively high viscosity of continental material. This results in a very low Reynolds number that implies that viscous forces dominate inertial forces in large scale continental deformation (Turcotte and Schubert, 1982, England and McKenzie, 1982). The reduced Navier-Stokes 3D force balance is therefore:

$$\frac{\partial \sigma_{ij}}{\partial x_j} - \rho g \delta_{iz} = 0 \tag{5.1}$$

where σ_{ij} is the ijth component of the total stress tensor, ρ is density, g is the gravitational acceleration, and δ_{iz} is the Kronecker delta (z is positive upwards). The indices i and j refer to each of the Cartesian coordinate directions x, y and z and the convention of summing repeated indices applies. The total stress tensor can be expressed in terms of the deviatoric stress τ and the pressure p:

$$\sigma_{ij} = \tau_{ij} + p\delta_{ij} \tag{5.2}$$

where $p = \frac{1}{3}(\sigma_{xx} + \sigma_{yy} + \sigma_{zz})$ is the mean total stress. Although negative and positive sign conventions are in use, here I choose that compression is negative. A power-law (i.e. non-Newtonian) viscous constitutive law is invoked to relate deviatoric stress to strain rate $\dot{\varepsilon}$:

$$\tau_{ij} = B\dot{E}^{(\frac{1}{n}-1)}\dot{\varepsilon}_{ij} \tag{5.3}$$

which depends on the power-law exponent n and the viscosity coefficient B (England and McKenzie, 1982, 1983). Strain rates are defined in terms of the velocity gradients:

$$\dot{\varepsilon}_{ij} = \frac{1}{2}\left(\frac{\partial u_i}{\partial x_j} + \frac{\partial u_j}{\partial x_i}\right) \tag{5.4}$$

and $\dot{E}$ is the second invariant of the strain-rate tensor (again assuming summation over repeated indices):

$$\dot{E} = (\dot{\varepsilon}_{ij}\dot{\varepsilon}_{ij})^{\frac{1}{2}}. \tag{5.5}$$

For a Newtonian fluid, $n = 1$ and $B = 2\eta$ where η is the fluid's viscosity, meaning Eq. 5.3 reduces to:

$$\tau_{ij} = 2\eta\dot{\varepsilon}_{ij}. \tag{5.6}$$

For non-Newtonian fluids, the effective viscosity is therefore:

$$\eta_{\text{eff}} = \frac{B}{2}\dot{E}^{(\frac{1}{n}-1)} \tag{5.7}$$

which is frame-independent along with $\dot{E}$. Incompressibility of the continuum flow field requires that the volume remains constant throughout deformation:

$$\nabla \cdot \mathbf{u} = 0. \tag{5.8}$$

5.2.2 Reducing the problem to 2-dimensions

The TVS approximation assumes that vertical gradients of deviatoric stress can be neglected, and velocity does not vary with depth (England and McKenzie, 1983):

$$\frac{\partial \tau_{ij}}{\partial z} = 0 \tag{5.9}$$

$$\dot{\varepsilon}_{xz} = \dot{\varepsilon}_{zx} = \dot{\varepsilon}_{yz} = \dot{\varepsilon}_{zy} = 0. \tag{5.10}$$

As mentioned in §5.1, this assumption is valid for regions where the deformation length scale D exceeds the thickness of the sheet L (i.e. $D >> L$) as long as gradients of crustal thickness are small. Effectively, the full stress tensor is reduced to 5 components (illustrated in Figure 2.17):

$$\sigma^{\text{TVS}} = \begin{bmatrix} \sigma_{xx} & \sigma_{xy} & 0 \\ \sigma_{yx} & \sigma_{yy} & 0 \\ 0 & 0 & \sigma_{zz} \end{bmatrix}. \tag{5.11}$$

Rearranging Eq. 5.8, the vertical strain rate can be determined from the horizontal components of strain rate:

$$\dot{\varepsilon}_{zz} = -(\dot{\varepsilon}_{xx} + \dot{\varepsilon}_{yy}) \tag{5.12}$$

and therefore the second invariant can be determined from only the horizontal gradients of velocity:

$$\dot{E} = \sqrt{2}(\dot{\varepsilon}_{xx}^2 + \dot{\varepsilon}_{yy}^2 + \dot{\varepsilon}_{xy}^2 + \dot{\varepsilon}_{xx}\dot{\varepsilon}_{yy})^{\frac{1}{2}}. \tag{5.13}$$

Given the assumptions of Eqs. 5.9 and 5.10, the horizontal equations of Eq. 5.1 are

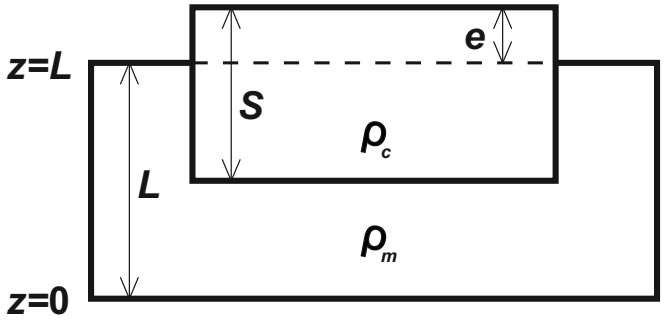

Figure 5.1: Schematic illustration showing the parameters used in the derivation of the buoyancy force term of the thin viscous sheet with a crustal layer in isostatic equilibrium.

averaged over the thickness of the lithosphere:

$$\frac{\partial \bar{\tau}_{\alpha\beta}}{\partial x_\beta} - \frac{\partial \bar{\tau}_{zz}}{\partial x_\alpha} = -\frac{\partial \bar{\sigma}_{zz}}{\partial x_\alpha} \tag{5.14}$$

where α and β refer only to the two horizontal coordinate directions x and y and over-bars indicate vertical averages. Similarly, Eq. 5.3 becomes:

$$\bar{\tau}_{\alpha\beta} = B\dot{E}^{(\frac{1}{n}-1)}\dot{\varepsilon}_{\alpha\beta} \tag{5.15}$$

where $\dot{E}$ is given by Eq. 5.13 and B now represents the depth-averaged effective viscosity coefficient of the lithosphere. The coefficient B provides a convenient way of parameterising lithospheric rheology without explicitly representing variation of temperature, or material properties with depth.

5.2.3 Buoyancy force term

The derivation proceeds by assuming that the vertical stress components (RHS of Eq. 5.14) are known based on the distribution of gravitational potential energy (GPE) per unit area. Pressure may then be eliminated from the force balance in order to solve for the gradients of velocity. Considering the assumption of Eq. 5.9 gives the following expression for the vertical stress balance:

$$\frac{\partial \sigma_{zz}}{\partial z} = \rho g. \tag{5.16}$$

Integrating Eq. 5.16 and substituting for Eq. 5.2:

$$p = \int_0^z \rho g dz - \tau_{zz} + C. \tag{5.17}$$

Consider a simple two layer lithospheric model of thickness L with an embedded crust of thickness S and constant crust and mantle densities of ρ_c and ρ_m (Figure 5.1). Horizontal stresses imparted on the vertical boundaries are balanced wholly within the lithospheric layer. If crustal thickness variations are in local isostatic equilibrium (i.e. the horizontal gradients of crustal thickness are small) then from Eq. 1.6, $e = S\left(1 - \frac{\rho_c}{\rho_m}\right)$ is the elevation above the top surface of the lithospheric reference column (initially $e = 0$). This situation gives the vertical boundary conditions that $\sigma_{zz} = 0$ when $z = L + e$ and $\sigma_{zz} = -\rho_m g L$ when $z = 0$. Therefore the base of the layer at $z = 0$ corresponds to the initially unperturbed Lithosphere-Asthenosphere boundary (LAB). Expanding Eq. 5.17:

$$p = \int_0^{L+e-S} \rho_m g dz + \int_{L+e-S}^{L+e} \rho_c g dz - \tau_{zz} - \rho_m g L. \tag{5.18}$$

Taking vertical averages of the parameters over the thickness of the lithosphere, Eq. 5.18 becomes:

$$\bar{p} = \frac{1}{L+e}\int_0^{L+e-S} \rho_m g dz + \frac{1}{L+e}\int_{L+e-S}^{L+e} \rho_c g dz - \bar{\tau}_{zz} - \rho_m g L. \tag{5.19}$$

After some algebraic manipulation, assuming $e << L$ and considering only the horizontal gradient terms, the horizontal gradients of vertically averaged vertical stress can be expressed as:

$$\frac{\partial \bar{\sigma}_{zz}}{\partial x_\alpha} = -\frac{g\rho_c}{2L}(1 - \rho_c/\rho_m)\frac{\partial S^2}{\partial x_\alpha}. \tag{5.20}$$

The crustal thickness evolves with time in a Lagrangian reference frame based on the local divergence of the horizontal flow field:

$$\frac{1}{S}\frac{\partial S}{\partial t} = -\left(\frac{\partial u_x}{\partial y} + \frac{\partial u_y}{\partial x}\right). \tag{5.21}$$

5.2.4 Non-dimensionalisation

When setting up numerical models of lithospheric deformation, it is convenient to non-dimensionalise the physical parameters. Solutions can then be scaled appropriately for different regions of interest without the need for recalculation. Here I choose the inden-

tation velocity U_0, mantle density ρ_m, and layer thickness L as the scaling parameters:

$$(x, y, z, S) = L(x', y', z', S') \tag{5.22a}$$

$$\mathbf{u} = U_0 \mathbf{u}' \tag{5.22b}$$

$$t = \frac{1}{\dot{\varepsilon}_0} t' \tag{5.22c}$$

$$\dot{\varepsilon} = \dot{\varepsilon}_0 \dot{\varepsilon}' \tag{5.22d}$$

$$\tau = B_0 \dot{\varepsilon}_0^{\frac{1}{n}} \tau' \tag{5.22e}$$

$$\rho = \rho_m \rho' \tag{5.22f}$$

where $\dot{\varepsilon}_0 = U_0/L$ is the reference strain rate, $\mathbf{u} = [u_x u_y u_z]$ and primes indicate dimensionless variables. Substituting Eq. 5.20 into Eq. 5.14 and non-dimensionalising gives:

$$\frac{\partial \bar{\tau}'_{\alpha\beta}}{\partial x'_\beta} - \frac{\partial \bar{\tau}'_{zz}}{\partial x'_\alpha} = \frac{Ar}{2} \frac{\partial S'^2}{\partial x'_\alpha}. \tag{5.23}$$

In this equation, the horizontal gradients of deviatoric stress (LHS) are balanced by horizontal gradients of GPE caused by variations in crustal thickness (RHS). The relative importance of buoyancy forces is determined by the Argand number Ar as discussed in §2.6.3 and §5.1 (England and McKenzie, 1983):

$$Ar = \frac{g\rho_c L(1 - \rho_c/\rho_m)}{B\dot{\varepsilon}_0^{\frac{1}{n}}}. \tag{5.24}$$

5.2.5 3-dimensional equivalent of the Argand number

The formulation used in fully 3D calculations is conceptually simpler since the viscous constitutive law includes the full 9-component deviatoric stress tensor. Substituting Eq. 5.2 into the 3D force balance (Eq. 5.1) and non-dimensionalising gives:

$$\frac{\partial \tau'_{ij}}{\partial x'_j} + \frac{\partial p'}{\partial x'_i} = \xi \rho' \delta_{iz} \tag{5.25}$$

where ξ is the dimensionless ratio of buoyancy derived stress to indentation derived stress:

$$\xi = \frac{g\rho_m L}{B\dot{\varepsilon}_0^{\frac{1}{n}}} \tag{5.26}$$

The body force coefficient ξ plays a similar role in the 3D formulation as the Argand number in 2D. For consistent comparison of 2D and 3D experiments the relationship between Ar and ξ is:

$$Ar = \xi \frac{\rho_c}{\rho_m} \left(1 - \frac{\rho_c}{\rho_m}\right) \tag{5.27}$$

5.3 Numerical solution

A non-linear system of partial differential equations as represented by Eqs. 5.23 and 5.25 for non-Newtonian fluids cannot be solved analytically and therefore an approximate solution must be obtained using numerical methods. The Finite Element Method (FEM; Zienkiewicz and Taylor, 2000) is now a well-established and powerful method for computing the solution to partial differential equations. Although the finite difference method is mathematically simpler, the equations must be solved on a regular Cartesian grid of points. The advantage of FEM is that the equations can be solved on a non-regular mesh with complex boundary geometries and a heterogeneous internal distribution of material properties. A brief description of the programs and method used is given in this section.

5.3.1 Programs used

I have used the 2D *Basil* program and 3D *Oregano* program for numerical modelling using the FEM. In both cases, a velocity-pressure formulation of the FEM is used in the programs.

Basil (Houseman et al., 2008) is a program for computing the finite deformation of viscous fluids in two dimensions. It can be used to model plane-stress, plane-strain or thin sheet problems. In 'thin sheet' mode, *Basil* works on the 'pure shear' TVS formulation of England and McKenzie (1982) but uses the Lagrangian-frame FEM implemented by Houseman and England (1986). By substituting Eqs. 5.4, 5.12 and 5.15, the two non-dimensional horizontal equations of Eq. 5.23 solved for in *Basil*

become:

$$\frac{\partial}{\partial x}\left[2\eta_{\text{eff}}\frac{\partial u_x}{\partial x}\right]+\frac{\partial}{\partial y}\left[\eta_{\text{eff}}\left(\frac{\partial u_x}{\partial y}+\frac{\partial u_y}{\partial x}\right)\right]+\frac{\partial}{\partial x}\left[2\eta_{\text{eff}}\left(\frac{\partial u_x}{\partial x}+\frac{\partial u_y}{\partial y}\right)\right]=\frac{Ar}{2}\frac{\partial S^2}{\partial x} \tag{5.28a}$$

$$\frac{\partial}{\partial x}\left[\eta_{\text{eff}}\left(\frac{\partial u_y}{\partial x}+\frac{\partial u_x}{\partial y}\right)\right]+\frac{\partial}{\partial y}\left[2\eta_{\text{eff}}\frac{\partial u_y}{\partial y}\right]+\frac{\partial}{\partial y}\left[2\eta_{\text{eff}}\left(\frac{\partial u_x}{\partial x}+\frac{\partial u_y}{\partial y}\right)\right]=\frac{Ar}{2}\frac{\partial S^2}{\partial y} \tag{5.28b}$$

with over-bars and dashes dropped for clarity. In Eq. 5.28 the TVS governing equations are expressed in terms of only the horizontal velocity gradients, viscosity distribution, crustal thickness and the Argand number; the gradients of pressure have been eliminated.

The *Oregano* program (Houseman et al., 2004) uses the same methods employed in *Basil* but extended to the third dimension. It is programmed using the Message Passing Interface (MPI) in order that the calculation can be parallelised and run on a multi-processor machine. It also uses the Lagrangian-frame FEM but operating on the full non-dimensionalised 3D force balance (Eq. 5.25):

$$\frac{\partial}{\partial x}\left[2\eta_{\text{eff}}\frac{\partial u_x}{\partial x}+p\right]+\frac{\partial}{\partial y}\left[\eta_{\text{eff}}\left(\frac{\partial u_x}{\partial y}+\frac{\partial u_y}{\partial x}\right)\right]+\frac{\partial}{\partial z}\left[\eta_{\text{eff}}\left(\frac{\partial u_x}{\partial z}+\frac{\partial u_z}{\partial x}\right)\right]=0 \tag{5.29a}$$

$$\frac{\partial}{\partial x}\left[\eta_{\text{eff}}\left(\frac{\partial u_y}{\partial x}+\frac{\partial u_x}{\partial y}\right)\right]+\frac{\partial}{\partial y}\left[2\eta_{\text{eff}}\frac{\partial u_y}{\partial y}+p\right]+\frac{\partial}{\partial z}\left[\eta_{\text{eff}}\left(\frac{\partial u_y}{\partial z}+\frac{\partial u_z}{\partial y}\right)\right]=0 \tag{5.29b}$$

$$\frac{\partial}{\partial x}\left[\eta_{\text{eff}}\left(\frac{\partial u_z}{\partial x}+\frac{\partial u_x}{\partial z}\right)\right]+\frac{\partial}{\partial y}\left[\eta_{\text{eff}}\left(\frac{\partial u_z}{\partial y}+\frac{\partial u_y}{\partial z}\right)\right]+\frac{\partial}{\partial z}\left[2\eta_{\text{eff}}\frac{\partial u_z}{\partial z}+p\right]=\xi\rho \tag{5.29c}$$

with dashes again dropped for clarity.

5.3.2 Finite element method

The mathematical detail of the FEM method is not given here for brevity, but is detailed in many other places (e.g. Zienkiewicz and Taylor, 2000).

Mesh

The FEM involves dividing the physical solution domain into a number of contiguous 'elements' that when taken together form a mesh. For a 2D mesh such as used in *Basil*, the commonly used element shape is the triangle since it can easily accommodate

complex boundary and internal geometries. Each triangular element has 6 nodes on which the equations are solved: 3 of these are at the triangle's vertices and the other 3 are located at the midpoints of the triangle's sides. Neighbouring elements share the same set of 3 nodes on their common side.

Oregano employs tetrahedral elements, which are constructed by first establishing a triangular mesh covering the region in 2D. This mesh is then duplicated at intervals equal to the node spacing to form pentahedral (prismoidal) elements in 3D. Two surfaces are used to cut the pentahedral elements into tetrahedra. Each tetrahedra has 4 vertex nodes and 6 midpoint nodes. Although in 2D the triangular elements used enables complex geometries to be used, the parallelisation of the 3D calculation means that *Oregano* is best suited to problems with regular shaped geometries (e.g. Houseman and Gemmer, 2007). In the following, reference is made to the simpler 2D case but the same principles apply in 3D.

Means of solution

The aim of the method is to find the approximate solution for the velocity components and pressure at each of the nodes. Constraint of the solution is provided by the use of a weighted residual function for each node. Equations from all the elements are discretised and assembled into a large matrix calculation which is solved using the conjugate gradient method (Hestenes and Stiefel, 1952). This is an iterative algorithm for solving a system of linear equations by minimising the residual function. *Basil* and *Oregano* use the Galerkin method to discretise the governing equations with weighting provided by predefined interpolation or 'shape' functions. The functions employ quadratic interpolation of the velocity field and linear interpolation of the pressure field. The quadratic interpolation uses all 6 nodal values, whereas the linear interpolation uses only the 3 vertex nodes. From Eq. 5.28 and Eq. 5.29, each node in an element has either 2 or 3 equations to be solved. However, because interior nodes belong to multiple elements, they receive constraints from all the elements they belong to.

Boundary conditions

Nodes on the perimeter of the domain provide control of the calculation by way of the boundary conditions applied to them *a-priori*. These conditions are given either in terms of traction (stress) or displacement rate (velocity) for problems in the velocity-

pressure formulation. For a well-conditioned calculation, the boundary conditions for the entire perimeter of the domain should be defined.

Deforming the mesh

After the conjugate gradient algorithm has converged on a solution, the mesh nodes are advected (displaced) in a Lagrangian fashion based on the updated velocities and the time-step. All material properties and boundaries are advected with the mesh. Therefore the change in mesh geometry reflects the finite deformation in the model. In 2D, the crustal thickness is updated for each mesh node following the solution of the velocity and pressure fields using Eq. 5.21. In the 2D calculation, the crustal thickness is updated for each node using the velocity gradients and Eq. 5.21. In 3D, the crustal thickness is defined locally by the depth of the nodes on the crust-mantle interface and evolves with the mesh advection between time steps.

Time stepping

A two-step Runge-Kutta time-stepping algorithm is used to advance the calculation from one time-step to the next. The time-step size is subject to defined conditions for accuracy and calculation stability. The new mesh configuration is then used to solve for the velocity and pressure fields at the next time-step. This iterative procedure continues until either a predefined final time-step is reached or finite deformation reaches a predefined level (useful for stopping run-away calculations).

Parallel operation in 3D

In order to run the parallelised calculation in *Oregano*, the 3D mesh is split equally among the available processors with each taking a sub-domain (layer) of elements. Neighbouring processors must then communicate with their neighbours to ensure they converge on the same solution at the boundary nodes in order to preserve continuity of the field. Information is exchanged between neighbouring processors during every iteration of the conjugate gradient solver. Therefore the number of iterations of the parallelised calculation is the same as if it were a single processor running the calculation.

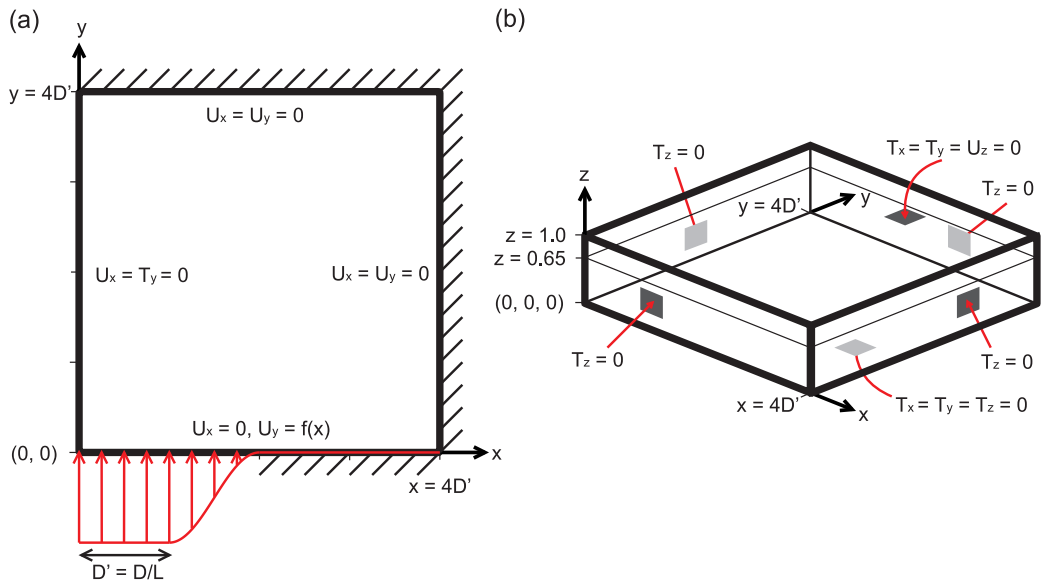

Figure 5.2: Geometry and boundary conditions of 2D and 3D models. a) Plan view of the 2D model domain and boundary conditions. U_i and T_i denote the velocity and traction components parallel to the i direction respectively. The grey lines graphically describe the indenting velocity function U_y imposed on the $y = 0$ boundary as described in the text. Hatching indicates a zero displacement boundary condition. b) Perspective view of the model domain showing additional boundary conditions used in 3D. The boundary conditions shown in a) also apply to the 3D model and are invariant in the z direction. The surface at $z = 0.65$ corresponds to the Moho. All quantities are dimensionless.

5.4 Comparison of 2D and 3D models

In this section I explore the differences between 2D TVS calculations and analogous 3D calculations of a simple indentation model. In this test problem inspired by continental collision, the lithosphere deforms in response to gravitational body forces (scaled using Ar and ξ) and a convergent boundary condition.

5.4.1 Model set-up

Geometry

A simple geometry was chosen for the experiments, similar to that used by (Houseman and England, 1986; Figure 5.2). Table 5.1 gives values of dimensional parameters that can be used to scale the solutions, although the comparison presented here is in terms of dimensionless parameters. The scaling parameters shown in Table 5.1 are the same as given by Houseman and England (1986) for their study of the India-Asia collision, except that the scaling factor for the horizontal length scale is not explicitly defined.

Table 5.1: Nominal dimensional values assumed for the 2D and 3D model physical parameters.

L	=	100 km	
S_0	=	35 km	
U_0	=	50 mm yr^{-1}	
ρ_m	=	3.27 $\times 10^3$ kg m^{-3}	
ρ_c	=	2.80 $\times 10^3$ kg m^{-3}	
g	=	10 m s^{-2}	for $Ar > 0$

The undeformed model lithosphere is represented by a box with edges of dimensionless length $4D'$ in both the x and y directions, and unit thickness in the z direction. In the dimensionless length scale, the half width of the indenter is $D' = D/L$. The solution domain is one half of a symmetrical experiment, with $x = 0$ as a plane of symmetry bisecting the indenter. The indenter is represented by the non-dimensional velocity function on the boundary $y = 0$:

$$U_y{}'(x) = \begin{cases} 4D' & 0 \leq x \leq D' \\ 4D' cos^2[\frac{\pi}{2D'}(x' - D')] & D' \leq x \leq 2D' \\ 0 & 2D' \leq x \leq 4D' \end{cases} \tag{5.30}$$

The dimensionless indentation velocity is defined as proportional to D' in order that experiments with different values of D/L have the same relative indentation at the same dimensionless time. With this choice the indenting boundary would travel across the whole solution domain in a dimensionless time of $t = 1.0$. Since the horizontal dimension of the solution region is proportional to the half-width of the indenter D', the geometry of deformation in the horizontal plane is the same for all experiments. I use the ratio D/L as an adjustable parameter in the experiments.

Boundary Conditions

The boundary conditions applied to the models are summarised in Figure 5.2. In 3D models at $t = 0$, $z = 1.0$ and $z = 0.0$ correspond to the top and bottom of the layer respectively. On the top surface, horizontal free slip and zero vertical displacement conditions are applied ($U_z = \sigma_{xz} = \sigma_{yz} = 0$ on $z = 1.0$). The zero vertical displacement condition is a simplifying assumption which enables approximate solutions to be obtained for any Argand number considered, without producing unrealistically large free-surface displacements. Incompressibility of the fluid requires that at least

one model boundary is deformable. Accordingly, thickening of the layer manifests as a downward movement of the bottom surface, which forms a lithospheric root zone. The asthenosphere, although not included in the model domain, is simulated as inviscid by the use of free slip conditions in all coordinate directions. Under a zero stress boundary condition on the top surface, a small fraction of the layer thickening would manifest as a topographic plateau above the location of the root in order to balance the vertical stress. In this situation the depth extent of the root would be marginally reduced. Nevertheless, the development of topography relative to the $z = 1.0$ surface is calculated by balancing the vertical stress component on that surface against the weight of topography (e.g. McKenzie, 1977).

I assume that the model lithosphere comprises a constant density crustal layer which sits above a denser mantle layer. The crust-mantle boundary (Moho) is the surface initially at $z = (1 - S_0/L)$, where S_0 is the initial crustal thickness (Figure 5.2b). For all experiments presented here, $S_0/L = 0.35$. The lithostatic pressure gradient is removed from the 3D calculations by subtracting the mantle density from the lithospheric column, so that the dimensionless densities in the mantle and crust are zero and $(\rho_c/\rho_m - 1)$ respectively. Removing the static part of the pressure field has no effect on the calculated velocity field, but it converts the hydrostatic stress condition on the deforming base of the lithospheric layer into a zero stress condition. In 2D TVS calculations the same crust-mantle density contrast is accounted for by the Argand number (Eq. 5.24).

In comparing the 2D and 3D experiments, equivalent parameters were used as far as possible. To avoid unnecessary complications and to isolate purely geometrical effects, the viscosity coefficient (B) is assumed constant with depth in 3D calculations. Lechmann et al. (2011) present calculations in which B varies with depth. I varied the power-law exponent n and the Argand number Ar (or its 3D proxy ξ). A zero Argand number implies that gravitational forces are negligible relative to the viscous stress induced by indentation; effectively $g = 0$. In this situation the density contrast across the Moho surface does not affect deformation.

A regularised triangulation with equal horizontal and vertical resolutions is used in the finite element meshes. For $D/L = 1$, 48 elements span the x and y directions, whilst 12 elements span the z direction of the 3D mesh. Figure 5.3c shows the $x - y$ configuration of the basal plane of the 3D mesh following deformation. For calculations where $D/L > 1$, the number of elements in x and y scale as $48D$. The original choice

of mesh size was governed by the need to have the Moho co-located with a horizontal layer of mesh nodes. With the chosen scheme where the number of layers is divisible by 3, the closest layer to the Moho is located at $z = 0.666$. After mesh generation, this layer is moved vertically so that it lies at $z = 0.65$, with the other layers remaining unperturbed. Other than the 'divisible by 3' criteria for the vertical mesh resolution, the choice of 12 mesh nodes was made based on the trade off between solution resolution and computational cost. The 3D calculations were parallelised in the y direction with 48 processors each calculating the solution for a layer D elements thick.

Results are compared at the dimensionless times $t = 0.0$, 0.1 and 0.2 when the indenter has moved dimensionless distances of 0.0, $0.4D'$ and $0.8D'$ respectively. For both 2D and 3D calculations, solution fields are interpolated on to a regular 401 by 401 grid (node spacing equal to $D'/100$) in the horizontal plane. The 8x oversampling of the original mesh resolution was performed to avoid the possible aliasing of short wavelength features. To compare 2D and 3D solutions, an approximate vertical average of the 3D vertical strain-rate field was calculated using interpolated values on four horizontal surfaces at $z = 1.0$, 0.7, 0.4, and 0.1. A surface at $z = 0.0$ is not used since thinning of the layer would result in an incomplete solution at this depth. A 'difference' field is obtained by subtracting the average of the four horizontal surface fields from the 2D field.

5.4.2 Deformation of a 3D model

In this section I describe the deformation of a 3D indentation experiment with $n = 3$, $Ar = 0$, and $D/L = 1$. Figure 5.3 shows that the layer deforms by a combination of shortening, thickening and shearing in response to indentation. Material immediately ahead of the indenting boundary is pushed downward, which displaces the Moho and the LAB to form a 'root' zone (Figure 5.3a and b). At $t = 0.2$, the maximum lithospheric and crustal thicknesses have increased by 44% and 53% respectively (see Figure 5.3a and b and values in Table 5.2a). The values in Table 5.2a confirm that rates of layer thickening increase sharply with n and decrease with Ar.

Interpolated vertical sections through the 3D solution domain (Figure 5.4) show that deformation varies laterally (in both x and y) and with depth. Thickening and shortening strain rates (the components $\dot{\varepsilon}_{zz}$ and $\dot{\varepsilon}_{yy}$) are greatest in the upper lithosphere (Figures 5.4a and b). These strain rate components decrease with depth in the root

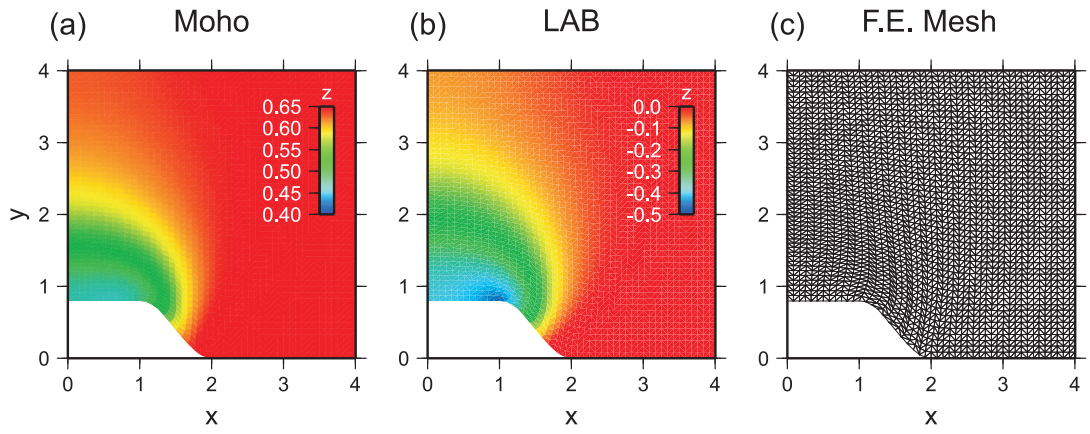

Figure 5.3: Deformed Moho surface, LAB surface and and basal plane of the finite element mesh in a 3D calculation at $t = 0.2$ with $n = 3$, $Ar = 0$ and $D/L = 1$. Distribution of vertical deflections of a) the Moho originally at the level $z = 0.65$ and b) the LAB originally at the level $z = 0.0$. The surfaces are coloured according to the z-coordinate at the centre of each triangular mesh element. c) Deformed LAB surface of the 3D finite element mesh at $t = 0.2$. All quantities are dimensionless.

zone because displacement of the root is not resisted by the asthenosphere below to the same extent as the lithosphere above (which is constrained by the remote rigid boundary condition at $y = 4$). As the root develops, a localised region of high shear-strain rate on horizontal and vertical planes ($\dot{\varepsilon}_{yz}$; Figure 5.4c) occurs towards the base of the layer due to gradients in the vertical (U_z) and horizontal (U_y) velocity components (Figures 5.4e and f respectively). The shear-strain rate is negative there because the rate of movement in the indentation direction at the bottom of the layer is greater than at the top. Thus the root is pushed ahead of the overlying layer whilst simultaneously growing in volume as material is forced downward ahead of the indenter. The sign of the x-vorticity component ($\Omega_x = \frac{1}{2}(\partial u_y/\partial z - \partial u_z/\partial y)$) confirms a circulating flow in which the fastest downward velocities occur close to the indenter as the whole body translates in the indenter-parallel direction (Figure 5.4d).

Figure 5.5 shows the variation of vertical strain rate ($\dot{\varepsilon}_{zz}$) with depth and time for experiments with $Ar = 0$ and varying n. Vertical gradients of strain rate increase with n, but all three cases show a similar evolution with time. In the upper part of the layer, vertical strain rate generally increases marginally with time as the horizontal domain is shortened. However, at the depth of the growing root zone strain rates decrease with time. As the root increases in volume it becomes less effectively constrained by the boundary conditions, and strain rates decrease. Conversely, the upper lithosphere

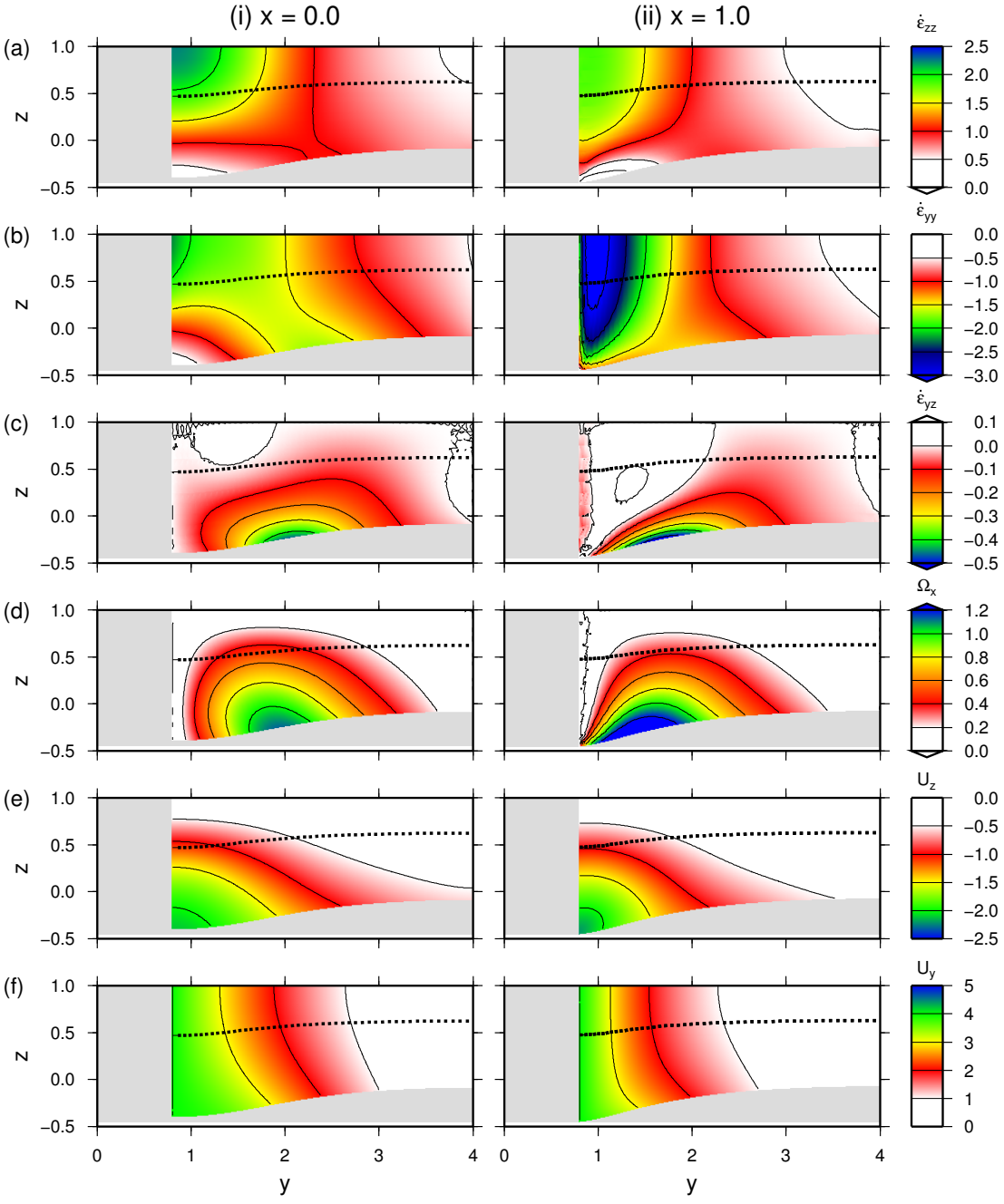

Figure 5.4: Vertical sections through the symmetry plane ($x = 0.0$, column (i)) and the indenter corner ($x = 1.0$, column (ii)) at $t = 0.2$ showing a) vertical strain rate ($\dot{\varepsilon}_{zz}$), b) horizontal strain rate (indenter parallel, $\dot{\varepsilon}_{yy}$), c) shear-strain rate ($\dot{\varepsilon}_{yz}$), d) vorticity component perpendicular to the plane (Ω_x), e) vertical velocity component (U_z), and f) indenter parallel horizontal velocity component (U_y) for an experiment with $n = 3$, $Ar = 0$ and $D/L = 1$. For normal components of strain rate, positive values indicate extension whilst negative values indicate shortening. Negative shear-strain rate and positive vorticity indicate that the bottom of the layer moves faster than the top in the positive y direction. The black dotted line represents the intersection with the Moho surface. Scalebar-end arrows indicate saturation of the colour scale. All quantities are dimensionless.

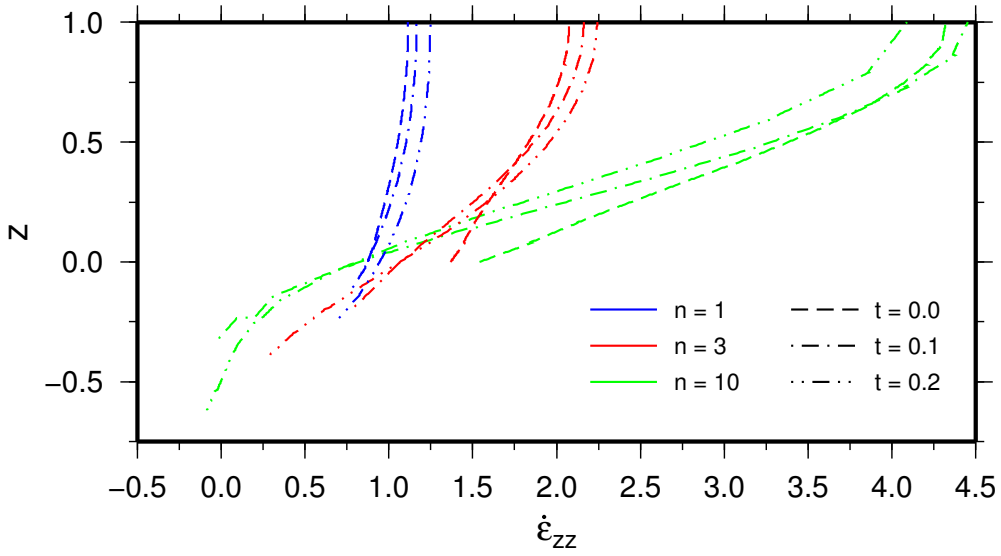

Figure 5.5: Vertical profiles showing the evolution through time of dimensionless vertical strain rate ($\dot{\varepsilon}_{zz}$) in experiments with $n = 1$, 3, 10, $Ar = 0$, and $D/L = 1$. The profile is located at the midpoint of the indenter ($x = 0$) and moves with the indenting boundary. Positive strain rates indicate thickening. All quantities are dimensionless.

remains confined in a contracting space, so material is strained at ever greater rates.

5.4.3 Differences between 2D and 3D calculations

In this section I compare 2D and 3D calculations in which the parameters n and Ar are varied for the case where $D/L = 1$. Since the predominant manifestation of the indenting boundary condition is thickening (e.g. Figure 5.3), I examine contours of the 2D and averaged 3D vertical strain-rate fields ($\dot{\varepsilon}_{zz}$) and their difference ($\Delta\dot{\varepsilon}_{zz} = \dot{\varepsilon}_{zz}^{2D} - \dot{\varepsilon}_{zz}^{3D}$) in x-y plan view at $t = 0.2$ (Figure 5.6). The greatest difference between 2D and average 3D solutions occurs systematically near the indenter corner (or geological syntaxis) where the 2D solutions consistently have greater strain rates. This strain-rate concentration, which has been observed in previous studies involving 2D TVS models (e.g. Houseman and England, 1986, 1993), is generally assumed to have the form of a weak singularity caused by the discontinuity in boundary conditions at the corner. The magnitude of the strain-rate concentration increases with time in 2D solutions, but decreases with time in 3D solutions (Figures 5.7a and b).

Horizontal profiles of vertical strain rate within the 3D solution (Figures 5.7c and d) show that at $t = 0$ the strain-rate concentration exists to some degree at all levels within the lithosphere. Moreover, the strain-rate magnitude increases with depth.

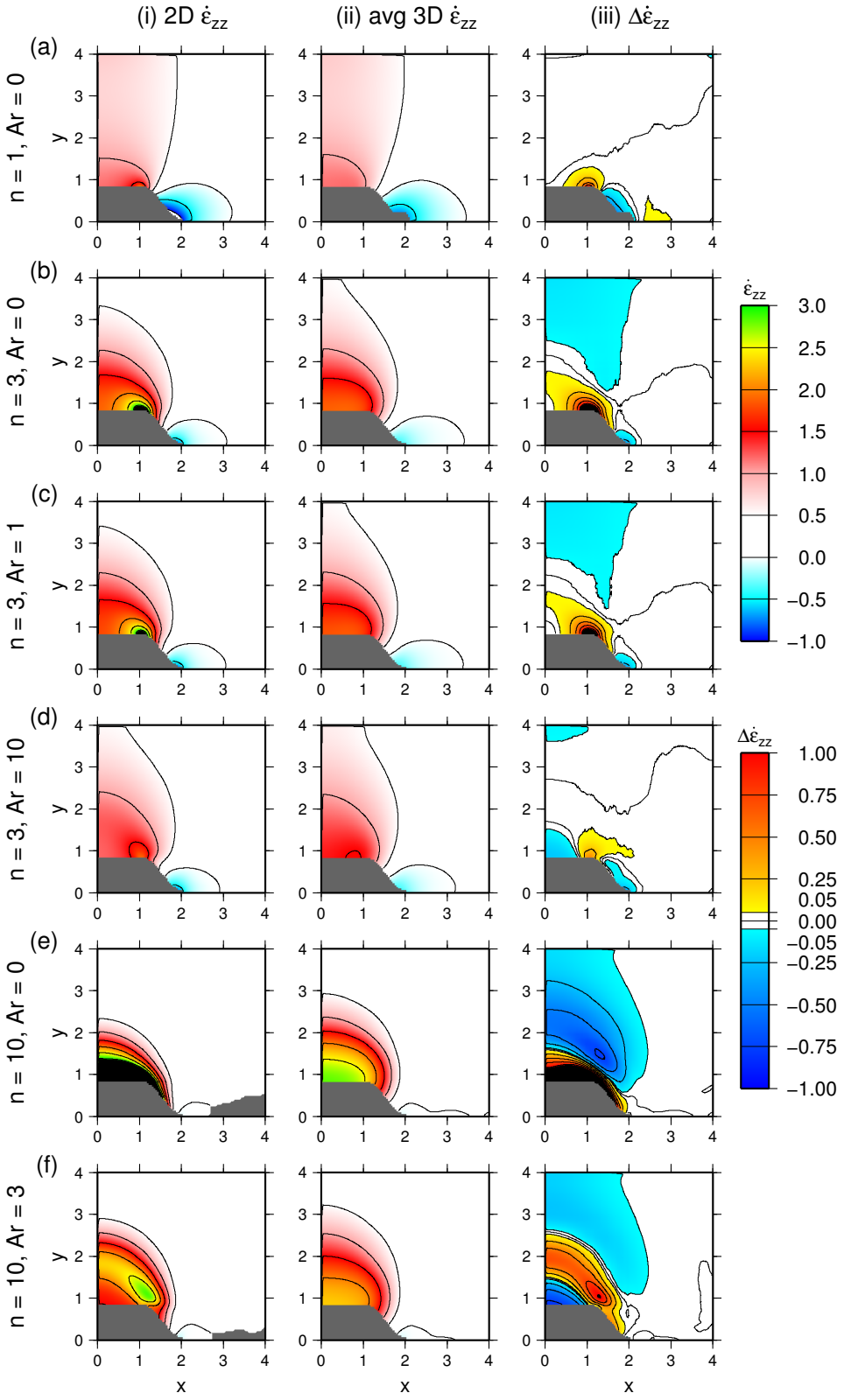

Figure 5.6: Plots of 2D (column (i)) and averaged 3D (column (ii)) vertical strain-rate field ($\dot{\varepsilon}_{zz}$), and their difference ($\Delta\dot{\varepsilon}_{zz} = \dot{\varepsilon}^{2D}_{zz} - \dot{\varepsilon}^{3D}_{zz}$, column (iii)) at $t = 0.2$ for experiments with $D/L = 1$ and varying n and Ar. The plotted fields have been smoothed using a circular averaging filter with radius 0.05 units to reduce interpolation noise. Grey regions show the extent of the indenting boundary condition. Black indicates saturation of the colour scale. All quantities are dimensionless.

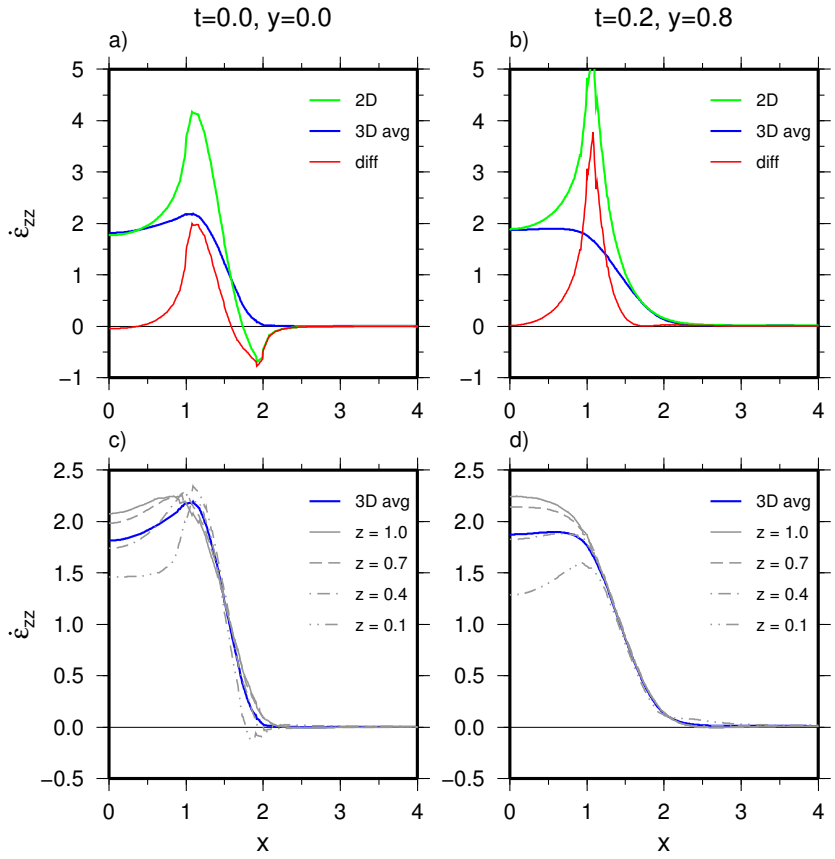

Figure 5.7: Profiles of vertical strain rate ($\dot{\varepsilon}_{zz}$) parallel to the x-axis ($y = 0.0$ and 0.8) for a calculation with $n = 3$, $Ar = 0$, and $D/L = 1$. a) and b) show the 2D solution, averaged 3D solution, and their difference at $t = 0.0$ and 0.2 respectively. c) and d) show the strain rates at the 4 depth levels used to construct the average of the 3D solution (also shown) at $t = 0.0$ and 0.2 respectively. All quantities are dimensionless.

At $t = 0.2$, however, the concentration is only evident towards the base of the layer. The diminution of this feature in 3D calculations shows that accurately accounting for vertical shear tractions has a considerable damping effect on the strain rates near the indenter corner relative to the predictions of the 2D TVS approximation. Unsurprisingly, the TVS approximation is least accurate where the horizontal gradients of strain rate are greatest.

Away from the indenter corner, solutions with $n \leq 3$ are characterised by differences of relatively low magnitude ($|\Delta\dot{\varepsilon}_{zz}| \leq 0.25$; Figures 5.6a-d). The difference between 2D and averaged 3D fields reduces as Ar is increased and buoyancy forces cause thickening to become more evenly distributed across the solution domain. In experiments where $Ar = 0$ (Figures 5.6a, b and e) and $n = 1$ the differences are small ($|\Delta\dot{\varepsilon}_{zz}| \leq 0.05$), but they increase significantly for $n = 3$, and further still for $n = 10$. At large n, the

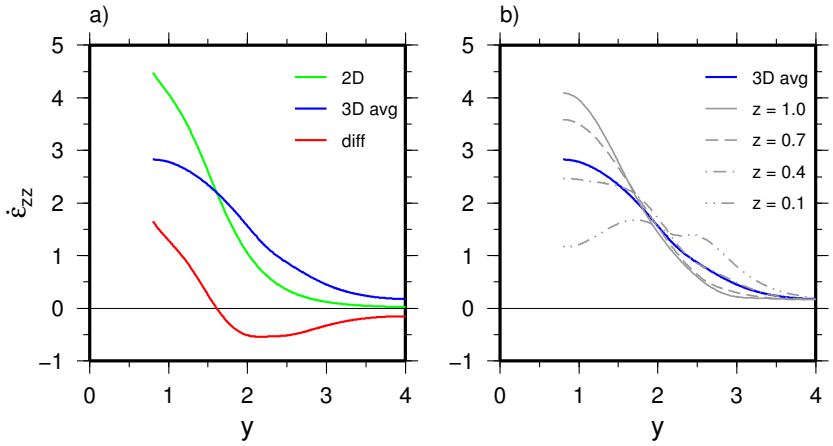

Figure 5.8: Profiles of vertical strain rate ($\dot{\varepsilon}_{zz}$) along the axis of symmetry ($x = 0.0$) for a calculation with $n = 10$, $Ar = 0$, and $D/L = 1$ at $t = 0.2$. a) shows the 2D solution, averaged 3D solution, and their difference. b) shows the strain rates at the 4 depth levels used to construct the average of the 3D solution (also shown). All quantities are dimensionless.

vertical strain rate is significantly greater in the 2D solution immediately in front of the indenter, but decays to lower strain rates over a shorter distance compared with the equivalent averaged 3D solution (Figure 5.8a). The variation of strain rate with depth within the 3D solution is also much greater when n is large; at the midpoint of the indenting boundary, there is a factor of 3 difference in the range of vertical strain rate with depth between the top surface ($z = 1.0$) and the surface at $z = 0.1$ ($n = 10$, Figure 5.8b).

In Table 5.2b the differences between 2D and averaged 3D solutions at $t = 0.2$ are quantified in terms of three single number measures:

- γ, the normalised mean of the absolute difference field:

$$\gamma = \frac{1}{\dot{\varepsilon}_{zz}^{\text{avg}}} \cdot \frac{1}{N} \sum_{i=1}^{N} |\Delta \dot{\varepsilon}_{zz}| \tag{5.31}$$

- κ, the normalised standard deviation of the absolute difference field:

$$\kappa = \frac{1}{\dot{\varepsilon}_{zz}^{\text{avg}}} \left(\frac{1}{N-1} \sum_{i=1}^{N} (|\Delta \dot{\varepsilon}_{zz}| - \gamma \cdot \dot{\varepsilon}_{zz}^{\text{avg}})^2 \right)^{\frac{1}{2}} \tag{5.32}$$

- λ, the normalised maximum of the absolute difference field (which systematically

Table 5.2: (a) Maximum values of lithospheric and crustal thickness for 3D models, and (b) measured differences in vertical strain rate ($\Delta\dot{\varepsilon}_{zz}$) between 2D and 3D models, at $t = 0.2$ for all twelve experiments with $D/L = 1$, and for the three experiments where D/L is varied. Refer to the text for descriptions of the measures γ (Eq. 5.31), κ (Eq. 5.32), and λ (Eq. 5.33). All quantities are dimensionless.

				(a)		(b)		
n	Ar	D/L	t	$\max(L)$	$\max(S)$	γ	κ	λ
1	0	1	0.2	1.259	0.444	0.062	0.140	3.140
1	1	1	0.2	1.258	0.444	0.062	0.137	3.068
1	3	1	0.2	1.258	0.443	0.062	0.131	2.951
1	10	1	0.2	1.255	0.440	0.064	0.111	2.556
3	0	1	0.2	1.441	0.537	0.146	0.381	8.539
3	1	1	0.2	1.438	0.533	0.129	0.318	6.036
3	3	1	0.2	1.432	0.525	0.105	0.232	4.055
3	10	1	0.2	1.412	0.504	0.069	0.106	1.831
10	0	1	0.2	1.641	0.760	0.578	1.469	28.774
10	1	1	0.2	1.630	0.734	0.361	0.682	6.615
10	3	1	0.2	1.610	0.686	0.291	0.448	2.664
10	10	1	0.2	1.550	0.576	0.194	0.282	1.515
3	0	1	0	1.000	0.350	0.078	0.267	5.292
3	0	2	0	1.000	0.350	0.030	0.136	3.520
3	0	4	0	1.000	0.350	0.019	0.070	2.069
3	0	1	0.1	1.220	0.435	0.120	0.335	6.698
3	0	2	0.1	1.288	0.460	0.121	0.235	5.181
3	0	4	0.1	1.350	0.487	0.140	0.219	3.927
3	0	1	0.2	1.441	0.537	0.146	0.381	8.539
3	0	2	0.2	1.578	0.586	0.201	0.322	7.358
3	0	4	0.2	1.711	0.651	0.247	0.342	6.209

occurs close to the indenter corner; Figure 5.6):

$$\lambda = \frac{1}{\dot{\varepsilon}_{zz}^{\text{avg}}} \cdot \max(|\Delta\dot{\varepsilon}_{zz}|) \tag{5.33}$$

where N is the number of interpolated points and each measure is normalised by the mean of the averaged 2D and 3D vertical strain-rate fields:

$$\dot{\varepsilon}_{zz}^{\text{avg}} = \frac{1}{2N}\left(\sum_{i=1}^{N}\dot{\varepsilon}_{zz}^{\text{3D}} + \sum_{i=1}^{N}\dot{\varepsilon}_{zz}^{\text{2D}}\right) \tag{5.34}$$

Consistent with mass conservation, variation of the normalisation factor for the twelve experiments at $t = 0.2$ ($0.4062 \leq \dot{\varepsilon}_{zz}^{\text{avg}} \leq 0.4077$) is attributable to numerical discretisation error. Figure 5.9 graphically displays the variation of these three difference

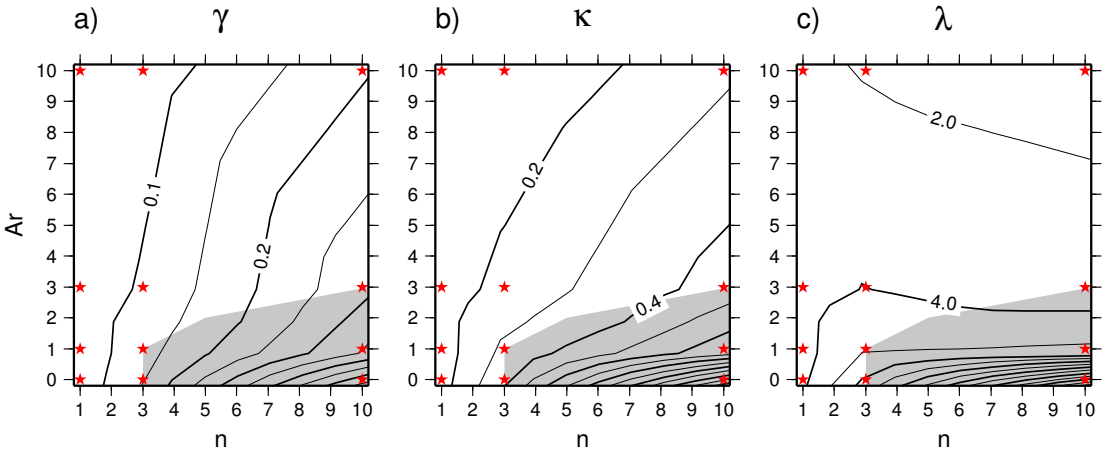

Figure 5.9: Contour plots of the three measures of difference a) γ, b) κ, and c) λ in the parameter space n versus Ar for $D/L = 1$ and $t = 0.2$. Interpolated contours are constrained by the irregularly spaced points plotted as red stars, which represent the twelve experiments with $D/L = 1$. The contour interval is 0.05 in a), 0.1 in b) and 2.0 in c). The grey shaded region indicates the approximate parameter range that England and Houseman (1986) find best fits observations from the Tibetan plateau. Refer to the text for descriptions of the measures γ, κ, and λ. All quantities are dimensionless.

measures (Table 5.2b) in the parameter space n versus Ar. For the experiments presented here, the greatest difference in vertical strain rate between 2D and 3D solutions is found when $n = 10$ and $Ar = 0$. For experiments with zero Argand number, the three difference measures increase monotonically with n. For Newtonian deformation ($n = 1$) the difference measures vary little with Ar. However, with greater values of n, the difference measures are more sensitive to Ar, and decrease rapidly as Ar is increased.

5.4.4 Varying the model geometry

As the geometry ratio D/L approaches infinity, the difference between 2D and 3D solutions is expected to vanish since the 2D TVS approximation assumes that $D >> L$. Further 3D experiments are conducted in order to examine this convergence using $D/L = 1$, 2 and 4 for the case where $n = 3$ and $Ar = 0$. When changing the value of D/L for each 3D mesh, the shape of the tetrahedral elements is unaltered whilst the number of elements in the x and y dimensions are 48, 96 and 192 for D/L ratios of 1, 2 and 4 respectively. The number of elements in the z dimension remains at 12 so that vertical resolution is constant for all experiments. In Figure 5.10 contours of the difference between 2D and averaged 3D vertical strain rates ($\Delta\dot{\varepsilon}_{zz}$) are plotted in x-y plan view at $t = 0.0$, 0.1, and 0.2. Additionally, the differences at these times are quantified in

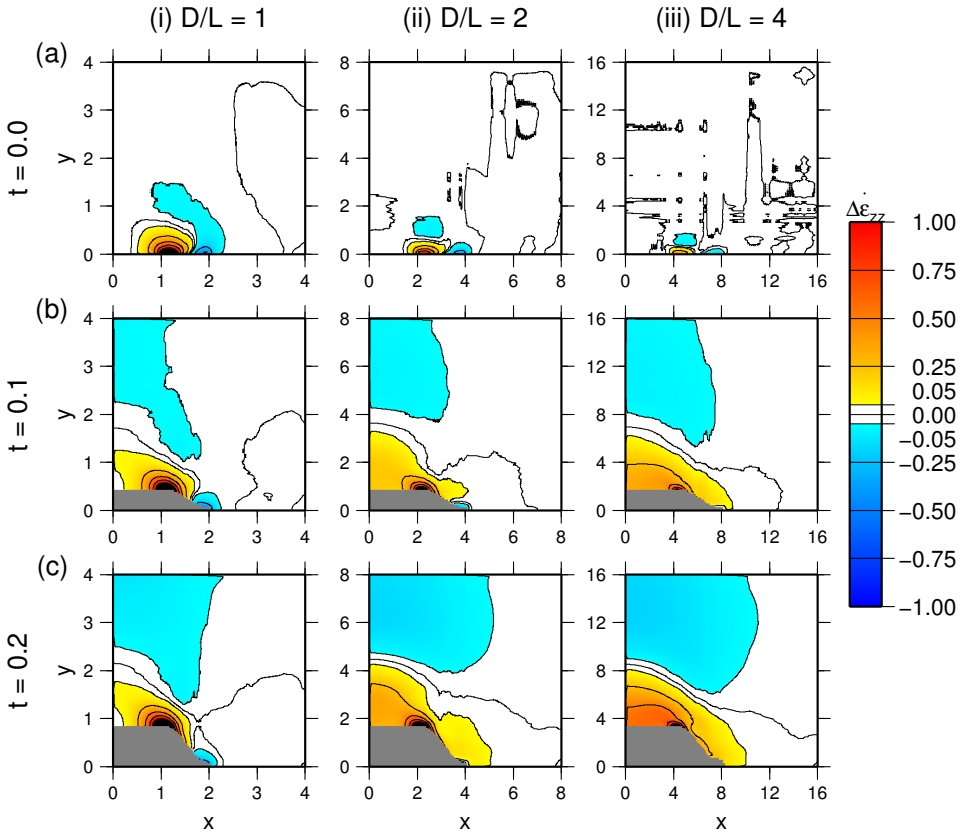

Figure 5.10: Plots of difference between 2D and averaged 3D vertical strain-rate fields ($\Delta\dot{\varepsilon}_{zz} = \dot{\varepsilon}^{2D}_{zz} - \dot{\varepsilon}^{3D}_{zz}$) at (a) $t = 0.0$, (b) $t = 0.1$, and (c) $t = 0.2$, for D/L values of 1, 2 and 4 (columns (i), (ii) and (iii) respectively) for the case $n = 3$, $Ar = 0$. The plotted fields have been smoothed using a circular averaging filter with radius 0.05 units to reduce interpolation noise. Grey regions show the extent of the indenting boundary condition at each time. Black indicates saturation of the colour scale. All quantities are dimensionless.

Table 5.2b using the three difference measures γ, κ, and λ defined in §5.4.3.

The time zero difference fields confirm that the 2D and averaged 3D solutions converge as D/L is increased (Figure 5.10a and quantity γ in Table 5.2b). The largest difference occurs at the indenter corner as described in §5.4.3, but this progressively reduces in magnitude with increasing D/L. Elsewhere in the solution domain the difference approaches zero with increasing D/L, indicated by the increased noisiness of the zero contour in a flat field. Differences near the indenter corner continue to increase with time as noted previously (Figures 5.7a and b). Directly in front of the indenter the difference can be seen to increase with time and D/L. After the root zone has begun to develop in 3D calculations (i.e. $t > 0$), the increased layer thickness in front of the indenter causes strain rates to be decreased in this region and increased further away where the layer has not thickened as much. This effect is amplified as deforma-

tion progresses since the contrast between the layer thickness close to and far from the indenting boundary only increases with time.

Increasing the ratio D/L in 3D reduces the layer thickness relative to the indenter half-width. Consequently, the same finite indentation stress is distributed over a smaller depth interval. In the 2D TVS approximation the same stress is assumed to be distributed over a layer of constant thickness (England and McKenzie, 1982). For $t > 0$, horizontal gradients of the stress-bearing layer thickness are no longer zero throughout the solution domain of a 3D calculation; though the gradients are reduced in proportion to D/L. The reduction of horizontal gradients of vertical shear stress permits the most highly stressed regions to strain faster. Consequently, the rate of thickening at the indenter corner increases with D/L and is closer in magnitude to the 2D solution. Another consequence of increasing D/L is that the maximum crust and layer thicknesses in the 3D calculations also increase (Table 5.2a).

5.4.5 Discussion

The comparison between 2D and 3D calculations of indentation have highlighted differences between the TVS approximation and the full 3D implementation for a collision-type model. The magnitude of the differences depends on the parameters n, Ar, D/L and on the total convergence. Larger values of Ar result in a more accurate TVS estimate, whilst larger values of n cause the solutions to diverge. At time zero, the 2D and 3D solutions converge as D/L is increased. The greatest difference between 2D and 3D solutions occurs systematically at the indenter corner. The TVS approximation neglects vertical shear tractions, so errors that scale with the horizontal gradients of strain rate are introduced. These errors increase with n and decrease with Ar (Table 5.2b). For small Argand numbers, vertical strain rates near the indenter corner may be in error by 50% or more.

Evolution of layer thickness

The ability of the stress-supporting layer to vary in thickness through time in 3D is one important contributor to differences between 2D and 3D solutions. In-plane stress is always distributed over a constant layer thickness (L) and consequently the 2D strain rate is overestimated compared with the 3D solution after the thickened lithospheric root develops (i.e. when $t > 0$). Moreover, this difference amplifies with both time

and increasing D/L. Because deformation in the 3D model is described in terms of the full 9-component stress tensor, vertical gradients of horizontal velocity develop (Figure 5.4e), which can not exist in the TVS. Although the crustal thickness distribution can be estimated from 2D TVS calculations, the variation of strain rate with depth is lost. In particular, in 3D calculations the lithospheric root may be forced ahead of the upper lithosphere in the collision zone.

Horizontal length scale

The TVS approximation is most accurate when the modelled layer is thin compared to the length scale (i.e. $D >> L$). The tendency of the 2D and 3D solutions to converge as D/L is increased confirms the validity of the TVS for larger values of D/L. However, when horizontal gradients of strain rate are large (i.e. D/L is small in these experiments) it is clearly preferable to use a fully 3D model. Of present-day orogens resulting from continent-continent collision, the India-Asia system (e.g. Dayem et al., 2009a,b) and the European Alps (e.g. Robl et al., 2008) have recently been modelled using the 2D TVS approximation. The half-width of the Indian indenter is approximately 1250 km. In contrast, the half-width of the Adriatic indenter is approximately 250 km. Assuming a pre-collisional lithospheric thickness of 100 km as in the models here (Table 5.1), these half-widths correspond to D/L ratios of 12.5 for the India-Asia collision and 2.5 for the Alpine collision. The observations in §5.4.4 show that certainly the length scale of the India-Asia system satisfies the condition $D >> L$ required by the TVS approximation. England and Houseman (1986) found that the best match between a TVS model (with no lateral strength heterogeneities) and topography in the Tibetan plateau occurred with $Ar \leq 1$ when $n = 3$, or $Ar \leq 3$ when $n = 10$. For these parameter ranges there are significant differences between the 2D and 3D solutions close to the indenter when $D/L = 1$ (Figures 5.6c and f). While increasing D/L to 12.5 will reduce the errors in the 2D solution attributed to the neglect of vertical shear tractions, increasing D/L will also increase those errors attributed to the 2D assumption that the stress bearing layer is of constant thickness (Figure 5.10). Clearly the TVS should be treated with some caution whenever large gradients of strain rate are expected (e.g. at a syntaxis) or when n is large. Despite this, the TVS is a valuable and useful approximation in parts of the solution not affected by large gradients of strain rate even when D/L is as low as 1.

Rheological layering

In this work the impact of sub-horizontal layering in the rheological properties of the models has not been considered. Strong vertical variations in strength can cause important changes to the mode of deformation within the lithosphere. For instance, Schmalholz et al. (2002) argue that under the conditions favoured by England and Houseman (1986) the lithosphere will deform by a combination of homogeneous thickening and folding. Furthermore, folding should dominate at the indenter corners. The use here of rheological parameters that are invariant with both horizontal position and depth, and the choice of upper boundary condition prevents deformation by thrusting or folding. Despite this, the calculations clearly reveal the physical processes that underlie the geometrical differences between 2D and 3D models without introducing additional complications. However, there is clearly scope for further investigation of the collision problem in the presence of a layered rheological structure.

Lechmann et al. (2011) analyse the differences between a 2D TVS model and a rheologically layered 3D model using a similar model set-up as presented here. In the horizontal plane, they assign free-slip conditions parallel to the model boundaries, whereas I used rigid conditions (Figure 5.2) like the set-up of Houseman and England (1986). Whereas the top surface cannot move vertically in the models presented here, Lechmann et al. (2011) instead chose to apply this condition to the base of their model. Instead of varying the model geometry and Ar as in the experiments presented here, Lechmann et al. (2011) fixed D/L at $\sim$1.04 and Ar at 2.98 (when $n = 1$) or 3.63 (when $n = 3$). They concentrate on analysing the effect of a simple 4-layered rheology on the viscous deformation style in the 3D model. A power-law viscous model exhibits both folding and lower crustal flow occurring with the same importance as homogeneous thickening. Additionally, folding and crustal flow are most significant at distances on the order of the indenter half width from the indenting boundary ($\sim$100 km in their case). Lechmann et al. (2011) also find that differences between TVS and 3D models are greater for a $n = 3$ rheology than the linear case. However, they corroborate my findings that the TVS adequately reproduces the long wavelength features of the deformation field.

Basal shear stress

The contribution of basal shear stress has also been neglected in these calculations. Ghosh et al. (2008; Appendix D) calculate the present day deviatoric stress field in a global thin sheet calculation and compare with the output of a 3D mantle convection model. They find that two components are required in the force balance before the deviatoric stress fields of thin sheet and 3D models are equivalent. The first is a GPE term calculated by vertically integrating the vertical stress down to a reference level at 100 km depth, as used in the classic TVS approximation (RHS of Eq. 5.14). The second term relates to shear tractions which are applied at the base of the sheet by density driven mantle circulation (an additional $\tau_{\alpha z}(L)$ term on the RHS of Eq. 5.14). Without the basal tractions, Ghosh et al. (2008) conclude that the thin sheet model underestimates the total deviatoric stress field by approximately 50%. Their calculation highlights the possible importance of basal shear stress in any lithospheric-scale geodynamic models. However this importance is limited regionally by the variability of the resolution in the modelled mantle flow field.

Calculation cost

A further consideration when choosing between 2D and 3D calculations is the much greater computational cost involved with 3D. Even at $D/L = 4$, the cost of 3D calculations is high. So for any experiment with $D/L > 4$ it can be cost effective to use 2D calculations for initial exploration of the parameter space. Subsequent 3D calculations can then be used to focus on smaller areas of the parameter space, where high strain rate gradients are indicated.

Summary

In summary, the results show that the TVS approximation is adequate to model long wavelength deformation for D/L as low as 1 providing that n is less than $\sim$3. However, a fully 3D model is required to obtain accurate solutions wherever the horizontal gradients of deformation are high, for example close to an indenter corner.

Chapter 6

Thin Viscous Sheet models of Tibet

In this Chapter I explore the question of whether the TVS approximation can be used to explain the present-day velocity field observed in Asia. Flesch et al. (2001), Whitehouse (2004), England and Molnar (2005) and Vergnolle et al. (2007) all comment that some lateral heterogeneity in strength will be required in order to get a good fit to the geodetic velocity field.

In order to test this assertion, I use instantaneous (i.e. time zero) calculations that determine the balance of forces within the lithosphere, depending on the boundary conditions applied and an assumed spatial variation of GPE throughout the model region. This method contrasts with previous TVS studies that have concentrated on the evolution through time of finite strain in Asia (e.g. Houseman and England, 1986, England and Houseman, 1989, Dayem et al., 2009a,b). To model finite strain evolution numerically a simplified geometry must be used, similar in style to that described in §5.4.1. However, when the instantaneous deformation field is modelled, a realistic boundary and internal geometry can be implemented in 2D calculations.

6.1 Model set-up

TVS equations describing deformation of a thin spherical shell are used in the *Basil* program (after Houseman, 2003). Instead of Cartesian coordinates x, y and z, the spherical coordinate system is based on the radius, co-latitude and longitude. An advantage of the spherical coordinate system is that velocity boundary conditions can be given in the form of an angular velocity around an Euler pole of rotation. Therefore an-

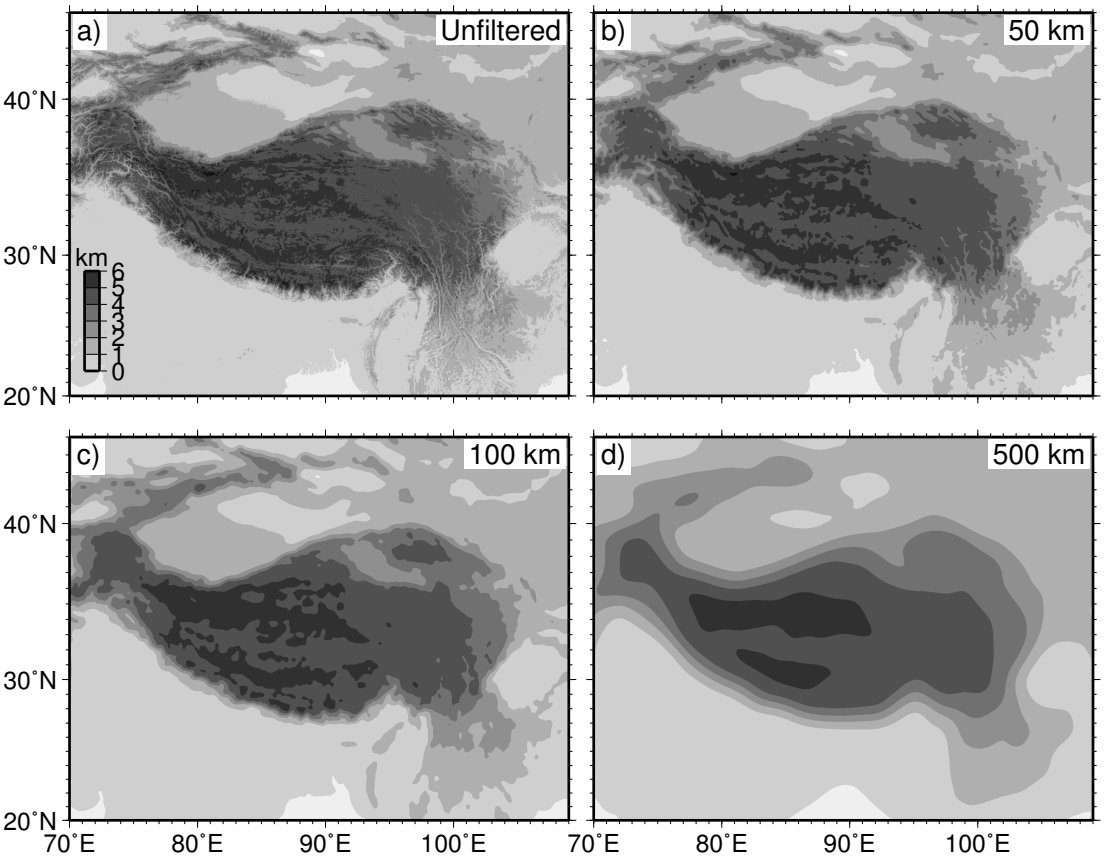

Figure 6.1: Smoothing of Asian topography by Gaussian filtering. a) Original topography, and smoothed topography with b) 50 km, c) 100 km and d) 500 km filter diameters.

gular velocities from global plate tectonic models can be used to constrain the modelled velocity field, with velocity increasing with distance from the Euler pole. Additionally, real data sets (such as topography) can be mapped on to the numerical solution, and model predictions (such as the relative velocity field) can be easily mapped onto the Earth.

6.1.1 GPE distribution from topography

The lateral distribution of GPE in the lithosphere is determined using Eq. 1.6 and the observed topography in the model region. This relationship assumes that the crust and mantle have constant density, that the topography is isostatically compensated and that variations in crustal thickness are the sole contributions to GPE. As discussed in §2.5, this oversimplifies the situation in southern Tibet where the under-thrust Indian lithosphere provides additional flexural support (Lyon-Caen and Molnar, 1985). By using $\rho_c = 2800$ kg m^{-3}, $\rho_m = 3270$ kg m^{-3}, $S_0 = 38$ km and $e_0 = 0.65$ km, an

elevation of 5 km implies a crustal thickness of ∼68 km. These values of S_0 and e_0 are the average values for continental crust given by the global 2°x2° resolution model CRUST2.0 of Laske et al. (after Mooney et al., 1998). A study of continental hypsometry with a similar spatial resolution (Harrison et al., 1983) finds a global mean continental elevation of 0.692 km but a mean value of 0.756 km for the Asian continent; increased on account of the Tibetan plateau.

Erosion at the Earth's surface results in the superposition of short wavelength features on top of the much broader regional topography. Due to the lack of erosional processes within the Earth, we can expect Moho topography to reflect the morphology of long wavelength surface topography. Therefore to avoid aliasing short wavelength features, I use a smoothed version of the topography. A 1-arc-minute DEM derived from SRTM data is smoothed by Gaussian filtering with a 6-sigma diameter window. Figure 6.1 shows the results of smoothing the DEM in this way with filter diameters of 50, 100 and 500 km. Too much smoothing results in the reduction of steep topographic gradients (e.g. across the Himalaya) and some features disappearing (e.g. the Qilian Shan cannot be distinguished from the Qaidam basin). However with minimal smoothing (50 km radius filter), considerable short wavelength features can still be seen. As a compromise between these two trade-offs, I used the 100 km filtered topography in the following numerical calculations.

In order to determine the topography at each node of the finite element mesh, *Basil* transfers the regularly-spaced filtered topography data on to the nodes of the triangular finite element mesh using bilinear interpolation. Crustal thickness values are then calculated using the isostatic assumption in order that gradients of gravitational potential energy can then be calculated using Eq. 5.23.

6.1.2 Strength regionalisation

As discussed in §2.2.1, evidence from seismicity, heat flow measurements and elastic thickness estimates suggest that the strength of the lithosphere varies laterally across Asia (Molnar and Tapponnier, 1981, Wang, 2001, Braitenberg et al., 2003). Many studies that use the TVS to describe deformation in Asia have found that including these lateral strength heterogeneities will be required before a model can describe all the features of the present-day velocity field (e.g. Flesch et al., 2001, Whitehouse, 2004, England and Molnar, 2005, Vergnolle et al., 2007) and the present-day crustal thickness

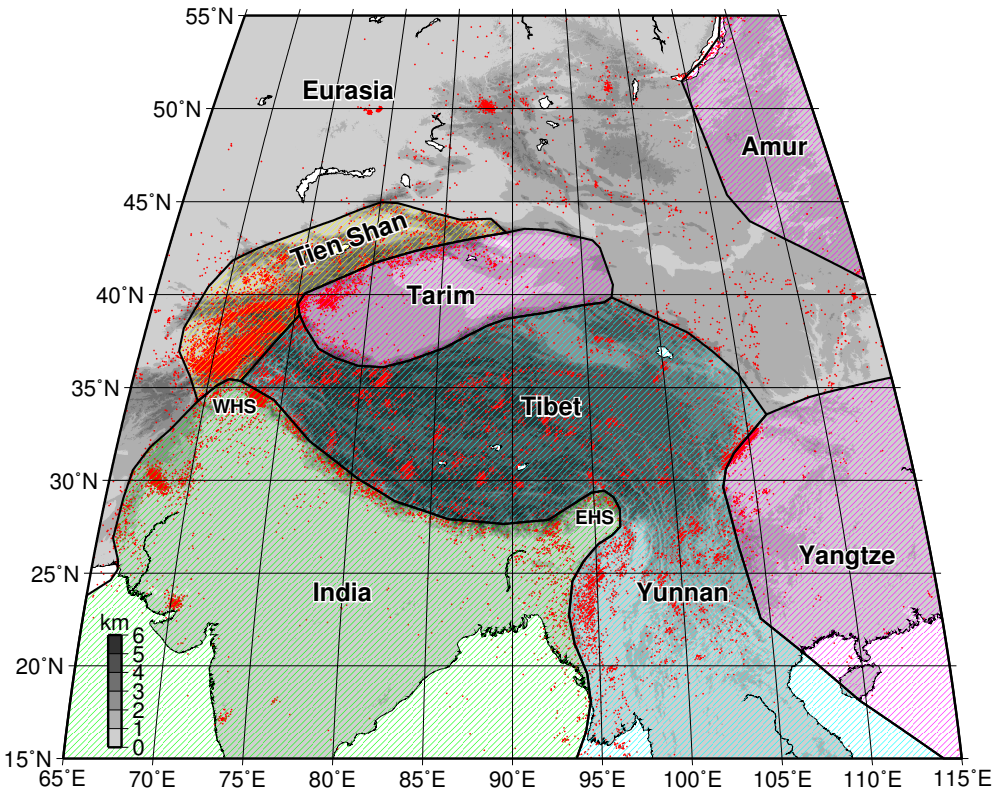

Figure 6.2: Regionalisation of the TVS model domain based on topographic variation and earthquake locations. Plotted as red dots are all earthquakes above M3.0 in the USGS catalogue (1973-2010). Grey-scale background is the unfiltered 1 arc-minute SRTM topography. Regions of magenta coloured hachure are those that are relatively rigid in the models ($B = 10$). Regions of yellow and blue coloured hachure are those that could be weaker than average lithosphere, and therefore the strength coefficient B is set to a value less than one in the model calculations. EHS and WHS mark the eastern and western Himalayan syntaxes respectively.

distribution (Neil and Houseman, 1997).

I have chosen a regionalisation of lithospheric strength based on the observed topography and the recent pattern of seismicity as indicated in Figure 6.2. The strength contrast between different regions is parameterised in the calculations via the non-dimensional coefficient B (Eq. 5.15), which represents the depth-integrated effective viscosity coefficient.

The foreland region of the Eurasian lithosphere north of the Tibetan plateau is assigned a value of $B = 1$. Six other regions are defined whose strength attributes differ significantly from the background Eurasian lithosphere. Three regions correspond to the Tarim, Amur and Yangtze (south China) blocks (magenta in Figure 6.2) that are known to be relatively rigid (e.g. Holt et al., 2000, England and Molnar, 2005). In all models presented in this thesis, $B = 10$ for these regions, which is enough to

render them as undeforming entities. In order that the Himalayan arc can be used as a model boundary, the Indian region (green in Figure 6.2) is not included in the model calculations. The Tibet region (blue in Figure 6.2) encompasses the high topography bounded by the India, Tarim and Yangtze regions. The north-east boundary is marked by the outboard edge of the Qilian Shan. In the calculations of §6.3, the strength in the Tibet region is reduced; B takes values between 0.1 and 1. The Tibet region also includes the Yunnan region sandwiched between the India and Yangtze regions, and also parts of the Indo-China peninsula. In some plate models Indo-China is described by a separate 'Sundaland' plate. I have not included this plate as a separate region in order to reduce the overall complexity of the model. The Tien Shan region includes the orogen north of the Tarim region, and includes the Pamir at the western end of the Himalaya. In the following calculations, the strength of the Tien Shan region is equal to that of Tibet.

6.1.3 GPS observations

To test the velocity field predicted by a model, RMS misfits between model and GPS velocities are calculated:

$$V_{\mathrm{RMS}} = \left(\frac{\sum_{i=1}^{N} \left(V_E^{\mathrm{obs}} - V_E^{\mathrm{mod}}\right)^2 + \sum_{i=1}^{M} \left(V_N^{\mathrm{obs}} - V_N^{\mathrm{mod}}\right)^2}{N+M} \right)^{\frac{1}{2}} . \tag{6.1}$$

A subset of GPS velocities from the data sets of Calais et al. (2006), Gan et al. (2007) and Zubovich et al. (2010) are selected and their station locations used as nodes in the finite element mesh. The velocities from the three data sets are given with respect to slightly different reference frames and so they must first be rotated into a common reference frame. I use a least squares inversion to find the rotation vector that minimises the misfit between the velocities at sets of co-located stations from each data set (e.g. Holt et al., 2000). The data set of Gan et al. is used as the reference into which both other data sets are transformed since this data set shares numerous stations with the other two. Calais et al. and Gan et al. have 46 co-located stations in the model region (5 additional co-located points are located on the Indian plate, but are not used here). Zubovich et al. and Gan et al. have 21 co-located stations. Transformed co-located velocities are plotted in Figure 6.3 and the full combined data

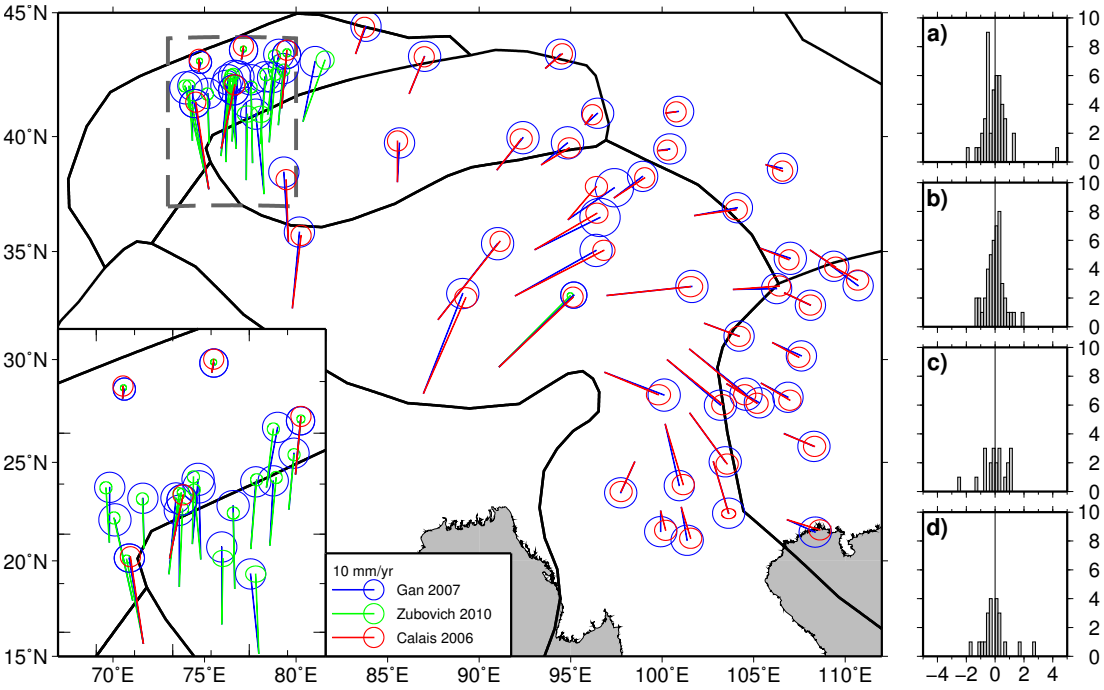

Figure 6.3: Co-located GPS measurements used to compute transformation parameters between the three GPS data sets Gan et al. (2007), Calais et al. (2006) and Zubovich et al. (2010). Plotted vectors are transformed to the frame of Gan et al.. Black lines show the chosen model region boundaries (see §6.1.2). Inset map in the main figure is an enlargement of the area in the grey dashed box. Histograms show the least squares residuals in bins of 0.2 mm/yr for east (a) and north (b) components of Calais et al. (46 points), and east (c) and north (d) components of Zubovich et al. (21 points).

set is plotted in Figure 2.6.

The combined GPS velocity data set is then decimated so that the finite element mesh does not contain closely spaced nodes that would result in excessively small triangular elements. Firstly, GPS points are removed if the 1-sigma error on either north or east component is greater than 4 mm/yr. A thinning algorithm is then applied that searches for the closest point to each node of a 1°x1° grid. Following this, individual stations are manually removed if they are located on the Indian plate, or are within close proximity to an internal boundary (see §6.1.2). The decimated GPS data locations used in the models are plotted in Figure 6.4.

Localised misfit between model predictions and observed GPS velocities may be explained in some instances by measurement error or local tectonic conditions. However, the systematic variation of the velocity observations shown in Figure 2.6 suggests that on a regional scale the measurements are well resolved and adequately represent the actual continental deformation field.

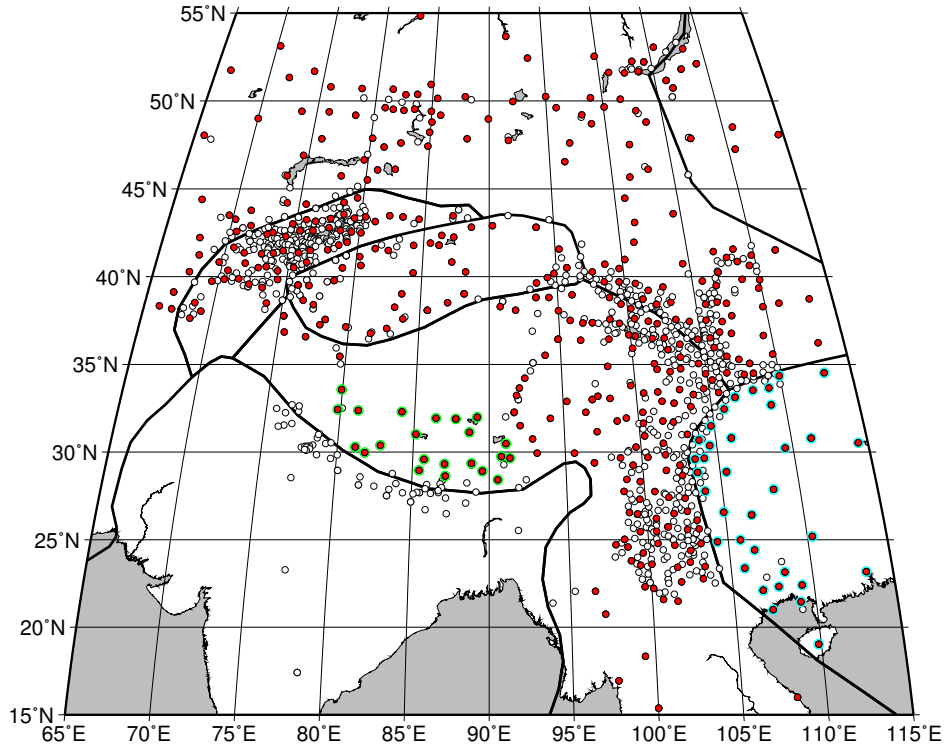

Figure 6.4: Decimated GPS points used to test the models. Circles show all 1307 points from the combined GPS data set within the model region. Red circles show the selected 416 data points which are used to test the finite element calculations. White points are those GPS velocities that are not used. Points with a cyan outline are the 35 used in §6.5. Points with a green outline are the 22 used in §6.4.

6.1.4 Boundary conditions

Since the GPS observations of Gan et al. (2007) are given in a stable Eurasia reference frame, the model is also calculated in this frame. The northern and western boundaries are chosen to be distant enough from active deformation that a zero velocity condition can be imposed for both east and north components on these boundaries. Where non-zero velocity boundary conditions are used, they are defined using poles of rotation from the MORVEL global plate model (Table 6.1, DeMets et al., 2010). The angular velocities of tectonic plates in the Asia region with respect to the Eurasian plate from the MORVEL model are shown in Figure 2.1.

Model boundaries intersected by the Amur and Yangtze regions are given the relevant MORVEL displacement rates. Due to their relative rigidity, these regions have a plate-like velocity field which does not change with variation of the other model parameters. The contribution to the misfit from the GPS points in these regions is

Table 6.1: MORVEL Euler poles and angular velocities with respect to fixed Eurasia (DeMets et al., 2010).

Plate	Longitude (°E)	Latitude (°N)	ω (deg/Ma)	ω (10^{-3} rad/Ma)
India	17.3	31.7	0.477	8.325
Amur	138.3	66.9	0.106	1.850
Yangtze	168.6	78.4	0.132	2.303
Sundaland	-73.2	49.1	0.120	2.094

therefore a constant in these models. The portion of the boundary between Amur and Yangtze is tapered between the velocities of these regions using a quarter wavelength of a squared-cosine function to ensure a smooth variation of velocity at the ends of this boundary segment.

The southern boundary segment between India and Yangtze runs through the region often named as Sundaland in plate models. In the models presented here, I choose to set a zero velocity boundary condition on this southern boundary on account of the low observed GPS velocities (Figure 2.6). Due to the low angular velocity of Sundaland in the MORVEL model, the difference between choosing a zero velocity or MORVEL velocity boundary condition here would make very little difference to the velocity field in the most actively deforming parts of the model.

I experiment with velocity and traction boundary conditions for the part of the model boundary created when the Indian block is removed from the finite element mesh. Using a velocity boundary condition on the Himalayan arc is complicated by the fact that ~20 mm/yr of convergence (approximately one third of the total) is accommodated by internal deformation of a narrow zone around the Himalayan mountain range (e.g. Bilham et al., 1997, Banerjee and Bürgmann, 2002; see Figure 2.7). Therefore, when using an applied velocity boundary condition on the Indian boundary I use the MORVEL India plate rotation rate reduced by 33%. A squared-cosine taper is used over a small distance at the intersections between the Indian boundary and the adjacent model boundaries in order to ensure a continuous transition of velocity.

In other models, I apply a constant boundary-normal traction to the Indian boundary via the dimensionless Γ parameter. The sign of Γ is negative, which results in an inward push acting on the boundary, in this case mimicking the stress imparted on Eurasia by the advancing Indian plate. Orientations of the principal stress field from

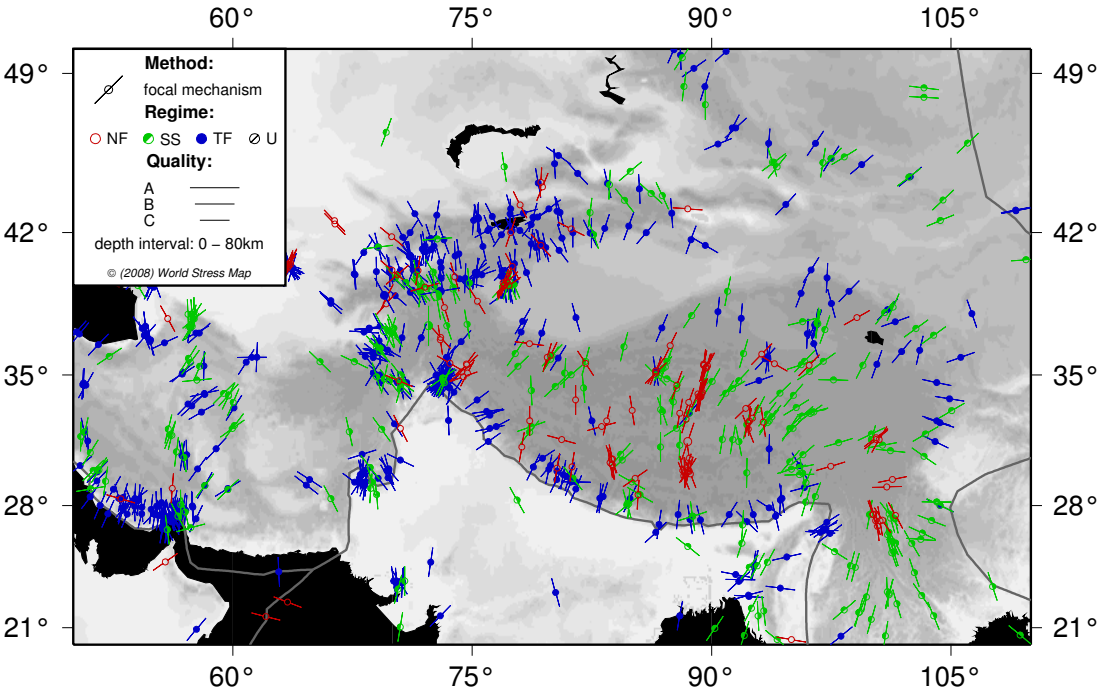

Figure 6.5: Orientations of the maximum horizontal principal stress field in Asia derived from focal mechanisms within the upper 80 km. Note that plate boundaries differ from those used in the TVS model regionalisation shown in Figure 6.2. Map produced using the online 'CASMO' tool using data from the World Stress Map project (Heidbach et al., 2008).

the World Stress Map (Heidbach et al., 2008) around the Himalayan arc indicate that the maximum horizontal stress direction is normal to the Himalayan arc (Figure 6.5).

The instantaneous velocity field depends on the interplay between the inwardly acting boundary force and the outwardly acting force generated by the greater GPE within the Tibetan plateau compared to the surrounding lowlands (see §1.3.3). For a particular calculation, an iterative procedure is followed to find the dimensionless Γ value that gives the minimum RMS misfit between the model and observed velocities.

I experiment with two versions of the traction boundary condition. The first has the normal traction component set for the entire Indian boundary (referred to as 'traction' boundary condition). The second has the traction condition set for the Himalayan arc between the eastern (EHS) and western (WHS) syntaxes (corresponding to the high topography). In this second case, the Indian boundary segments outside of the Himalayan arc have a zero velocity condition (referred to as 'composite' boundary condition).

Table 6.2: Values used to scale the dimensionless parameters in TVS models of Tibet.

L	=	100 km
R	=	6378 km
S_0	=	38 km
e_0	=	0.65 km
U_0	=	14.69 mm yr^{-1}
ρ_m	=	3270 kg m^{-3}
ρ_c	=	2800 kg m^{-3}
g	=	9.81 m s^{-2}

6.1.5 Dimensionalisation

Table 6.2 gives the parameters for scaling the non-dimensionalised model output. As in §5.2.4, the calculations are non-dimensionalised based on a length scale L and a velocity scale U_0. The assumed layer thickness is $L = 100$ km and the horizontal length scale is $R = 6378$ km, equal to one radian of the Earth's circumference (and also the radius since the circumference equals $2\pi r$). The ratio $R/L = 63.78$ for the spherical sheet models used here is broadly consistent with $D/L = 12.5$ for Tibet in §5.4.1, where D is defined as the indenter half-width.

Since deformation is sometimes driven by a traction boundary condition, the indentation velocity is not used for scaling the problem. Instead, the calculated velocity field is scaled to the angular velocity of the Yangtze plate using the expression:

$$U_0 = \omega R \tag{6.2}$$

in which ω is in units of rad Ma^{-1}. The observed GPS velocity field near the boundary between Yunnan and the Yangtze block indicates that the Yangtze motion is not controlled by the India-Asia collision but instead acts as an obstruction to motion of the Tibetan lithosphere. It is possible that the motion of Yangtze is controlled by forces associated with the Pacific subduction occurring on the block's eastern boundary (e.g. Houseman and England, 1993). On account of its relative rigidity and defined velocity, the solution in the Yangtze plate does not vary between different model calculations. Therefore, I choose to use the Yangtze rotation rate (Table 6.1) and Eq. 6.2 to define the dimensional velocity scale U_0 quoted in Table 6.2.

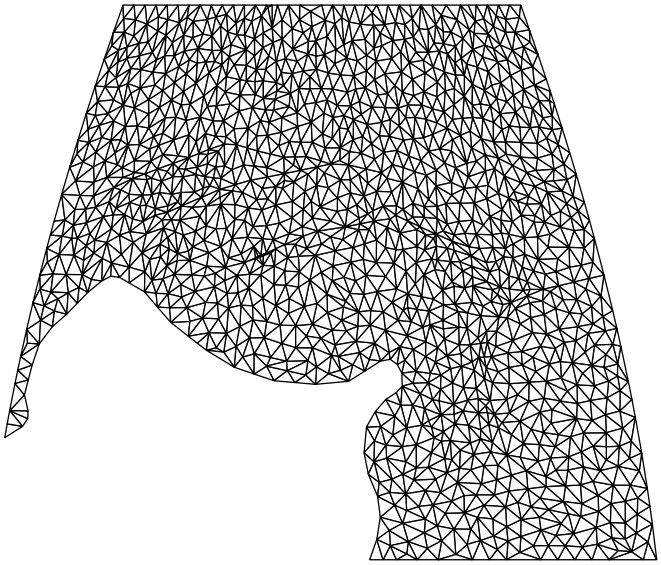

Figure 6.6: Finite element mesh used in the calculations generated using Delaunay triangulation. Corresponds to mesh D in Table 6.3 with an average element area of 5655 km^2.

The stress scale is defined by substituting Eq. 5.22e into Eq. 5.24:

$$\tau_0 = \frac{g\rho_c L(1 - \rho_c/\rho_m)}{Ar}. \tag{6.3}$$

Equation 6.3 ensures that the stress scale is consistent with the choice of Argand number. The Argand number is a variable parameter in these calculations, but constant for any particular experiment. With velocity and length scales defined, Eq. 5.22e can be used to define the scaling parameter for the viscosity coefficient B_0. The scale stress represents the vertical forces arising at the base of the layer due to GPE contrasts. For the parameters of Table 6.2 and $Ar = 1$, $\tau_0 = 394.8$ MPa.

6.1.6 Finite element mesh

The finite element mesh is generated using a Delaunay triangulation implemented by the *Triangle* program of Shewchuk (1996). The resolution of the mesh was tested using a calculation with a velocity boundary condition for the Indian boundary segment, $n = 3$, $Ar = 1$, $B = 1$ for Tibet and Tien Shan and element length scales on the order of ∼35-123 km (Table 6.3). By decreasing the element size, the computational cost increases and the accuracy increases marginally. However, the discretisation error is much less than 1% of the model misfit even for the coarsest mesh. These tests show that discretisation error is negligible in the following calculations, which use mesh D. I

Table 6.3: Results of resolution tests of the finite element mesh for the 416 nodes co-located with GPS stations. For mesh A, with the smallest element area, the RMS misfit between model and GPS velocities in mm/yr is quoted. For each coarser mesh, the RMS misfit between that solution and the mesh A solution normalised to the RMS values of mesh A and expressed as a percentage, is quoted. Differences can be interpreted as the increase in model discretisation error. Total mesh area is $\sim$14.7x10^6 km^2.

Mesh	# elements	Avg. area (km^2)	Run time (s)	V_E^{RMS}	V_N^{RMS}	$V_{\mathrm{tot}}^{\mathrm{RMS}}$
A	24005	613	528	5.51	7.28	22.35
B	12407	1186	182	0.20%	0.22%	0.06%
C	4915	2995	44	0.32%	0.40%	0.11%
D	2603	5655	15	0.49%	0.56%	0.15%
E	1959	7514	11	0.62%	1.30%	0.32%

chose mesh D after considering the trade-off between computation time and accuracy (Figure 6.6). The mesh is sufficiently fine that its constituent elements are relatively homogeneous in area, even when allowing the constraint of forcing a set of node locations to coincide with the chosen GPS locations (Figure 6.4). However, some elements close to internal model boundaries are required to be smaller in area.

6.2 Models with no strength contrast

Firstly, I describe calculations for models with no strength contrast between Tibet, Tien Shan and the surrounding Eurasian lithosphere (i.e. $B = 1$ for these regions). There are two variable parameters in these experiments, n and Ar, which are both varied between 1 and 10. The three driving boundary conditions are tested on the Indian boundary as described in §6.1.4.

Figure 6.7 shows the velocity field for the $n = 10$, $Ar = 1$ calculations for each boundary condition. At face value these model velocity fields look very similar, though there are some important differences. However, none of these models give a satisfactory fit to the main features of the observed velocity field, particularly the orientation of velocities in Yunnan, Tarim and Tien Shan. The magnitudes are about right in Tarim but too high in the Tien Shan for the velocity boundary condition. The opposite situation is true for the traction and composite boundary conditions. In south Tibet, the best fit to the observed velocity magnitudes is seen with the composite boundary, but the best vector directions are seen with the velocity boundary condition. At the EHS, observed velocity vector directions rotate in a clockwise fashion. The velocity boundary condition does not promote this motion, but instead provides a high magnitude motion

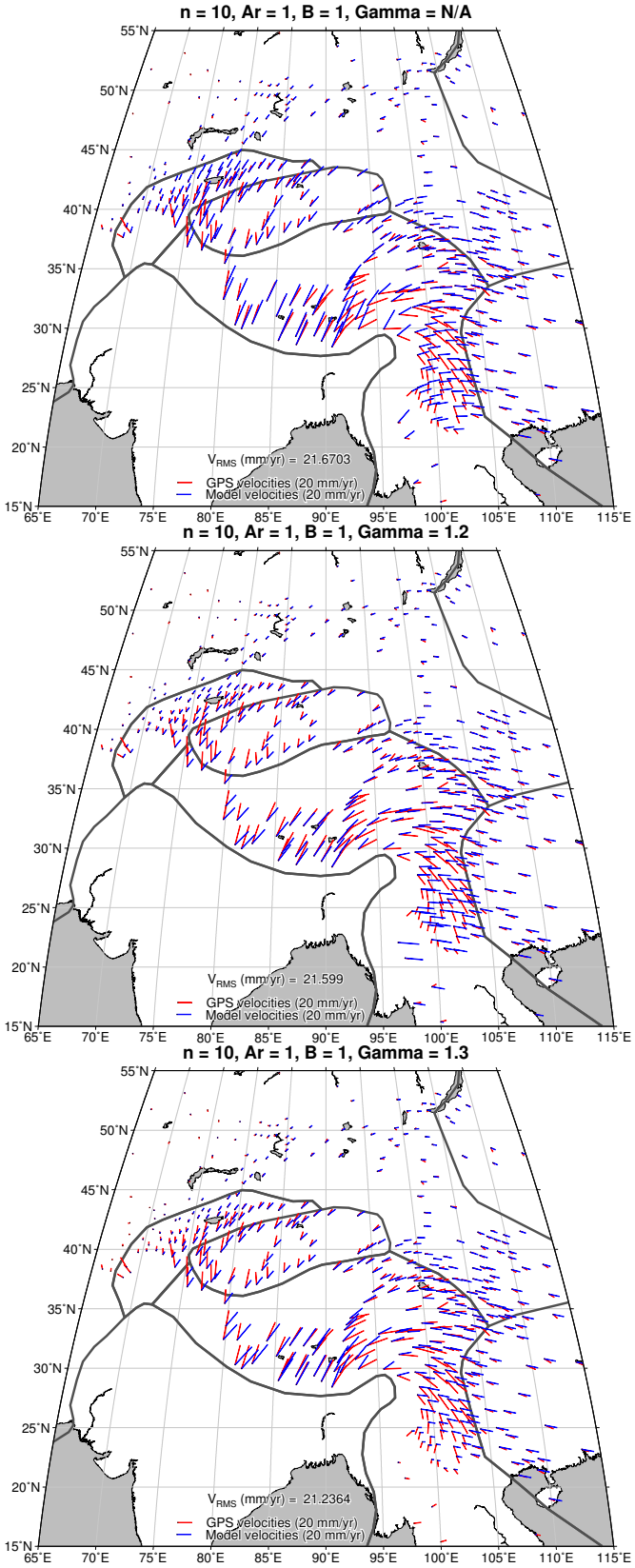

Figure 6.7: Comparison of model and GPS velocities for calculations with different boundary conditions for India. The three models shown are for $n = 10$ and $Ar = 1$; parameters which produced the minimum RMS misfit to data when $B = 1$ in the Tibet and Tien Shan regions. The three plotted models make use of the velocity (top), traction (middle) and composite (bottom) Indian boundary conditions as described in §6.1.4.

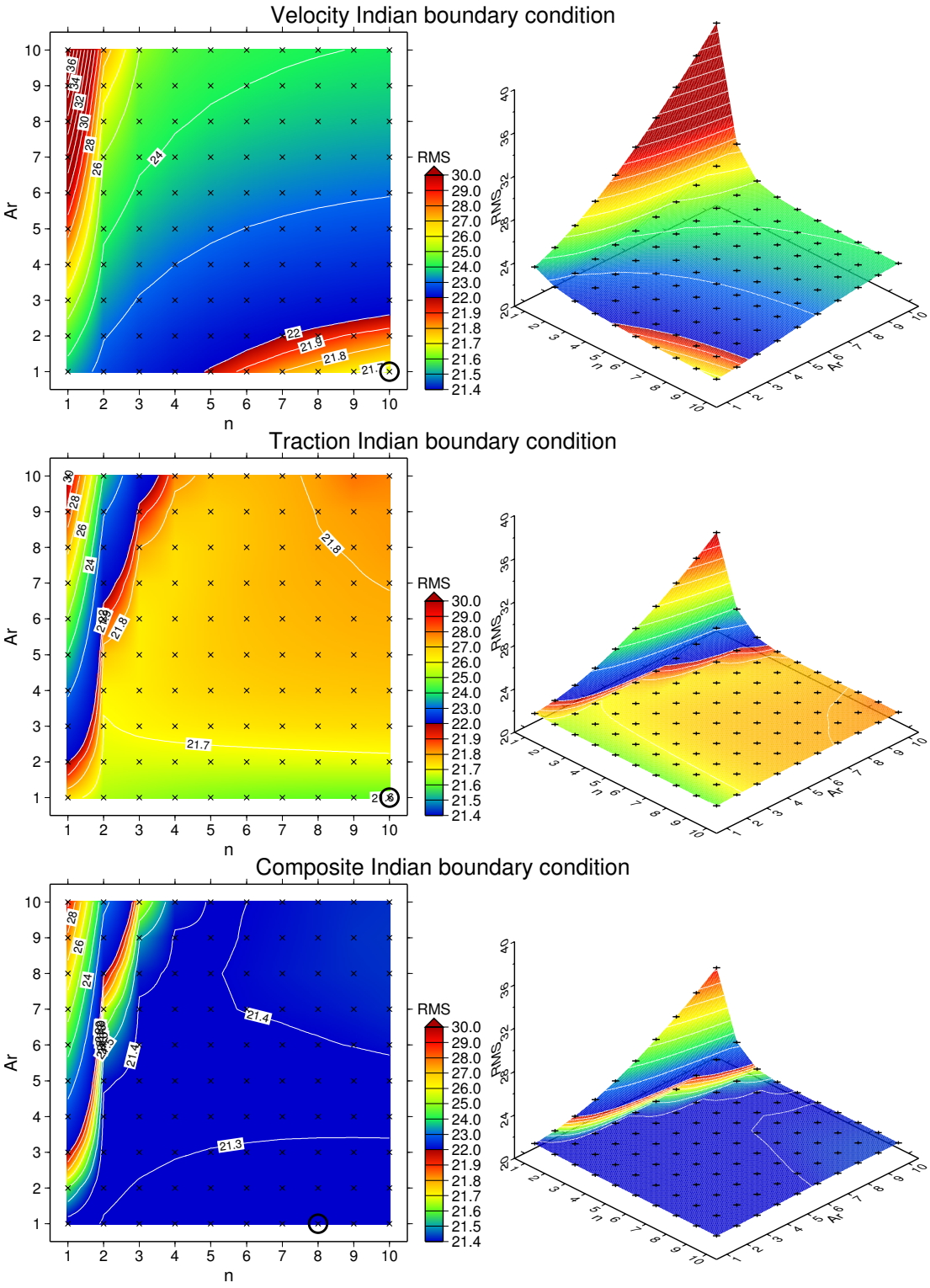

Figure 6.8: RMS misfit (mm/yr) between model and GPS velocities in the parameter space n versus Ar. Boundary condition for the Indian boundary is velocity (top), traction (middle) and composite (bottom) as discussed in §6.1.4. Both plan (left) and perspective (right) plots show the RMS surface after bilinear interpolation through the parameter space. Individual calculations are marked as black crosses. The calculation with minimum RMS misfit is highlighted with a black circle.

in a north-eastward direction. The traction and composite conditions, however, allow a larger component of eastward motion in this region.

South-east of the EHS, observed velocities rotate through south-east to a southerly direction in Yunnan. None of the three boundary conditions allow for this southerly motion in Yunnan. Instead, it appears that motion in this region of the model is influenced primarily by the eastward pull of Yangtze as vectors in the adjacent region of Yunnan align with motion of the Yangtze plate. The main contribution to the difference between the composite and traction models comes from the velocity field in the Yunnan region. Setting a normal traction on the Indian boundary between the EHS and the Indian ocean promotes a net-flux of material eastward away from this boundary. Setting a zero velocity boundary instead demonstrates that although orientations are inaccurate, velocity magnitudes can decay with southward position as seen in the observed velocities.

Figure 6.8 summarises the results of all calculations for which $B = 1$ in Tibet and Tien Shan; equal to the rest of the Eurasia region. Figure 6.8 shows the RMS misfit between model and GPS velocity fields computed at the 416 co-located mesh nodes. The RMS misfit surface is interpolated across the n vs Ar parameter space using the values obtained from 100 calculations for each boundary condition. High values of Ar coupled with low values of n yield very high misfits for all boundary conditions. For traction and composite conditions, the lowest RMS misfit is achieved with low Ar, but is not sensitive to the value of n providing it is greater than 1. Within the set of model parameters tested, the minimum misfit for the velocity boundary condition is comparatively well defined: $n = 10$, $Ar = 1$. Despite this, the true minimum lies outside the parameter space explored for all three driving boundary conditions. Figure 6.8 shows that for each boundary condition type, a calculation with $n = 10$ and $Ar = 1$ has the lowest (or close to lowest) RMS misfit for the parameter space explored.

Although $n = 10$, $Ar = 1$ provides the best fit of the experiments with no strength contrast, we see that the RMS misfit of these models is still at least 21 mm/yr (Figure 6.8). This is at least partly because of the failure of the models to predict the direction of movement in eastern Tibet and Yunnan. In the following section, I therefore consider the effect of decreasing the value of B in the Tibet and Tien Shan regions.

6.3 Models with weakened Tibet region

I further explore the parameter space using models with the composite Indian boundary condition, n taking the values 2, 3, 5, 8 and 10, and Ar taking the integer values between 1 and 6 inclusive. The strength in the combined Tibet and Tien Shan regions is also varied, taking values of B between 0.1 and 1 (which weakens the lithosphere in these regions relative to the foreland).

Figures 6.9 and 6.10 show the variation of RMS misfit between model and GPS velocity fields at the 416 co-located mesh nodes. Although minor improvement in RMS misfit (compared with the bottom panel in Figure 6.8) is obtained by using a reduced strength coefficient in the Tibet and Tien Shan regions, it remains above 20 mm/yr in all experiments presented here. For $n = 2$, 3 and 5, the lowest overall RMS misfit occurs when $Ar = 1$ and $B = 0.1$. However, the RMS misfit of ~21 mm/yr is not a significant improvement and visual inspection of the predicted velocity field (Figure 6.11) reveals a persistent misfit of vector directions, particularly in the Yunnan region.

Any mismatch of vector directions in south Tibet can result in a significant increase in RMS misfit due to the relatively large magnitude of the observed velocities. In particular, the low RMS misfit for $Ar = 1$, $n = 2$ or 3 models can be attributed solely to a good match in south Tibet, with poor fits in other parts of the solution region (e.g. Figure 6.11). Vector directions in south Tibet are strongly controlled by the interplay between the Argand number and to a lesser degree by the strength of the Tibet region. As Ar increases, buoyancy forces contribute more to the overall deformation field. Therefore when Ar is high, flow velocities can be fast around the plateau edges whilst vectors in south Tibet can be pointing radially outward from the plateau towards India. This shows that when Ar is high, deformation is primarily controlled by the GPE distribution, and the Himalayan boundary traction (Γ) has little influence on the overall deformation field.

Decreasing the strength of Tibet for any combination of n and Ar allows the vectors in Yunnan to become more southerly orientated and increases the magnitude of vectors within the Tarim and Tien Shan regions. Figure 6.12 shows profiles through calculations with $n = 3$ and $Ar = 2$ for $B = 0.25$ and 0.125. They show that for a relatively weak Tibet region ($B = 0.125$) the velocities are well fit in Yunnan but not in south Tibet. Conversely, when Tibet is stronger ($B = 0.25$), Yunnan is not well fit but the north

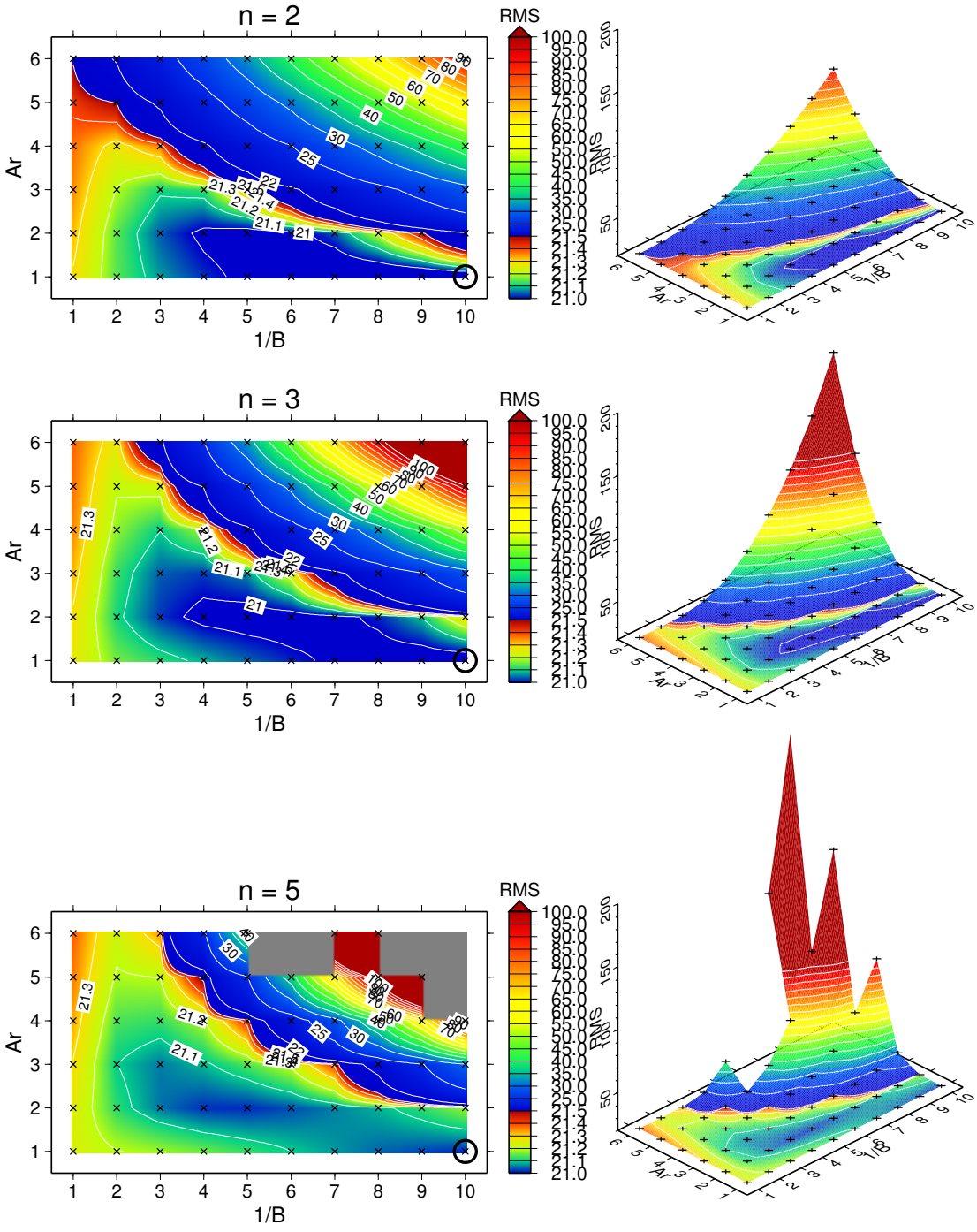

Figure 6.9: RMS misfit (mm/yr) between model and GPS velocities in the parameter space B versus Ar for $n = 2$ (top), $n = 3$ (middle) and $n = 5$ (bottom). Both plan (left) and perspective (right) plots show the RMS surface after bilinear interpolation through the parameter space. Individual calculations are marked as black crosses. Missing crosses are due to non-convergence of the solver. The calculation with minimum RMS misfit is highlighted with a black circle. All calculations use the composite Indian boundary condition.

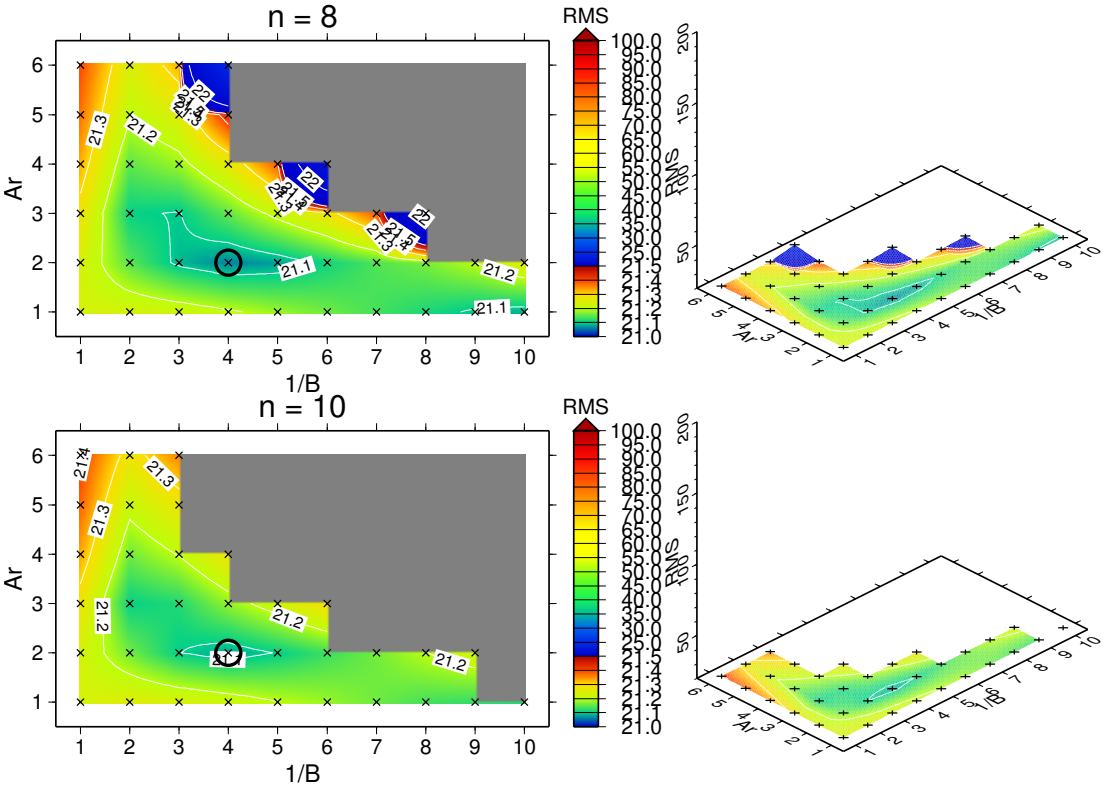

Figure 6.10: RMS misfit (mm/yr) between model and GPS velocities in the parameter space B versus Ar for $n = 8$ (top) and $n = 10$ (bottom). Both plan (left) and perspective (right) plots show the RMS surface after bilinear interpolation through the parameter space. Individual calculations are marked as black crosses. Missing crosses are due to non-convergence of the solver. The calculation with minimum RMS misfit is highlighted with a black circle. All calculations use the composite Indian boundary condition.

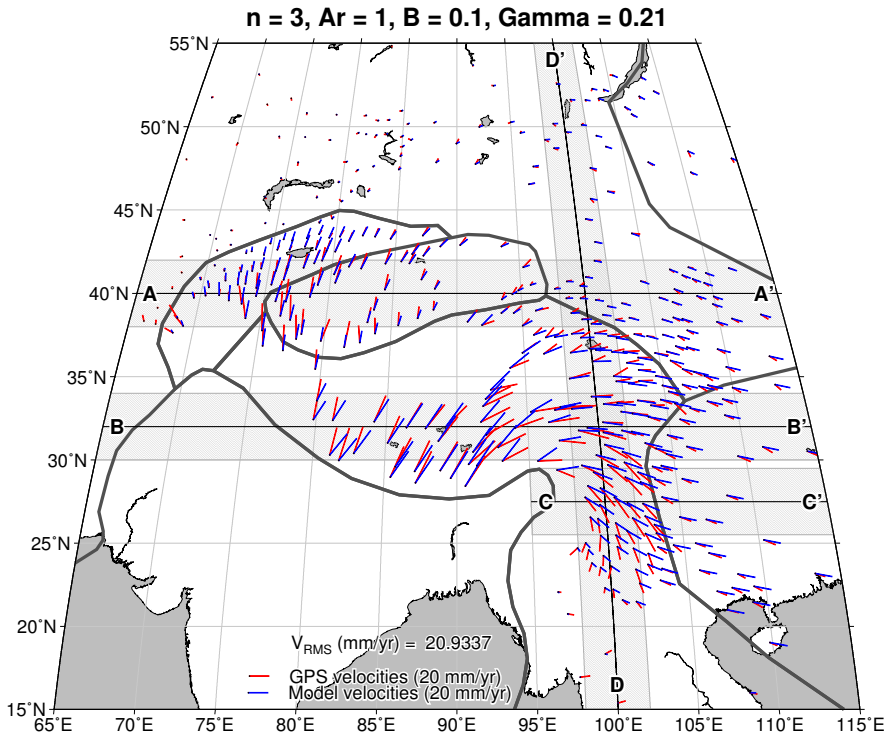

Figure 6.11: Comparison of model and GPS velocities for a calculation with $n = 3$, $Ar = 1$ and $B = 0.1$. The composite Indian boundary condition is used. Profile locations A-A', B-B', C-C' and D-D' are used in Figure 6.12. Grey polygons show the regions for which GPS are collapsed onto the profiles.

component of velocity in south Tibet is. In this example, profile A-A' shows that the velocity gradient through Tarim is similar for both cases. However, the magnitudes north of the profile in the Tien Shan do increase as B is decreased. At any n, when Ar increases the strength contrast required to give the best fit in Yunnan is decreased. In terms of RMS misfit, this situation occurs for models close to the contour adjacent to the region where the RMS misfit blows up (e.g. ~21.5 mm/yr in Figures 6.9 and 6.10 for $n = 2$, 3, 5, and 8).

When the vector orientations are most realistic in Yunnan, the orientations in Tarim and Tien Shan have an unrealistically large northward component. Although this mismatch in the Tarim and Tien Shan is observed for all values of n between 2 and 10, the effect is reduced as n increases. For a fixed value of B the vector magnitude in Tarim and Tien Shan tends to increase with Ar. The impact of increasing the influence of buoyancy forces can be seen in Figures 6.13 and 6.14 where vectors in Tarim/Tien Shan and Yunnan increase in magnitude with Ar, whereas magnitudes in south Tibet simultaneously decrease.

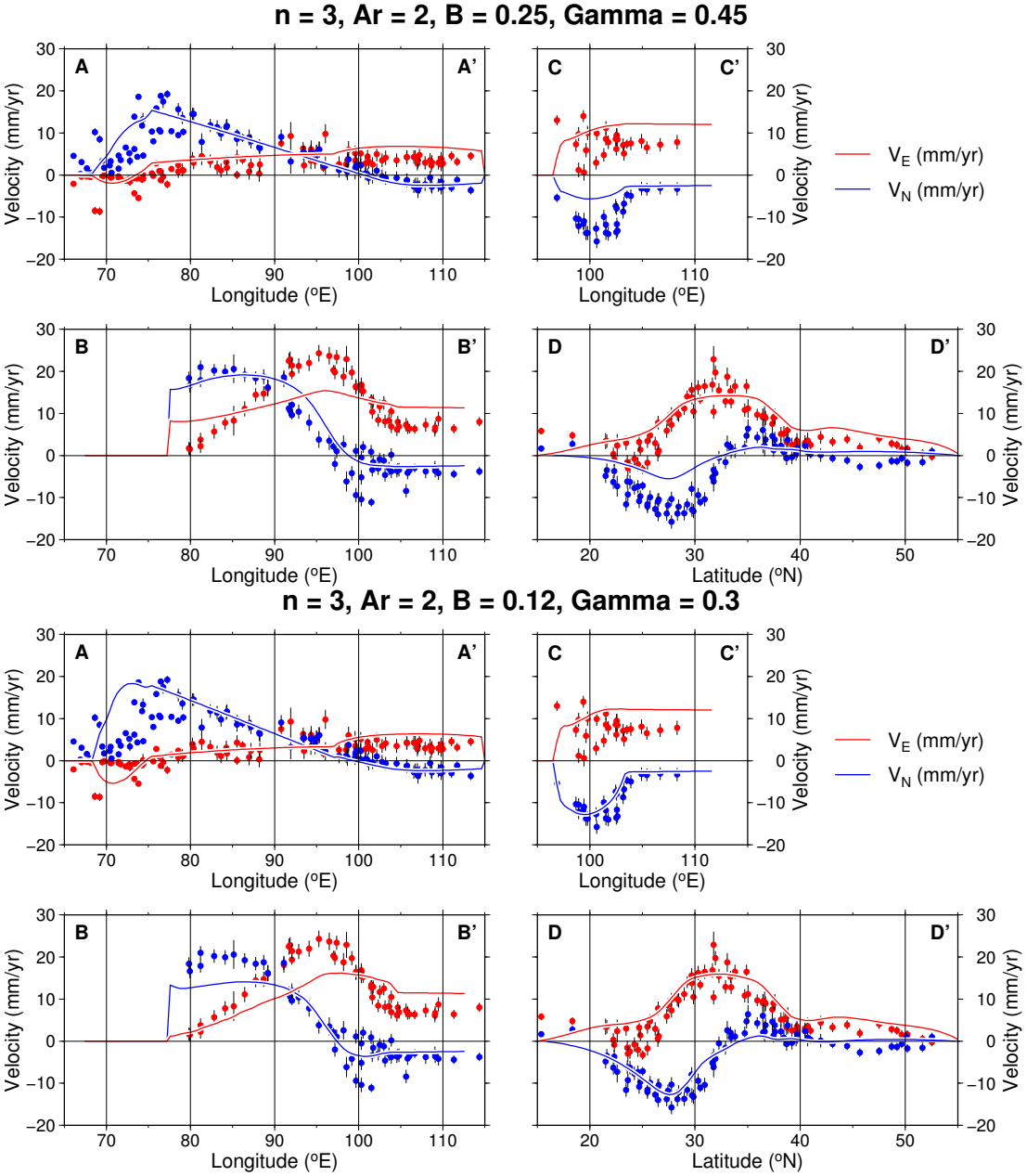

Figure 6.12: Comparison of model and GPS velocity profiles for calculations with $n = 3$ and $Ar = 2$. The upper four profiles are for $B = 0.25$ and the lower four for $B = 0.12$. A better fit is achieved in profiles A-A', C-C' and D-D' for a weaker Tibet, but the central plateau itself (B-B') is fit better for higher values of B. Profile locations are shown in Figure 6.11. Both models use the composite Indian boundary condition.

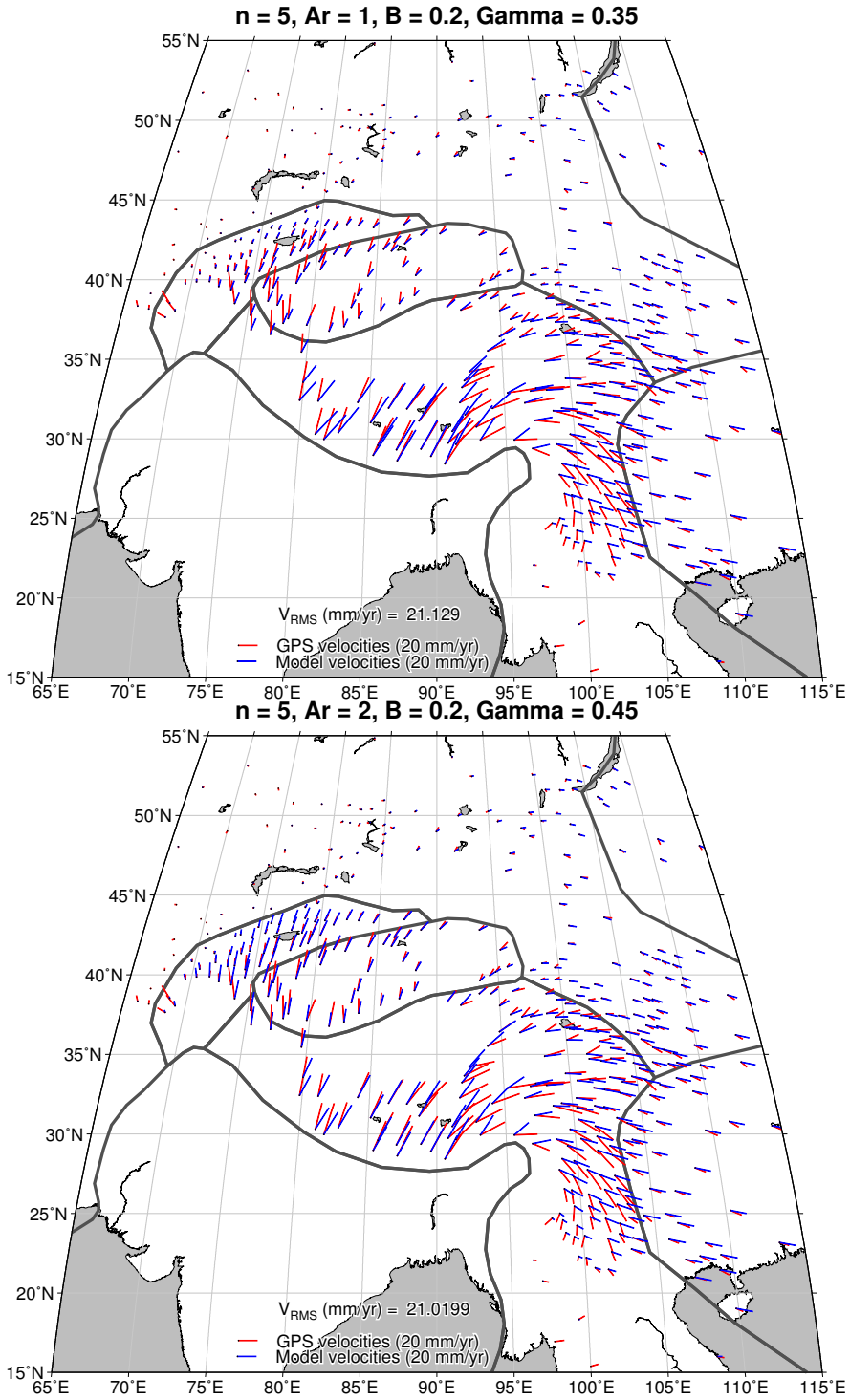

Figure 6.13: Comparison of model and GPS velocities for calculations with $n = 5$ and $B = 0.2$. The plotted models have $Ar = 1$ (top) and $Ar = 2$ (bottom). As Ar increases, vectors in Yunnan become more southerly orientated, but vectors in Tarim and Tien Shan increase in magnitude whilst vectors in south Tibet reduce in magnitude. All models use the composite Indian boundary condition.

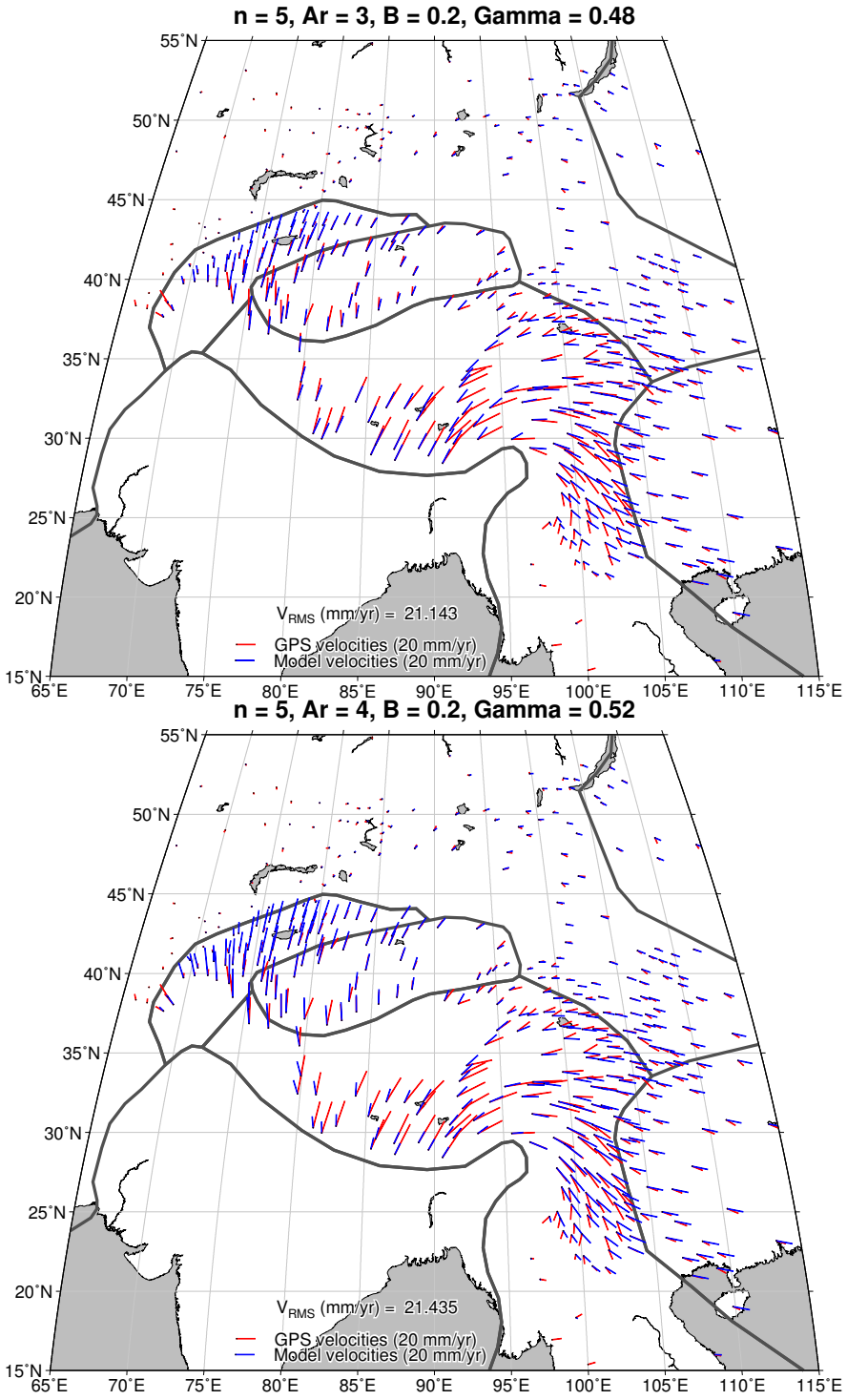

Figure 6.14: Comparison of model and GPS velocities for calculations with $n = 5$ and $B = 0.2$. The plotted models have $Ar = 3$ (top) and $Ar = 4$ (bottom). As Ar increases, vectors in Yunnan become more southerly orientated, but vectors in Tarim and Tien Shan increase in magnitude whilst vectors in south Tibet reduce in magnitude. All models use the composite Indian boundary condition.

When $n = 5$ and $B = 0.2$, the velocities in Tarim are well fit when $Ar = 4$, however the velocities in the Tien Shan are too high. Conversely, when $Ar = 1$ the velocities are reasonably well fit in the Tien Shan but are too low in Tarim (Figures 6.13 and 6.14). The inability of this model to predict the velocity fields in both regions might be reconciled by introducing a further strength contrast between Tibet and the Tien Shan, such that $B < B_{\text{Eurasia}}$ in these regions and $B_{\text{Tien Shan}} \neq B_{\text{Tibet}}$. Increasing the strength of the Tien Shan relative to Tibet could have the additional benefit of promoting eastward motion in the Tibetan plateau. If this were the case, the Tarim basin would transmit less stress through to the Tien Shan, meaning that additional stress must be accommodated in Tibet.

When the velocity magnitude is reasonable in Yunnan, there is a misfit at some GPS points in Yunnan where observations have a westward component of velocity (near 25°N, 100°E). The model velocity field does not reproduce this westward motion because the eastern boundary of India is fixed, and the Yangtze plate moves in a south-east direction. Some further adjustment of the constraint on these boundaries seems to be necessary to get a better prediction of the observed velocity field in Yunnan.

The limit between vectors having good orientations and too large a magnitude is approximately shown by the 21.5 mm/yr contour in Figures 6.9 and 6.10, adjacent to where the RMS misfit begins to blow up. Models close to this contour tend to show a reasonable match in the Tarim, Tien Shan and Yunnan regions (e.g. lower panels in Figures 6.14 and 6.12), but have a higher RMS misfit than the 'best' models (i.e. lowest RMS misfit models) on account of the velocities in south Tibet being too low. The blow up of RMS misfit is attributable to the effect of buoyancy forces being too high in the calculations, either because Ar is too high or B is too low in the Tibet region.

6.4 Quantifying the driving force

The magnitude of the dimensionless normal traction Γ on the Himalayan boundary, determined by fitting the GPS velocity field in south Tibet, can be used to evaluate the magnitude of the horizontal driving force applied to the Tibetan plateau by the colliding Indian plate. The vertically integrated horizontal driving force in units of N

m^{-1} is:

$$F_L = \Gamma \tau_0 L. \tag{6.4}$$

Figure 6.15 shows contours of F_L in the parameter space B vs Ar for n values between 2 and 10. RMS misfits plotted in Figure 6.15 are calculated using only the 22 GPS stations in south Tibet shown in Figure 6.4. Since these GPS stations are closest to the Himalayan boundary, they should give the clearest indication of the most appropriate value of Γ needed in the model. For all values of n, the best fit is achieved when F_L is in the range ~9-15x10^{12} N m^{-1}, although when n is 2 or 3 the lower bound is ~7x10^{12} N m^{-1}. The minimum RMS misfit is achieved in models with $Ar = 2$ and $B = 0.25$, except for $n = 2$ when the best parameters are $Ar = 1$ and $B = 0.1$. As observed in §6.3, the good fit when $n = 2$ can be attributed to a close match in south Tibet and the 'best' models indicated by the minimum RMS misfits in Figure 6.15 do not necessarily provide the best fit to observations in other parts of the solution domain.

From a series of finite-strain TVS models, England and Houseman (1986) find that for models that give an acceptable fit to observed topography data in Asia ($n = 3$ $Ar = 1$, $n = 5$ $Ar = 2$ and $n = 10$ $Ar = 3$), the value of F_L is in the range 1.5-2.5x10^{13} N m^{-1}. For the models presented here, a driving force of this magnitude indicates $Ar \approx 1$ for $n = 2$, $Ar \leq 2$ for $n = 3$ and $Ar \leq 3$ when $n = 5$. Decreasing the strength of the plateau requires a reduction of Ar for the same driving force to be applicable. When $n \leq 10$, the F_L estimates of England and Houseman (1986) require that the minimum strength of the plateau is 0.2 times that in the foreland. However, the best fit to GPS velocities in south Tibet indicates that the lower bound of England and Houseman (1986), 1.5x10^{13} N m^{-1}, is the maximum magnitude of the force required for n between 2 and 10 in my models.

The estimates of F_L given here (and by England and Houseman (1986)) are larger than the vertically integrated strength required to balance the GPE of the Tibetan plateau (5-7x10^{12} N m^{-1} e.g. Molnar and Lyon-Caen, 1988, Copley et al., 2010). This is expected since this force must drive the present-day deformation we see in Asia, in addition to balancing the additional GPE of the thickened plateau.

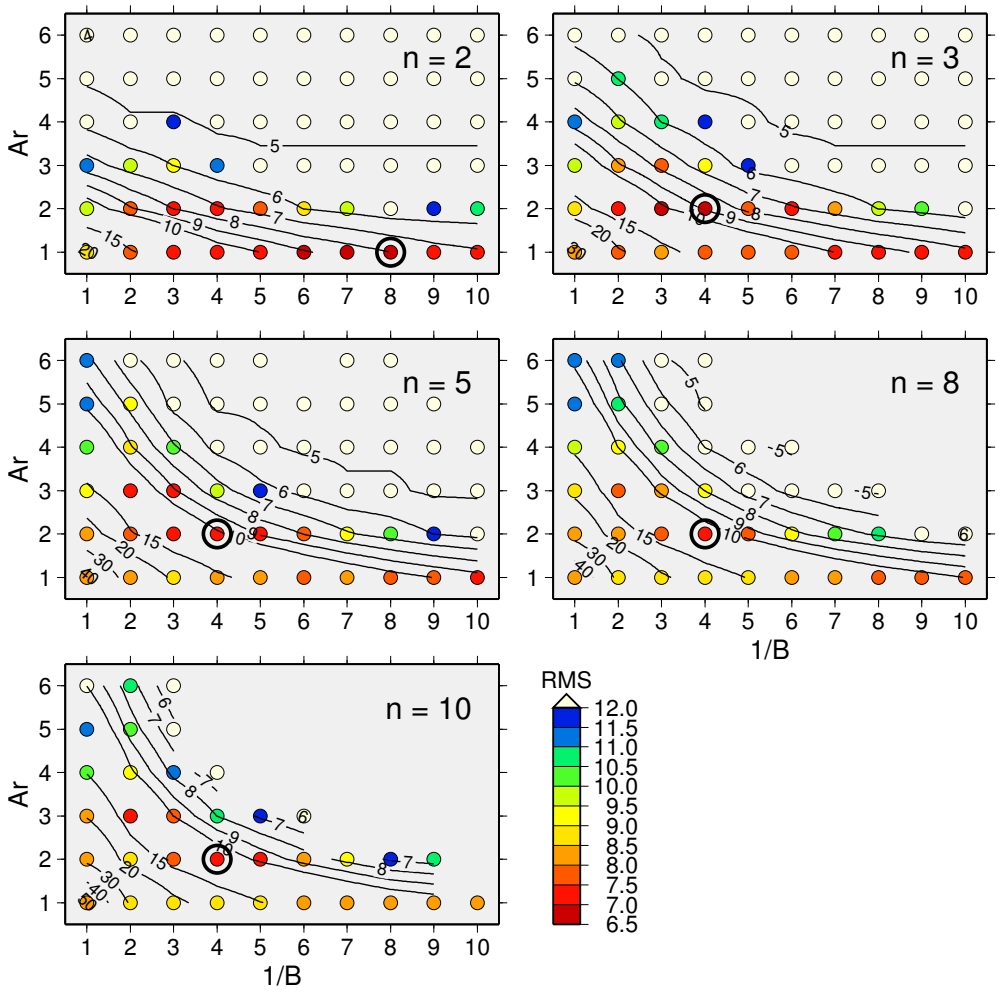

Figure 6.15: Contour plots of the force per unit length F_L on the Himalayan arc in the parameter space B vs Ar for n = 2, 3, 5, 8 and 10. The plotted values, scaled using Eq. 6.4, have units of 10^{12} N m^{-1}. Coloured dots are the RMS misfit for each experiment calculated using only the 22 GPS points in southern Tibet as shown in Figure 6.4. The circled experiment has the minimum RMS misfit. All calculations use the composite Indian boundary condition.

6.5 Differences attributed to Yangtze velocity

In all models there is a systematic misfit between observed and modelled velocities in the Yangtze region, with the east component consistently too large. Since the Yangtze region is rigid it does not deform in the models. Therefore the observed misfit is presumably a result of a difference in the reference frames used in the MORVEL model and the GPS velocity solution of Gan et al. (2007).

Gan et al. (2007) report the use of a Eurasia-fixed frame relative to the ITRF2000 reference frame. Their GPS data set is the combination of four separate data sets, each with a slightly different Eurasia-fixed frame. They used a Helmert transformation to

Table 6.4: Comparison of the MORVEL Euler pole for Yangtze and the pole that best fits the 35 GPS observations within the Yangtze region. a) MORVEL and estimated Euler poles with associated RMS misfits in mm/yr with respect to the observations. b) RMS misfits (mm/yr) between observations and a model with $n = 5$, $Ar = 2$ and $B = 0.2$ calculated with the MORVEL and estimated Euler poles.

a)	Lon (°E)	Lat (°N)	ω (deg/Ma)	V_e^{RMS}	V_n^{RMS}	$V_{\mathrm{tot}}^{\mathrm{RMS}}$
MORVEL	168.6	78.4	0.132	7.60	0.85	9.67
New pole	181.86	66.59	0.0649	1.17	0.74	6.08

b)	F_L (10^{12} N m^{-1})	V_e^{RMS}	V_n^{RMS}	$V_{\mathrm{tot}}^{\mathrm{RMS}}$
MORVEL	8.835	3.7104	3.4739	21.0199
New pole	9.975	3.7525	3.6622	21.0593
Difference	11.4%	1.1%	5.1%	0.18%

convert each data set to a common frame at co-located stations. Gan et al. (2007) find that maximum differences at the co-located stations are 2.6 and 1.7 mm/yr in north and east components respectively; within the 2-sigma error of the whole data set.

DeMets et al. (2010) use GPS velocities to integrate the separate Yangtze, Amur and Sundaland blocks into the global MORVEL plate model. Using the Earth's centre-of-mass as the origin for geodetic observations, they transform GPS velocities (from several studies) from their native reference frames to that of ITRF2005. The reported fixed Eurasia Euler poles (in Table 6.1) are therefore with respect to ITRF2005.

Since the Yangtze plate velocity is used as the dimensional scaling factor U_0, the difference between MORVEL (that uses ITRF2005) and Gan et al. (who use ITRF2000) reference frames could impact on predictions of my TVS models. Here, I determine the potential error introduced to the TVS calculations by the difference in reference frame.

Using the 35 GPS observations located within the defined Yangtze region (see Figure 6.4), I estimate the best fitting Euler pole of rotation (Table 6.4) by using non-linear optimisation with a downhill simplex method. A parameter set is found that minimises the objective function, which in this case is the RMS misfit between the observed velocities and those predicted by the new Euler pole. The solution may be non-unique since the global minimum of the objective function may not have been located. The non-systematic pattern of residuals between GPS velocities and estimates for the new pole confirms the inference that the Yangtze region is undeforming (e.g. Holt et al., 2000, England and Molnar, 2005, DeMets et al., 2010).

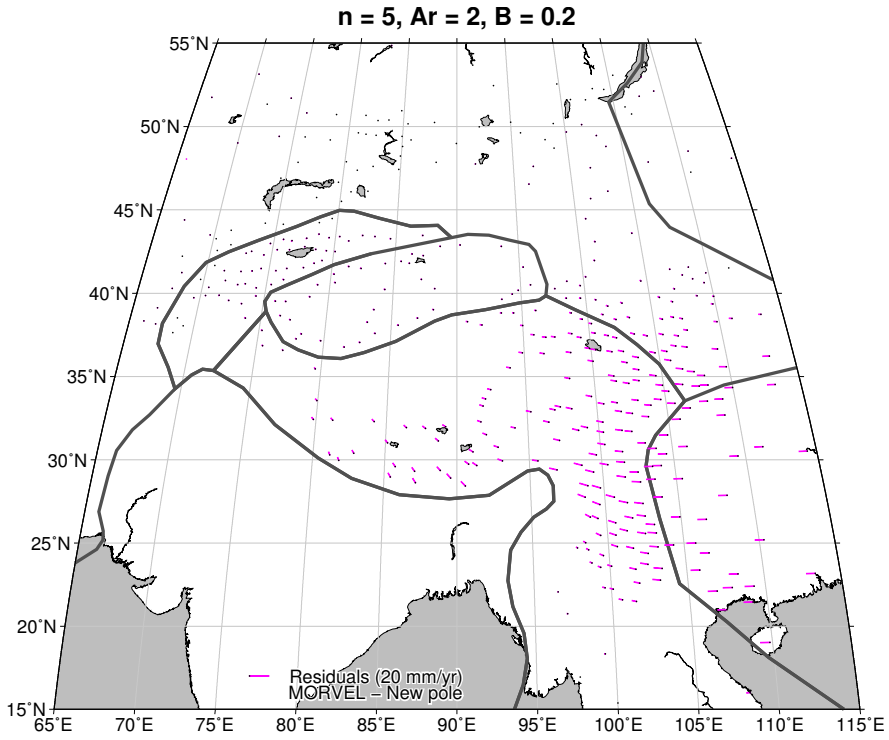

Figure 6.16: Residual velocities for calculations using the MORVEL Euler pole for Yangtze and a pole best-fitting the observed GPS in the Yangtze region. Residual velocities are calculated by subtracting estimates of a model using the new pole from those estimated using the MORVEL pole (Table 6.1). Velocity scale is the same as in Figures 6.7, 6.11, 6.13 and 6.14.

I also sought a best fitting Euler pole for the Amur region, but the number of GPS observations (nine) and the low magnitude of the velocities resulted in convergence on a worse solution. The importance of the Amur region on the model velocity field is less significant due to the low velocity magnitude and its distant location from the main deforming regions.

I use the new Yangtze Euler pole in a TVS calculation with $n = 5$ $Ar = 2$ and $B = 0.2$. The RMS values for the original (MORVEL pole) and new (estimated pole) models are given in Table 6.4. The new solution has a worse overall RMS misfit than the MORVEL constrained model on account of a change in the direction of velocity vectors across some of the model domain (Figure 6.16). The greatest change in velocities is in Yunnan and east Tibet, where the new pole predicts a reduced magnitude in the east component of velocity. The different Yangtze Euler poles also have an effect on velocities in south Tibet, although this is not as great as in Yunnan. Velocities in Tarim, Tien Shan and the foreland are hardly affected by the different Euler pole. Furthermore, the estimated boundary driving force is increased by ∼10% when using

the new Euler pole (Table 6.4).

The overall observations of using the different Yangtze Euler poles suggest that the pull of the Yangtze plate has an important bearing on the deformation field in Asia, particularly in regions bordering Yangtze. In order to achieve a better TVS model fit, either the GPS observations should be transformed to the ITRF2005 frame, or the MORVEL Euler poles should be transformed to the ITRF2000 frame.

6.6 Summary

In this Chapter I have found that TVS models can reproduce the broad-scale features of the present day velocity field reasonably well with only 4 variable parameters (n, Ar, B and Γ). However, some further experimentation is required to explain all features in a single model. Models that are driven by a normal traction on the Himalayan arc give the best fit to observed velocities throughout the solution domain. Models with a normal boundary traction for the entire Indian boundary lead to misfits in the velocity field in the Yunnan region, where observations show a southerly orientated, but spreading flow. Models that are driven by a velocity boundary condition on the Indian boundary cannot reproduce the pattern of deformation observed. Models with a composite Indian boundary condition can yield a minimum RMS misfit (~21 mm/yr) when $n = 2$, 3 or 5, but do not necessarily give the best fit in all parts of the deforming region. For instance, $n = 2$ models have a good fit in south Tibet but can not explain the southerly motion in Yunnan. Conversely, models with $n = 3$ or 5 can go some way to explaining the southerly motion in Yunnan but at the expense of mismatch in south Tibet. Generally, increasing the Argand number or decreasing the strength of the Tibetan plateau encourages southerly flow in Yunnan and increased velocity magnitudes in Tarim and the Tien Shan. In order to reproduce the distribution of velocity magnitudes between Tarim and Tien Shan, it may be necessary to vary the strength of Tien Shan relative to Eurasia and Tibet. Estimates of the vertically integrated horizontal driving force increase as the Argand number and the strength of Tibet decreases, but increase with n. The best fit to GPS observations in south Tibet occurs for driving forces within the approximate range of 7-15x10^{12} N m^{-1}. When $n = 3$ or 5, this range of F_L requires $0.1 < B < 0.25$ when $Ar = 1$, $0.16 < B < 0.5$ when $Ar = 2$ or $0.33 < B < 0.5$ when $Ar = 3$. The upper bound of these estimates is in agreement with the lower bound on the previous estimate made by England and Houseman (1986) of 15-25x10^{12} N m^{-1}.

Chapter 7

Discussion

7.1 Faults and the earthquake cycle

The transition between concentrated strain in the elastic crust to ductile deformation at depth in fault zones remains an unresolved issue in continental dynamics. As with many geophysical phenomena, it is not possible to make direct measurements within the Earth, so we must rely on detecting signals at the surface to infer the processes at depth. The difficulty in resolving the depth distribution of deformation during the earthquake cycle is that geodetically-determined surface velocities may not be diagnostic of secular velocities in the deep crust and mantle (e.g. Zatman, 2000, Savage, 2000, Hetland and Hager, 2004).

Choosing a model *a-priori* to explain observed geodetic velocity signals involves making a fundamental assumption about the localisation of interseismic deformation laterally and with depth in the lithosphere. The elastic screw dislocation model (e.g. Savage and Burford, 1973) implies that below the seismogenic layer, relative motion between the two blocks is localised on the continuation of the fault to the base of the lithosphere. This assumption is in line with the early extrusion-type models used to characterise the kinematics of the India-Asia collision (e.g. Tapponnier et al., 1982, Avouac and Tapponnier, 1993; see §2.6.1).

The alternative shear-zone model (e.g. Prescott and Nur, 1981) implies that deformation below the seismogenic layer is broadly distributed and that motion of the elastic upper layer is driven by shear tractions imparted by the ductile layer beneath. This assumption is in line with continuum-type models that have been used to explain the dynamics of the India-Asia collision (e.g. England and Houseman, 1986, England and

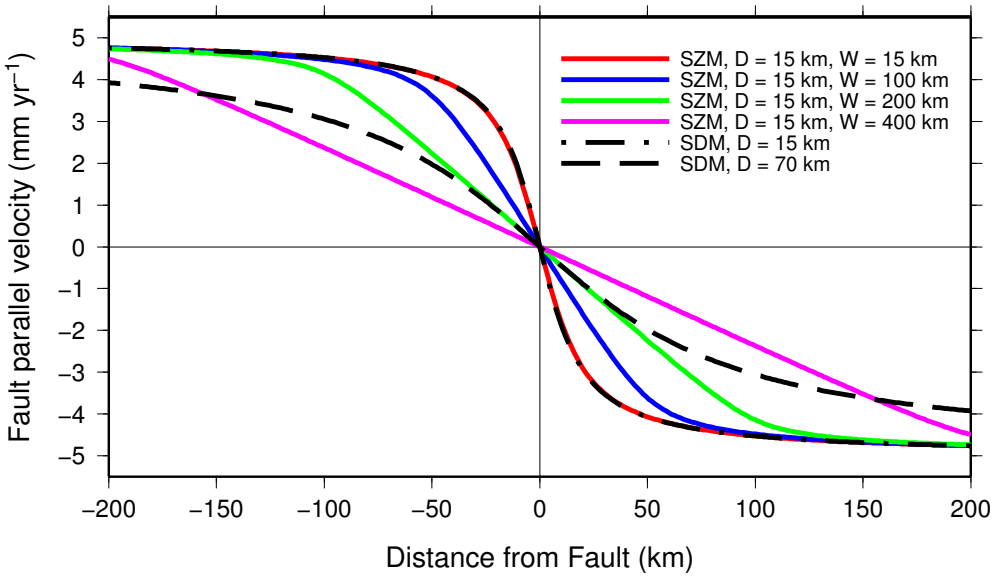

Figure 7.1: Comparison of screw dislocation model (SDM) and shear zone model (SZM) for a single strike-slip fault. Each model is calculated for a relative across-fault velocity of 10 mm/yr and with a locking depth D. In the shear zone model, the velocity in the ductile layer beneath the elastic layer (of thickness D) is assumed to vary linearly within a zone of width W. Varying W has a profound effect on the resulting velocity gradient across the fault.

Molnar, 1997b; see §2.6.3).

Figure 7.1 shows predictions of the fault-parallel velocity profile across a single strike-slip fault for both elastic dislocation and shear zone models during the interseismic period. Two important observations are clear from these predictions:

- Increasing the locking depth in the elastic dislocation model spreads deformation out laterally, but the surface velocity gradient is always steepest at the fault.
- Narrow shear zones result in an interseismic velocity profile at the surface that is virtually indistinguishable from that of an elastic dislocation.
- Wide shear zones create a shallow velocity gradient at the surface with no localisation at the fault.

My InSAR-derived velocity profile spanning ∼1000 km across central Tibet shows no evidence of localisation at known strike-slip fault zones. Instead, we see a long-wavelength variation of velocity across the plateau broadly consistent with sparse GPS observations. This observation suggests that the shear zone model is more applicable for wide deforming zones such as the Tibetan plateau (Bourne et al., 1998).

Molnar and Dayem (2010) observe that fast continental strike-slip faults tend to occur adjacent to strong regions. Furthermore, they infer that the more distributed deformation and lower slip-rates within continental regions is a direct consequence of the lack of strength heterogeneities. In Tibet, the Altyn Tagh fault is adjacent to the strong Tarim basin, and has an observed slip rate of ∼10 mm/yr in many other geodetic studies (e.g. Wallace et al., 2004, Elliott et al., 2008, Jolivet et al., 2008). Although there is no evidence for slip of this magnitude on the Altyn Tagh fault in my InSAR results, the estimates could be biased by atmospheric noise.

The broad-scale InSAR signal may be compatible with the summation of numerous screw dislocations spaced at intervals of ∼500 km, but this would require an unrealistically large elastic locking depth in order to spread the deformation out sufficiently (e.g. see $D = 70$ km curve in Figure 7.1). The locking depth in such models is taken to represent the depth to the base of the seismogenic layer. From earthquake locations, Jackson et al. (2008) find that $D \leq 20$ km for Tibet. For locking depths of this size, the shear zone model can produce the required shallow velocity gradients provided that the width of the shear zone is very wide (Figure 7.1).

Postseismic transients add an additional complication to the earthquake cycle that can't be explained by simple models that assume linear deformation between earthquakes (e.g. Savage and Burford, 1973, Prescott and Nur, 1981). I have shown that the transient signal generated in the viscoelastic layer can be observed geodetically, and a model (from Ryder et al., 2011) can be used to remove the effects from the data in order to presumably leave behind only the linear interseismic signal. This approach can work well for known large earthquakes, for which the postseismic signal is large enough to detect, but there are many more small earthquakes occurring that presumably also create disturbances to the secular velocity field (e.g. Figure 4.6).

As shown in §4.4, the longevity of large postseismic transients means that large earthquakes that occurred before the modern era of accurate seismic location may still be producing a sizeable deformation signal. One such earthquake is the great M8.6 Assam earthquake of 1950, which occurred near the EHS and was found to have a predominantly right-lateral strike-slip mechanism from seismic first-motion estimates (Ben-Menahem et al., 1974). A transient postseismic signal from this earthquake may still perturb the large scale horizontal velocity field on the margin between the Tibetan plateau and Yunnan. This could therefore impact on my large-scale TVS models that

aim to match GPS velocities in this region.

Field evidence of exhumed fault zones shows that ductile deformation below the seismogenic layer is localised (Bürgmann and Dresen, 2008). Meanwhile, recent earthquake cycle models have found that either layered viscoelastic rheologies (e.g. Hetland and Hager, 2006, Johnson et al., 2007) or lateral strength variations beneath the fault zone (e.g. Hetland and Hager, 2004) are required to reconcile both early-cycle rapid transients and late-cycle focussed interseismic deformation. In truth, the structure of a fault zone in the lower crust and upper mantle remains poorly known.

A project to image the North Anatolian fault in Turkey using array seismology should help provide a better understanding of the distribution of deformation laterally and with depth around the fault (Sebastian Rost, *pers. comm.*). Coupled with geodetic observations covering the entire earthquake cycle, these measurements will be used to constrain numerical earthquake cycle models that aim to quantify parameters of the shear zone at depth (Houseman and Yamasaki, *pers. comm.*).

7.2 Block or continuum?

Block models aim to explain the kinematic deformation field implied by geodetic measurements. Where measurements are dense, the block size is required to be small in order to reduce velocity residuals (e.g. in California; Meade and Hager, 2005). However, where measurements are sparse, larger blocks with arbitrarily defined boundaries can provide good fits to the data. This is the case in Tibet, where large parts of the central and western plateau are without GPS observations. Thatcher (2007) and Meade (2007) give independent block definitions of the Tibetan plateau as shown in Figure 2.16. A profile through these block models coincident with my InSAR profile is plotted in Figure 7.2. Aside from block-boundary effects (i.e. elastic strain accumulation on locked faults, which Meade includes but Thatcher does not), the profile shows the difference in the velocity field resulting from the different block boundary definitions.

Once the spatial resolution of velocity observations increases markedly (i.e. with InSAR), the block model no-longer provides an accurate representation of the velocity field. In this case, the correspondence between both models and the InSAR data is reasonable north of the Kunlun fault, with the differences between model and observation less than the overall RMS difference of ~3.5-3.9 mm/yr for the full profile (Table 7.1). However, south of the Kunlun fault there is a significant deviation, greater than the

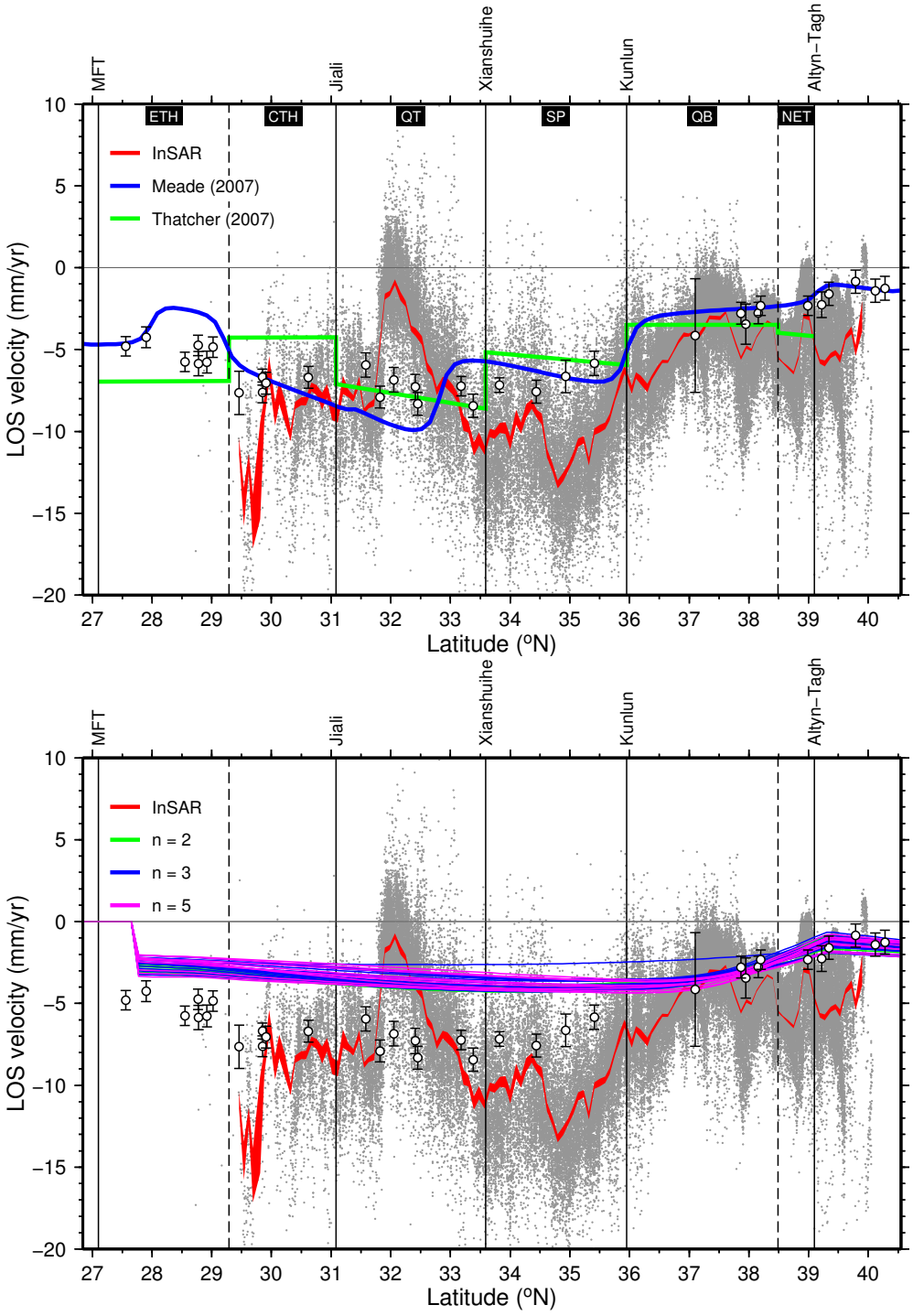

Figure 7.2: Comparison of co-located InSAR, block model and TVS model velocity profiles. Block models (top) of Meade (2007) and Thatcher (2007) are converted to the satellite's LOS. Block boundary definition of Thatcher (2007) is shown by vertical black lines. Dashed lines delineate boundaries that are not linked to a mapped fault. Abbreviated names of blocks are shown in black filled boxes. Profiles through TVS calculations (bottom) from Chapter 6 converted to the satellite's LOS. Calculations with $n = 2$, 3 and 5 with an RMS misfit of 8.0 mm/yr or less in Figure 6.15 are plotted (Ar in the range 1-3 and B in the range 1-10). InSAR profile is the same as in Figure 4.15, from the 70 interferogram rate map after postseismic correction.

Table 7.1: Comparison of model predictions with measured InSAR and GPS deformation rates in mm/yr. The GPS comparison is made with the Initial Deformation Model (IDM; §3.3.4) profile since it is calculated by interpolating over the unevenly distributed GPS points across the plateau. The InSAR comparison is with the *π-rate* result using 70 interferograms and with the Kunlun postseismic signal removed. Regular typed values are the differences in rate (model minus observation) at each location along profile, spaced one latitude degree apart. The bold values give the single RMS value for the differences from all eleven locations.

Latitude (°N)		29	30	31	32	33	34	35	36	37	38	39	RMS (mm/yr)
Meade (2007)	GPS	3.39	-0.28	-1.76	-2.88	1.11	0.76	-0.65	0.56	1.43	0.59	-0.04	**1.59**
block model	InSAR	0.05	0.03	0.23	-8.17	1.16	4.73	5.24	2.52	1.38	2.49	0.98	**3.48**
Thatcher (2007)	GPS	-0.45	2.39	2.31	-0.96	-1.03	1.44	0.48	1.65	0.66	-0.42	-2.25	**1.47**
block model	InSAR	-3.78	2.69	4.30	-6.25	-0.98	5.41	6.37	3.62	0.62	1.48	-1.23	**3.90**
TVS model	GPS	3.21	3.11	2.76	2.66	3.03	2.45	1.89	1.12	0.52	0.32	0.44	**2.24**
n=2 Ar=1 B=8	InSAR	-0.13	3.41	4.75	-2.63	3.07	6.42	7.78	3.08	0.47	2.23	1.46	**3.92**
TVS model	GPS	3.80	3.71	3.36	3.25	3.59	2.95	2.27	1.35	0.58	0.23	0.25	**2.68**
n=3 Ar=2 B=4	InSAR	0.47	4.01	5.35	-2.03	3.64	6.93	8.16	3.31	0.54	2.14	1.26	**4.20**
TVS model	GPS	3.97	3.84	3.47	3.36	3.69	3.02	2.27	1.22	0.35	0.05	0.29	**2.75**
n=5 Ar=2 B=4	InSAR	0.63	4.14	5.46	-1.93	3.73	6.99	8.16	3.18	0.31	1.95	1.31	**4.22**

overall RMS difference. Ignoring block boundary effects, the largest deviation occurs in the central portion of the profile where InSAR indicates increased motion toward the satellite. As discussed in §4.5.2, this deviation could be explained by vertical uplift with a magnitude of ∼8 mm/yr, additional horizontal motion with a magnitude of ∼20 mm/yr, or some unknown combination of vertical uplift and horizontal motion. Both block models fit the GPS observations better than they do the InSAR, with overall RMS differences of ∼1.5 mm/yr. Since the GPS data is used to constrain these models, the fit is expected to be relatively good.

Figure 7.2 also shows profiles through the TVS models of Chapter 6 converted to the LOS, and plotted alongside the InSAR results. Although some TVS models can match the north component of velocity well in the Tibetan plateau, the models tend to be unable to explain the increasing eastward velocity gradient from west to east (see Figure 6.12). Since the Envisat descending LOS geometry is more sensitive to east-west motion than north-south, the LOS TVS profiles can not match the magnitude of the InSAR or GPS observations, with overall RMS differences of between 2.2-2.8 mm/yr when compared to GPS and 3.9-4.2 mm/yr when compared to InSAR (Table 7.1). In addition, the vertical component of velocity is not explicitly considered in TVS calculations (see §5.2.2). This can introduce an additional source of deviation between InSAR observations and TVS models. Despite this, the fit between TVS and the observations of GPS and InSAR is good locally north of ∼37°N (differences of $\leq$ 0.6 mm/yr and $\leq$ 2.2 mm/yr respectively) once the northward-directed gradient of east-west velocity has become small (i.e. see Figure 2.7).

7.3 Large-scale dynamic models

Although the TVS modelling of Chapter 6 has had some success in explaining the present-day Asian velocity field, clearly there is room for further experimentation. A TVS model that can explain the InSAR velocity profile has not been found (Figure 7.2; Table 7.1), but it appears that the smooth long wavelength variation of the InSAR is more likely to be explained by such a model rather than a kinematic block model.

An alternative TVS modelling strategy might involve fixing the value of the boundary-normal traction on the Himalayan arc rather than iterating to find the minimum RMS as I have done. The observations of earthquake-type versus elevation (Elliott et al., 2010; Figure 2.5) imply that the vertical stress is equal to the horizontal stress at ∼4750

m elevation. Therefore at this elevation the GPE of the plateau is just large enough to balance the force applied to its boundary by the Indian plate. Using the equation for F_L given by Molnar and Lyon-Caen (1988; p. 200) and the parameters of Table 6.2, the horizontal driving force applied to the Himalayan arc is $\sim$7x10^{12} N m^{-1}. Constraining the boundary traction to this value in TVS models would allow more effective bounding of the n, Ar and B parameters.

One idea for further exploration of the parameter space is to use a zero or negative traction on the Indian boundary segment south of the eastern syntaxis to promote more southerly and even westerly components of motion in Yunnan. Altering the strength of the Tien Shan relative to the Tibetan plateau seems to be required to produce a good fit to the observations in both the Tien Shan and Tarim. It could also affect the eastward component of motion in Tibet if the Tien Shan region is stronger than Tibet since a smaller proportion of the stress will be guided through Tarim into the Tien Shan. Neil and Houseman (1997) investigated the magnitude of the strength contrast between the Tien Shan, Tarim and the rest of Eurasia by matching topographic observations with predictions from a TVS model. For calculations with $n = 3$ and $B = 1$ in the surrounding regions, the strength coefficient of Tarim is found to be between $B = 1.0$-2.25, whereas for Tien Shan $B = 0.65$-1.0. Notably, Neil and Houseman (1997) found that the strength of the Tien Shan was required to be less than in the Tibetan plateau.

Another possibility that could improve the RMS misfit of the models is the use of faults within the TVS. Barr and Houseman (1996) implemented faults within the TVS framework as vertical surfaces that allow free slip, but normal to which velocity and stress is continuous. Robl et al. (2008) found that the inclusion of strike-slip faults in a TVS model was necessary to explain extension in the Tauern window of the eastern European Alps. Figure 7.3 shows an example of their model geometry, which includes some strength regionalisation. When the faults are locked, no slip occurs and the calculation proceeds as if there were no faults. However, when the faults are unlocked, a considerable east component of motion is generated within the fault-bounded blocks. The north component of velocity is broadly similar between the two calculations. Inclusion of the major faults of the Tibetan plateau in my TVS models may promote the eastern component of motion observed in the GPS velocities but lacking in the calculations presented in Chapter 6.

The assumptions of the TVS are not consistent with the tectonic situation in south-

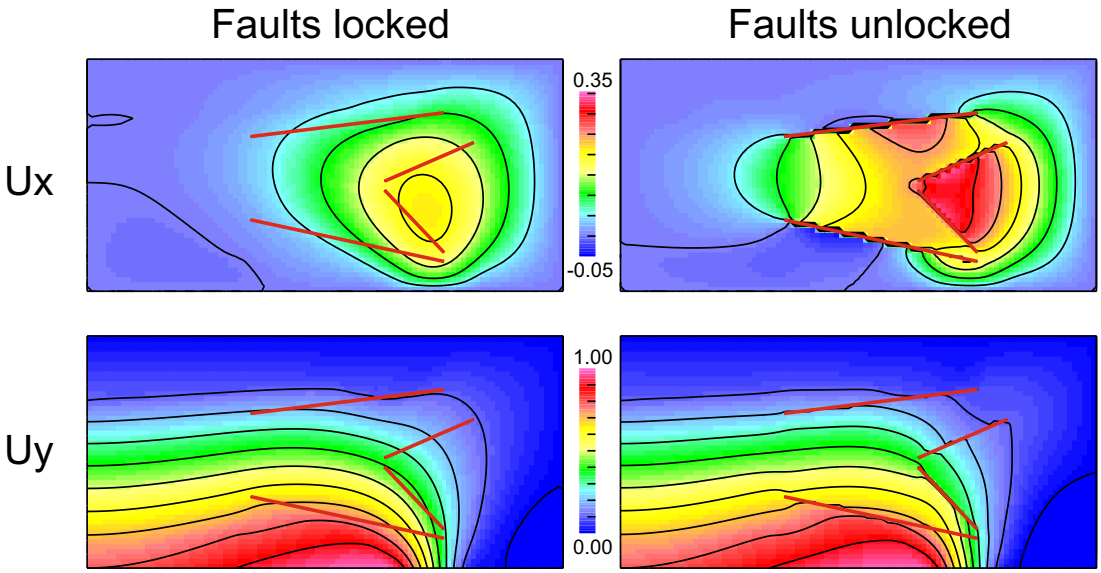

Figure 7.3: Thin viscous sheet calculation showing the effect of embedded faults on the velocity field. The $n = 1$, $Ar = 0$ calculation is driven by an indenter on the southern boundary. The fault geometry of the Tauern window of the European eastern Alps is approximated by the red lines (after Robl et al., 2008). Contour plots of east (U_x top) and north (U_y bottom) components of the instantaneous velocity field are shown for the cases where the faults are locked and don't affect the calculation (left), and unlocked where free slip is allowed (right). Velocities are dimensionless by the indentation velocity U_0. *Basil* calculation input files courtesy of Lynn Evans.

ern Tibet. Constraints from seismology (e.g. Li et al., 2008; Figure 2.11) indicate that Indian lithosphere is under-thrusting Tibet to a latitude of ~32°N, near the BNS at the surface. Copley et al. (2011) find that the approximate partitioning of strike-slip earthquakes north of the BNS, and normal-faulting earthquakes south of the BNS requires mechanical coupling of the Tibetan crust and under-thrusting Indian crust. This implies that channel flow in the lower crust in south Tibet is not occurring, but that basal shear tractions may be an important driving force in Tibetan deformation.

Although Ellis et al. (1995) found that both edge and basal boundary driving forces reproduced the observed length-scale of deformation in Tibet, the basal driving force may be more appropriate due to the interpreted cross-sectional geometry of the India-Asia collision (e.g. Figure 2.14). Therefore, further experimentation could make use of the adaptation to the TVS governing equations for basally-driven deformation (Medvedev and Podladchikov, 1999), or a 3D model in which application of basal boundary conditions is more straight-forward.

The main advantage of the TVS is that it can adequately approximate the full

3-dimensional deformation field over a broad area using very basic computational facilities. This treatment is all that is needed for evaluating stress and strain distributions from present day velocity observations. However, a 3D model can provide a more accurate explanation of the evolution of deformation in a continent, especially around small-scale high-strain features such as the indenter syntaxes. Lechmann et al. (2011) showed that even simple 3D models that account for depth-variation of lithospheric strength can exhibit folding and lower crustal flow occurring simultaneously with crustal thickening. In addition, I demonstrated that 3D models with a homogeneous rheology show that the velocity field can vary significantly with depth (§5.4.2). The computational resources required to run complex 3D models efficiently are now becoming readily available. With this in mind, future numerical models should explore the consequences of a basal driving force on the deformation of the wider Asian continent.

7.4 Global velocity fields

In order to improve our ability to mitigate the effects of large earthquakes we need to have a better understanding of where the regions with greatest seismic hazard are located. Current global products, such as the Global Strain Rate Map (GSRM, 2010, Kreemer et al., 2003; Figure 3.1), are restricted by the distribution of GPS velocities, which tend to be dense in the developed world but sparse elsewhere. In GSRM (2010), regions devoid of observations are assumed to act as rigid plates. This is a circular argument, since regional-scale GPS networks have not been deployed in regions assumed to be undeforming. A better approach would be to not make such assumptions *a-priori*, but let the calculated deformation field guide such interpretation. Since there could be significant deformation in plate interiors (e.g. the New Madrid Seismic Zone, USA (Smalley et al., 2005) or the South West Seismic Zone, Western Australia (Dawson et al., 2008)), a network covering the entire continental land surface would be needed to proceed in this way. To sufficiently characterise the non-linearity of 100-km-scale interseismic strain signals with GPS, a station spacing of at least 25 km is required. This spacing implies that $\sim 4 \times 10^4$ stations are needed to complete a homogeneous network over the entire continental land surface. Clearly, this would result in an expensive and unmanageable network.

The use of InSAR in tandem with much sparser GPS observations offers a plausible alternative solution. Building on the methods of England and Molnar (2005).

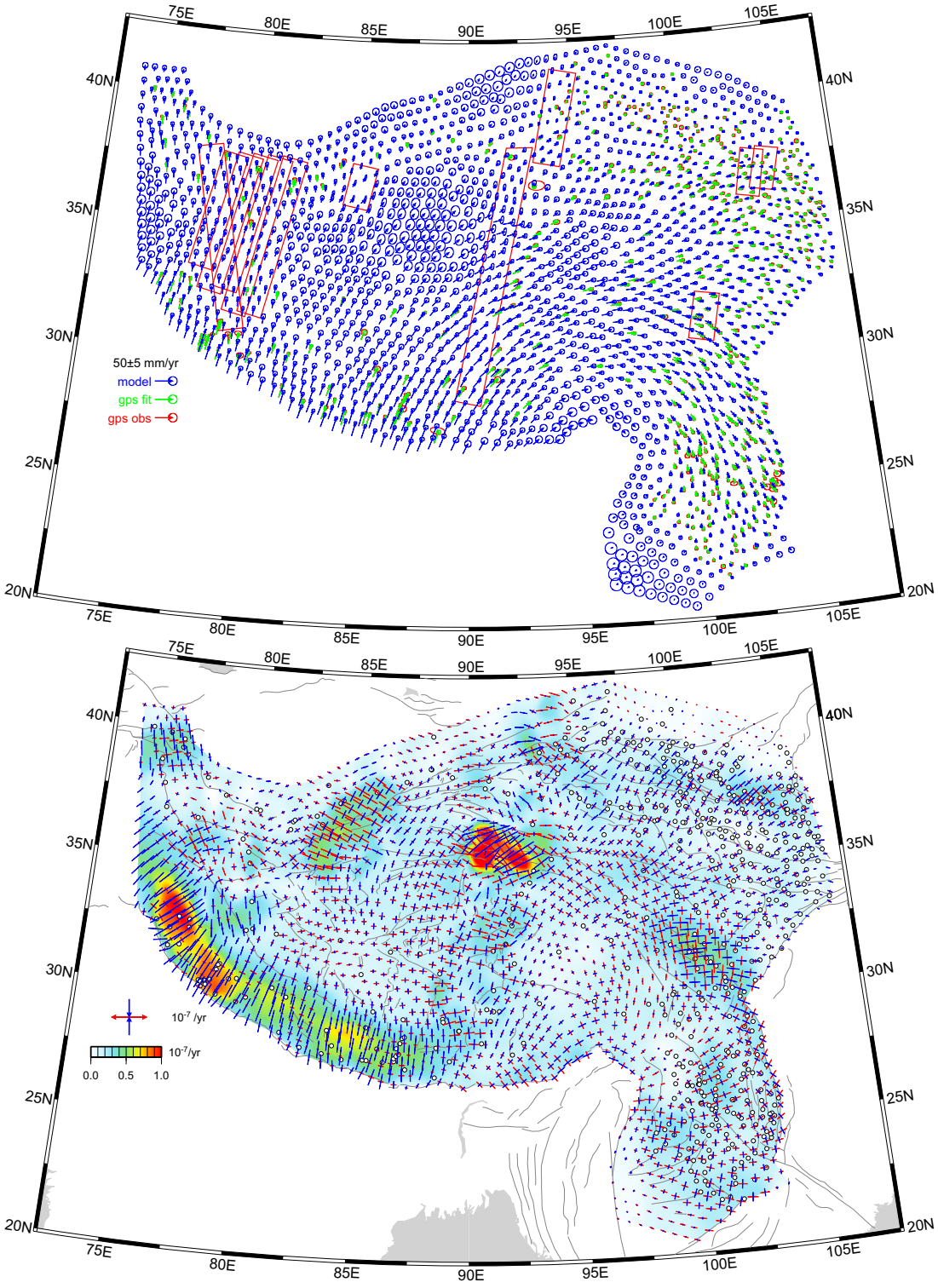

Figure 7.4: Large scale velocity and strain rate fields for Tibet determined from InSAR and GPS. Top: Smoothed velocity field determined from GPS and InSAR data using the methods of Wang and Wright (2011) and England and Molnar (2005). Blue arrows show the smoothed velocity vectors at each mesh node. Red and green arrows show the observed and modelled velocities at GPS stations. Red polygons show the spatial extent of InSAR rate maps used in the inversion. Bottom: Strain rate field calculated from the smoothed velocity field. Crosses are principal axes of the strain rate tensor. Red bars indicate extension and blue indicate compression. Colour background is the second invariant of the strain rate tensor. Lambert conic conformal projection. Figure courtesy of Hua Wang.

Wang and Wright (2011) combine multiple InSAR rate maps and other geodetic measurements into a single self-consistent velocity field for western Tibet. The method is briefly described in §3.3.4. Figure 7.4 gives an example of a dense velocity field for the whole Tibetan plateau region. This velocity field is created using constraint from my InSAR rate map and those from the studies of Elliott et al. (2008), Cavalié et al. (2008), Jolivet et al. (2008), Wang et al. (2009) and Wang and Wright (2011), in addition to the horizontal GPS velocity observations of Gan et al. (2007). Errors on the model velocities are greatest where there are no GPS or InSAR observations (central plateau). Where there are InSAR observations, only the east-west error bar is reduced in magnitude. High magnitude strain rates (in the corresponding strain rate map) occur at the locations of InSAR data. In particular, my uncorrected rate map was used, which contributes the postseismic deformation from the Kokoxili earthquake; the dominant signal in this velocity field. Once a more even coverage of SAR data is available, the method promises to give the spatially dense velocity observations we require to test models of continental deformation and characterise regions of elevated seismic hazard. Additionally, this method can be extended to use InSAR time series products to produce time-varying velocity maps (Hua Wang, *pers. comm.*). Such a method would not require decomposition of the measured velocities into postseismic and interseismic components. In the future, a velocity-field-time-series could provide a way of monitoring strain accumulation across whole continents and aid the identification of potentially hazardous, but currently unknown faults.

7.5 Routine InSAR monitoring

The exciting prospect of routine monitoring of strain accumulation should soon become reality, but before this can happen two things must occur:

- The accuracy of interseismic and postseismic deformation estimates must be improved by mitigation of atmospheric noise in SAR data.
- A large archive of SAR data with homogeneous global coverage must be acquired.

Many of the difficulties encountered in measuring slow deformation in this thesis should be overcome in the near future. Particularly, the effect of the atmospheric noise component of the signal will soon be mitigated by the use of corrections at the spatial

resolution of the interferogram. Corrections for each SAR scene can be generated from the predictions of global weather models (e.g. Jolivet et al., 2011) and remotely sensed data (e.g. Li et al., 2009c). In the near future such corrections will be available to download from online services (e.g. von Allmen et al., 2010). A retrieval system for the atmospheric corrections can easily be built into existing linear rate or time-series estimation algorithms such as π-*rate*.

Future satellites with appropriately tuned orbits and duty cycles will enable acquisitions to be collected on every orbit with a shorter revisit period. This will result in the rapid accrual of large volumes of data that will help increase the SNR in InSAR rate maps. The challenge for the scientific community will be to deal with the large volumes of acquired data by developing efficient processing algorithms and strategies for amalgamating individual rate maps with complimentary observations from other geodetic methods (e.g. §7.4).

The accuracy of unwrapping algorithms is perhaps the largest barrier to routine processing of large SAR data sets. However, the number of unwrapping errors should be reduced by processing only interferograms with short temporal baseline; made possible by acquiring data on every repeat orbit. The fact that not every possible acquisition is made with current systems is one reason why the current SAR data archive is not adequate for production of large-scale strain maps. As seen in §4.2, there has been no policy of routine monitoring with Envisat over Tibet. As a result, it has often been necessary to use pairs of acquisitions with long temporal baselines, which increases the likelihood of temporal decorrelation. Furthermore, along-track coverage has been inconsistent over the Tibetan plateau (Figure 4.3), which makes it difficult to produce very long rate maps because spurious signals can be introduced and possibly misinterpreted (e.g. the large magnitude velocity gradient at the CTCFZ; §4.5.2).

ESA's Sentinel-1 series of satellites, due to begin operation in 2013 and funded for 20 years, should change this situation. In an initial two-satellite constellation, operational by 2015, the repeat time will be only 6 days. The system also has the capability to acquire data on ascending and descending passes, possibly at a reduced frequency of 12 days. By combining interferograms from ascending and descending passes it is possible to discriminate between eastward and upward displacements (Wright et al., 2004b), which would be beneficial in an orogenic environment such as the Tibetan plateau. Additional improvement should also come from the planned tight-orbital control of

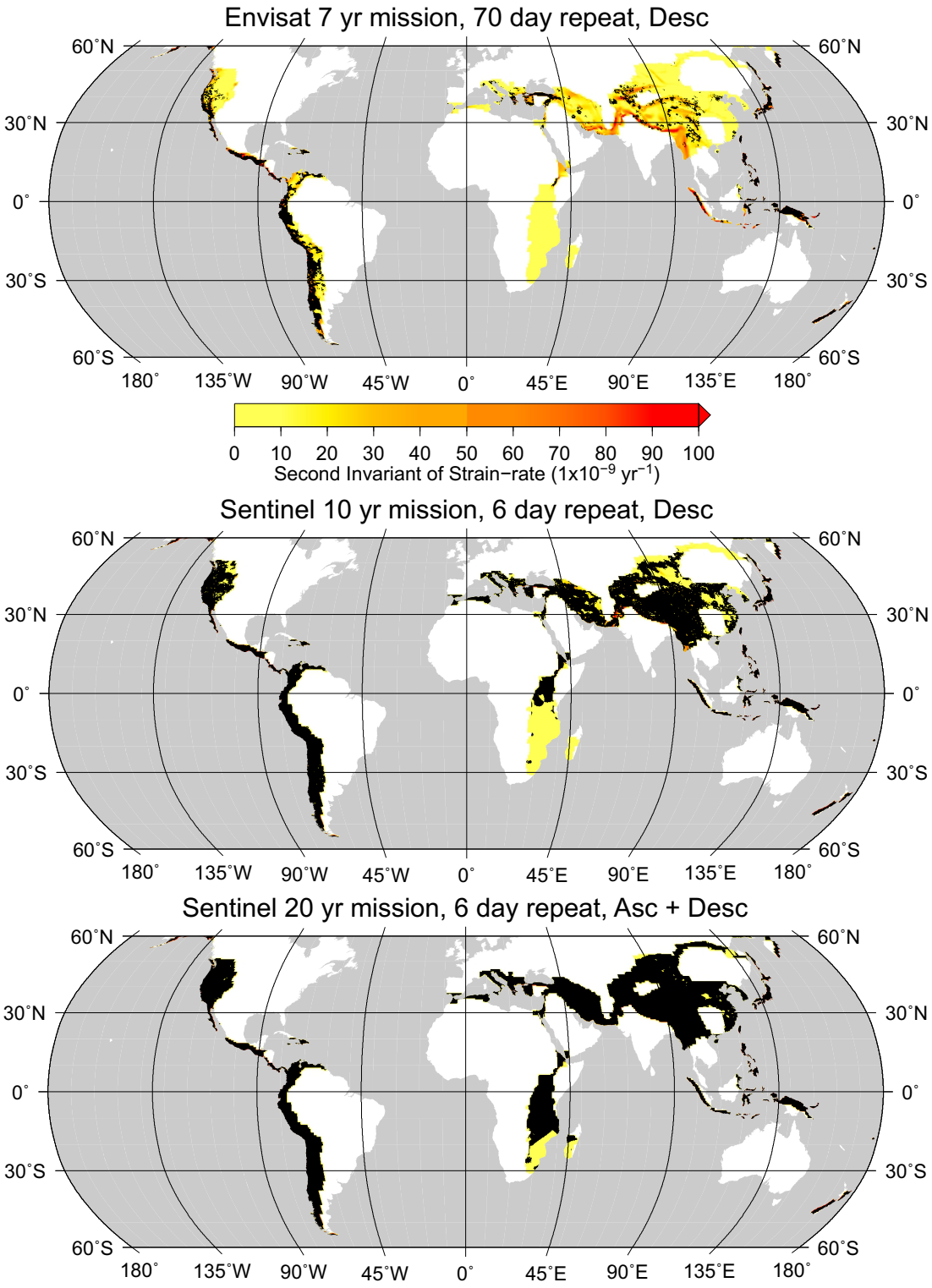

Figure 7.5: Ability of three InSAR mission configurations to resolve interseismic strain of 1 mm/yr over a distance of 100 km. Black regions show the potential coverage for each configuration for the assumed mission length and repeat time. Calculations assume perfect coherence, which is not guaranteed globally for C-band (Figure 3.3). Acquiring data on both ascending and descending passes is critical for being able to resolve strain gradients in the north-south orientation. This is because conventional side-looking SAR geometries are insensitive to north-south motion due to the LOS vector of the Sentinel and Envisat satellites (see §3.2.2). Background colour is the second invariant of strain rate of the GSRM in units of $1\text{x}10^{-9}$ yr^{-1} (Kreemer et al., 2003).

Sentinel-1 to within a 50 m tube. This will reduce the magnitude of orbital errors, which is particularly important for the production of long interferograms.

Figure 7.5 shows the potential capability of Sentinel-1 to measure interseismic deformation of 1 mm/yr over a distance of 100 km (i.e. strain rates of $1\text{x}10^{-8}$ yr^{-1}). Also plotted is the current capability with the Envisat archive, assuming the average repeat time is on the order of ∼70 days (twice the nominal repeat). The global coverage of each mission is determined by first calculating the uncertainty on the linear-rate, which is inversely proportional to the mission length but proportional to the orbital repeat time. The uncertainty is then used to recover the global coverage for each satellite mission by thresholding velocity gradients calculated from the horizontal velocity field of GSRM (Kreemer et al., 2003) and converted to the LOS of the satellite. It is clear from Figure 7.5 that Sentinel-1 is capable of covering a much vaster proportion of the Earth's deforming zones than the current Envisat archive.

Current SAR missions (Table 3.1) use a side looking antenna with a narrow squint range, resulting in sensitivity to ground displacements perpendicular to the track azimuth. Therefore, displacements parallel to the ground track (approximately north-south orientated) cannot be resolved. A future mission using either a configuration with forward- and backward-looking SAR antennae on both ascending and descending passes, or a left- and right-looking geometry on both ascending and descending passes would be able to resolve the full 3-dimensional displacement field within the error magnitudes of the SAR data (Wright et al., 2004b, 2010).

7.6 Concluding remarks

- I have validated the *π-rate* method of determining linear deformation rates on a pixel-by-pixel basis using synthetic InSAR data. By including more interferograms in the analysis, the RMS misfit between synthetic and estimated rate is reduced. Furthermore, I have shown that the *π-rate* method out-performs the stacking method when interferometric conditions are challenging.

- I have produced an InSAR rate map covering ∼1000 km north to south across the central Tibetan plateau. The rate map shows no evidence for localised velocity gradients across mapped fault zones that are expected if a kinematic block model provides the best explanation of the interseismic velocity field.

- I have compared 2D (TVS) and 3D models of continuum deformation and found that the TVS provides a reasonable approximation when the indenter half-width is greater than the lithospheric thickness.

- Using the TVS approximation, I have found that large-scale continuum models covering the Asia region can explain many features of the present-day velocity field observed by GPS if n is 3 or 5 and Ar is between 1 and 3. Further experimentation, possibly with additional parameters, is required to find a single model that gives a good fit in all regions simultaneously.

References

Allen, C. R., A. R. Gillespie, Y. A. Han, K. E. Sieh, B. C. Zhang, and C. N. Zhu (1984), Red River and associated faults, Yunnan province, China - Quaternary geology, slip rates, and seismic hazard, *Geol. Soc. Am. Bull.*, *95*(6), 686–700, doi:10.1130/0016-7606(1984)95. 2.3.2

Amelung, F., D. L. Galloway, J. W. Bell, H. A. Zebker, and R. J. Laczniak (1999), Sensing the ups and downs of Las Vegas: InSAR reveals structural control of land subsidence and aquifer-system deformation, *Geology*, *27*(6), 483–486, doi:10.1130/0091-7613(1999)027. 3.1

Amelung, F., S. Jónsson, H. Zebker, and P. Segall (2000), Widespread uplift and 'trapdoor' faulting on Galapagos volcanoes observed with radar interferometry, *Nature*, *407*(6807), 993–996, doi:10.1038/35039604. 3.1

Argand, E. (1924), La tectonique de l'Asie, in *Proc. 13th Int. Geol. Cong.*, vol. 1, pp. 171–372, Vaillant Carmanne, Liège. 2.1, 2.6.3

Argus, D. F., R. G. Gordon, M. B. Heflin, C. Ma, R. J. Eanes, P. Willis, W. R. Peltier, and S. E. Owen (2010), The angular velocities of the plates and the velocity of Earth's centre from space geodesy, *Geophys. J. Int.*, *180*(3), 913–960, doi:10.1111/j.1365-246X.2009.04463.x. 1.4.2

Armijo, R., P. Tapponnier, J. L. Mercier, and T. L. Han (1986), Quaternary extension in southern Tibet: Field observations and tectonic implications, *J. Geophys. Res.*, *91*(B14), 13,803–13,872, doi:10.1029/JB091iB14p13803. 2.1.3, 2.6.3

Armijo, R., P. Tapponnier, and H. Tonglin (1989), Late cenozoic right-lateral strike-slip faulting in southern Tibet, *J. Geophys. Res.*, *94*(B3), 2787–2838, doi:10.1029/JB094iB03p02787. 2.1, 2.3.2

Avouac, J. P., and E. B. Burov (1996), Erosion as a driving mechanism of intracontinental mountain growth, *J. Geophys. Res.*, *101*(B8), 17,747–17,769, doi:10.1029/96JB01344. 2.6.4

Avouac, J. P., and P. Tapponnier (1993), Kinematic model of active deformation in central Asia, *Geophys. Res. Lett.*, *20*(10), 895–898, doi:10.1029/93GL00128. 2.3.2, 2.6.1, 2.6.1, 7.1

Bamler, R., and P. Hartl (1998), Synthetic aperture radar interferometry, *Inverse Probl.*, *14*(4), R1–R54, doi:10.1088/0266-5611. 3.1

Banerjee, P., and R. Bürgmann (2002), Convergence across the northwest Himalaya from GPS measurements, *Geophys. Res. Lett.*, *29*(13), 1652, doi:10.1029/2002GL015184. 2.3.1, 2.4.1, 6.1.4

Barr, T. D., and G. A. Houseman (1996), Deformation fields around a fault embedded in a non-linear ductile medium, *Geophys. J. Int.*, *125*(2), 473–490, doi:10.1111/j.1365-246X.1996.tb00012.x. 7.3

Barron, J., and K. Priestley (2009), Observations of frequency-dependent Sn propagation in northern Tibet, *Geophys. J. Int.*, *179*(1), 475–488, doi:10.1111/j.1365-246X.2009.04318.x. 2.5.1

Beaumont, C., R. A. Jamieson, M. H. Nguyen, and B. Lee (2001), Himalayan tectonics explained by extrusion of a low-viscosity crustal channel coupled to focused surface denudation, *Nature*, *414*(6865), 738–742, doi:10.1038/414738a. 2.6.4

Beaumont, C., R. A. Jamieson, M. H. Nguyen, and S. Medvedev (2004), Crustal channel flows: 1. Numerical models with applications to the tectonics of the Himalayan-Tibetan orogen, *J. Geophys. Res.*, *109*(B06406), doi:10.1029/2003JB002809. 2.1.3, 2.6.4

Ben-Menahem, A., E. Aboodi, and R. Schild (1974), The source of the great Assam earthquake - an interplate wedge motion, *Phys. Earth Planet. Inter.*, *9*(4), 265 – 289, doi:10.1016/0031-9201(74)90056-9. 7.1

Bendick, R., R. Bilham, J. Freymueller, K. Larson, and G. H. Yin (2000), Geodetic evidence for a low slip rate in the Altyn Tagh fault system, *Nature*, *404*(6773), 69–72, doi:10.1038/35003555. 2.3.2

Berardino, P., G. Fornaro, R. Lanari, and E. Sansosti (2002), A new algorithm for surface deformation monitoring based on small baseline differential SAR interferograms, *IEEE T. Geosci. Remote Sens.*, *40*(11), 2375–2383, doi:10.1109/TGRS.2002.803792. 3.2.5, 3.3.8, 3.3.9, 3.3.9, 3.3.9

Biggs, J. (2007), InSAR observations of the Earthquake cycle on the Denali fault, Alaska, Ph.D. thesis, Department of Earth Sciences, University of Oxford. 3.2.4, 3.2.6, 3.4, 3.4.3

Biggs, J., T. Wright, Z. Lu, and B. Parsons (2007), Multi-interferogram method for measuring interseismic deformation: Denali Fault, Alaska, *Geophys. J. Int.*, *170*(3), 1165–1179, doi:10.1111/j.1365-246X.2007.03415.x. 3.2.5, 3.2.6, 3.3, 3.3.3, 3.3.6

Bilham, R., K. Larson, J. Freymueller, and Project Idylhim members (1997), GPS measurments of present-day convergence across the Nepal Himalaya, *Nature*, *386*(6620), 61–64, doi:10.1038/38606a0. 6.1.4

Bird, P. (1991), Lateral extrusion of lower crust from under high topography, in the isostatic limit, *J. Geophys. Res.*, *96*(B6), 10,275–10,286, doi:10.1029/91JB00370. 2.6.4

Bird, P. (2003), An updated digital model of plate boundaries, *Geochem. Geophys. Geosyst.*, *4*(3), 1027, doi:10.1029/2001GC000252. 1.1, 2.1

Bird, P., and K. Piper (1980), Plane-stress finite-element models of tectonic flow in Southern California, *Phys. Earth Planet. Inter.*, *21*(2-3), 158–175, doi:10.1016/0031-9201(80)90067-9. 5.1

Bourne, S. J., P. C. England, and B. Parsons (1998), The motion of crustal blocks driven by flow of the lower lithosphere and implications for slip rates of continental strike-slip faults, *Nature*, *391*, 655–659, doi:10.1038/35556. 1.4.2, 1.9, 2.6, 7.1

Brace, W. F., and D. L. Kohlstedt (1980), Limits on lithospheric stress imposed by laboratory experiments, *J. Geophys. Res.*, *85*(B11), 6248–6252, doi:10.1029/JB085iB11p06248. 1.2, 1.2, 1.2.1, 2.5.4

Braitenberg, C., Y. Wang, J. Fang, and H. T. Hsu (2003), Spatial variations of flexure parameters over the Tibet-Qinghai plateau, *Earth Planet Sci. Lett.*, *205*(3-4), 211–224, doi:10.1016/S0012-821X(02)01042-7. 2.2.1, 2.3.2, 6.1.2

Brown, E., R. Bendick, D. Bourles, V. Gaur, P. Molnar, G. Raisbeck, and F. Yiou (2002), Slip rates of the Karakoram Fault, Ladakh, India, determined using cosmic ray exposure dating of debris flows and moraines, *J. Geophys. Res.*, *107*(B9), 2192, doi:10.1029/2000JB000100. 2.3.2

Bürgmann, R., and G. Dresen (2008), Rheology of the lower crust and upper mantle: Evidence from rock mechanics, geodesy, and field observations, *Annu. Rev. Earth Pl. Sc.*, *36*, 531–567, doi:10.1146/annurev.earth.36.031207.124326. 1.2, 1.2, 1.2.2, 1.4, 1.11, 1.4.3, 7.1

Bürgmann, R., P. A. Rosen, and E. J. Fielding (2000), Synthetic aperture radar interferometry to measure Earth's surface topography and its deformation, *Annu. Rev. Earth Pl. Sc.*, *28*, 169–209, doi:10.1146/annurev.earth.28.1.169. 3.1, 3.2, 3.2.2

Bürgmann, R., S. Ergintav, P. Segall, E. H. Hearn, S. McClusky, R. E. Reilinger, H. Woith, and J. Zschau (2002), Time-dependent distributed afterslip on and deep below the Izmit earthquake rupture, *Bull. Seismol. Soc. Am.*, *92*(1), 126–137, doi:10.1785/0120000833. 1.4.3

Burov, E. B., and A. B. Watts (2006), The long-term strength of continental lithosphere: 'jelly sandwich' or 'crème brûlée'?, *GSA Today*, *16*, 4–10, doi:10.1130/1052-5173(2006)016. 1.2, 1.2.2

Byerlee, J. (1978), Friction of rocks, *Pure Appl. Geophys.*, *116*(4), 615–626, doi:10.1007/BF00876528. 1.2

Calais, E., L. Dong, M. Wang, Z. Shen, and M. Vergnolle (2006), Continental deformation in Asia from a combined GPS solution, *Geophys. Res. Lett.*, *33*(L24319), doi:10.1029/2006GL028433. 2.6, 2.4.1, 6.1.3, 6.3

Cavalié, O., C. Lasserre, M. P. Doin, G. Peltzer, S. J., X. Xu, and Z. K. Shen (2008), Measurement of interseismic strain across the Haiyuan fault (Gansu, China), by InSAR, *Earth Planet Sci. Lett.*, *275*(3-4), 246–257, doi:10.1016/j.epsl.2008.07.057. 2.3.2, 3.2.5, 4.1, 7.4

Cavalié, O., M. P. Doin, C. Lasserre, and P. Briole (2007), Ground motion measurement in the Lake Mead area, Nevada, by differential synthetic aperture radar interferometry time series analysis: Probing the lithosphere rheological structure, *J. Geophys. Res.*, *112*(B03403), doi:10.1029/2006JB004344. 3.2.5

Chen, J., B. Huang, and L. Sun (2010), New constraints to the onset of the India-Asia collision: Paleomagnetic reconnaissance on the Linzizong Group in the Lhasa Block, China, *Tectonophysics*, *489*(1-4), 189–209, doi:10.1016/j.tecto.2010.04.024. 2.1.1

Chen, W.-P., and P. Molnar (1983), Focal depths of intracontinental and intraplate earthquakes and their implications for the thermal and mechanical-properties of the lithosphere, *J. Geophys. Res.*, *88*(B5), 4183–4214, doi:10.1029/JB088iB05p04183. 1.2, 1.2.1, 2.5.4

Chen, W. P., M. Martin, T. L. Tseng, R. L. Nowack, S. H. Hung, and B. S. Huang (2010), Shear-wave birefringence and current configuration of converging lithosphere under Tibet, *Earth Planet Sci. Lett.*, *295*(1-2), 297–304, doi:10.1016/j.epsl.2010.04.017. 2.5.3

Chen, Y., S. Gilder, N. Halim, J. P. Cogné, and V. Courtillot (2002), New paleomagnetic constraints on central Asian kinematics: Displacement along the Altyn Tagh fault and rotation of the Qaidam Basin, *Tectonics*, *21*(5), 1042, doi:10.1029/2001TC901030. 2.3.2

Chen, Z., B. C. Burchfiel, Y. Liu, R. W. King, L. Royden, W. Tang, E. Wang, J. Zhao, and Z. X. (2000), Global Positioning System measurements from eastern Tibet and their implications for India/Eurasia intercontinental deformation, *J. Geophys. Res.*, *105*(B7), 16,215–16,227, doi:10.1029/2000JB900092. 2.4.1

Cheng, G., and T. Wu (2007), Responses of permafrost to climate change and their environmental significance, Qinghai-Tibet Plateau, *J. Geophys. Res. -Ea. Surf.*, *112*(F02S03), doi:10.1029/2006JF000631. 4.2.2

Chevalier, M. L., F. J. Ryerson, P. Tapponnier, R. C. Finkel, J. Van der Woerd, H. Li, and Q. Liu (2005), Slip-rate measurements on the Karakorum fault may imply secular variations in fault motion, *Science*, *307*, 411–414, doi:10.1126/science.1105466. 2.3.2, 2.3.2

Christensen, N. I., and W. D. Mooney (1995), Seismic velocity structure and composition of the continental crust - A global view, *J. Geophys. Res.*, *100*(B6), 9761–9788, doi:10.1029/95JB00259. 2.5

Clark, M. K., and L. H. Royden (2000), Topographic ooze: Building the eastern margin of Tibet by lower crustal flow, *Geology*, *28*, 703–706, doi:10.1130/0091-7613(2000)28. 2.2.2, 2.21, 2.6.4

Clark, M. K., J. W. M. Bush, and L. H. Royden (2005), Dynamic topography produced by lower crustal flow against rheological strength heterogeneities bordering the Tibetan Plateau, *Geophys. J. Int.*, *162*(2), 575–590, doi:10.1111/j.1365-246X.2005.02580.x. 2.6.4

COMET+ working group (2011), Centre for the Observation and Modelling of Earthquakes, Volcanoes and Tectonics, `http://comet.nerc.ac.uk/current_research.html`, Retrieved 24/07/2011. 1.4.1

Cook, K. L., and L. H. Royden (2008), The role of crustal strength variations in shaping orogenic plateaus, with application to Tibet, *J. Geophys. Res.*, *113*(B08407), doi:10.1029/2007JB005457. 2.6.4

Copley, A. (2008), Kinematics and dynamics of the southeastern margin of the Tibetan Plateau, *Geophys. J. Int.*, *174*(3), 1081–1100, doi:10.1111/j.1365-246X.2008.03853.x. 2.3.1, 2.4.1, 2.6.4

Copley, A., and D. McKenzie (2007), Models of crustal flow in the India-Asia collision zone, *Geophys. J. Int.*, *169*(2), 683–698, doi:10.1111/j.1365-246X.2007.03343.x. 2.8, 2.4.1, 2.6.4

Copley, A., J. P. Avouac, and J. Y. Royer (2010), India-Asia collision and the Cenozoic slowdown of the Indian plate: Implications for the forces driving plate motions, *J. Geophys. Res.*, *115*(B03410), doi:10.1029/2009JB006634. 1.2.1, 2.1.2, 6.4

Copley, A., J. P. Avouac, and B. P. Wernicke (2011), Evidence for mechanical coupling and strong Indian lower crust beneath southern Tibet, *Nature*, *472*(7341), 79–81, doi:10.1038/nature09926. 2.6.4, 7.3

Costantini, M. (1998), A novel phase unwrapping method based on network programming, *IEEE T. Geosci. Remote Sens.*, *36*(3), 813–821, doi:10.1109/36.673674. 3.2.4

Cowgill, E. (2007), Impact of riser reconstructions on estimation of secular variation in rates of strike slip faulting: Revisiting the Cherchen River site along the Altyn Tagh Fault, NW China, *Earth Planet Sci. Lett.*, *254*, 239–255, doi:10.1016/j.epsl.2006.09.015. 2.3.2

Cowgill, E., R. D. Gold, C. Xuanhua, W. Xiao-Feng, J. R. Arrowsmith, and J. Southon (2009), Low Quaternary slip rate reconciles geodetic and geologic rates along the Altyn Tagh fault, north-western Tibet, *Geology*, *37*(7), 647–650, doi:10.1130/G25623A.1. 2.3.2

Curlander, J. C., and R. N. McDonough (1991), *Synthetic aperture radar - Systems and signal processing*, New York: John Wiley & Sons, Inc. 3.1

Dalmayrac, B., and P. Molnar (1981), Parallel thrust and normal faulting in Peru and constraints on the state of stress, *Earth Planet Sci. Lett.*, *55*(3), 473 – 481, doi:10.1016/0012-821X(81)90174-6. 1.3.3

Davis, P., P. England, and G. Houseman (1997), Comparison of shear wave splitting and finite strain from the India-Asia collision zone, *J. Geophys. Res.*, *102*(B12), 27,511–27,522, doi:10.1029/97JB02378. 2.5.3

Davy, P., and P. R. Cobbold (1988), Indentation tectonics in nature and experiment. 1. Experiments scaled for gravity, *Bull. Geol. Inst. Uppsala*, *14*, 129–141. 2.6.3

Dawson, J., P. Cummins, P. Tregoning, and M. Leonard (2008), Shallow intraplate earthquakes in Western Australia observed by Interferometric Synthetic Aperture Radar, *J. Geophys. Res.*, *113*(B11408), doi:10.1029/2008JB005807. 7.4

Dayem, K. E., G. A. Houseman, and P. Molnar (2009a), Localization of shear along a lithospheric strength discontinuity: Application of a continuous deformation model to the boundary between Tibet and the Tarim Basin, *Tectonics*, *28*(TC3002), doi:10.1029/2008TC002264. 2.3.2, 2.6.3, 5.4.5, 6

Dayem, K. E., P. Molnar, M. K. Clark, and G. A. Houseman (2009b), Far-field lithospheric deformation in Tibet during continental collision, *Tectonics*, *28*(TC6005), doi:10.1029/2008TC002344. 2.6.3, 5.4.5, 6

DeMets, C., R. G. Gordon, D. F. Argus, and S. Stein (1990), Current plate motions, *Geophys. J. Int.*, *101*(2), 425–478, doi:10.1111/j.1365-246X.1990.tb06579.x. 1.1

DeMets, C., R. G. Gordon, D. F. Argus, and S. Stein (1994), Effect of recent revisions to the geomagnetic reversal time-scale on estimates of current plate motions, *Geophys. Res. Lett.*, *21*(20), 2191–2194, doi:10.1029/94GL02118. 1.1

DeMets, C., R. G. Gordon, and D. F. Argus (2010), Geologically current plate motions, *Geophys. J. Int.*, *181*(1), 1–80, doi:10.1111/j.1365-246X.2009.04491.x. 1.1, 2.1, 2.4.1, 6.1.4, 6.1, 6.5

Dewey, J. F., R. M. Shackleton, C. Chengfa, and S. Yiyin (1988), The Tectonic Evolution of the Tibetan Plateau, *Phil. Trans. R. Soc. Lond. A*, *327*(1594), 379–413, doi:10.1098/rsta.1988.0135. 2.1, 2.1.3

Dixon, T. H. (1991), An introduction to the global positioning system and some geological applications, *29*, 249–276, doi:10.1029/91RG00152. 2.4.1

Doin, M. P., C. Lasserre, G. Peltzer, O. Cavalie, and C. Doubre (2009a), Corrections of stratified tropospheric delays in SAR interferometry: Validation with global atmospheric models, *J. Appl. Geophys.*, *69*(1), 35–50, doi:10.1016/j.jappgeo.2009.03.010. 3.2.5

Doin, M. P., C. Lasserre, S. Guillaso, and J. Sun (2009b), Visco-elastic rebound of the lithosphere around the lake Siling Co in Tibet: an InSAR study, *Proceedings of Fringe Workshop 2009, ESA-ESRIN*. 4.3

Duvall, A. R., and M. K. Clark (2010), Dissipation of fast strike-slip faulting within and beyond northeastern Tibet, *Geology*, *38*(3), 223–226, doi:10.1130/G30711.1. 2.3.2

Elliott, J. R. (2009), Strain accumulation and release on the Tibetan Plateau measured using InSAR, Ph.D. thesis, Department of Earth Sciences, University of Oxford. 1.3, 1.4.1, 3.1, 3.2.5, 3.3.5

Elliott, J. R., J. Biggs, B. Parsons, and T. J. Wright (2008), InSAR slip rate determination on the Altyn Tagh Fault, northern Tibet, in the presence of topographically correlated atmospheric delays, *Geophys. Res. Lett.*, *35*(L12309), doi:10.1029/2008GL033659. 2.3.2, 3.2.2, 3.2.5, 3.3, 3.3.5, 4.1, 7.1, 7.4

Elliott, J. R., R. J. Walters, P. C. England, J. A. Jackson, Z. Li, and B. Parsons (2010), Extension on the Tibetan plateau: recent normal faulting measured by InSAR and body wave seismology, *Geophys. J. Int.*, *183*(2), 503–535, doi:10.1111/j.1365-246X.2010.04754.x. 2.5, 2.3.1, 4.3, 4.7, 4.5.2, 7.3

Ellis, S., P. Fullsack, and C. Beaumont (1995), Oblique convergence of the crust driven by basal forcing: implications for length-scales of deformation and strain partitioning in orogens, *Geophys. J. Int.*, *120*(1), 24–44, doi:10.1111/j.1365-246X.1995.tb05909.x. 5.1, 7.3

Emardson, T. R., M. Simons, and F. H. Webb (2003), Neutral atmospheric delay in interferometric synthetic aperture radar applications: Statistical description and mitigation, *J. Geophys. Res.*, *108*(B5), 2231, doi:10.1029/2002JB001781. 3.2.2, 3.2.5, 3.3.6, 3.4.2

England, P., and G. Houseman (1985), Role of lithospheric strength heterogeneities in the tectonics of Tibet and neighbouring regions, *Nature*, *315*, 297–301, doi:10.1038/315297a0. 2.2.1, 2.6.3

England, P., and G. Houseman (1986), Finite strain calculations of continental deformation 2. Comparison with the India-Asia collision zone, *J. Geophys. Res.*, *91*(B3), 3664–3676, doi:10.1029/JB091iB03p03664. 2.6.3, 2.6.3, 5.9, 5.4.5, 5.4.5, 6.4, 6.6, 7.1

England, P., and G. Houseman (1989), Extension during continental convergence, with application to the Tibetan Plateau, *J. Geophys. Res.*, *94*(B12), 17,561–17,579, doi:10.1029/JB094iB12p17561. 1.5, 1.3.4, 2.1.2, 2.3.1, 2.6.3, 6

England, P., and D. McKenzie (1982), A thin viscous sheet model for continental deformation, *Geophys. J. R. Astron. Soc.*, *70*, 295–321, doi:10.1111/j.1365-246X.1982.tb04969.x. 2.6.3, 2.6.3, 5.1, 5.2.1, 5.2.1, 5.3.1, 5.4.4

England, P., and D. McKenzie (1983), Correction to: a thin viscous sheet model for continental deformation, *Geophys. J. R. Astron. Soc.*, *73*, 523–532, doi:10.1111/j.1365-246X.1983.tb03328.x. 5.1, 5.2.1, 5.2.2, 5.2.4

England, P., and P. Molnar (1990), Right-lateral shear and rotation as the explanation for strike-slip faulting in eastern Tibet, *Nature*, *344*(6262), 140–142, doi:10.1038/344140a0. 2.6.1

England, P., and P. Molnar (1997a), The field of crustal velocity in Asia calculated from Quaternary rates of slip on faults, *Geophys. J. Int.*, *130*, 551–582, doi:10.1111/j.1365-246X.1997.tb01853.x. 2.4.2

England, P., and P. Molnar (1997b), Active deformation of Asia: From kinematics to dynamics, *Science*, *278*, 647–650, doi:10.1126/science.278.5338.647. 2.4.2, 7.1

England, P., and P. Molnar (2005), Late Quaternary to decadal velocity fields in Asia, *J. Geophys. Res.*, *110*(B12401), doi:10.1029/2004JB003541. 2.4.2, 2.9, 2.18, 2.6.3, 3.3.4, 6, 6.1.2, 6.5, 7.4

England, P., G. Houseman, and L. Sonder (1985), Length scales for continental deformation in convergent, divergent, and strike-slip environments: Analytical and approximate solutions for a thin viscous sheet model, *J. Geophys. Res.*, *90*(B5), 3551–3557, doi:10.1029/JB090iB05p03551. 5.1

Fan, G. W., J. F. Ni, and T. C. Wallace (1994), Active tectonics of the Pamirs and Karakoram, *J. Geophys. Res.*, *99*(B4), 7131–7160, doi:10.1029/93JB02970. 2.2.1

Farr, T. G., P. A. Rosen, E. Caro, R. Crippen, R. Duren, S. Hensley, M. Kobrick, M. Paller, E. Rodriguez, L. Roth, D. Seal, S. Shaffer, J. Shimada, J. Umland, M. Werner, M. Oskin, D. Burbank, and D. Alsdorf (2007), The shuttle radar topography mission, *Rev. Geophys.*, *45*(2), RG2004, doi:10.1029/2005RG000183. 3.2.4

Ferretti, A., C. Prati, and F. Rocca (2001), Permanent scatterers in SAR interferometry, *IEEE T. Geosci. Remote Sens.*, *39*(1), 8–20, doi:10.1109/36.898661. 3.2.5, 3.3.8

Fielding, E., B. Isacks, M. Barazangi, and C. Duncan (1994), How flat is Tibet?, *Geology*, *22*(2), 163–167, doi:10.1130/0091-7613(1994)022. 2.2.1

Fielding, E. J., R. G. Blom, and R. M. Goldstein (1998), Rapid subsidence over oil fields measured by SAR interferometry, *Geophys. Res. Lett.*, *25*(17), 3215–3218, doi:10.1029/98GL52260. 3.1

Flesch, L., and R. Bendick (2007), Present-day kinematics at the India-Asia collision zone: Comment, *Geology*, *35*(1), e160, doi:10.1130/G24443C.1. 2.6.2

Flesch, L. M., A. J. Haines, and W. E. Holt (2001), Dynamics of the India-Eurasia collision zone, *J. Geophys. Res.*, *106*(B8), 16,435–16,460, doi:10.1029/2001JB000208. 2.6.3, 6, 6.1.2

Flesch, L. M., W. E. Holt, P. G. Silver, M. Stephenson, C. Y. Wang, and W. W. Chan (2005), Constraining the extent of crust-mantle coupling in central Asia using GPS, geologic, and shear wave splitting data, *Earth Planet Sci. Lett.*, *238*(1-2), 248–268, doi:10.1016/j.epsl.2005.06.023. 2.5.3

Floyd, M. A., H. Billiris, D. Paradissis, G. Veis, A. Avallone, P. Briole, S. McClusky, J.-M. Nocquet, K. Palamartchouk, B. Parsons, and P. C. England (2010), A new velocity field for Greece: Implications for the kinematics and dynamics of the Aegean, *J. Geophys. Res.*, *115*(B10403), doi:10.1029/2009JB007040. 1.1

Fruneau, B., J. Achache, and C. Delacourt (1996), Observation and modelling of the Saint-Etienne-de-Tinee landslide using SAR interferometry, *Tectonophysics*, *265*(3-4), 181–190, doi:10.1016/S0040-1951(96)00047-9. 3.1

Funning, G. J. (2005), Source parameters of large shallow earthquakes in the Alpine-Himalayan belt from InSAR and waveform modelling, Ph.D. thesis, Faculty of Physical Sciences, University of Oxford. 3.1

Funning, G. J., B. Parsons, and T. J. Wright (2007), Fault slip in the 1997 Manyi, Tibet earthquake from linear elastic modelling of InSAR displacements, *Geophys. J. Int.*, *169*(3), 988–1008, doi:10.1111/j.1365-246X.2006.03318.x. 2.3.2

Gan, W., P. Zhang, Z.-K. Shen, Z. Niu, M. Wang, Y. Wan, D. Zhou, and J. Cheng (2007), Present-day crustal motion within the Tibetan Plateau inferred from GPS measurements, *J. Geophys. Res.*, *112*(B08416), doi:10.1029/2005JB004120. 2.6, 2.4.1, 2.7, 2.4.1, 2.6.2, 3.3.4, 3.3.4, 6.1.3, 6.3, 6.1.4, 6.5, 7.4

Garthwaite, M. C., and G. A. Houseman (2011), Validity of the thin viscous sheet approximation in models of continental collision, *J. Geophys. Res.*, *116*(B02404), doi:10.1029/2010JB007770. 5

Geller, R. J., D. D. Jackson, Y. Y. Kagan, and F. Mulargia (1997), Earthquakes cannot be predicted, *Science*, *275*(5306), 1616–1617, doi:10.1126/science.275.5306.1616. 1

Ghosh, A., W. E. Holt, L. Wen, A. J. Haines, and L. M. Flesch (2008), Joint modeling of lithosphere and mantle dynamics elucidating lithosphere-mantle coupling, *Geophys. Res. Lett.*, *35*(L16309), doi:10.1029/2008GL034365. 5.1, 5.4.5

Goetze, C. (1978), The mechanisms of creep in Olivine, *Phil. Trans. R. Soc. Lond. A*, *288*(1350), 99–119, doi:10.1098/rsta.1978.0008. 1.2

Goldstein, R. M., and C. L. Werner (1998), Radar interferogram filtering for geophysical applications, *Geophys. Res. Lett.*, *25*(21), 4035–4038, doi:10.1029/1998GL900033. 3.2.4

Goldstein, R. M., H. A. Zebker, and C. L. Werner (1988), Satellite radar interferometry - two-dimensional phase unwrapping, *Radio Sci.*, *23*(4), 713–720, doi:10.1029/RS023i004p00713. 3.2.4

Goldstein, R. M., H. Engelhardt, B. Kamb, and R. M. Frolich (1993), Satellite radar interferometry for monitoring ice-sheet motion - application to an Antarctic ice stream, *Science*, *262*(5139), 1525–1530, doi:10.1126/science.262.5139.1525. 3.1

Gourmelen, N., and F. Amelung (2005), Postseismic Mantle Relaxation in the Central Nevada Seismic Belt, *Science*, *310*(5753), 1473–1476, doi:10.1126/science.1119798. 1.4

Gourmelen, N., F. Amelung, and R. Lanari (2010), Interferometric synthetic aperture radar-GPS integration: Interseismic strain accumulation across the Hunter Mountain fault in the eastern California shear zone, *J. Geophys. Res.*, *115*(B09408), doi:10.1029/2009JB007064. 3.2.6

Gourmelen, N., A. Shepherd, D. Angus, Q. Fisher, and D. Lesnic (2011), Quantifying the success of onshore carbon capture and storage, *Geology*, In review. 3.1

Green, O. R., M. P. Searle, R. I. Corfield, and R. M. Corfield (2008), Cretaceous-Tertiary Carbonate Platform Evolution and the Age of the India-Asia Collision along the Ladakh Himalaya (Northwest India), *J. Geol.*, *116*(4), 331–353, doi:10.1086/588831. 2.1.1

GSRM (2010), Global Strain Rate Map Project, http://gsrm.unavco.org/, Retrieved 17/10/2011. 3.1, 7.4, 7.5

Guarnieri, A. M., F. Rocca, L. Perletta, D. Scapin, and A. Broquetas (2011), Design of a geosynchronous SAR system for water-vapour maps and deformation estimation, *Proceedings of Fringe Workshop 2011, ESA-ESRIN*. 1.4.1

Guillot, S., E. Garzanti, D. Baratoux, D. Marquer, G. Maheo, and J. de Sigoyer (2003), Reconstructing the total shortening history of the NW Himalaya, *Geochem. Geophys. Geosyst.*, *4*(7), 1064, doi:10.1029/2002GC000484. 2.1.1

Hager, B. H., R. W. King, and M. H. Murray (1991), Measurement of Crustal Deformation Using the Global Positioning System, *Annual Review of Earth and Planetary Sciences*, *19*(1), 351–382, doi:10.1146/annurev.ea.19.050191.002031. 2.4.1

Hamling, I. J., A. Ayele, L. Bennati, E. Calais, C. J. Ebinger, D. Keir, E. Lewi, T. J. Wright, and G. Yirgu (2009), Geodetic observations of the ongoing Dabbahu rifting episode: new dyke intrusions in 2006 and 2007, *Geophys. J. Int.*, *178*(2), 989–1003, doi:10.1111/j.1365-246X.2009.04163.x. 3.1

Hamlyn, J. (2011), Assessing the variability in the slip rate of the Altyn Tagh Fault using InSAR data, Master's thesis, School of Earth and Environment, University of Leeds. 4.1

Hammond, W. C., G. Blewitt, and C. Kreemer (2011), Block modeling of crustal deformation of the northern Walker Lane and Basin and Range from GPS velocities, *J. Geophys. Res.*, *116*(B04402), doi:10.1029/2010JB007817. 1.1

Hanssen, R. F. (2001), *Radar interferometry - Data interpretation and error analysis*, Kluwer Academic Publishers, Netherlands. 3.1, 3.2.1, 3.2.2, 3.2.2, 3.2.5, 3.3.6, 3.3.6

Harrison, C. G. A., K. J. Miskell, G. W. Brass, E. S. Saltzman, and J. L. Sloan (1983), Continental hypsography, *Tectonics*, *2*(4), 357–377, doi:10.1029/TC002i004p00357. 6.1.1

He, J., and J. Chery (2008), Slip rates of the Altyn Tagh, Kunlun and Karakorum faults (Tibet) from 3D mechanical modeling, *Earth Planet Sci. Lett.*, *274*(1-2), 50–58, doi:10.1016/j.epsl.2008.06.049. 1.4.2

Heidbach, O., M. Tingay, A. Barth, J. Reinecker, D. Kurfeß, and B. Müller (2008), The World Stress Map database release 2008, http://dc-app3-14.gfz-potsdam.de/, doi:10.1594/GFZ.WSM.Rel2008, Retrieved 3/10/2011. 6.5, 6.1.4

Hestenes, M. R., and E. Stiefel (1952), Methods of conjugate gradients for solving linear systems, *J. Res. Nat. Bur. Stand.*, *49*(6), 409–436. 5.3.2

Hetland, E. A., and B. H. Hager (2004), Relationship of geodetic velocities to velocities in the mantle, *Geophys. Res. Lett.*, *31*(L17604), doi:10.1029/2004GL020691. 1.4.2, 7.1, 7.1

Hetland, E. A., and B. H. Hager (2006), Interseismic strain accumulation: Spin-up, cycle invariance, and irregular rupture sequences, *Geochem. Geophys. Geosyst.*, *7*(Q05004), doi:10.1029/2005GC001087. 1.4.2, 2.3.2, 7.1

Hi-CLIMB (2005), Himalayan-Tibetan Continental Lithosphere during Mountain Building, `http://quakes.oce.orst.edu/Nabelek/Hiclimb/index.html`, Retrieved 11/08/2011. 2.5

Hilley, G. E., R. Bürgmann, P. Z. Zhang, and P. Molnar (2005), Bayesian inference of plastosphere viscosities near the Kunlun Fault, northern Tibet, *Geophys. Res. Lett.*, *32*(L01302), doi:10.1029/2004GL021658. 2.3.2

Hilley, G. E., K. M. Johnson, M. Wang, Z. K. Shen, and R. Bürgmann (2009), Earthquake-cycle deformation and fault slip rates in northern Tibet, *Geology*, *37*(1), 31–34, doi:10.1130/G25157A.1. 2.3.2, 2.3.2

Hodges, K. V. (2000), Tectonics of the Himalaya and southern Tibet from two perspectives, *Geol. Soc. Am. Bull.*, *112*(3), 324–350, doi:10.1130/0016-7606(2000)112¡0324:TOTHAS¿2.3.CO;2. 2.2.1

Holt, W., N. Chamot-Rooke, X. Le Pichon, A. Haines, B. Shen-Tu, and J. Ren (2000), Velocity field in Asia inferred from Quaternary fault slip rates and Global Positioning System observations, *J. Geophys. Res.*, *105*(B8), 19,185–19,209, doi:10.1029/2000JB900045. 2.4.2, 6.1.2, 6.1.3, 6.5

Holt, W. E. (2000), Correlated crust and mantle strain fields in Tibet, *Geology*, *28*(1), 67–70, doi:10.1130/0091-7613. 2.5.3

Houlié, N., and R. J. Phillips (2011), Quaternary rupture behavior of the Karakoram fault, NW Himalaya, *Nature*, Submitted. 2.3.2, 2.3.2

Houseman, G., and P. England (1986), Finite strain calculations of continental deformation: 1. Method and general results for convergent zones, *J. Geophys. Res.*, *91*(B3), 3651–3663, doi:10.1029/JB091iB03p03651. 2.6.3, 5.1, 5.3.1, 5.4.1, 5.4.3, 5.4.5, 6

Houseman, G., and P. England (1993), Crustal thickening versus lateral expulsion in the Indian-Asian continental collision, *J. Geophys. Res.*, *98*(B7), 12,233–12,249, doi:10.1029/93JB00443. 2.6.3, 5.4.3, 6.1.5

Houseman, G., and P. England (1996), A lithospheric-thickening model for the Indo-Asian collision, in *The Tectonic Evolution of Asia*, edited by A. Yin and T. M. Harrison, pp. 3–17, Cambridge University Press, New York. 2.17, 2.18

Houseman, G., and L. Gemmer (2007), Intra-orogenic extension driven by gravitational instability: Carpathian-Pannonian orogeny, *Geology*, *35*(12), 1135–1138, doi:10.1130/G23993A.1. 1.2.2, 5.3.2

Houseman, G. A. (2003), Basil equations: Spherical geometry of the thin viscous sheet, Unpublished manuscript. 6.1

Houseman, G. A., L. Gemmer, and S. Borthwick (2004), 3D finite element program - Oregano, *Unpublished manuscript*, pp. 1–60. 5.3.1

Houseman, G. A., T. D. Barr, and L. A. Evans (2008), Basil: stress and deformation in a viscous material, in *Microdynamics Simulation*, edited by P. D. Bons, D. Koehn, and M. W. Jessell, pp. 139–154, Springer-Verlag, doi:10.1007/978-3-540-44793-1. 5.3.1

Houseman, G. A., D. P. McKenzie, and P. Molnar (1981), Convective instability of a thickened boundary-layer and its relevance for the thermal evolution of continental convergent belts, *J. Geophys. Res.*, *86*(B7), 6115–6132, doi:10.1029/JB086iB07p06115. 2.6.3

Huang, W.-C., J. F. Ni, F. Tilmann, D. Nelson, J. Guo, W. Zhao, J. Mechie, R. Kind, J. Saul, R. Rapine, and T. M. Hearn (2000), Seismic polarization anisotropy beneath the central Tibetan Plateau, *J. Geophys. Res.*, *105*(B12), 27,979–27,989, doi:10.1029/2000JB900339. 2.5.3

INDEPTH (2002), INternational DEep Profiling of Tibet and the Himalayas, `http://www.geo.cornell.edu/geology/indepth/indepth.html`, Retrieved 11/08/2011. 2.5, 2.5.1

Isacks, B., J. Oliver, and L. R. Sykes (1968), Seismology and new global tectonics, *J. Geophys. Res.*, *73*(18), 5855–5899, doi:10.1029/JB073i018p05855. 1.1

Jackson, J. (2002), Strength of the continental lithosphere: Time to abandon the jelly sandwich?, *GSA Today*, *12*, 4–9, doi:10.1130/1052-5173(2002)012. 1.2, 1.3, 1.2, 1.2.2

Jackson, J., D. McKenzie, K. Priestley, and B. Emmerson (2008), New views on the structure and rheology of the lithosphere, *J. Geol. Soc. London*, *165*, 453–465, doi:10.1144/0016-76492007-109. 1.2.2, 7.1

Jiménez-Munt, I., and J. P. Platt (2006), Influence of mantle dynamics on the topographic evolution of the Tibetan Plateau: Results from numerical modeling, *Tectonics*, *25*(TC6002), doi:10.1029/2006TC001963. 2.6.3

Jiménez-Munt, I., D. Garcia-Castellanos, and M. Fernandez (2005a), Thin-sheet modelling of lithospheric deformation and surface mass transport, *Tectonophysics*, *407*(3-4), 239–255, doi:10.1016/j.tecto.2005.08.015. 5.1

Jiménez-Munt, I., D. Garcia-Castellanos, A. M. Negredo, and J. P. Platt (2005b), Gravitational and tectonic forces controlling postcollisional deformation and the present-day stress field of the Alps: Constraints from numerical modeling, *Tectonics*, *24*(TC5009), doi:10.1029/2004TC001754. 5.1

Johnson, K. M., G. E. Hilley, and R. Bürgmann (2007), Influence of lithosphere viscosity structure on estimates of fault slip rate in the Mojave region of the San Andreas fault system, *J. Geophys. Res.*, *112*(B07408), doi:10.1029/2006JB004842. 1.4.2, 7.1

Jolivet, R., R. Cattin, N. Chamot-Rooke, C. Lasserre, and G. Peltzer (2008), Thin-plate modeling of interseismic deformation and asymmetry across the Altyn Tagh fault zone, *Geophys. Res. Lett.*, *35*(L02309), doi:10.1029/2007GL031511. 2.3.2, 4.1, 4.6, 7.1, 7.4

Jolivet, R., C. Lasserre, M. P. Doin, S. Guillaso, O. Cavalié, G. Peltzer, J. Sun, D. Rong, Z.-K. Shen, and X. Xu (2010), Time series analysis of strain accumulation along the Haiyuan fault (Gansu, China) over the 1993-2009 period, from ERS and ENVISAT InSAR data, *Geophys. Res. Abstr.*, *12*, 10,381. 4.1

Jolivet, R., R. Grandin, C. Lasserre, M.-P. Doin, and G. Peltzer (2011), Systematic InSAR tropospheric phase delay corrections from global meteorological reanalysis data, *Geophys. Res. Lett.*, *38*(L17311), doi:10.1029/2011GL048757. 3.2.5, 4.6, 7.5

Jónsson, S., P. Segall, R. Pedersen, and G. Björnsson (2003), Post-earthquake ground movements correlated to pore-pressure transients, *Nature*, *424*(6945), 179–183, doi:10.1038/nature01776. 1.4.3

Karplus, M. S., W. Zhao, S. L. Klemperer, Z. Wu, J. Mechie, D. Shi, L. D. Brown, and C. C. (2011), Injection of Tibetan crust beneath the south Qaidam Basin: Evidence from INDEPTH IV wide-angle seismic data, *J. Geophys. Res.*, *116*(B07301), doi:10.1029/2010JB007911. 2.5.2

Kidd, W. S. F., and P. Molnar (1988), Quaternary and active faulting observed on the 1985 Academia Sinica-Royal Society Geotraverse of Tibet, *Phil. Trans. R. Soc. Lond. A*, *327*(1594), 337–363, doi:10.1098/rsta.1988.0133. 2.3.2

Kimura, H., and Y. Yamaguchi (2000), Detection of landslide areas using satellite radar interferometry, *Photogramm. Eng. Rem. S.*, *66*(3), 337–344. 3.1

Kind, R., X. Yuan, J. Saul, D. Nelson, S. V. Sobolev, J. Mechie, W. Zhao, G. Kosarev, J. Ni, U. Achauer, and M. Jiang (2002), Seismic images of crust and upper mantle beneath Tibet: Evidence for Eurasian plate subduction, *Science*, *298*(5596), 1219–1221, doi:10.1126/science.1078115. 2.5.2

Kirby, E., N. Harkins, E. Wang, X. Shi, C. Fan, and B. D. (2007), Slip rate gradients along the eastern Kunlun fault, *Tectonics*, *26*(TC2010), doi:10.1029/2006TC002033. 2.3.2

Kosarev, G., R. Kind, S. V. Sobolev, X. Yuan, W. Hanka, and S. Oreshin (1999), Seismic evidence for a detached Indian lithospheric mantle beneath Tibet, *Science*, *283*(5406), 1306–1309, doi:10.1126/science.283.5406.1306. 2.5.2

Kreemer, C. (2009), Absolute plate motions constrained by shear wave splitting orientations with implications for hot spot motions and mantle flow, *J. Geophys. Res.*, *114*(B10405), doi:10.1029/2009JB006416. 1.1

Kreemer, C., W. E. Holt, and A. J. Haines (2003), An integrated global model of present-day plate motions and plate boundary deformation, *Geophys. J. Int.*, *154*(1), 8–34, doi:10.1046/j.1365-246X.2003.01917.x. 1.1, 3.1, 7.4, 7.5

Kruskal, J. B. (1956), On the shortest spanning subtree of a graph and the traveling salesman problem, *Proc. Am. Math. Soc.*, *7*(1), 48–50, doi:10.1090/S0002-9939-1956-0078686-7. 3.3.1

Laske, G., G. Masters, and C. Reif. (2011), CRUST 2.0: A new global crustal model at 2x2 degrees, `http://igppweb.ucsd.edu/~gabi/crust2.html`, Retrieved 2/10/2011. 6.1.1

Lasserre, C., Y. Gaudemer, P. Tapponnier, A. S. Mériaux, J. Van der Woerd, D. Yuan, F. J. Ryerson, R. C. Finkel, and M. Caffee (2002), Fast late Pleistocene slip rate on the Leng Long Ling segment of the Haiyuan fault, Qinghai, China, *J. Geophys. Res.*, *107*(B11), 2276, doi:10.1029/2000JB000060. 2.3.2

Lasserre, C., G. Peltzer, F. Crampe, Y. Klinger, J. Van der Woerd, and P. Tapponnier (2005), Coseismic deformation of the 2001 Mw 7.8 Kokoxili earthquake in Tibet, measured by synthetic aperture radar interferometry, *J. Geophys. Res.*, *110*(B12408), doi:10.1029/2004JB003500. 2.3.2, 4.3

Lasserre, C., O. Cavalié, G. Peltzer, A. Socquet, M. P. Doin, J. Sun, X. Xu, Z.-K. Shen, Q. Wang, and Y. Gaudemer (2007), Interseismic strain across the Altyn Tagh and Haiyuan faults at the northern edge of the Tibetan plateau, measured by space geodesy, *Geophys. Res. Abstr.*, *9*, 10,102. 4.1

Le Pichon, X. (1968), Sea-floor spreading and continental drift, *J. Geophys. Res.*, *73*(12), 3661–3697, doi:10.1029/JB073i012p03661. 1.1

Le Pichon, X., J. Francheteau, and J. Bonnin (1973), *Plate Tectonics*, 300 pp., Elsevier, Amsterdam. 1.1

Lebedev, S., and R. D. van der Hilst (2008), Global upper-mantle tomography with the automated multimode inversion of surface and S-wave forms, *Geophys. J. Int.*, *173*(2), 505–518, doi:10.1111/j.1365-246X.2008.03721.x. 2.5.1

Lechmann, S. M., D. A. May, B. J. P. Kaus, and S. M. Schmalholz (2011), Comparing thin-sheet models with 3D multilayer models for continental collision, *Geophys. J. Int.*, *187*(1), 10–33, doi:10.1111/j.1365-246X.2011.05164.x. 2.6.4, 5.4.1, 5.4.5, 7.3

Lev, E., M. D. Long, and R. D. van der Hilst (2006), Seismic anisotropy in Eastern Tibet from shear wave splitting reveals changes in lithospheric deformation, *Earth Planet Sci. Lett.*, *251*(3-4), 293–304, doi:10.1016/j.epsl.2006.09.018. 2.5.3

Li, C., R. D. van der Hilst, A. S. Meltzer, and E. R. Engdahl (2008), Subduction of the Indian lithosphere beneath the Tibetan plateau and Burma, *Earth Planet Sci. Lett.*, *274*(1-2), 157–168, doi:10.1016/j.epsl.2008.07.016. 2.11, 2.5.1, 2.5.2, 7.3

Li, C. Y., P. Z. Zhang, J. H. Yin, and W. Min (2009a), Late Quaternary left-lateral slip rate of the Haiyuan fault, northeastern margin of the Tibetan Plateau, *Tectonics*, *28*(TC5010), doi:10.1029/2008TC002302. 2.3.2

Li, Z., Y. Liu, X. Zhou, P. Cross, and W. Feng (2009b), Using small baseline interferometric SAR to map nonlinear ground motion: a case study in Northern Tibet, *J. Appl. Geodesy*, pp. 163–170, doi:10.1515/JAG.2009.017. 3.1

Li, Z., E. J. Fielding, and P. Cross (2009c), Integration of InSAR time-series analysis and water-vapor correction for mapping postseismic motion after the 2003 Bam (Iran) earthquake, *IEEE T. Geosci. Remote Sens.*, *47*(9), 3220–3230, doi:10.1109/TGRS.2009.2019125. 3.2.5, 7.5

Li, Z., E. J. Fielding, P. Cross, and R. Preusker (2009d), Advanced InSAR atmospheric correction: MERIS/MODIS combination and stacked water vapour models, *Int. J. Remote Sens.*, *30*(13), 3343–3363, doi:10.1080/01431160802562172. 3.2.5, 4.6

Lin, Y. N., M. Simons, E. A. Hetland, P. Muse, and C. DiCaprio (2010), A multiscale approach to estimating topographically correlated propagation delays in radar interferograms, *Geochem. Geophys. Geosyst.*, *11*(Q09002), doi:10.1029/2010GC003228. 3.2.5

Liu, Q. (1993), Paléoclimat et contraintes chronologiques sur les mouvements récent dans l'Ouest du Tibet: Failles du Karakorum et de Longmu Co-Gozha Co, lacs en pull-apart de Longmu Co et de Sumxi Co., Ph.D. thesis, Universite Paris VII. 2.3.2, 2.6.1

Lohman, R. B., and M. Simons (2005), Locations of selected small earthquakes in the Zagros mountains, *Geochem. Geophys. Geosyst.*, *6*(Q03001), doi:10.1029/2004GC000849. 4.3

Lopez-Quiroz, P., M. P. Doin, F. Tupin, P. Briole, and J. M. Nicolas (2009), Time series analysis of Mexico City subsidence constrained by radar interferometry, *J. Appl. Geophys.*, *69*(1), 1–15, doi:10.1016/j.jappgeo.2009.02.006, Fringe 2007 Workshop, ESA ESRIN, Frascati, ITALY, NOV 26-30, 2007. 3.1

Lorinczi, P., and G. Houseman (2010), Geodynamical models of lithospheric deformation, rotation and extension of the Pannonian Basin of Central Europe, *Tectonophysics*, *492*(1-4), 73–87, doi:10.1016/j.tecto.2010.05.007. 5.1

Loveland, T. R., B. C. Reed, J. F. Brown, D. O. Ohlen, Z. Zhu, L. Yang, and J. W. Merchant (2000), Development of a global land cover characteristics database and IGBP DISCover from 1 km AVHRR data, *Int. J. Remote Sens.*, *21*(6-7), 1303–1330, doi:10.1080/014311600210191. 3.3

Loveless, J. P., and B. J. Meade (2011), Partitioning of localized and diffuse deformation in the Tibetan Plateau from joint inversions of geologic and geodetic observations, *Earth Planet Sci. Lett.*, *303*(1-2), 11–24, doi:10.1016/j.epsl.2010.12.014. 2.6.2

Lyon-Caen, H., and P. Molnar (1985), Gravity-anomalies, flexure of the Indian plate, and the structure, support and evolution of the Himalaya and Ganga Basin, *Tectonics*, *4*(6), 513–538, doi:10.1029/TC004i006p00513. 2.5, 6.1.1

Maggi, A., J. A. Jackson, D. McKenzie, and K. Priestley (2000a), Earthquake focal depths, effective elastic thickness, and the strength of the continental lithosphere, *Geology*, *28*(6), 495–498, doi:10.1130/0091-7613(2000)28. 1.2.2

Maggi, A., J. A. Jackson, K. Priestley, and C. Baker (2000b), A re-assessment of focal depth distributions in southern Iran, the Tien Shan and northern India: do earthquakes really occur in the continental mantle?, *Geophys. J. Int.*, *143*(3), 629–661, doi:10.1046/j.1365-246X.2000.00254.x. 1.2.2, 2.5.4

Massonnet, D., and K. L. Feigl (1998), Radar interferometry and its application to changes in the earth's surface, *Rev. Geophys.*, *36*(4), 441–500, doi:10.1029/97RG03139. 3.1, 3.1

Massonnet, D., M. Rossi, C. Carmona, F. Adragna, G. Peltzer, K. Feigl, and T. Rabaute (1993), The displacement field of the Landers earthquake mapped by radar interferometry, *Nature*, *364*(6433), 138–142, doi:10.1038/364138a0. 1.4.1, 3.1

Massonnet, D., P. Briole, and A. Arnaud (1995), Deflation of Mount Etna monitored by spaceborne radar interferometry, *Nature*, *375*(6532), 567–570, doi:10.1038/375567a0. 3.1

Maurin, T., F. Masson, C. Rangin, U. T. Min, and P. Collard (2010), First global positioning system results in northern Myanmar: Constant and localized slip rate along the Sagaing fault, *Geology*, *38*(7), 591–594, doi:10.1130/G30872.1. 2.3.2

McKenzie, D. (1972), Active tectonics of the Mediterranean region, *Geophys. J. R. Astron. Soc.*, *30*(2), 109–185, doi:10.1111/j.1365-246X.1972.tb02351.x. 1.1

McKenzie, D. (1977), Surface deformation, gravity anomalies and convection, *Geophys. J. R. Astron. Soc.*, *48*(2), 211–238, doi:10.1111/j.1365-246X.1977.tb01297.x. 5.4.1

McKenzie, D. P. (1967), Some remarks on heat flow and gravity anomalies, *J. Geophys. Res.*, *72*(24), 6261–6273, doi:10.1029/JZ072i024p06261. 1.1

McKenzie, D. P., and R. L. Parker (1967), The North Pacific - an example of tectonics on a sphere, *Nature*, *216*(5122), 1276–1280, doi:10.1038/2161276a0. 1.1

McNamara, D. E., T. J. Owens, P. G. Silver, and F. T. Wu (1994), Shear-wave anisotropy beneath the Tibetan plateau, *J. Geophys. Res.*, *99*(B7), 13,655–13,665, doi:10.1029/93JB03406. 2.5.3

Meade, B. J. (2007), Present-day kinematics at the India-Asia collision zone, *Geology*, *35*(1), 81–84, doi:10.1130/G22924A.1. 1.1, 2.16, 2.6.2, 7.2, 7.2, 7.1

Meade, B. J., and B. H. Hager (2005), Block models of crustal motion in southern California constrained by GPS measurements, *J. Geophys. Res.*, *110*(B03403), doi:10.1029/2004JB003209. 1.1, 2.6.2, 7.2

Medvedev, S. E., and Y. Y. Podladchikov (1999), New extended thin-sheet approximation for geodynamic applications - I. Model formulation, *Geophys. J. Int.*, *136*(3), 567–585, doi:10.1046/j.1365-246x.1999.00734.x. 5.1, 7.3

Menke, W. (1984), *Geophysical Data Analysis: Discrete Inverse Theory*, Academic Press, Inc. 3.3.3, 3.3.3, 3.3.9, 3.3.10

Mériaux, A. S., F. J. Ryerson, P. Tapponnier, J. Van der Woerd, R. C. Finkel, X. Xu, Z. Xu, and M. W. Caffee (2004), Rapid slip along the central Altyn Tagh fault: Morphochronologic evidence from Cherchen He and Sulamu Tagh, *J. Geophys. Res.*, *109*(B06401), doi:10.1029/2003JB002558. 2.3.2

Meyer, B., P. Tapponnier, Y. Gaudemer, G. Peltzer, S. M. Guo, and Z. T. Chen (1996), Rate of left-lateral movement along the easternmost segment of the Altyn Tagh fault, east of 96 degrees E (China), *Geophys. J. Int.*, *124*(1), 29–44, doi:10.1111/j.1365-246X.1996.tb06350.x. 2.3.2

Molnar, P., and W.-P. Chen (1983), Focal depths and fault plane solutions of earthquakes under the Tibetan plateau, *J. Geophys. Res.*, *88*(B2), 1180–1196, doi:10.1029/JB088iB02p01180. 2.5.4

Molnar, P., and K. E. Dayem (2010), Major intracontinental strike-slip faults and contrasts in lithospheric strength, *Geosphere*, *6*(4), 444–467, doi:10.1130/GES00519.1. 2.1, 2.3.2, 2.3.2, 2.3.2, 7.1

Molnar, P., and H. Lyon-Caen (1988), Some simple physical aspects of the support, structure, and evolution of mountain belts, *Geol. Soc. Am. Sp. Pap.*, *218*, 123–153. 1.2.1, 1.4, 6.4, 7.3

Molnar, P., and H. Lyon-Caen (1989), Fault plane solutions of earthquakes and active tectonics of the Tibetan plateau and its margins, *Geophys. J. Int.*, *99*(1), 123–153, doi:10.1111/j.1365-246X.1989.tb02020.x. 2.5, 2.3.1

Molnar, P., and J. M. Stock (2009), Slowing of India's convergence with Eurasia since 20 Ma and its implications for Tibetan mantle dynamics, *Tectonics*, *28*(TC3001), doi:10.1029/2008TC002271. 2.1.2

Molnar, P., and P. Tapponnier (1975), Cenozoic tectonics of Asia: Effects of a continental collision, *Science*, *189*, 419–426, doi:10.1126/science.189.4201.419. 1.1, 2.3.2, 2.3.2, 2.6.1

Molnar, P., and P. Tapponnier (1978), Active tectonics of Tibet, *J. Geophys. Res.*, *83*(B11), 5361–5375, doi:10.1029/JB083iB11p05361. 2.3.1

Molnar, P., and P. Tapponnier (1981), A possible dependence of tectonic strength on the age of the crust in Asia, *Earth Planet Sci. Lett.*, *52*(1), 107–114, doi:10.1016/0012-821X(81)90213-2. 2.2.1, 2.2.2, 2.3.2, 6.1.2

Molnar, P., P. England, and J. Martinod (1993), Mantle dynamics, uplift of the Tibetan plateau, and the Indian monsoon, *Rev. Geophys.*, *31*(4), 357–396, doi:10.1029/93RG02030. 1.1, 2, 2.1.2, 2.1.3, 2.6.3

Molnar, P., G. A. Houseman, and P. C. England (2006), Palaeo-altimetry of Tibet, *Nature*, *444*, E4–E5, doi:10.1038/nature05368. 2.1.3

Mooney, W. D., G. Laske, and T. G. Masters (1998), CRUST 5.1: A global crustal model at 5 degrees x 5 degrees, *J. Geophys. Res.*, *103*(B1), 727–747, doi:10.1029/97JB02122. 2.10, 2.5, 6.1.1

Morgan, W. J. (1968), Rises trenches great faults and crustal blocks, *J. Geophys. Res.*, *73*(6), 1959–1982, doi:10.1029/JB073i006p01959. 1.1, 1.1

Nabelek, J., G. Hetenyi, J. Vergne, S. Sapkota, B. Kafle, M. Jiang, H. Su, J. Chen, B. S. Huang, and Hi-CLIMB Team (2009), Underplating in the Himalaya-Tibet Collision Zone Revealed by the Hi-CLIMB Experiment, *Science*, *325*(5946), 1371–1374, doi:10.1126/science.1167719. 2.3.1, 2.5.2

Neil, E., and G. A. Houseman (1997), Geodynamics of the Tarim Basin and the Tian Shan in central Asia, *Tectonics*, *16*(4), 571–584, doi:10.1029/97TC01413. 2.6.3, 6.1.2, 7.3

Nicolas, A., and N. I. Christensen (1987), Formation of anisotropy in upper mantle peridotites - A review, in *Composition, Structure and Dynamics of the Lithosphere-Asthenosphere System*, *Geodyn. Ser.*, vol. 16, edited by K. Fuchs and C. Froidevaux, pp. 111–123, AGU, Washington D. C. 2.5.3

Nur, A., and G. Mavko (1974), Postseismic viscoelastic rebound, *Science*, *183*(4121), 204–206, doi:10.1126/science.183.4121.204. 1.4.2, 1.4.3

Okada, Y. (1985), Surface deformation due to shear and tensile faults in a half-space, *Bull. Seismol. Soc. Am.*, *75*(4), 1135–1154. 1.4.1

Oliver, J., and B. Isacks (1967), Deep earthquake zones anomlalous structures in upper mantle and lithosphere, *J. Geophys. Res.*, *72*(16), 4259–4275, doi:10.1029/JZ072i016p04259. 1.1

Parsons, P., T. Wright, P. Rowe, J. Andrews, J. Jackson, R. Walker, M. Khatib, M. Talebian, E. Bergman, and E. R. Engdahl (2006), The 1994 Sefidabeh (eastern Iran) earthquakes revisited: new evidence from satellite radar interferometry and carbonate dating about the growth of an active fold above a blind thrust fault, *Geophys. J. Int.*, *164*, 202–217, doi:10.1111/j.1365-246X.2005.02655.x. 3.3.6, 3.4.2

Pegler, G., and S. Das (1998), An enhanced image of the Pamir Hindu Kush seismic zone from relocated earthquake hypocentres, *Geophys. J. Int.*, *134*(2), 573–595, doi:10.1046/j.1365-246x.1998.00582.x. 2.2.1

Peltzer, G., and F. Saucier (1996), Present-day kinematics of Asia derived from geologic fault rates, *J. Geophys. Res.*, *101*(B12), 27,943–27,956, doi:10.1029/96JB02698. 2.6.1, 2.6.1, 2.6.3

Peltzer, G., and P. Tapponnier (1988), Formation and evolution of strike-slip faults, rifts, and basins during the India-Asia collision - an experimental approach, *J. Geophys. Res.*, *93*(B12), 15,085–15,117, doi:10.1029/JB093iB12p15085. 2.15, 2.6.1, 2.6.1

Peltzer, G., P. Tapponnier, and R. Armijo (1989), Magnitude of late Quaternary left-lateral displacements along the north edge of Tibet, *Science*, *246*, 1285–1289, doi:10.1126/science.246.4935.1285. 2.3.2, 2.6.1

Peltzer, G., P. Rosen, F. Rogez, and K. Hudnut (1998), Poroelastic rebound along the Landers 1992 earthquake surface rupture, *J. Geophys. Res.*, *103*(B12), 30,131–30,145, doi:10.1029/98JB02302. 1.4.3

Peltzer, G., F. Crampe, S. Hensley, and P. Rosen (2001), Transient strain accumulation and fault interaction in the Eastern California shear zone, *Geology*, *29*(11), 975–978, doi:10.1130/0091-7613(2001)029¡0975:TSAAFI¿2.0.CO;2. 1.4.2

Peyret, M., S. Dominguez, R. Cattin, J. Champenois, M. Leroy, and A. Zajac (2011), Present-day interseismic surface deformation along the Longitudinal Valley, eastern Taiwan, from a PS-InSAR analysis of the ERS satellite archives, *J. Geophys. Res.*, *116*(B03402), doi:10.1029/2010JB007898. 3.2

Phillips, R. J., R. R. Parrish, and M. P. Searle (2004), Age constraints on ductile deformation and long-term slip rates along the Karakoram fault zone, Ladakh, *Earth Planet Sci. Lett.*, *226*(3-4), 305–319, doi:10.1016/j.epsl.2004.07.037. 2.3.2

Pollitz, F. F. (1992), Postseismic relaxation theory on the spherical Earth, *Bull. Seismol. Soc. Am.*, *82*(1), 422–453. 4.5.2

Pollitz, F. F. (1997), Gravitational viscoelastic postseismic relaxation on a layered spherical Earth, *J. Geophys. Res.*, *102*(B8), 17,921–17,941, doi:10.1029/97JB01277. 1.4.3, 4.5.2

Pollitz, F. F. (2003a), The relationship between the instantaneous velocity field and the rate of moment release in the lithosphere, *Geophys. J. Int.*, *153*(3), 595–608, doi:210.1046/j.1365-246X.2003.01924.x. 1.4.2

Pollitz, F. F. (2003b), Transient rheology of the uppermost mantle beneath the Mojave Desert, California, *Earth Planet Sci. Lett.*, *215*(1-2), 89–104, doi:10.1016/S0012-821X(03)00432-1. 1.4.3

Prescott, W. H., and A. Nur (1981), The accommodation of relative motion at depth on the San Andreas fault system in California, *J. Geophys. Res.*, *86*(B2), 999–1004, doi:10.1029/JB086iB02p00999. 1.4.2, 7.1, 7.1

Priestley, K., E. Debayle, D. McKenzie, and S. Pilidou (2006), Upper mantle structure of eastern Asia from multimode surface waveform tomography, *J. Geophys. Res.*, *111*(B10304), doi:10.1029/2005JB004082. 2.5.1, 2.5.4

Priestley, K., J. Jackson, and D. McKenzie (2008), Lithospheric structure and deep earthquakes beneath India, the Himalaya and southern Tibet, *Geophys. J. Int.*, *172*(1), 345–362, doi:10.1111/j.1365-246X.2007.03636.x. 2.5, 2.14, 2.5.4

Pritchard, M. E., and E. J. Fielding (2008), A study of the 2006 and 2007 earthquake sequence of Pisco, Peru, with InSAR and teleseismic data, *Geophys. Res. Lett.*, *35*(L09308), doi:10.1029/2008GL033374. 3.1

Reid, H. F. (1910), The mechanics of the earthquake: the California earthquake of 18 April 1906, *Report of the State Earthquake Investigation Commission. Carnegie Institution of Washington*, *2*(87), 16–28. 1.4

Ren, Y., and Y. Shen (2008), Finite frequency tomography in southeastern Tibet: Evidence for the causal relationship between mantle lithosphere delamination and the north-south trending rifts, *J. Geophys. Res.*, *113*(B10316), doi:10.1029/2008JB005615. 2.5.1, 2.5.2

Robl, J., and K. Stüwe (2005a), Continental collision with finite indenter strength: 1. Concept and model formulation, *Tectonics*, *24*(TC4005), doi:10.1029/2004TC001727. 5.1

Robl, J., and K. Stüwe (2005b), Continental collision with finite indenter strength: 2. European Eastern Alps, *Tectonics*, *24*(TC4014), doi:10.1029/2004TC001741. 5.1

Robl, J., K. Stüwe, S. Hergarten, and L. Evans (2008), Extension during continental convergence in the Eastern Alps: The influence of orogen-scale strike-slip faults, *Geology*, *36*(12), 963–966, doi:10.1130/G25294A.1. 5.1, 5.4.5, 7.3, 7.3

Rosen, P. A., S. Hensley, H. A. Zebker, F. H. Webb, and E. J. Fielding (1996), Surface deformation and coherence measurements of Kilauea volcano, Hawaii, from SIR-C radar interferometry, *J. Geophys. Res. -Planets*, *101*(E10), 23,109–23,125, doi:10.1029/96JE01459. 3.2.3

Rosen, P. A., S. Hensley, I. R. Joughin, F. K. Li, S. N. Madsen, E. Rodriguez, and R. M. Goldstein (2000), Synthetic aperture radar interferometry, *Proceedings of the IEEE*, *88*(3), 333–382, doi:10.1109/5.838084. 3.1

Rosen, P. A., S. Hensley, G. Peltzer, and M. Simons (2004), Updated repeat orbit interferometry package released, *EOS Trans. Am. Geophys. Un.*, *85*(5), 47, doi:10.1029/2004EO050004. 3.3

Rowley, D. B. (1996), Age of initiation of collision between India and Asia: A review of stratigraphic data, *Earth Planet Sci. Lett.*, *145*(1-4), 1–13, doi:10.1016/S0012-821X(96)00201-4. 2.1.1

Rowley, D. B. (1998), Minimum age of initiation of collision between India and Asia north of Everest based on the subsidence history of the Zhepure mountain section, *J. Geol.*, *106*(2), 220–235, doi:10.1086/516018. 2.1.1

Rowley, D. B., and B. S. Currie (2006), Palaeo-altimetry of the late Eocene to Miocene Lunpola basin, central Tibet, *Nature*, *439*, 677–681, doi:10.1038/nature04506. 2.1.3

Royden, L. (1996), Coupling and decoupling of crust and mantle in convergent orogens: Implications for strain partitioning in the crust, *J. Geophys. Res.*, *101*(B8), 17,679–17,705, doi:10.1029/96JB00951. 2.6.4

Royden, L. H., B. C. Burchfiel, R. W. King, E. Wang, Z. Chen, F. Shen, and Y. Liu (1997), Surface deformation and lower crustal flow in eastern Tibet, *Science*, *276*, 788–790, doi:10.1126/science.276.5313.788. 2.6.4

Royden, L. H., B. C. Burchfiel, and R. D. van der Hilst (2008), The geological evolution of the Tibetan plateau, *Science*, *321*, 1054–1058, doi:10.1126/science.1155371. 2.1, 2.3.1

Royer, J.-Y., and R. G. Gordon (1997), The Motion and Boundary Between the Capricorn and Australian Plates, *Science*, *277*(5330), 1268–1274, doi:10.1126/science.277.5330.1268. 1.1

Ryder, I., B. Parsons, T. J. Wright, and G. J. Funning (2007), Post-seismic motion following the 1997 Manyi (Tibet) earthquake: InSAR observations and modelling, *Geophys. J. Int.*, *169*(3), 1009–1027, doi:10.1111/j.1365-246X.2006.03312.x. 2.3.2

Ryder, I., R. Bürgmann, and F. Pollitz (2011), Lower crustal relaxation beneath the Tibetan Plateau and Qaidam Basin following the 2001 Kokoxili earthquake, *Geophys. J. Int.*, *187*, 613–630, doi:10.1111/j.1365-246X.2011.05179.x. 1.4.3, 2.3.2, 4.1, 4.4, 4.8, 4.9, 4.4.1, 4.10, 4.5.2, 4.8, 7.1

Sandwell, D. T., D. Myer, R. Mellors, M. Shimada, B. Brooks, and J. Foster (2008), Accuracy and Resolution of ALOS Interferometry: Vector Deformation Maps of the Father's Day Intrusion at Kilauea, *IEEE T. Geosci. Remote Sens.*, *46*(11, Part 1), 3524–3534, doi:10.1109/TGRS.2008.2000634. 3.2.3

Savage, J. (2000), Viscoelastic-coupling model for the earthquake cycle driven from below, *J. Geophys. Res.*, *105*(B11), 25,525–25,532, doi:10.1029/2000JB900276. 1.4.2, 7.1

Savage, J., and R. O. Burford (1973), Geodetic determination of relative plate motion in central California, *J. Geophys. Res.*, *78*(B5), 832–845, doi:10.1029/JB078i005p00832. 1.4.2, 1.4.2, 1.4.2, 2.6.2, 3.4.2, 4.1, 4.6, 7.1, 7.1

Savage, J., and W. H. Prescott (1978), Asthenosphere Readjustment and the Earthquake Cycle, *J. Geophys. Res.*, *83*(B7), 3369–3376, doi:10.1029/JB083iB07p03369. 1.4.2

Scharroo, R., and P. Visser (1998), Precise orbit determination and gravity field improvement for the ERS satellites, *J. Geophys. Res. -Oceans*, *103*(C4), 8113–8127, doi:10.1029/97JC03179. 3.2.2, 3.2.2, 3.2.6

Schmalholz, S. M., Y. Y. Podladchikov, and J. P. Burg (2002), Control of folding by gravity and matrix thickness: Implications for large-scale folding, *J. Geophys. Res.*, *107*(B1), 2005, doi:10.1029/2001JB000355. 5.4.5

Schmidt, D. A., and R. Bürgmann (2003), Time-dependent land uplift and subsidence in the Santa Clara valley, California, from a large interferometric synthetic aperture radar data set, *J. Geophys. Res.*, *108*(B9), 2416, doi:10.1029/2002JB002267. 3.3.9, 3.3.9

Schueller, S., and P. Davy (2008), Gravity influenced brittle-ductile deformation and growth faulting in the lithosphere during collision: Results from laboratory experiments, *J. Geophys. Res.*, *113*(B12404), doi:10.1029/2007JB005560. 2.6.3

Searle, M. P., J. R. Elliott, R. J. Phillips, and S. L. Chung (2011), Crustal-lithospheric structure and continental extrusion of Tibet, *J. Geol. Soc. London*, *168*(3), 633–672, doi:10.1144/0016-76492010-139. 2.3.2, 2.3.2, 2.3.2

Segall, P. (2010), *Earthquake and volcano deformation*, 1 ed., Princeton University Press. 1.4.3

Sella, G. F., T. H. Dixon, and A. L. Mao (2002), REVEL: A model for Recent plate velocities from space geodesy, *J. Geophys. Res.*, *107*(B4), 2081, doi:10.1029/2000JB000033. 2.9

Shen, F., L. H. Royden, and B. C. Burchfiel (2001), Large-scale crustal deformation of the Tibetan Plateau, *J. Geophys. Res.*, *106*(B4), 6793–6816, doi:10.1029/2001JB000349. 2.20, 2.6.4, 2.6.4

Shen, Z. K., J. Lü, M. Wang, and R. Bürgmann (2005), Contemporary crustal deformation around the southeast borderland of the Tibetan Plateau, *J. Geophys. Res.*, *110*(B11409), doi:10.1029/2004JB003421. 2.3.2, 2.4.1, 2.8

Shepherd, A., D. J. Wingham, J. A. D. Mansley, and H. F. J. Corr (2001), Inland thinning of Pine Island Glacier, West Antarctica, *Science*, *291*(5505), 862–864, doi:10.1126/science.291.5505.862. 3.1

Shewchuk, J. R. (1996), Triangle: Engineering a 2D quality mesh generator and Delaunay triangulator, in *Applied Computational Geometry Towards Geometric Engineering*, vol. 1148, edited by M. C. Lin and D. Manocha, pp. 203–222, Springer Berlin / Heidelberg, doi:10.1007/BFb0014497. 6.1.6

Silver, P. G., and W. W. Chan (1991), Shear-wave splitting and subcontinental mantle deformation, *J. Geophys. Res.*, *96*(B10), 16,429–16,454, doi:10.1029/91JB00899. 2.5.3

Smalley, R., M. A. Ellis, J. Paul, and R. B. V. Arsdale (2005), Space geodetic evidence for rapid strain rates in the New Madrid seismic zone of central USA, *Nature*, *435*(7045), 1088–1090, doi:10.1038/nature03642. 7.4

Smith, S. W., and M. Wyss (1968), Displacement on San Andreas fault subsequent to 1966 Parkfield earthquake, *Bull. Seismol. Soc. Am.*, *58*(6), 1955–1973. 1.4.3

Sol, S., A. Meltzer, R. Bürgmann, R. D. van der Hilst, R. King, Z. Chen, P. O. Koons, E. Lev, Y. P. Liu, P. K. Zeitler, X. Zhang, J. Zhang, and B. Zurek (2007), Geodynamics of the southeastern Tibetan Plateau from seismic anisotropy and geodesy, *Geology*, *35*(6), 563–566, doi:10.1130/G23408A.1. 2.5.3

Sonder, L. J., and P. England (1986), Vertical averages of rheology of the continental lithosphere: relation to thin sheet parameters, *Earth Planet Sci. Lett.*, *77*(1), 81–90, doi:10.1016/0012-821X(86)90134-2. 1.2.1, 1.2.1, 5.1

Stüwe, K. (2002), *Geodynamics of the lithosphere: An introduction*, 1 ed., Springer-Verlag. 1.3, 1.3.2, 1.3.3

Stüwe, K., J. Robl, S. Hergarten, and L. Evans (2008), Modeling the influence of horizontal advection, deformation, and late uplift on the drainage development in the India-Asia collision zone, *Tectonics*, *27*(TC6011), doi:10.1029/2007TC002186. 5.1

Talebian, M., E. J. Fielding, G. J. Funning, M. Ghorashi, J. Jackson, H. Nazari, B. Parsons, K. Priestley, P. A. Rosen, R. Walker, and T. J. Wright (2004), The 2003 Bam (Iran) earthquake: Rupture of a blind strike-slip fault, *Geophys. Res. Lett.*, *31*(L11611), doi:10.1029/2004GL020058. 1.4.1, 3.1

Tapponnier, P., G. Peltzer, A. Y. Le Dain, R. Armijo, and P. Cobbold (1982), Propagating extrusion tectonics in Asia: New insights from simple experiments with plasticine, *Geology*, *10*, 611–616, doi:10.1130/0091-7613(1982)10. 2.3.2, 2.3.2, 2.6.1, 2.6.1, 7.1

Tapponnier, P., G. Peltzer, and R. Armijo (1986), On the mechanics of the collision between India and Asia, in *Collision Tectonics*, edited by M. P. Coward and A. C. Ries, pp. 115–157, Geological Society, London. 2.3.2, 2.6.1

Tapponnier, P., F. J. Ryerson, J. Van der Woerd, A. S. Mériaux, and C. Lasserre (2001a), Long-term slip rates and characteristic slip: keys to active fault behaviour and earthquake hazard, *Comptes Rendus de l'Académie des Sciences - Series IIA - Earth and Planetary Science*, *333*(9), 483–494, doi:10.1016/S1251-8050(01)01668-8. 2.3.2

Tapponnier, P., X. Zhiqin, F. Roger, B. Meyer, N. Arnaud, G. Wittlinger, and Y. Jingsui (2001b), Oblique stepwise rise and growth of the Tibet plateau, *Science*, *294*(5547), 1671–1677, doi:10.1126/science.105978. 2.3.2, 2.5.1, 2.6.1

Taylor, M., and G. Peltzer (2006), Current slip rates on conjugate strike-slip faults in central Tibet using synthetic aperture radar interferometry, *J. Geophys. Res.*, *111*(B12402), doi:10.1029/2005JB004014. 2.1, 2.3.2, 3.2.5, 4.1, 4.3, 4.7

Taylor, M., and A. Yin (2009), Active structures of the Himalayan-Tibetan orogen and their relationships to earthquake distribution, contemporary strain field, and Cenozoic volcanism, *Geosphere*, *5*(3), 199–214, doi:10.1130/GES00217.1. 2.2, 2.3, 2.6, 4.1, 4.2, 4.6, 4.11, 4.13, 4.16, 4.5.4

Taylor, M., A. Yin, F. J. Ryerson, P. Kapp, and L. Ding (2003), Conjugate strike-slip faulting along the Bangong-Nujiang suture zone accommodates coeval east-west extension and north-south shortening in the interior of the Tibetan Plateau, *Tectonics*, *22*(4), 1044, doi:10.1029/2002TC001361. 2.3.2

Thatcher, W. (1975), Strain accumulation and release mechanism of 1906 San Francisco earthquake, *J. Geophys. Res.*, *80*(35), 4862–4872, doi:10.1029/JB080i035p04862. 1.4.3, 1.4.3

Thatcher, W. (1983), Non-linear strain buildup and the earthquake cycle on the San Andreas fault, *J. Geophys. Res.*, *88*(B7), 5893–5902, doi:10.1029/JB088iB07p05893. 1.10, 1.4.3

Thatcher, W. (2007), Microplate model for the present-day deformation of Tibet, *J. Geophys. Res.*, *112*(B01401), doi:10.1029/2005JB004244. 1.1, 2.16, 2.6.2, 7.2, 7.2, 7.1

Thatcher, W. (2009), How the Continents Deform: The Evidence From Tectonic Geodesy, *Annu. Rev. Earth Pl. Sc.*, *37*, 237–262, doi:10.1146/annurev.earth.031208.100035. 1.1, 1.2

Tilmann, F., J. Ni, and INDEPTH III Seismic Team (2003), Seismic imaging of the downwelling Indian lithosphere beneath central Tibet, *Science*, *300*(5624), 1424–1427, doi:10.1126/science.1082777. 2.5.1

Turcotte, D. L., and G. Schubert (1982), *Geodynamics: Applications of continuum physics to geological problems*, 1 ed., New York: John Wiley & Sons, Inc. 1.3.2, 1.3.3, 5.2.1

Van der Woerd, J., F. Ryerson, P. Tapponnier, Y. Gaudemer, R. Finkel, A. Meriaux, M. Caffee, Z. Guoguang, and H. Qunlu (1998), Holocene left-slip rate determined by cosmogenic surface dating on the Xidatan segment of the Kunlun fault (Qinghai, China), *Geology*, *26*, 695–698, doi:10.1130/0091-7613(1998)026. 2.3.2

Vasco, D. W., A. Rucci, A. Ferretti, F. Novali, R. C. Bissell, P. S. Ringrose, A. S. Mathieson, and I. W. Wright (2010), Satellite-based measurements of surface deformation reveal fluid flow associated with the geological storage of carbon dioxide, *Geophys. Res. Lett.*, *37*(L03303), doi:10.1029/2009GL041544. 3.1

Vergnolle, M., E. Calais, and L. Dong (2007), Dynamics of continental deformation in Asia, *J. Geophys. Res.*, *112*(B11403), doi:10.1029/2006JB004807. 2.6.3, 2.19, 6, 6.1.2

Vigny, C., A. Socquet, C. Rangin, N. Chamot-Rooke, M. Pubelier, M. N. Bouin, G. Bertrand, and M. Becker (2003), Present day crustal deformation around Sagaing fault, Burma, *J. Geophys. Res.*, *108*(B11), 2533, doi:10.1029/2002JB001999. 2.3.2

Vilotte, J. P., M. Daignières, and R. Madariaga (1982), Numerical modeling of intraplate deformation: simple mechanical models of continental collision, *J. Geophys. Res.*, *87*(B13), 10,709–10,728, doi:10.1029/JB087iB13p10709. 2.6.3

Vilotte, J. P., M. Daignières, R. Madariaga, and O. C. Zienkiewicz (1984), The role of a heterogeneous inclusion during continental collision, *Phys. Earth Planet. Inter.*, *36*(3-4), 236–259, doi:10.1016/0031-9201(84)90049-9. 2.6.3

Vilotte, J. P., R. Madariaga, M. Daignières, and O. C. Zienkiewicz (1986), Numerical study of continental collision: Influence of buoyancy forces and a stiff inclusion, *Geophys. J. R. Astron. Soc.*, *84*, 279–310, doi:10.1111/j.1365-246X.1986.tb04357.x. 2.6.3

von Allmen, P. A., Z. Xing, E. J. Fielding, E. Fishbein, L. Pan, and Z. Li (2010), OSCAR: Online service for correcting atmosphere in radar, *AGU Fall Meeting 2010*, (IN43B-1396). 3.2.5, 4.6, 7.5

Wallace, K., G. Yin, and R. Bilham (2004), Inescapable slow slip on the Altyn Tagh fault, *Geophys. Res. Lett.*, *31*(L09613), doi:10.1029/2004GL019724. 2.3.2, 7.1

Wang, C. Y., L. M. Flesch, P. G. Silver, L. J. Chang, and W. W. Chan (2008), Evidence for mechanically coupled lithosphere in central Asia and resulting implications, *Geology*, *36*(5), 363–366, doi:10.1130/G24450A.1. 2.13, 2.5.3

Wang, C. Y., L. Zhu, H. Lou, B. S. Huang, Z. Yao, and X. Luo (2010), Crustal thicknesses and Poisson's ratios in the eastern Tibetan Plateau and their tectonic implications, *J. Geophys. Res.*, *115*(B11301), doi:10.1029/2010JB007527. 2.5.2

Wang, H., and T. J. Wright (2010), PIRATE (V2.0b2): Poly-Interferogram Rate And Time-series Estimator, `http://homepages.see.leeds.ac.uk/~earhw/pirate/`, Retrieved 24/07/2011. 3.3

Wang, H., and T. J. Wright (2011), Satellite geodetic imaging reveals high strain away from major faults of Western Tibet, *Unpublished manuscript*. 2.3.2, 3.3.4, 4.1, 7.4

Wang, H., T. J. Wright, and J. Biggs (2009), Interseismic slip rate of the northwestern Xianshuihe fault from InSAR data, *Geophys. Res. Lett.*, *36*(L03302), doi:10.1029/2008GL036560. 2.3.2, 3.3, 4.1, 7.4

Wang, H., M. Liu, J. Cao, X. Shen, and G. Zhang (2011), Slip rates and seismic moment deficits on major active faults in mainland China, *J. Geophys. Res.*, *116*(B02405), doi:10.1029/2010JB007821. 2.6.2

Wang, Q., P. Z. Zhang, J. T. Freymueller, R. Bilham, K. M. Larson, X. Lai, X. Z. You, Z. J. Niu, J. C. Wu, Y. X. Li, J. N. Liu, Z. Q. Yang, and Q. Z. Chen (2001), Present-day crustal deformation in China constrained by global positioning system measurements, *Science*, *294*(5542), 574–577, doi:10.1126/science.1063647. 2.4.1, 2.4.1

Wang, Y. (2001), Heat flow pattern and lateral variations of lithosphere strength in China mainland: constraints on active deformation, *Phys. Earth Planet. Inter.*, *126*(3-4), 121–146, doi:10.1016/S0031-9201(01)00251-5. 2.2.1, 6.1.2

Wang, Y. H., G. A. Houseman, G. Lin, F. Guo, Y. J. Wang, W. M. Fan, and X. Chang (2005), Mesozoic lithospheric deformation in the North China block: Numerical simulation of evolution from orogenic belt to extensional basin system, *Tectonophysics*, *405*(1-4), 47–63, doi:10.1016/j.tecto.2005.05.012. 5.1

Wei, M., D. Sandwell, and B. Smith-Konter (2010), Optimal combination of InSAR and GPS for measuring interseismic crustal deformation, *Advances in Space Research*, *46*(2), 236–249, doi:10.1016/j.asr.2010.03.013. 3.2.6

Wen, Y., Z. Li, C. Xu, I. Ryder, and R. Bürgmann (2011), Postseismic motion after the 2001 Mw 7.8 Kokoxili earthquake in Tibet observed by InSAR time series, *J. Geophys. Res.*, in review. 4.1

Werner, C., U. Wegmuller, T. Strozzi, and A. Weismann (2000), Gamma SAR and interferometric processing software, *Proceedings of the ERS-ENVISAT symposium*. 3.2.4

Weston, J., A. M. G. Ferreira, and G. J. Funning (2011), Global compilation of interferometric synthetic aperture radar earthquake source models: 1. Comparisons with seismic catalogs, *J. Geophys. Res.*, *116*(B08408), doi:10.1029/2010JB008131. 1.4.1

Whitehouse, P. L. (2004), The mechanics of continental deformation in Asia and California, Ph.D. thesis, Faculty of Physical Sciences, University of Oxford. 2.6.3, 6, 6.1.2

Whitehouse, P. L., P. C. England, and G. A. Houseman (2005), A physical model for the motion of the Sierra Block relative to North America, *Earth Planet Sci. Lett.*, *237*(3-4), 590–600, doi:10.1016/j.epsl.2005.03.028. 5.1

Windley, B. F., M. B. Allen, C. Zhang, Z. Y. Zhao, and G. R. Wang (1990), Paleozoic accretion and Cenozoic redeformation of the Chinese Tien-Shan-range, central Asia, *Geology*, *18*(2), 128–131, doi:10.1130/0091-7613(1990)018¡0128:PAACRO¿2.3.CO;2. 2.4.1

Wright, T. J. (2000), Crustal deformation in Turkey from synthetic aperture radar interferometry, Ph.D. thesis, Faculty of Physical Sciences, University of Oxford. 3.1, 3.2.2, 3.2.2, 3.2.2

Wright, T. J. (2002), Remote monitoring of the earthquake cycle using satellite radar interferometry, *Phil. Trans. R. Soc. Lond. A*, *360*(1801), 2873–2888, doi:10.1098/rsta.2002.1094. 1.6, 1.7, 1.4.1

Wright, T. J., P. J. Clarke, and G. J. Funning (2005), Realistic errors for models derived from InSAR data, *Unpublished manuscript*. 3.3.6

Wright, T. J., E. J. Fielding, and B. Parsons (2001a), Triggered slip: observations of the 17 August 1999 Izmit (Turkey) earthquake using radar interferometry, *Geophys. Res. Lett.*, *28*(6), 1079–1082, doi:10.1029/2000GL011776. 1.7, 1.4.1, 3.1

Wright, T. J., B. Parsons, and E. J. Fielding (2001b), Measurement of interseismic strain accumulation across the North Anatolian Fault by satellite radar interferometry, *Geophys. Res. Lett.*, *28*(10), 2117–2120, doi:10.1029/2000GL012850. 1.4.2, 3.1

Wright, T. J., B. Parsons, P. C. England, and E. J. Fielding (2004a), InSAR observations of low slip rates on the major faults of western Tibet, *Science*, *305*(5681), 236–239, doi:10.1126/science.1096388. 2.3.2, 2.3.2, 4.1

Wright, T. J., B. E. Parsons, and Z. Lu (2004b), Toward mapping surface deformation in three dimensions using InSAR, *Geophys. Res. Lett.*, *31*(L01607), doi:10.1029/2003GL018827. 7.5

Wright, T. J., C. Ebinger, J. Biggs, A. Ayele, G. Yirgu, D. Keir, and A. Stork (2006), Magma-maintained rift segmentation at continental rupture in the 2005 Afar dyking episode, *Nature*, *442*(7100), 291–294, doi:10.1038/nature04978. 3.1

Wright, T. J., M. C. Garthwaite, H. Jung, and A. Shepherd (2010), How accurately can current, planned and proposed InSAR missions measure slow, long-wavelength tectonic strain?, `http://adsabs.harvard.edu/abs/2010AGUFM.G13B..06W`, AGU Fall Meeting, Dec 2010, G13B-06. 7.5

Wright, T. J., N. Houlié, M. Hildyard, and T. Iwabuchi (2011), Rapid, reliable magnitudes for large earthquakes from GPS, *Geophys. Res. Lett.*, In Review. 1.4.1

Yin, A. (2006), Cenozoic tectonic evolution of the Himalayan orogen as constrained by along-strike variation of structural geometry, exhumation history, and foreland sedimentation, *Earth Sci. Rev.*, *76*(1-2), 1–131, doi:10.1016/j.earscirev.2005.05.004. 2.2.1

Yin, A., and T. M. Harrison (2000), Geologic evolution of the Himalayan-Tibetan orogen, *Annu. Rev. Earth Pl. Sc.*, *28*, 211–280, doi:10.1146/annurev.earth.28.1.211. 2.1, 2.1.3, 2.3.1

Zatman, S. (2000), On steady rate coupling between an elastic upper crust and a viscous interior, *Geophys. Res. Lett.*, *27*(16), 2421–2424, doi:10.1029/2000GL011592. 1.4.2, 7.1

Zebker, H. A., P. A. Rosen, and S. Hensley (1997), Atmospheric effects in interferometric synthetic aperature radar surface deformation and topographic maps, *J. Geophys. Res.*, *102*(B4), 7547–7564, doi:10.1029/96JB03804. 3.2.2

Zhang, P.-Z., Z. Shen, M. Wang, W. Gan, R. Bürgmann, P. Molnar, Q. Wang, Z. Niu, J. Sun, J. Wu, S. Hanrong, and Y. Xinzhao (2004), Continuous deformation of the Tibetan Plateau from global positioning system data, *Geology*, *32*(9), 809–812, doi:10.1130/G20554.1. 2.3.2, 2.4.1, 2.16, 2.6.2

Zhang, P.-Z., P. Molnar, and X. Xu (2007), Late Quaternary and present-day rates of slip along the Altyn Tagh Fault, northern margin of the Tibetan Plateau, *Tectonics*, *26*(TC5010), doi:10.1029/2006TC002014. 2.3.2

Zhang, Z., Y. Wang, Y. Chen, G. A. Houseman, X. Tian, E. Wang, and J. Teng (2009), Crustal structure across Longmenshan fault belt from passive source seismic profiling, *Geophys. Res. Lett.*, *36*(L17310), doi:10.1029/2009GL039580. 2.5.2

Zhao, J., X. Yuan, H. Liu, P. Kumar, S. Pei, R. Kind, Z. Zhang, J. Teng, L. Ding, X. Gao, Q. Xu, and W. Wang (2010), The boundary between the Indian and Asian tectonic plates below Tibet, *Proc. Natl. Acad. Sci. U.S.A.*, *107*(25), 11,229–11,233, doi:10.1073/pnas.1001921107. 2.12, 2.5.2, 2.5.3

Zhao, W. J., K. D. Nelson, J. Che, J. Quo, D. Lu, C. Wu, and X. Liu (1993), Deep seismic-reflection evidence for continental underthrusting beneath southern Tibet, *Nature*, *366*(6455), 557–559, doi:10.1038/366557a0. 2.3.1

Zhao, W. L., and W. J. Morgan (1987), Injection of Indian crust into Tibetan lower crust - A two-dimensional finite-element model study, *Tectonics*, *6*(4), 489–504, doi:10.1029/TC006i004p00489. 2.6.4

Zienkiewicz, O., and R. Taylor (2000), *The finite element method*, 5 ed., Elsevier Butterworth-Heinemann, Oxford. 5.3, 5.3.2

Zubovich, A. V., X.-Q. Wang, Y. G. Scherba, G. G. Schelochkov, R. Reilinger, C. Reigber, O. I. Mosienko, P. Molnar, W. Michajljow, V. I. Makarov, J. Li, S. I. Kuzikov, T. A. Herring, M. W. Hamburger, B. H. Hager, Y.-M. Dang, V. D. Bragin, and R. T. Beisenbaev (2010), GPS velocity field for the Tien Shan and surrounding regions, *Tectonics*, *29*(TC6014), doi:10.1029/2010TC002772. 2.3.1, 2.6, 2.4.1, 6.1.3, 6.3

Appendix A

SAR Data

Table A.1: Details of acquisitions in the Envisat archive for descending track 176 in the region of the Tibetan plateau and plotted in Figure 4.3. Epochs in format YYMMDD. Baselines and Coverage are given relative to epoch 070520. An ID is given to epochs used in this thesis, and plotted in Figure 3.16. Columns headed '31' and '70' give the number of connections for each epoch in those networks.

ID	Epoch	Orbit	Baseline (m)	Coverage (%)	31	70
1	030406	5741	299	78.33	1	3
	030511	6242	-519	78.33		
2	030615	6743	175	42.34	1	2
	030615	6743	99	27.98		
3	030720	7244	267	78.33	3	5
4	030928	8246	272	78.33	3	5
	031102	8747	1003	15.19		
5	031102	8747	983	89.42	1	2
	031102	8747	977	73.61		
	031102	8747	930	10.46		
	031207	9248	334	23.84		
6	031207	9248	300	73.73	3	6
7	040111	9749	-467	100.00	2	4
8	040215	10250	374	100.00	1	3
9	040321	10751	-981	100.00	1	3
	040530	11753	-432	8.23		
10	040530	11753	-534	89.33	2	6
11	041121	14258	6	62.67	2	5
	041226	14759	-28	67.77		
	041226	14759	-22	73.60		
12	041226	14759	-20	75.28	2	4

Continued on next page

Table A.1 – continued from previous page

ID	Epoch	Orbit	Baseline (m)	Coverage (%)	31	70
	041226	14759	55	6.90		
	050306	15761	-144	53.78		
	050515	16763	-473	33.76		
	050619	17264	-286	20.39		
13	050724	17765	-546	97.37	2	4
14	050828	18266	-635	88.37	3	4
	051002	18767	-282	20.08		
	051211	19769	-32	62.13		
	060115	20270	871	26.12		
	060115	20270	839	36.18		
	060219	20771	163	30.42		
	060430	21773	-309	24.06		
	060604	22274	585	11.90		
	060604	22274	615	24.05		
	060709	22775	-1011	23.77		
15	060813	23276	-903	80.66	1	3
	061022	24278	434	14.81		
	061022	24278	411	24.19		
16	061126	24779	148	100.00	2	5
17	070311	26282	-384	100.00	2	6
18	070415	26783	126	100.00	2	3
19	070520	27284	0	100.00	3	6
20	070624	27785	-9	100.00	3	5
21	070729	28286	51	78.80	2	3
22	070902	28787	-310	34.41	1	5
	070902	28787	-243	9.87		
	071007	29288	185	14.50		
	071007	29288	158	9.87		
23	071111	29789	-190	98.61	3	4
	080120	30791	140	23.67		
	080224	31292	265	14.50		
24	080504	32294	10	86.01	2	6
25	080713	33296	-229	86.01	1	5
26	080921	34298	193	96.87	2	6
27	081026	34799	-48	100.00	1	5
28	090104	35801	-123	100.00	2	3
29	090315	36803	509	100.00	1	2

Continued on next page

Table A.1 – continued from previous page

ID	Epoch	Orbit	Baseline (m)	Coverage (%)	31	70
30	090419	37304	295	100.00	4	4
31	090524	37805	-65	100.00	2	5
32	090628	38306	-221	100.00	1	3
	090802	38807	-1	100.00		
	090906	39308	-298	100.00		
	091115	40310	-203	62.84		
	091220	40811	150	100.00		
	100124	41312	-215	100.00		
	100228	41813	242	100.00		
	100404	42314	-454	94.69		
	100509	42815	-230	97.16		
	100613	43316	-198	99.21		
	100718	43817	129	94.02		
	100822	44318	79	98.30		
	100926	44819	-255	26.89		